MEASUREMENT OF FIELD ALIGNED ELECTRON DENSITY DISTRIBUTION, DUCTS, AND Z MODE CAVITIES FROM DUCTED AND NONDUCTED FAST Z MODE ECHOES OBSERVED ON THE IMAGE SATELLITE

by

Kumar Mayank

RECOMMENDED:

Dr. Joan Braddock

Dr. Martin Truffer

Dr. William Simpson

Dr. David Newman
Advisory Committee Chair

Dr. Curt Szuberla
Chair, Department of Physics

APPROVED:

Dr. Paul Layer
Dean, College of Natural Science and Mathematics

Dr. John Eichelberger
Dean of the Graduate School

24 April 2015
Date

MEASUREMENT OF FIELD ALIGNED ELECTRON DENSITY DISTRIBUTION, DUCTS, AND Z MODE CAVITIES FROM DUCTED AND NONDUCTED FAST Z MODE ECHOES OBSERVED ON THE IMAGE SATELLITE

A

DISSERTATION

Presented to the Faculty

of the University of Alaska Fairbanks

in Partial Fulfillment of the Requirements

for the Degree of

DOCTOR OF PHILOSOPHY

By

Kumar Mayank

Fairbanks, Alaska

May 2015

Abstract

Z mode (ZM) sounding from the Radio Plasma Imager (RPI) onboard the Imager for Magnetopause-to-Aurora Global Exploration (IMAGE) satellite has provided a new method to measure the geomagnetic field aligned electron density (N_e) distribution, magnetospheric ducts, and Z mode cavities in the low- to mid-latitude region of the magnetosphere from the ducted and nonducted fast ZM echoes observed from radio sounding at 20-1000 kHz. Z mode is a trapped wave mode of the plasma confined in frequency between the ZM cutoff frequency, f_z, and the upper hybrid resonance frequency, f_{uh}. In the past, trapped ducted Z mode echoes in the ZM cavity were used to measure field aligned electron density thousands of kilometers above the satellite altitude. However, no attempt was made to study the properties of the ducts that can guide ZM waves. Magnetospheric ducts play an important role in the propagation of plasma waves, wave particle interactions, particle acceleration, and precipitation. In the past, ducts have been known since the discovery of the plasmasphere, but there is limited knowledge of the properties of ducts, their origins and occurrence patterns, and their distribution on a global scale in the magnetosphere especially for ducts extending to high altitudes (above 1000 km). Analysis of ducted echoes from the conjugate and local hemispheres has enabled nearly instantaneous magnetic field aligned electron density profiles. Field aligned density distribution plays an important role in magnetospheric dynamics. Despite its importance, there is a lack of accurate representation of the latitudinal dependence of density distribution along the field lines by the existing empirical models, due to limited measurement of off-equatorial electron density profiles and availability of relatively fewer measurements of N_e at higher altitudes. There is also a need to describe the transition of field aligned electron densities from the topside ionosphere into the plasmasphere properly.

RPI on IMAGE, designed to sweep from 3 kHz to 3 MHz, has observed both ducted and nonducted ZM echoes in the frequency range of 40 - 800 kHz in an altitude range of ~600-10,000 km, invariant latitude of ~20°-90°, at all magnetic local times (MLTs) and for an f_{pe}/f_{ce} range of 0.25-6, where f_{pe} and f_{ce} are electron plasma frequency and electron gyro frequency respectively. About 72,000 plasmagrams have been surveyed, out of which ~1500 cases of ducted- and ~3500 cases of nonducted fast ZM echoes have been identified. Two cases of ducted, two cases of nonducted, and a set of seven successive cases of nonducted and ducted fast ZM echoes have been analyzed to study the propagation, reflection, and guidance of fast ZM waves in the magnetosphere and measure: (1) field aligned electron density distribution; (2) duct parameters (half-width ΔL and density variation $\Delta N/N$); and (3) Z mode cavity parameters. In absence of ducts, four nonducted

echoes are obtained, each reflecting from locations where $f_z \sim f$, where f is the wave frequency. Three of the echoes retrace their path after reflection and one forms a loop. When a N_e depletion duct is present inside a Z mode cavity, fast Z mode waves can be guided within the duct and propagate back and forth between their reflection points above and below the satellite altitude. Ray tracing calculations of ducted Z mode echoes show that: (1) in the presence of ducts, both nonducted and ducted echoes are obtained, and echoes are formed from both looping as well as retracing paths; (2) average time delays (t_g) depend upon the electron density distribution along geomagnetic field lines and the shape of the Z mode cavity; (3) time delay spread (Δt_g) and upper cutoff frequency (f_{uc}) depend upon duct half-width (ΔL) and density perturbation ($\Delta N/N$); (4) echoes are obtained from local as well as conjugate hemispheres when the duct extends to the conjugate hemisphere; and (5) the discovery of a new phenomenon of gap in frequency for echoes reflecting from below the satellite altitude. The gap frequency range depends upon the duct parameters and is a consequence of the peculiar shape of the refractive index surface for $f \sim f_{pe}$. From ZM soundings of 11 case studies, it is found that the measured ducts have half-widths of ~160-500 km at the equator and density depletions of ~1%-6%, covering an altitude range of ~1000-10,000 km. The first quantitative measurements of ZM cavities have been presented in this thesis. The bandwidth and the length of ZM cavities lie in the range of ~10-50 kHz and ~3800-15,000 km, respectively. From the inversion of time delay versus frequency dispersion of the fast ZM echoes, field aligned electron density distributions both above and below the satellite from an altitude of ~1000-10,000 km (and ~90-10,000 km if accompanied by Whistler mode echoes) are obtained. The electron density profiles obtained from ZM sounding are in good agreement with in-situ electron density measurements from the CHAMP(~350 km) and DMSP(~850 km) satellites, from RPI passive measurements, and give a better estimate of electron density as compared to empirical density models.

Our results demonstrate that ZM sounding is a new and powerful method to measure field aligned electron density distribution, magnetospheric ducts, and ZM cavities in the altitude range of ~1000-10,000 km (and ~90-10,000 km if accompanied by Whistler mode echoes) at low- to mid-latitude region of the magnetosphere. These measurements can improve the existing empirical density models and provide a new understanding of the magnetospheric ducts as well as of waves propagating therein.

Table of Contents

List of Figures

Page

Page

Page

Page

Page

Page

List of Tables

Page

Page

Page

Acknowledgments

I would like to acknowledge Professor Vikas Sonwalkar for introducing me to this research subject. I am grateful to my principal dissertation advisor, Professor David Newman, for his encouragement and valuable comments on improving my thesis. I would like to express my gratitude to my committee members: Professor Joan Braddock, Professor Martin Truffer, and Professor William Simpson for their encouragement, support, and a careful review of this dissertation. I owe a special thanks to Dean John Eichelberger, without whose constant encouragement, help, and support this dissertation would not have been possible. I would like to thank the graduate school staff for working on my behalf and making my graduation possible. I acknowledge international school advisor, Carol Holz, for her support and taking care of my official paperwork. I am grateful to all my friends for their moral support and encouragement.

I would like to thank my parents, Sidheshwar Prasad Chauhan and Poonam Chauhan, and my sister, Pallavi, my brother Amit and sister in law Tanuja for believing in me and for their unconditional love, support and encouragement. Above all, I thank my wife Susmita Hazra for her love, patience and emotional support throughout this long and difficult process and my little angel Ojasvi for bestowing happiness and love on me.

This research was supported in part by the National Aeronautics and Space Administration graduate assistantship. I also acknowledge the support from College of Natural Science and Mathematics through teaching assistantship and University of Alaska Fairbanks Graduate School for providing the support through the thesis completion fellowship.

Chapter 1 Introduction

1.1 Objectives and Motivation

The Earth has an intrinsic magnetic field which is generated by the combination of radial convection and rotation of the highly conductive molten metal core. The Earth's magnetic field resembles a huge bar magnet whose north pole is aligned towards the geographic south and vice-versa. For distances close to the Earth's surface ($\sim$5 Earth radii), the magnetic field can be approximated as a dipolar field. The Earth's magnetic field interacts with the solar wind, a stream of plasma emanating continuously from the sun, forming a geomagnetic cavity. The aggregation of positively and negatively charged particles is called as plasma. The solar wind particles are not able to penetrate the Earth's magnetic field and flows around it. The magnetic field is distorted due to this interaction and is compressed on the dayside and is elongated on the night side. The cavity formed due to this interaction is called the magnetosphere where the motion of charged particles are dominated by the Earth's magnetic field. The Earth's magnetosphere consists of various plasma regions of varying densities and temperature. The ionosphere is the partially ionized part of the atmosphere and the innermost region of the magnetosphere. It consists of electrons and positive ions formed by the ionization of neutral particles by the solar radiation such as extreme ultra violet (EUV), ultra violet (UV), Lyman alpha and X rays and particle precipitation at higher latitudes and galactic cosmic rays. The fraction of ionization is of the order of $10^{-11} - 10^{-5}$. The ionosphere starts at $\sim$60 km and extends up to $\sim$1000 km. The magnetospheric region above the ionosphere is called as the plasmasphere. It is a doughnut shaped region of high density ($10 - 10^4\,\mathrm{cm}^{-3}$), relatively cold plasma ($\sim$1 eV), which corotates with the Earth. The cold plasma density distribution of the plasmasphere affects the generation and propagation of the natural wave emissions. These wave emissions interact with the energetic particles and influence the radiation belt dynamics. The Earth's magnetosphere consists of electrons, positive ions, and the background magnetic field, therefore, it can support a wide varieties of electromagnetic, electrostatic and magnetosonic waves.

These waves are important because they transfer energy and information from one part of the magnetosphere to another. These waves have been used as an important diagnostic tools to study the plasma environment. One of the wave modes that exist in the magnetospheric plasma is the Z mode wave. The Z mode wave is a trapped wave mode of the plasma. Z mode wave exists between the cutoff frequency f_z and the upper hybrid resonance frequency f_{uh}. A more detailed description is provided in the subsequent sections.

The objectives of this research are to study the propagation of Z mode (ZM) waves in the magnetosphere based on ZM echoes observed on the IMAGE satellite, to develop a novel method of ZM radio sounding and, to apply the sounding technique to measure parameters of magnetospheric ducts, ZM cavities, and field aligned electron density (N_e) distributions. The work presented in this thesis provides direct measurements of magnetospheric ducts and ZM cavities obtained from ducted ZM echoes. It provides duct parameters, including duct half-width, density depletions and occurrence patterns in the region extending from outside the plasmapause region to well inside the plasmasphere. Measurement of field aligned electron density, duct parameters (half-width and density perturbation), and ZM cavities is important to test theoretical and numerical models of plasma density distribution and identify various regions of electromagnetic wave emissions in the magnetosphere.

ZM waves' phase refractive index (μ) varies from the superluminous range ($\mu < 1$) to the subluminous range ($\mu > 1$). ZM frequency bandwidth, ranging from ZM cutoff frequency (f_z) to upper hybrid resonance frequency (f_{uh}), is strongly dependent upon electron plasma frequency (f_{pe}) and electron gyro frequency (f_{ce}). Due to these typical characteristics, ZM echoes have been observed over a wide range of plasma parameters (f_{pe}/f_{ce} ranging from 0.25 to 6) on the IMAGE/RPI and from equatorial to polar regions of the magnetosphere in the frequency range of 10 kHz-10 MHz. In the past, ZM echoes were observed by ground-based radio sounding experiments [Eckersley, 1933] and on topside sounders [Calvert, 1966; Nelms et al., 1966; Benson, 1982] but was not considered to be an important diagnostic tool for electron density profile measurements [Jackson et al., 1980]. However, the ZM sounding experiments on the IMAGE/RPI have proved to be an important diagnostic tool to determine field aligned electron density profiles [Reinisch et al., 2001; Carpenter et al., 2003]. Z mode traces obtained from vertical and oblique propagation, field aligned ducted propagation have been observed and reported on the topside sounders [Calvert, 1966; Nelms et al., 1966; Colin and Chan, 1969; Hagg et al., 1969; Muldrew, 1969]. Besides the above mentioned echoes, IMAGE/RPI has also recorded nonducted and ducted ZM echoes reflecting from above the

satellite altitude inside the ZM cavity and from outside the plasmapause. This type of echo has not been reported in the previous literature.

A refractive index cavity, called the ZM cavity, is observed in the magnetosphere in the altitude range of ~1000 - 10,000 km due to the variation of ZM cutoff frequency (f_z) profiles with f_{pe} and f_{ce} along geomagnetic field lines. ZM waves propagating in this cavity reflect while propagating both downwards and upwards and are essentially trapped in the presence of a duct to form spectacular ducted signatures on the IMAGE/RPI plasmagrams [Carpenter et al., 2003]. The optimum frequency range of IMAGE/RPI and its orbit coverage from equatorial to polar region has permitted the observation of ZM echoes within these cavities. The ZM cavity phenomenon has rarely been observed and reported in the past literature. Gurnett et al., (1983) have observed the trapped ZM radiation in the ZM cavity in the polar region on DE1 satellite. Carpenter et al., (2003) reported the first observation of ducted ZM echoes, on IMAGE/RPI, trapped within the ZM cavity in the magnetosphere. No measurement of the ZM cavity region exist in the past literature. This thesis presents the first measurement of the ZM cavity region observed on the IMAGE satellite. The ZM cavity phenomenon, observed on IMAGE/RPI, has been observed from outside the plasmapause to well within the plasmasphere from high to low latitude regions of the magnetosphere. ZM cavity regions may play an important role in the propagation of natural ZM emissions in the magnetosphere.

An important aspect of the ZM sounding on IMAGE/RPI is the observation of ZM echoes, which are guided along magnetospheric ducts. Magnetospheric ducts are large scale density structures aligned along the geomagnetic field lines ($\mathbf{B_0}$). The plasma density varies in direction perpendicular to ($\mathbf{B_0}$) and the spatial scale sizes in the cross field ($\mathbf{B_0}$) direction range from 1-1000 km and density perturbation of few percent to a few tens of percent [Sonwalkar, 2006]. Magnetospheric ducts play an important role in the magnetospheric dynamics. Ducts are responsible for wave-particle interactions and observations of natural wave emissions [Burgess and Inan 1993; Bell et al., 2009; Haque et al., 2011]. In the past, ducts have been observed since the discovery of the plasmasphere, but there is limited knowledge of the properties of ducts, their origins and occurrence patterns, and their distribution on a global scale in the magnetosphere [Darrouzet et al., 2009; Sonwalkar, 2006], especially for ducts extending to high altitudes (above 1000 km). Carpenter et al., (2003) have discussed the trapped ducted ZM echoes in the ZM cavity and used them to measure field aligned N_e thousands of kilometers above the satellite altitude. However, no attempt was made by the authors to study the properties of the ZM ducts. In this thesis measurements of duct parameters

obtained from ducted ZM echoes observed on the IMAGE satellite are presented.

Z mode sounding on IMAGE/RPI provides a powerful method for measurement of (1) field aligned electron density distributions; (2) field aligned magnetospheric ducts; and (3) ZM refractive index cavities in the 1000 - 10,000 km altitude range. Most of the ducted ZM echoes have been observed in the field lines near the plasmapause, providing an excellent opportunity to study the properties of ducts, ZM cavities, and electron density distribution in this poorly known region of space.

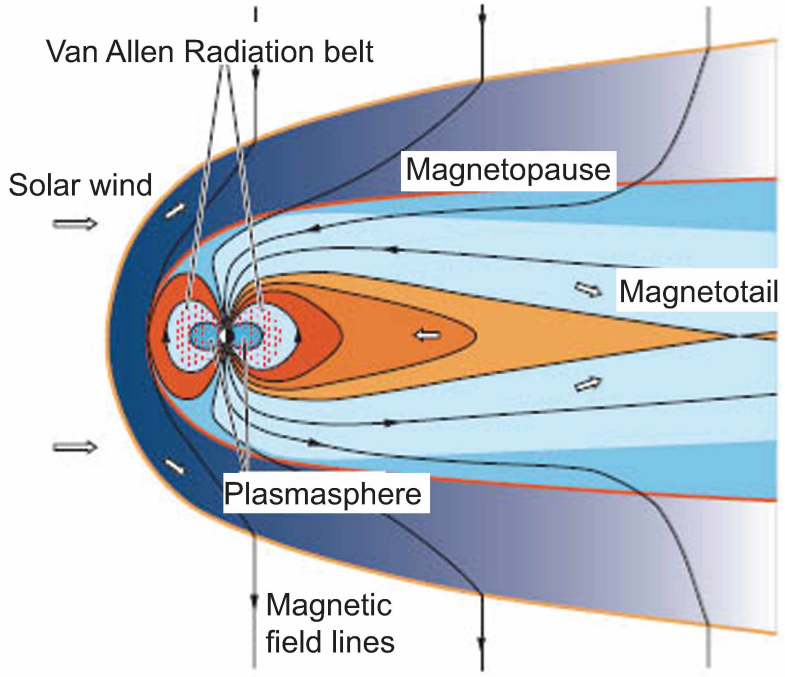

Figure 1.1 Schematic of the Earth's magnetosphere and its various plasma regions (http://nova.stanford.edu/vlf/IHY_Test/img/magnetosphere.jpg).

1.2 The Earth's Magnetosphere

The Earth's magnetosphere is a region of ionized gas or plasma whose dynamics are primarily governed by the geomagnetic field ($\mathbf{B_0}$). It is a complex region containing plasmas with a wide range of densities and temperatures. The Earth's magnetosphere behaves like a giant conducting fluid and is highly influenced by the solar wind. The solar wind is fully ionized plasma that continuously streams outward from the Sun. The geomagnetic field is generated by electric currents flowing in the Earth's molten, electrically conducting core [Chapman and Bartels, 1940]. The geomagnetic field in the inner magnetosphere, within 60° geomagnetic latitude and ~5 R_E, can be

approximated by a dipolar field whose axis is tilted by $\sim 11^{\circ}$ from the Earth's spin axis [Walker and Russell, 1995]. The dipole moment of the Earth's magnetic field is $\sim 8 \times 10^{15}$ Tm^3 [Barker et al., 1986]. The Earth's dipole field has its North pole pointing towards the Earth's South pole and vice-versa. Its strength is $\sim$0.3 Gauss at the equator and is 0.6 Gauss at the poles [http://www.ngdc.noaa.gov/IAGA/vmod/igrfhw.html]. At larger distances, the geomagnetic field departs significantly from the dipole field configuration, hence, higher order field equations are required to express the non-dipole geomagnetic field [Walker and Russell, 1995]. One such model is the International Geomagnetic Reference Field (IGRF) model. IGRF is a series of mathematical models of the main geomagnetic field and its annual rate of change (secular variation). The models consists of sets of spherical harmonic coefficients [Barker et al., 1986; http://www.ngdc.noaa.gov/IAGA/vmod/igrf.html]. The flow speed of solar wind is on the order of 300 - 800 km/s. Solar wind is mainly comprised of equal numbers of protons and electrons, with a small amount (5% by number) of ionized helium and other heavier ions. The average plasma density is ~ 5 cm^{-3} and an average energy of solar wind particles is $\sim$10 eV [Neugebauer and Snyder, 1966; Hundhausen, 1995].

The Earth's magnetic field provides an effective obstacle to the solar wind plasma. The solar wind dynamic pressure (typically 1.7 nPa) presses on the Earth's magnetic field, confining it to a magnetospheric cavity which is called the magnetosphere. The Earth's magnetic field pressure balances the solar wind dynamic pressure at $\sim 10\, R_E$, forming the cavity with its 'nose' in the sunward direction along the Sun-Earth line. A boundary layer, called the 'Magnetopause', which separates Earth's magnetic field and plasma from the solar wind plasma, is formed due to this interaction [Chapman and Ferraro 1931]. The cavity extends to ~ 15 R_E on either side of the Earth above the dawn-dusk terminators, and the solar wind stretches the terrestrial magnetic field for ~ 200 R_E in the anti-solar direction, forming the 'Magnetotail' [Kivelson and Russell, 1995]. The magnetotail acts as an energy reservoir, releasing energy during substorms. Figure 1.1 shows different regions of charged particles and electrical currents flowing in the magnetosphere. The region of cold plasma in the innermost region of the magnetosphere is the plasmasphere, which is the high altitude extension of the ionosphere.

1.3 Plasmasphere

The Plasmasphere is a doughnut-shaped region above the ionosphere which contains high density ($\sim 10-10^4 \mathrm{cm}^{-3}$), relatively cold ($\simeq$1eV), collisionless plasma consisting mainly of electrons, protons (H^+) and small population of Helium (He^+) and Oxygen (O^+) ions. In the plasmasphere, H^+ is the dominant species but He^+,O^+,O^{2+}, N^+, and N^{2+} are also observed [Kivelson and Russell, 1995; Goldstein, 2006]. The plasmasphere occupies roughly the same region of the inner magnetosphere as the Van Allen radiation belts and ring current and is populated by the steady flow of upper-ionospheric plasma called the 'polar wind' [Kivelson and Russell, 1995; Banks and Holzer, 1969; Nagai et al., 1984; Lemaire, 1989]. The plasmaspheric plasma corotates with the Earth and can also flow from one hemisphere to the other. An abrupt gradient or drop in density of the plasmaspheric plasma is caused by the convection-driven erosion of the outer plasmasphere. This steep drop in density is called the 'Plasmapause'. The plasmapause is a field aligned surface where the electron density drops by a factor of 5 or more in a span of $\sim$0.5 L [Carpenter and Anderson, 1992], where L is a parameter that describes a particular geomagnetic field line that crosses the Earth's magnetic equator at a distance of L Earth radii from the center of the Earth [McIlwain, 1961]. During quiet geomagnetic conditions, the plasmasphere is roughly circular in shape, with a slight bulge in the dusk sector, typically lying in the range of $\sim$3-5 R_E in the equatorial plane. During prolonged periods of very low geomagnetic activity, the plasmasphere can become quite large, reaching beyond geosynchronous orbit ($\sim$6.6 R_E), due to the dominant effect of the ionospheric refilling. During strongly active times, the plasmapause may come as close to the Earth as $L = 2.5$. The depleted region of plasma just outside the plasmapause is referred to as the plasma trough. The typical plasma density ranges from 1-10 particles/cm^3. The plasma trough consists of material that has been eroded from the main body of the plasmasphere that is being convected toward the magnetopause [Carpenter, 1963; Lemaire and Gringauz, 1998].

1.4 Waves in the Magnetosphere

Waves are periodic disturbances that travel through medium or space and can transfer energy from one point to another. There are two types of waves: (1) longitudinal waves, and (2) transverse waves. In a longitudinal waves the particle displacement is parallel to the direction of propagation of waves. In a transverse waves the particle displacement is perpendicular to the direction of

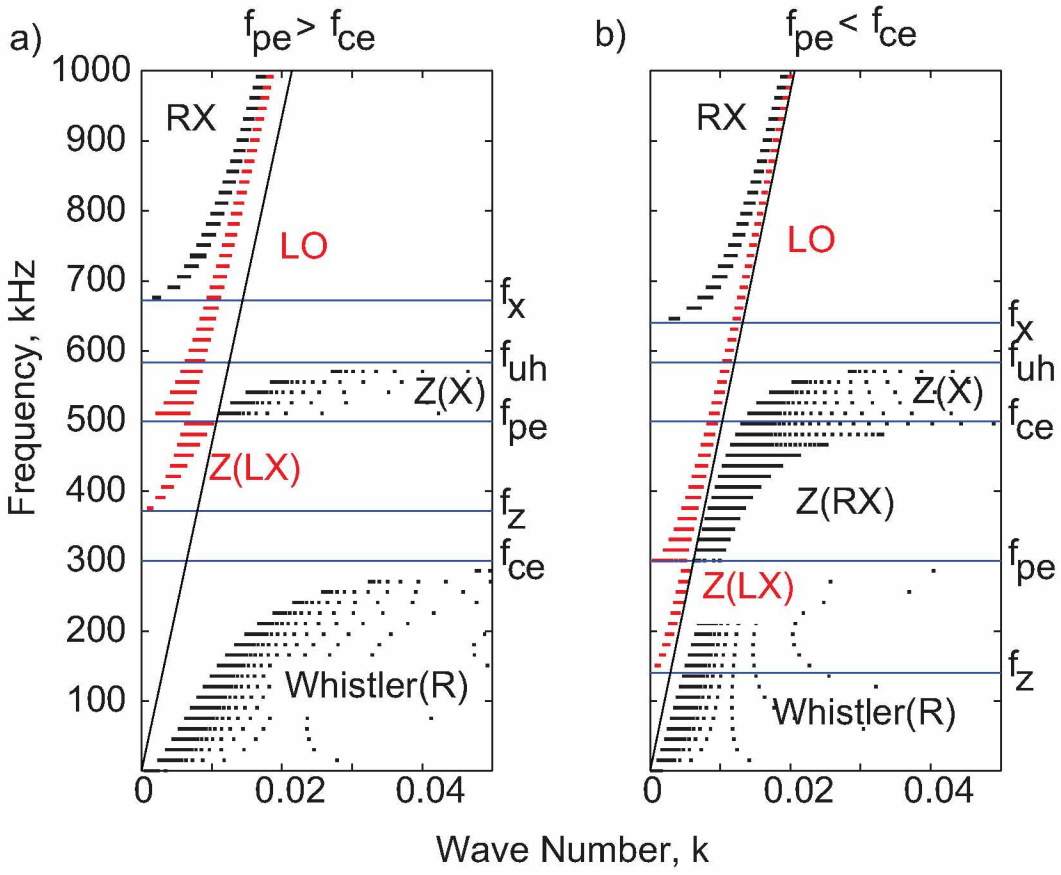

Figure 1.2 Dispersion diagram of electron and proton cold plasma wave modes in coordinates of wave frequency f and wave number k. (a) Diagram for $f_{pe} > f_{ce}$, a situation common in the equatorial region and plasmasphere. (b) Diagram for $f_{pe} < f_{ce}$, a situation common poleward of the plasmapause, where, f_{pe} and f_{ce} are electron plasma- and electron gyro-frequency, respectively. (Adapted from Goertz and Strangeways, (1995)).

propagation of waves. Plasma consists of charged particles, for example, electrons and positive ions. The charged particles can interact with the electric and magnetic fields and, therefore, can support a large varieties of waves. According to fluid model of plasmas, plasma consists of at least two fluids, electrons and positive ions, therefore, the number of possible waves is larger than the normal fluid. In normal media, such as neutral gas, only acoustic waves can exists. Acoustic waves are longitudinal waves that are associated with sinusoidal pressure variations. The gas particles moves back and forth in the direction of propagation of waves. Acoustic waves exists in plasmas too, for example, ion-acoustic waves. Ion-acoustic waves are associated with sinusoidal pressure variations. Due to the displacement of charged particles an electric field is also present, besides the pressure gradient, and acts as a restoring force. Thus, ion-acoustic waves can interact with electromagnetic fields. Plasmas have a large classification of waves. These classifications are based

on the thermal motion of the particles, mass of electrons and ions, orientation of wave vector $\vec{\mathbf{k}}$ with respect to the background magnetic field, and the electric and magnetic field perturbations of the waves. For example, in the cold plasma approximation, thermal motion of the particles are considered to be negligible as compared to the phase velocity of the waves. In a cold plasma only the bulk motion of the plasma is considered. The motion of electrons and ions are treated separately and/or combined because electrons being lighter are very mobile as compared to heavier ions. If the plasma is perturbed, electrons are displaced with the background of positive ions. An electric field is created, which acts as a restoring force. Electrons starts to oscillate about their mean position. These oscillations are called as electron plasma oscillation and the frequency of this oscillation is called as electron plasma frequency, $\mathrm{f_{pe}}$. The dispersion relation is given as:

$$\omega_{pe}^2 = \frac{N_e\, e^2}{m_e\, \epsilon_0} \tag{1.1}$$

where, ω_{pe} is the angular electron plasma frequency and $\omega_{\mathrm{pe}} = 2\pi \mathrm{f_{pe}}$, $\mathrm{N_e}$ is electron density, e is electronic charge, $\mathrm{m_e}$ is electronic mass, and ϵ_0 is the electric permittivity of free space. There is no wave propagation in this case. Now, if we consider the finite electron temperature, then the thermal motion of the electrons are superimposed on the electron plasma oscillations and we get a propagating wave mode called Langmuir waves [Kivelson and Russell, 1995]. This wave is unaffected by the ions. The wave dispersion relation is given as:

$$\omega^2 = \omega_{pe}^2 + \frac{3}{2}k^2 v_e^2 \tag{1.2}$$

where, ω is angular wave frequency, k is the magnitude of wave propagation vector also called as wave number, and v_e is thermal velocity of electrons. $v_e = \sqrt{\frac{2\mathrm{T_e}}{\mathrm{m_e}}}$, where, $\mathrm{T_e}$ is the temperature of the electrons. When the plasma is perturbed, the information is propagated from one point to another. Waves transmit information out of plasma and can be detected by an observer. The Earth's magnetosphere consists of electrons, positive ions, and background magnetic field and therefore can support a wide varieties of electromagnetic, electrostatic, and magnetosonic waves that cannot exist in free space. The plasma wave modes that are observed to exist in a range of frequencies can be described in terms of characteristic plasma frequencies. These frequencies include: electron plasma frequency ($\mathrm{f_{pe}}$); ion plasma frequency ($\mathrm{f_{pi}}$); electron gyro frequency ($\mathrm{f_{ce}}$); and ion gyro frequency ($\mathrm{f_{ci}}$). There are four plasma wave modes that are predicted by the linear

theory of cold plasma and have been observed in space [Gurnett et al., 1983; Gurnett and Inan, 1988; Sonwalkar, 1995]. These modes are: (1) Whistler mode; (2) Z mode; (3) free space LO mode; and (4) free space RX mode.

Figure 1.2 shows dispersion diagrams for cold plasma wave modes in coordinates of wave frequency f and wave number k, which is related to the refractive index μ by $\mu = \mathbf{k}c/\omega$ using the Appleton-Hartree dispersion relation. The Appleton-Hartree equation is the dispersion relation for waves in a cold plasma for arbitrary propagation, which neglects the motion of ions and collisions. Figure 1.2(a) shows dispersion curves when the electron plasma frequency (f_{pe}) is greater than electron cyclotron frequency (f_{ce}). This situation is common within the plasmasphere. Figure 1.2(b) shows dispersion curves when f_{pe} is less than f_{ce}, a situation common poleward of the plasmasphere. In each panel the modes are labeled by their common names. A straight line represents the speed of light. The modes above this line are superluminous modes (phase velocity faster than the speed of light), while those below it are subluminous modes (phase velocity slower than the speed of light).

The labels of the wave modes in Figure 1.2 are given according to the polarization with respect to the geomagnetic field $\mathbf{B_0}$. R and L represent right- and left-hand polarization for parallel propagation ($\theta = 0$), while X and O represent extraordinary and ordinary mode polarization for perpendicular propagation ($\theta = \pi/2$), where θ is the wave-normal angle with respect to $\mathbf{B_0}$ [Benson et al., 2006]. The dispersion diagram shows all the four plasma wave modes in their corresponding frequency regimes. One of the wave modes is the Z mode.

Z mode (ZM) wave is a trapped wave mode because it can only exist in a plasma and cannot propagate in free space as it is bounded by lower and upper frequency cutoffs. The ZM is named after the Z trace observed on ground ionograms [Eckersely, 1933]. The ZM is bounded by an $L = 0$ cutoff frequency, called ZM cutoff frequency (f_z), and by upper hybrid resonance frequency (f_{uh}). f_z and f_{uh} are functions of f_{pe} and f_{ce} and are given as:

$$f_z = \frac{f_{ce}}{2}\left[-1 + \left(1 + 4\frac{f_{pe}^2}{f_{ce}^2}\right)^{\frac{1}{2}}\right] \tag{1.3}$$

$$f_{uh} = \left(f_{pe}^2 + f_{ce}^2\right)^{\frac{1}{2}} \tag{1.4}$$

The ZM is further classified into the fast ZM (superluminous mode) and the slow ZM (subluminous mode). The refractive index of the ZM undergoes a peculiar change near the plasma frequency for

parallel propagation ($\theta = 0$) with respect to the geomagnetic field. When the wave frequency is between f_z and f_{pe}, the refractive index is less than one, indicating phase velocity is greater than the speed of light. The wave mode in this frequency regime is called *"fast Z mode"*. When the wave frequency is between f_{pe} and f_{uh}, the refractive index is greater than one, indicating phase velocity is less than the speed of light. The wave mode in this frequency regime is called *"slow Z mode"*. The refractive index surface is closed for f <max(f_{pe}, f_{ce}) and open for f >max(f_{pe}, f_{ce}). The bandwidth of ZM is very sensitive to the ratio of electron plasma frequency to electron gyro frequency, f_{pe}/f_{ce}. When $f_{pe}/f_{ce} > 1$, the bandwidth is very narrow, whereas when $f_{pe}/f_{ce} < 1$, the bandwidth is very broad. A band of no propagation occurs between f_{ce} and f_z when $f_{pe}/f_{ce} > \sqrt{2}$. In the magnetospheric regions of high plasma density ($f_{pe} \geq f_{ce}$), for e.g., plasmasphere, ZM emissions called upper hybrid band emissions appear in a narrowband near f_{uh} [Benson et al., 2004]. Z mode waves have been observed in frequency range of 10 kHz - 10 MHz from the equatorial to polar regions of the magnetosphere. Z mode waves has been used as an important diagnostic tool for sensing electron density in the magnetosphere. Z mode waves play an important role in the wave-particle interactions and are important to explain natural wave emissions.

1.5 Magnetospheric Ducts

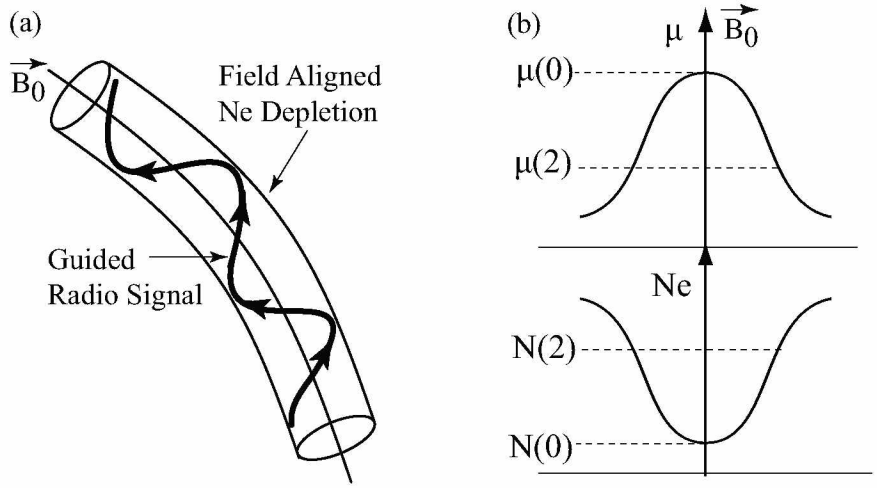

Figure 1.3 (a) Profile of magnetic field ($\mathbf{B_0}$) aligned magnetospheric duct and the guided radio signal propagation. (b) Cross-$\mathbf{B_0}$ profiles of the electron density (N_e) and refractive index (μ) of the duct.

Ducts are large scale field aligned irregularities that extend over a significant fraction of field lines and exhibit an enhanced refractive index for propagation of radio waves. The typical width varies

in the range of 1-1000 km in cross $\mathbf{B_0}$ direction and density varies from 1% to a factor of 10. Ducts have spatial scale sizes in the cross $\mathbf{B_0}$ direction, large as compared to the wavelength of waves, i.e., the medium (ΔN/N) is slowly varying over one wavelength (λ) compared to the dimensions of ducts. Ducts can guide energy along a field line over long distances. These irregularities are present in all parts of the magnetosphere. Magnetospheric ducts are believed to play an important role in many physical processes at low and high latitudes, e.g., for wave-particle interactions, mode conversion, particle acceleration and precipitation (including auroral precipitation), visible and radar aurora, and substorm activity [James 2000; James 2006; Sonwalkar, 2006; Bell et al., 2009; Darrouzet et al., 2009; Benson 2010; Haque et al., 2011].

1.6 Literature Review

The first observations of ZM echoes were made by ground-based radar experiments. The observed ZM had the same polarization as free space O mode and were called the ZM due to unique 'Z' shaped signature on the ionograms [Eckersely, 1933]. A Z-O mode coupling process was proposed to explain the ground observations of ZM echoes [Eckersely, 1950; Ellis, 1956; Ratcliffe, 1959]. In the past, topside sounders have frequently recorded ZM echo traces [Nelms et al., 1966; Calvert and VanZandt, 1966; Calvert, 1966; Hagg et al., 1969; Franklin and Maclean, 1969]. Two types of ZM traces were observed namely normal ZM (Z) and oblique ZM (Z'). Normal and oblique Z modes result from normal and oblique ionospheric reflections of ZM waves at $f_z = f$ and $f_{pe} = f$ levels, respectively [Calvert, 1966]. Muldrew (1969) has discussed observations of coupled ZM waves in topside ionosphere. O-Z-O mode coupling has been proposed to explain the observations of terrestrial kilometric and Jovian decametric radiations [Jones, 1977] and explain long range echoes observed on IMAGE/RPI [Reinisch et al., 2001]. ZM signals have also been recorded during inter-satellite propagation of ZM waves by ISIS 1 and ISIS 2 during rendezvous situations [James 1978, 1979].

Ducted ZM echoes were commonly observed near magnetic-dip equator by topside sounders [Muldrew 1969; Benson and Calvert, 1979; Benson, 1982]. At high latitudes, ionogram traces due to coupled ZM wave propagation have been observed, but rarely [Muldrew, 1969]. Benson (1985), in a statistical study of Alouette ionograms at 400-500 km, found that ZM wave ducting in $f_z < f < f_{pe}$ is commonly observed at lower equatorial latitudes (within 15° dip latitudes) in the topside post-sunset ionosphere. Slow ZM echoes inside field aligned irregularities (FAIs) are

observed at high-polar cap latitudes as a series of vertical bars on the ionograms. 'Kinked' Z traces observed on Alouette 2 ionograms in mid- to high latitude ionosphere were attributed to the field aligned propagation of ZM waves [Colin and Chan, 1969]. Short duration (< 10 ms) ZM signatures observed at low latitudes at frequencies just above the ZM cutoff frequency for large values of f_{pe}/f_{ce} were attributed to ducting of sounder-generated ZM waves in sounder-stimulated FAIs [Benson, 1997]. A bistatic experiment conducted on plasma waves in the ionosphere by the OEDIPUS rocket experiment produced signatures of slow ZM waves guided along depletion ducts [James, 1991; James, 2006]. Carpenter et al., (2003) reported observations of ducted ZM echoes when the sounder was within the ZM cavity in the magnetosphere. Benson (2006) has provided a comprehensive review of observations of ZM waves by active experiments on topside and magnetospheric sounders, and passive recording of ZM natural emissions.

Naturally occurring ZM echoes have been observed on satellites ISIS 1, 2, DE1, and Akebono [Gurnett and Inan, 1988; Calvert and Hashimoto, 1990; Benson, 1993; Nishimura et al., 2006; Nishimura et al., 2007]. The spectra of ZM emissions have been investigated for source mechanism and propagation of these waves [Gurnett et al., 1983, Benson, 1985; Cairns and Menietti, 1997; Cairns, 1999; Santolik et al., 2001; Menietti and Yoon, 2006]. The ZM emissions have been found to resonate with electrons and contribute to their stochastic acceleration [Horne and Thorne, 1998; Summers et al., 2001; Glauert and Horne, 2005; Xiao et al., 2012]. ZM waves have also been observed in the solar wind [Krauss-Varban, 1989] and in Jovian and Saturn magnetospheres [Barbosa et al., 1990; Ye et al.,2010; Kurth et al., 2011; Gu et al., 2013]. LaBelle and Treumann (2002) present a comprehensive review of the auroral ZM emissions.

Trapping region of ZM waves (ZM cavity) has been observed in the ionospheric polar region and has been used to explain the narrowband ZM emissions observed on the DE-1 satellite [Gurnett et al., 1983]. A diffuse band of emissions near 8 kHz in Neptune's magnetosphere has been interpreted as trapped ZM emissions near the $L = 0$ cutoff [Farrell, 1996]. ZM trapping was discovered by Carpenter et al., (2003) in IMAGE satellite data near and within the plasmasphere in a 3000-10,000 km altitude range. The trapped ZM echoes on IMAGE have been proposed as a new tool to study the distribution of plasma along the field lines above the ionosphere.

Ray tracing in ZM has been performed in the past to explain the propagation and coupling of ZM waves in the ionosphere [Lockwood, 1962; Muldrew, 1969; Calvert, 1966; Colin and Chan, 1969; James, 1978, 1979; Budden, 1985; Horita and James, 2002, 2004] and to study natural ZM emissions [Menietti and Lin, 1985 1986; Hashimoto and Calvert, 1990; Horne, 1995]. Herring (1980)

performed ray tracing to study the propagation of ZM rays in the magnetosphere at one frequency of 100 kHz and investigated the propagation of radio waves through mode conversion.

Z mode echoes have been used as an important diagnostic tool. Normal ZM traces were used to determine the vertical electron density profile out to a few hundred km from the spacecraft [Jackson, 1969]. However, Z traces are observed over a restricted frequency range and have not proved very useful in the measurement of vertical electron density $N_e(h)$ profiles [Jackson et al., 1980]. IMAGE/RPI Z mode echoes have been used to determine accurate N_e profiles along $\mathbf{B_0}$ for thousands of km above the IMAGE satellite [Carpenter et al., 2003]. The N_e profile along $\mathbf{B_0}$ can be calculated from ducted ZM traces using an inversion technique developed by Carpenter et al., (2003). Reinisch et al., (2001) have used O-Z-O mode coupling to explain the long range echoes observed on IMAGE/RPI. These echoes have been used to measure the plasma density profiles in the plasmasphere. In polar regions, the diffuse ZM echoes with a sharp cutoff at f_{uh}, provide a useful means of measuring local f_{pe} from f_{ce} and f_{uh} [Bauer and Stone, 1968; Benson et al., 2003, 2004; Sonwalkar et al., 2004; Masson et al., 2009]. In contrast to O- and X- mode echoes, which have a limit of 0.3 R_E on the apparent range at low altitude ($\sim$4000 km), W- and Z- mode echoes are not restricted to an apparent range because of their low group velocity. Thus, the W- and Z-mode results complement the RPI results obtained from the free space modes [Carpenter et al., 2003; Sonwalkar et al., 2004, 2011a, 2011b].

The existence of ducts in the magnetosphere was invoked to explain ground-based observations of Whistler mode waves [Helliwell, 1965]. The first observations of ducts in space were made by Knecht et al., (1961) on a rocket-borne fixed frequency sounder experiment. The high frequency traces were due to multiple reflections of echoes in a loss-free field aligned duct between sounder and X mode reflection level in the ionosphere.

Field aligned ducts were frequently observed on topside radio sounders [Muldrew, 1963; Lockwood and Petrie, 1963; Calvert and Schmid, 1964; Hice and Frank, 1966; Hagg et al., 1969; Muldrew, 1980a, 1980b; Calvert, 1981; Benson, 1982; Benson, 1985]. On topside sounder ionograms, ducted echoes were discovered by Muldrew (1963) at low latitudes. The ducts of half-width $\sim$0.6 km, and $\sim$1% N_e deviation were aligned North-South, and ducted echoes were observed in the Z, O, and X modes near the equator. Ducts 10s of m-100s of km in cross section and aligned along the field line have been observed on the topside sounders [Herman, 1966; Cohen and Bowles, 1961; Petrie, 1963]. Statistical study of ducts were carried out by Loftus et al., (1966) using Explorer data. The ratio of observed thickness of ducts to free-space wavelength was found to be of the order

of 30. The distribution curve for horizontal duct thickness showed a peak at ∼4 km and varied from 1 km - 40 km. Density perturbation ($\Delta N/N$) varied between $1\% - 8\%$. In another statistical study by Muldrew (1967) of conjugate echoes on Alouette 1, Alouette 2, and Explorer XX, ducts were observed to occur ∼5% of the time. The occurrence of ducts were found to be independent of geomagnetic index K_p and increased with decreasing L-shell from 4 to 1.35.

Ducts of enhanced and depleted densities with dimensions ranging from few kilometers to hundreds of kilometers have been observed from the equatorial region to the polar region of the magnetsosphere. The first in situ observations of Whistler ducts in the equatorial region were made by OGO1 satellite [Smith and Angerami, 1968]. The thickness of ducts was ∼400 km at equator and duct separation ranged from 50-500 km at $L = 3$. Angerami (1970) reported ducts of dimension 223-430 km (0.03-0.07L) and $6 - 22\%$ enhancement observed on $L = 4.1 - 4.7$ in the equatorial region (6.5°-9.1°) on OGO 3. Ducts hundreds of km of thickness, with density perturbation of $1\% - 10\%$ to factors of < 2-10, have been observed on topside sounders Alouette 1, Alouette 2, ISIS 1 in the equatorial region [Scarf and Chappell, 1973; Dyson and Benson, 1978; Carpenter et al., 1981, Benson, 1982; Calvert, 1982; Haque et al., 2011].

At high latitudes Herzberg and Nelms (1968) reported Alouette 2 duct density depletion of ∼40% and width of ∼2 km. Irregularities of density variation from $5\% - 70\%$ and dimensions of less than 2 km along the satellite path have been recorded by Alouette 2 at high to low latitudes [Dyson, 1969]. Duct enhancement and depletion of $75\% - 90\%$ for ducts of width 200-400 m have been observed at 1000 km at 36°N on ISIS 1 satellite [Muldrew, 1970]. Persoon et al., (1988) reported DE-1 wideband data showing ducts of thickness 0.03-1.8 L and depletion of $47\% - 97\%$ and enhancements of $96\% - 900\%$ on the nightside auroral field lines at $70° \pm 5°$ invariant latitudes. Ducted ZM echoes were observed in the auroral ionosphere by the OEDIPUS rocket experiments [James, 2000; James, 2006]. The magnitude of depletions lies in the range of $7 - 21\%$, and cross field dimensions of a few kilometers. Ducts of very narrow width (100m-10s km) and shallow density variation of ∼1% have been observed from the equatorial to auroral regions of the ionosphere [Gross and Muldrew, 1984; James, 2000; James, 2006] and in the magnetosphere [Fung et al., 2003; Fung and Green, 2005].

The regions near the plasmapause have been observed to be regularly permeated by density structures. Ducts of large spatial scale sizes of 0.1 to 0.2 R_E and densities within ±30% have been observed in the plasmapause region on ISEE-1 satellite [Carpenter et al., 1981]. Carpenter et al., (1993) have reported density structures of < 1000 km scale sizes and density variation by factors

of 2-10 observed on DE-1 and ISEE-1 satellites in the plasmapause region ($L = 5.1 - 5.5$). LeDocq et al., (1994) have observed large scale irregularities of 100s of km in the L-shell range of 3-6 along the orbit of CRRES satellite. Density fluctuations of $1\% - > 10\%$ were observed. Similar in situ density measurements made near the plasmapause have shown the regular occurrence of density structures in the region. The structures vary over 100s of km in cross section and over a few % in density [Moldwin et al., 1995; Fung et al., 2000; Koons, 1989; Moullard et al., 2002; Darrouzet et al., 2004, 2009].

Magnetospheric ducts play an important role in the propagation of plasma waves, mode conversion, and wave-particle interactions. Measurements of duct properties are important to evaluate theories of wave-particle interactions and the extent of particle precipitation due to ducted waves and explain models of natural wave emissions in the magnetosphere [Calvert, 1982; James, 1991, 2000, 2006; Sonwalkar, 2006]. Observations on CRRES, DEMETER, and POES satellites suggested that ducted VLF waves are effective in driving electron precipitation from the inner radiation belt [Clilverd et al., 2008; Rodger et al., 2010]. ELF and VLF chorus emissions that are excited in ducts of enhanced or depleted cold plasma density play an important role in the acceleration of 10-100 keV radiation belt electrons to MeV energies [Bell et al., 2009]. Electron density observations from WHISPER, and EFW instruments onboard CLUSTER satellites confirm the source of the banded chorus to be Whistler mode ducts of depleted or enhanced electron densities. Chorus waves can increase the flux of relativistic electrons by accelerating electrons with energies in the keV range to energies in the MeV range. These relativistic electrons pose a serious hazard for spacecraft systems, as they may cause damage to the onboard electronics or even system failure [Haque et al., 2011]. Yearby et al., (2011) have used CLUSTER spacecraft potential as a proxy for high time resolution electron density measurements and showed that increased chorus wave power, observed within the radiation belts, correlates with observations of density enhancements. De Soria-Santacruz et al., (2013) have analyzed the growth rates of EMIC waves within cold plasma density irregularities, characteristic of plasmaspheric plumes, and found that wave ducting and wave growth occur within the density enhancements. The ducts and other field aligned density structures cause degradation and disruption of communication and satellite navigation systems [Sonwalkar, 2006; Huba and Joyce, 2007; Huba et al., 2008]. Although the study of ducts is important, there is only limited knowledge of the properties of ducts, their occurrence patterns, and their distribution on a global scale in the magnetosphere [Darrouzet et al., 2009; Sonwalkar, 2006], especially for ducts extending to high altitudes (above 1000 km). The irregularities observed from ground based observations

and on topside sounders were usually studied indirectly through their transmission properties as wave guides. The IMAGE mission provided the first opportunity to measure magnetospheric ducts directly using radio sounding by RPI [Darrouzet et al., 2009]. Wave propagation in the field aligned irregularities in W, Z, O, and X modes have been observed on the IMAGE [Reinisch et al., 2001; Carpenter et al., 2002, 2003; Fung et al., 2003; Fung and Green, 2005]. A few percent density depletion is required for LO and RX mode ducting [Muldrew, 1963, 1967; Platt and Dyson, 1989; Calvert, 1995; Fung et al., 2003; Fung and Green, 2005;] while density enhancement is required for WM ducting [Smith, 1961; Helliwell, 1965]. Carpenter et al., (2003) observed ducted ZM echoes when the sounder was within the ZM cavity in the magnetosphere. This phenomenon involves echoes returning from turning points in denser regions Earthward of the sounder, and from more tenuous regions above in the presence of ducts. However, no attempts were made by the authors to study the properties of these ducts that can guide Z mode waves.

Analysis of ducted echoes from the conjugate and local hemispheres has enabled nearly instantaneous magnetic field aligned electron density profiles [Calvert, 1981; Reinisch et al., 2001, 2004; Fung et al., 2003; Fung and Green, 2005; Tu et al., 2006; Benson, 2010; Ozhogin et al., 2012]. Ducted ZM echoes within ZM cavities observed on IMAGE/RPI have been used to obtain the field aligned electron density distribution above the satellite altitude [Carpenter et al., 2003]. Instantaneous measurement of electron density along a magnetic field line is necessary in order to determine the plasma density distribution along a field line accurately. This is particularly important for realistic modeling of the plasmaspheric refilling and loss processes [Reinisch et al., 2001; Reinisch et al., 2004; Tu et al., 2006; Smith and Gallagher 2008]. The cold plasma density distribution of the plasmasphere plays an important role in the generation and propagation of plasma waves. These waves interact with the energetic particles and lead to the acceleration and precipitation of these particles and thus influence the radiation belt dynamics [Kozyra et al., 1997; Horne, 2002]. Therefore, it is important to measure the plasmaspheric density distribution and develop reliable empirical models of the plasma density distribution. Empirical models can be used as a benchmark for the theoretical and numerical models [Siscoe et al., 2004] and are vital for the design and operation of manmade satellites [Gallagher et al., 2000]. Empirical models are important to investigate the wave generation and propagation, radiation belt modeling, and with forecasting of space weather [Reinisch et al., 2004; Tu et al., 2006; Denton et al., 2012; Ozhogin et al., 2012]. Empirical models of equatorial electron density profile are well developed [Carpenter and Anderson, 1992; Sheeley et al., 2001; Denton et al., 2004; Reinisch et al., 2004; Tu et al., 2006; Larsen et al., 2007]. Measurements

from the satellites such as DE-1, CRRES, and ISEE-1 have been used to develop the statistical models of the off-equatorial electron density distribution in the plasmasphere/plasmatrough region [Gallagher et al., 1988, 1998, 2000; Goldstein et al., 2001; Denton et al., 2002, 2004, 2006; Huang et al., 2004; Reinisch et al., 2004; Tu et al., 2006]. Unfortunately, these statistical model are unable to accurately represent the off-equatorial global electron density distribution. The reason of this inaccuracy is because these electron density measurements have been made in situ along the satellite orbits and at limited geophysical locations and geomagnetic conditions. The averaging of these in situ measurements masks the latitudinal dependence of the field aligned electron density distribution [Reinisch et al., 2001, 2009]. Other reasons include a lack of the measurement of instantaneous field aligned electron density distribution in the off-equatorial region and availability of relatively fewer measurements of N_e at higher altitudes. Recently, Ozhogin et al., (2012) have presented the observations of the off-equatorial electron density distribution and developed an empirical model based on these measurements, however, the limitations of this model is that it provides the density distribution above 2000 km and has higher uncertainty in the electron density distribution at higher latitudes. Comparisons of ionospheric topside sounder measurements from ISIS satellite data and total electron content (TEC) data shows shortcomings in the International Reference Ionosphere (IRI) representation of the topside electron density profile. Although, recent attempts have been made to construct density models that can smoothly connect a topside profile to a plasmasphere model, there is still a need to describe the transition of densities from high altitude into the topside ionosphere properly [Reinisch et al., 2007]. Global Core Plasma Model (GCPM) of the inner magnetosphere has been developed by integrating various region specific models for core plasma density. There is an inherent discontinuity between the ionospheric model (IRI) and the plasmaspheric models used by the GCPM. A power law function is used to interpolate between the topside ionospheric profile of IRI and plasmaspheric density profile. Thus, there is a need to bridge the gap in the representation of the density distribution from the topside ionosphere to $\sim$1 R_e ($\sim$6370 km) extending into the plasmasphere [Gallagher et al., 2000]. Plasmasphere, besides the ionosphere, is a significant source of the total electron content (TEC) which causes the global positioning satellite inaccuracies, range errors in the global navigation satellite system, and communication problems [Gerzen et al., 2015]. In a recent study, it has been found that the plasmasphere TEC contribution from the Global Core Plasma Model (GCPM) and International Reference Ionosphere (IRI) extension with plasmasphere model contribute to $\sim$10-60% depending upon the time of the day, season, geographic location, solar activity, and geomagnetic activity. Thus, an accurate representation of

the plasmaspheric density distribution is necessary for optimal performance of the GPS-TEC applications [Gulyaeva and Gallagher, 2007]. Gerzen et al., (2015) have pointed out that there is a need of additional measurements of the electron density, e.g., the IMAGE RPI active mode sounding measurements, for modeling of the upper part of the plasmasphere ($L > 4$).

1.7 Scientific Contributions and Importance of this Research

This work presents observations of fast Z mode echoes on the IMAGE satellite during years 2001 to 2005. Carpenter et al., (2003) have surveyed a small subset of the IMAGE data set from 28 June 2001-31 July 2001 obtained from low altitude RPI sounding (~1000-5000 km) and categorized the ducted fast Z mode echoes as AB or CD type. We have surveyed about 72,000 plasmagrams for both nonducted and ducted fast Z mode echoes using the same categorization as Carpenter et al., (2003) and have expanded the dataset to ~5 years of IMAGE mission from 2001-2005 for the altitude range of ~1000-10,000 km. Besides finding the categories of ducted echoes as described by Carpenter et al., (2003), we have found several new observations and features of nonducted and ducted ZM echoes which are presented in chapter 3 of this thesis. In this research, we present observations of nonducted fast ZM echoes that were reflected from altitudes below as well as above the IMAGE satellite inside the Z mode cavities. We also present the first observations of nonducted and ducted fast ZM echoes reflecting from above the satellite altitude outside the plasmasphere. We have discovered new phenomenon of a frequency gap in echo trace reflecting from below the satellite altitude. This phenomenon is important as it is a direct manifestation of the presence of ducts in the magnetosphere and is important to study the dispersion relations and wave properties in the vicinity of characteristic plasma frequency.

A new method of Z mode sounding has been developed to measure the magnetospheric duct parameters, field aligned electron density distribution and Z mode cavity. The work presented in this thesis provides first direct measurements of magnetospheric ducts obtained from ducted ZM echoes observed inside the ZM cavities in the low- to mid-latitude region of the magnetosphere and in the 1,000-10,000 km altitude range. The magnetospheric ducts are important to study because they play an important role in the generation and propagation of natural wave emissions, and wave-particle interactions and therefore influence the radiation belt dynamics. Duct sounding can be used for measuring instantaneous field aligned electron density distribution.

Instantaneous measurements of field aligned electron density distribution is important in or-

der to test theoretical and numerical models of magnetospheric density distribution and study the plasma loss and refilling processes. Measurement of electron density is important to develop and improve the physics based empirical models of the Earths ionosphere and the magnetosphere. These models are necessary for optimum performance of communication and navigational satellite systems. Global density distribution of the off-equatorial electron density profile are not yet represented accurately by the existing statistical models. This is because the previous electron density measurements have been made in situ along the satellite orbits and in limited locations and there is a lack of measurement of instantaneous field aligned electron density distribution in this region. The fast Z mode echoes data set presented in this study is an ideal data set to fill this gap and it provides an unique opportunity to measure the field aligned electron density profile in the poorly known low to mid-latitude region of the magnetosphere in the altitude range of 1000-10,000 km. Quantitative measurements of ZM cavities in the magnetosphere has been presented for the first time. This study shows that the ZM cavity is a real phenomenon that occurs mostly inside the plasmasphere and rarely outside the plasmasphere. ZM cavity is important in explaining the observations of natural ZM emissions in the magnetosphere.

ZM sounding provides a new and powerful method to measure: (1) field aligned electron density distribution; (2) field aligned magnetospheric ducts; and (3) ZM cavities observed in the magnetosphere. A large number of cases of nonducted and ducted ZM echoes have been observed by the IMAGE satellite in 1000-10,000 km altitude range in the low to mid-latitude region of the magnetosphere inside the plasmasphere and near the plasmapause, thus, providing a unique opportunity to study field aligned electron density distribution, properties of ducts, and ZM cavities in this poorly known region of space. The main contributions of the present work are summarized as follows:

1. Provided first observations of ducted and nonducted fast ZM echoes reflecting from above the satellite altitude outside the plasmasphere. We have surveyed occurrence of ZM echoes from 2001-2005 and identified several new features of ZM echoes.

2. A new ZM sounding method has been developed to measure magnetospheric duct parameters, ZM cavity parameters, and field aligned electron density distributions using ducted and nonducted ZM echoes.

3. Measured duct parameters using ZM echoes observed on IMAGE/RPI in the plasmasphere in low to mid-latitude regions of the magnetosphere in the altitude range of ~1000- 10,000 km. Earlier studies found the duct width and density perturbation in the region near the

plasmapause in the range of 100s of km and a few percent to a factor of 10, respectively. The present study finds the duct width and density perturbation in the range of ~160-500 km and depletions of ~1% - 6%, which is in agreement with the previous observations.

4. Provided first quantitative measurement of ZM cavity parameters in the magnetosphere.

5. Provided measurements of field aligned N_e distribution in the altitude range of ~1000-10,000 km (or 90-10,000 km if Whistler mode echoes are present) using ducted and nonducted ZM echoes.

6. Studied propagation, reflection and guidance of the nonducted and ducted ZM waves in the ZM cavity in the magnetosphere using ray tracing calculations, refractive index surfaces, and Snell's Law. Demonstrated that fast ZM waves can be guided by depletion ducts.

7. Discovered a new phenomenon: The occurrence of a frequency gap in the echo trace reflecting from below the satellite altitude of ducted fast ZM echoes and explained it using ray tracing calculations, refractive index surfaces, and Snell's Law.

1.8 Dissertation Organization

The present work is organized into six chapters:

Chapter 1 (current chapter) gives a brief introduction of the magnetosphere, plasmasphere, and waves in the magnetosphere. This chapter introduces the ZM (non ducted and ducted) and reviews past research on the ZM waves and duct measurements.

Chapter 2 discusses the theory of cold plasma wave modes with emphasis on Z mode, ray tracing code and diffusive equilibrium density model, ZM inversion technique, density model optimization, and automatic ray tracing code for ZM echoes.

Chapter 3 discusses the IMAGE/RPI experiment and observational techniques. This chapter gives a detailed account of observations of the ZM echoes and ducts on IMAGE/RPI and discusses statistics in the context of various geophysical parameters.

Chapter 4 presents a case study of the ducted fast ZM echoes observed on 10 July 2001 to demonstrate the new ZM sounding method to measure the duct parameters, field aligned electron density distribution, and ZM cavity from the ZM echoes. Theory of propagation and reflection of ZM waves (both nonducted and ducted) in the magnetosphere are discussed with the aid of ray tracings, refractive index surfaces, Poeverlein's construction, and Snell's Law.

In *Chapter 5*, ZM sounding method developed in *Chapter 4* is applied to 10 cases of fast ZM echoes to measure: (1) field aligned electron density distribution; (2) duct parameters; and (3) ZM cavity parameters.

Chapter 6 provides a summary, conclusions, and suggestions for future research.

Part of this research has been presented in Mayank and Sonwalkar (2011, 2012).

Chapter 2 Theory of Z Mode Waves in the Magnetosphere and Analysis Tools

This chapter discusses cold plasma wave theory, Z mode (ZM) refractive index surfaces, diffusive equilibrium density model, and analysis tools developed: the ZM inversion method, density model optimization, and automated ZM ray tracing code for ZM echoes.

2.1 Theory of Waves in Cold Plasma

Magnetospheric plasma consists of electrons and ions and is permeated by the geomagnetic field. It can support a large variety of electromagnetic, electrostatic, and magnetosonic wave modes that do not exist in free space. These wave modes exist for a range of frequencies that can be understood in terms of characteristic frequencies of plasma. In linear theory, solutions to Maxwell's equations are obtained for plane waves of the form

$$\mathbf{E} = \mathbf{E_0} \exp[j(\mathbf{k} \cdot \mathbf{r} - \omega t)] \tag{2.1}$$

where $\mathbf{E_0}$, $\mathbf{k}$, and ω are the wave polarization, wave vector, and angular wave frequency, respectively. The angle between the static magnetic field $\mathbf{B_0}$ and the wave vector $\mathbf{k}$ is called the wave normal angle, θ. The wave refractive index μ is defined as:

$$\mu = \frac{c|\mathbf{k}|}{\omega} \tag{2.2}$$

where c is the speed of light in vacuum. The wave vector $\mathbf{k}$ can be written in terms of refractive index μ:

$$\mathbf{k} = \frac{\omega\mu}{c}\hat{\mathbf{u}}(\theta, \phi) \tag{2.3}$$

where $\hat{\mathbf{u}}(\theta, \phi)$ is the unit vector in the direction of the wave vector. This equation is the dispersion relation. The solution to Maxwell's equation for a plane wave in a cold magnetoplasma is obtained in terms of general expression for wave refractive index μ [Stix, 1962; Sonwalkar, 1995]:

$$A\mu^4 - B\mu^2 + C = 0 \tag{2.4}$$

where

$$A = S\sin^2\theta + P\cos^2\theta \tag{2.5}$$

$$B = RL\sin^2\theta + PS(1 + \cos^2\theta) \tag{2.6}$$

$$C = PRL \tag{2.7}$$

The quantities R(right), L(left), S(sum), D(difference), and P(plasma) are defined in terms of wave frequency f, plasma frequency, f_{ps}, and the gyro frequency f_{cs}, where 's' denotes the electron or ion species. These quantities are functions of electron density (N_e), mass of electron (m_e), ion density (N_i), mass of ion species (m_s), and the ambient magnetic field strength (B). Equation 2.4 is a biquadratic equation and is the dispersion relation. We define the quantities R, L, S, D, P as follows:

$$R = 1 - \sum_s \frac{f_{ps}^2}{f(f + \epsilon_s f_{cs})} \tag{2.8}$$

$$L = 1 - \sum_s \frac{f_{ps}^2}{f(f - \epsilon_s f_{cs})} \tag{2.9}$$

$$S = \frac{1}{2}(R + L) \tag{2.10}$$

$$D = \frac{1}{2}(R - L) \tag{2.11}$$

$$P = 1 - \sum_s \frac{f_{ps}^2}{f^2} \tag{2.12}$$

where f_{ps} is the plasma frequency of species s, f_{cs} is the gyro frequency of the species s, and ϵ_s is $+1$ for positive ions and -1 for electrons and negative ions. As the wave propagates in the plasma, it encounters regions where the refractive index, μ, goes to zero (cutoff) or infinity (resonance). When the wave goes through a cutoff, μ^2 goes through zero and reflection occurs. According to

equations 2.4, 2.8, 2.9, and 2.12, cutoff occurs when $P = 0$, $R = 0$ or $L = 0$. Resonance occurs when waves propagate at wave normal angles that satisfy the criterion $\tan^2\theta = -P/S$.

Solving the quadratic equation 2.4 for μ^2 gives

$$\mu^2 = \frac{B \pm F}{2A} \tag{2.13}$$

where

$$F^2 = (RL - PS)^2 \sin^4\theta + 4P^2D^2\cos^2\theta \tag{2.14}$$

Neglecting the effects of ions and collisions, the refractive index can be approximated by the Appleton-Hartree equation [Goertz and Strangeway, 1995]:

$$\mu^2 = \frac{X}{1 - \frac{0.5Y^2\sin^2\theta}{1-X} \pm \{(\frac{0.5Y^2\sin^2\theta}{1-X})^2 + Y^2\cos^2\theta\}^{\frac{1}{2}}} \tag{2.15}$$

where $X = f_{pe}^2/f^2$, $Y = f_{ce}/f$, f is wave frequency. Figure 2.1 is the dispersion diagram obtained from

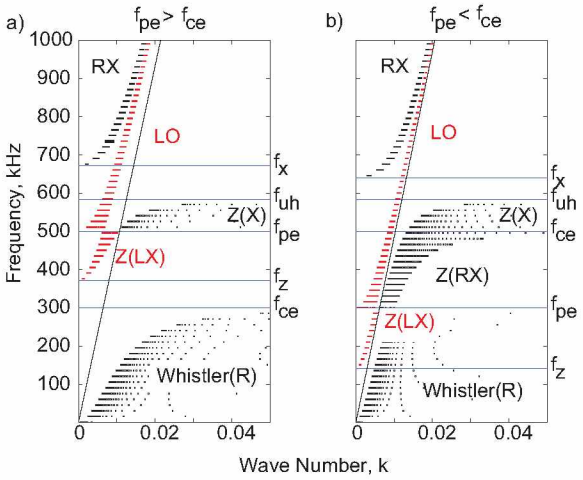

Figure 2.1 Dispersion diagram derived from the Appleton-Hartree dispersion relation. (a) shows dispersion diagram for conditions when $f_{pe} > f_{ce}$, (b) diagram for condition when $f_{pe} < f_{ce}$. The band of no propagation between f_z and f_{ce} in 1(a) occurs only when $f_{pe}/f_{ce} > \sqrt{2}$ [adapted from Goertz and Strangeway, (1995)].

the Appleton-Hartree equation. This is the plot of wave frequency (f) versus wave number (k). The diagram illustrates the various cold plasma wave modes that exist in different frequency regimes for various plasma conditions representative of the Earth's magnetosphere. Figure 2.1(a) shows the dispersion diagram when $f_{pe} > f_{ce}$, a region common near the equatorial region and in the plasma-

sphere. Figure 2.1(b) shows the dispersion diagram when $f_{pe} < f_{ce}$, a region common poleward of the plasmasphere. Different wave propagation modes and polarizations are also indicated in both figures. The area shaded in red (black) is obtained as a solution of the Appleton-Hartree equation for the plus (minus) sign in the denominator in equation 2.15. In Figure 2.1(a) the plasma frequency is 500 kHz and the gyro frequency is 300 kHz. In Figure 2.1(b), the plasma frequency is 300 kHz and the gyro frequency is 500 kHz. The wave modes are labeled based on their polarization with respect to their direction of propagation relative to the ambient magnetic field direction. Thus, R or L stands for right- or left-hand polarization when $\theta = 0$ (parallel propagation with respect to direction of $\mathbf{B_0}$), and X or O stands for extraordinary and ordinary mode polarizations when $\theta = \pi/2$ (perpendicular propagation with respect to direction of $\mathbf{B_0}$). Thus, a mode represented by two letters indicate that both parallel ($\theta = 0$) and perpendicular propagation ($\theta = \pi/2$) is possible in that mode. Resonance occurs when the refractive index $\mu \to \infty$ and cutoff occurs when $\mu \to 0$. The plasma resonances and cutoffs are given as

Electron gyro-frequency

$$f_{ce} = \frac{|e|}{2\pi m_e}|\mathbf{B}| \tag{2.16}$$

Electron plasma frequency

$$f_{pe} = \left[\frac{e^2}{4\pi\epsilon_0 m_e}\right]^{\frac{1}{2}} N_e^{\frac{1}{2}} \tag{2.17}$$

Lower hybrid resonance frequency

$$\frac{1}{f_{lh}^2} = m_{\text{eff}}\left(\frac{1}{f_{pe}^2} + \frac{1}{f_{ce}^2}\right) \tag{2.18}$$

Upper hybrid resonance frequency

$$f_{uh} = \left(f_{pe}^2 + f_{ce}^2\right)^{\frac{1}{2}} \tag{2.19}$$

R-X mode cutoff frequency

$$f_x = \frac{f_{ce}}{2}\left[1 + \left(1 + 4\frac{f_{pe}^2}{f_{ce}^2}\right)^{\frac{1}{2}}\right] \tag{2.20}$$

ZM cutoff frequency

$$f_z = \frac{f_{ce}}{2}\left[-1 + \left(1 + 4\frac{f_{pe}^2}{f_{ce}^2}\right)^{\frac{1}{2}}\right] \tag{2.21}$$

where e is electron charge, m_e is electron mass, ϵ_0 is permittivity of free space, and m_{eff} is effective ion mass. Four cold plasma wave modes can be identified from the dispersion diagram: (1) Whistler mode (WM), which exists between the lower hybrid resonance frequency (f_{lh}) and min(f_{pe},f_{ce}), (2) ZM, which exists between the ZM cutoff frequency f_z (L=0 cutoff) and the upper hybrid resonance frequency f_{uh}, and free space modes (3) Left hand Ordinary (L-O) mode, which has a lower cutoff at f_{pe} and (4) right hand extraordinary (R-X) mode, which has a lower cutoff at X mode cutoff frequency f_x (at R = 0 cutoff). The term free space is used to indicate that these modes can propagate at the speed of light in the free space. These modes do not have an upper frequency limit to the dispersion curve, and therefore they can propagate large distances and escape the magnetosphere. Whistler and ZM are the trapped modes because they cannot propagate in free space. The ZM is named after the Z trace observed on ground ionograms [Eckersley, 1933]. When the wave frequency is between f_z and f_{pe}, the refractive index is less than 1, indicating that phase velocity is greater than the speed of light. The wave mode in this frequency regime is called *"fast ZM"*. When the wave frequency is between f_{pe} and f_{uh}, the refractive index is greater than 1, indicating that phase velocity is less than the speed of light. The wave mode in this frequency regime is called *"slow ZM"*. The bandwidth of ZM is very sensitive to the ratio of electron plasma frequency to electron gyro frequency, f_{pe}/f_{ce}. When $f_{pe}/f_{ce} \gg 1$, the bandwidth is very narrow, whereas when $f_{pe}/f_{ce} \ll 1$, the bandwidth is very broad. A band of no propagation occurs between f_{ce} and f_z when $f_{pe}/f_{ce} > \sqrt{2}$. In the magnetospheric regions of high plasma density ($f_{pe} > f_{ce}$), e.g., plasmasphere, Z-mode emissions appear in a narrowband near f_{uh}, called upper hybrid emissions [Benson et al., 2004]. For Z mode, the resonance condition for $\theta = 0$ and $\theta = \pi/2$ is given by equations 2.17 and 2.19, respectively. For $0 < \theta < \pi/2$, the resonance condition is known as Z-infinity and is given by

$$f_{zI} = \frac{1}{\sqrt{2}} \left[f_{uh}^2 + \left(f_{uh}^2 - 4 f_{pe}^2 f_{ce}^2 \cos^2\theta \right)^{\frac{1}{2}} \right]^{\frac{1}{2}} \tag{2.22}$$

The Z-infinity is also referred to as the upper oblique resonance [Beghin et al., 1989; Benson et al., 2006]. The Whistler mode is named after the lightning generated whistlers that propagate in this wave mode [Helliwell, 1965]. The Whistler mode has a lower cutoff frequency at lower hybrid resonance frequency (f_{lh}) (equation 2.18) when propagating perpendicular to the ambient magnetic field, and an upper cutoff frequency at either f_{pe} or f_{ce}, whichever is lower. Whistler mode waves reflect in the magnetosphere when wave frequency is equal to local f_{lh}. It has right hand circular

polarization (R) when propagating parallel to the ambient magnetic field. Whistler mode waves are found throughout the magnetosphere from equatorial region to polar region.

2.2 Z Mode Refractive Index Surfaces

A useful representation of the refractive index is the refractive index surface, which is a plot of refractive index as a function of wave normal angle and a contour with surface of revolution about the magnetic field. For an anisotropic medium such as magnetospheric plasma, the energy of the wave, indicated by the direction of group velocity (V_g), travels in a different direction than the wave vector $\vec{\mathbf{k}}$ as described by the wave normal angle θ. The direction of the group velocity is given as the direction normal to the refractive index surface at the tip of the refractive index vector μ [Poeverlein, 1949; Helliwell, 1965]. The refractive index surfaces for ZM for the condition when $f_{pe} < f_{ce}$ and $f_{pe} > f_{ce}$ are shown in Figure 2.2. The refractive index surface for ZM is a closed surface for wave frequency $f < \max(f_{pe}, f_{ce})$. For wave frequency close to f_{pe}, the wave refractive index undergoes a complicated change for small wave normal angles ($\theta \sim 0°$). The refractive index surface is a perfect unit spheroid for wave frequency equal to f_{pe}. The refractive index exhibits a dimple for wave frequency just less than the f_{pe} and is an open surface for wave frequency just greater than f_{pe} for $f_{pe} > f_{ce}$, or exhibits a nipple for $f_{pe} < f_{ce}$. For wave frequency greater than $\max(f_{pe}, f_{ce})$, the refractive index surface is an open surface. This means that in this frequency regime, the ZM wave can only propagate when the wave normal angle (θ) is greater than the resonance angle (θ_{res}) in a direction oblique to the magnetic field direction. The phase refractive index for the ZM is less than unity for wave frequency less than f_{pe}, that is the propagation mode is superluminous and is called fast ZM. For wave frequency greater than f_{pe}, the refractive index is greater than unity (subluminous mode) and is called slow ZM. The expressions for group velocity V_g and the angle between the ray direction and the magnetic field, α, are given as [Helliwell, 1965]

$$V_g = \frac{\partial \omega}{\partial \vec{\mathbf{k}}} = \hat{\mathbf{k}} \frac{\partial \omega}{\partial |\vec{\mathbf{k}}|} + \hat{\theta} \frac{1}{|\vec{\mathbf{k}}|} \frac{\partial \omega}{\partial \theta} \tag{2.23}$$

$$\tan \alpha = \frac{1}{\mu} \frac{\partial \mu}{\partial \theta} \tag{2.24}$$

where $\hat{\mathbf{k}}$ and $\hat{\theta}$ are unit vectors along and perpendicular to wave vector $\vec{\mathbf{k}}$, $\omega = 2\pi f$ is the wave angular frequency, and μ is the phase refractive index. For a given wave propagation mode, the group velocity and ray direction of the wave can be determined by the equations 2.4, 2.23, and 2.24. The group velocity can also be described in terms of the group refractive index μ' [Helliwell, 1965]

$$\mu' = \frac{d}{df}(\mu f) \tag{2.25}$$

$$V_g = \frac{c}{\mu'} \tag{2.26}$$

where f is the wave frequency and c is the speed of light in free space. The group velocity is a function of wave frequency, electron plasma frequency (f_{pe}), electron gyro frequency (f_{ce}), and wave normal angle (θ). The analytical expression for group velocity is difficult to solve. However, a simple analytical expression can be given for special cases, for example, for wave propagation parallel to the magnetic field line, which commonly occurs when a wave is trapped inside a field aligned duct. Solving equations 2.15 and 2.25, and assuming a wave normal angle $\theta = 0°$, we obtain following expression for group refractive index (μ')

$$\mu' = \frac{1}{2}\frac{f f_{pe}^2 (2f + f_{ce})}{(f^2 + f_{ce}f)^2\sqrt{1 - \frac{f_{pe}^2}{f^2 + f_{ce}f}}} + \sqrt{1 - \frac{f_{pe}^2}{f^2 + f_{ce}f}} \tag{2.27}$$

Now using equations 2.27 and 2.26, we obtain the expression for group velocity for fast ZM wave parallel propagation as

$$V_g = \frac{c(f^2 + f f_{ce} - f_{pe}^2)}{\sqrt{f^2 + f f_{ce}}(1 - \frac{f_{pe}^2 f_{ce}}{2f(f_{ce}+f)^2})} \tag{2.28}$$

2.3 Analysis Tools

This section discusses the ray tracing simulation tool and three important analysis tools that were developed and used in this study to analyze the fast ZM echoes observed by the IMAGE satellite and to measure the field aligned electron density distribution, duct parameters, and ZM cavity. These tools are (1) MATLAB implementation of ZM inversion technique; (2) optimization of diffusive equilibrium density model input parameters; and (3) automatic ray tracing code for calculating ZM echoes. We have modified the Stanford 2D ray tracing code to be used on a standalone PC

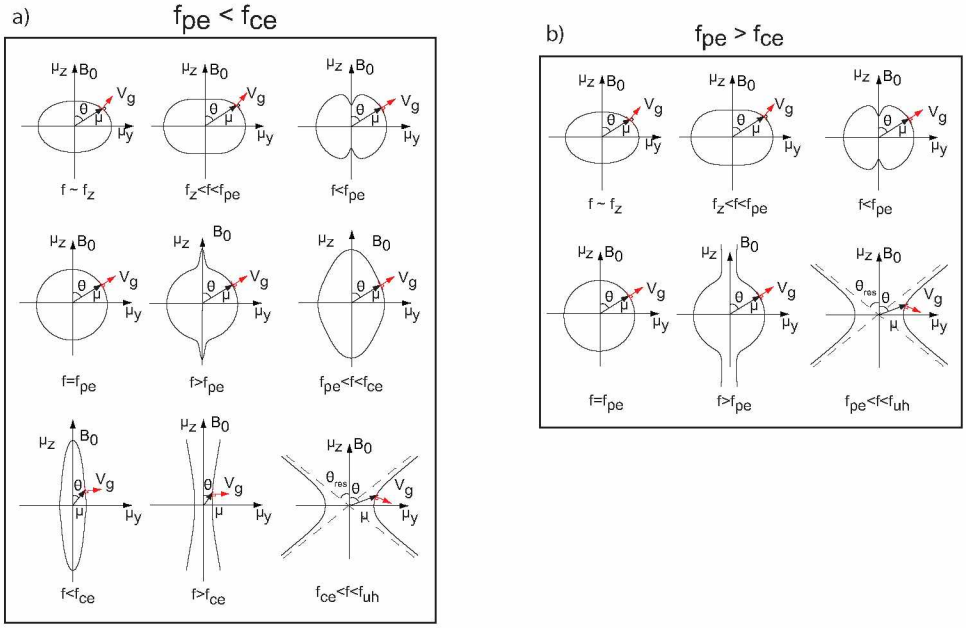

Figure 2.2 Refractive index surfaces for ZM wave propagation. (a) Refractive index surfaces when $f_{pe} < f_{ce}$. Refractive index surfaces are closed surfaces for $f \leq f_{pe}$ and are open for $f > f_{pe}$. (b) Refractive index surfaces when $f_{pe} > f_{ce}$. Refractive index surfaces are closed surfaces for $f < f_{pe}$ and are open for $f > f_{pe}$.

and have integrated it with MATLAB using MEX files for automated calculations and detection of ZM echoes.

2.3.1 Stanford 2D Ray Tracing Program

The program uses a Runge-Kutta routine to integrate a system of linear differential equations given by the ray theory [Kimura, 1966]. The program uses a centered dipole magnetic field model for the Earth's geomagnetic field, a diffusive equilibrium density model for the distribution of electrons and ions in the plasmasphere, and an r^{-n} density falloff model outside the plasmasphere. The program performs ray tracings in the two-dimensional magnetic meridional plane [Inan and Bell, 1977]. The ray path can be computed through numerical integration of a closed set of first order differential equations [Haselgrove, 1955]. The set of equations [Kimura, 1966] are expressed as

$$\frac{\partial r}{\partial s} = \frac{1}{\mu^2}(\rho_r - \mu\frac{\partial \mu}{\partial \rho_r}) \tag{2.29}$$

$$\frac{\partial \psi}{\partial s} = \frac{1}{r\mu^2}(\rho_\psi - \mu\frac{\partial \mu}{\partial \rho_\psi}) \tag{2.30}$$

Table 2.1 Refractive index values in various frequency regimes for plasma condition $f_{pe} < f_{ce}$ where f_{pe} =300 kHz, f_{ce} =500 kHz, f_z =141 kHz, and f_{uh} =583 kHz. The parameters listed are frequency regimes, frequency in kHz, refractive index in parallel direction, refractive index in transverse direction, resonance cone angle, and refractive index in special direction.

	f (kHz)	$\mu(0°)$	$\mu(90°)$	θ_{res}	μ (special dir.)
$f \sim f_z$	140.6	0.03	0.04	closed	
$f_z < f < f_{pe}$	240	0.70	0.91	closed	
$f < f_{pe}$	299	0.79	0.99	closed	0.89(5°), 0.96(10°)
$f = f_{pe}$	300	1	1	closed	
$f > f_{pe}$	301	1.58	1.00	closed	1.16(5°), 1.04(10°)
$f_{pe} < f < f_{ce}$	400	1.8028	1.104	closed	
$f < f_{ce}$	495	6.11	1.26	closed	
$f > f_{ce}$	505	14.2 (12°)	1.3	11.1°	
$f_{ce} < f < f_{uh}$	540	14.03(38°)	1.51	37.6°	

Table 2.2 Refractive index values in various frequency regimes for plasma condition $f_{pe} > f_{ce}$ where f_{pe} =500 kHz, f_{ce} =300 kHz, f_z =372 kHz, and f_{uh} =583 kHz. The parameters listed are same as in table 2.1 .

	f (kHz)	n(0°)	n(90°)	θ_{res}	μ(special dir.)
$f \sim f_z$	373	0.064	0.09	closed	
$f_z < f < f_{pe}$	450	0.51	0.76	closed	
$f < f_{pe}$	499	0.61	0.99	closed	0.71(5°), 0.86(10°)
$f = f_{pe}$	500	1	1	closed	
$f > f_{pe}$	501	5.96(5°)	1.01	4.9°	
$f_{pe} < f < f_{uh}$	560	11.66(53°)	1.71	52.7°	

$$\frac{\partial \phi}{\partial s} = \frac{1}{r\mu^2 \sin\psi}(\rho_\phi - \mu \frac{\partial \mu}{\partial \rho_\phi}) \tag{2.31}$$

$$\frac{\partial \rho_r}{\partial s} = \frac{1}{\mu}\frac{\partial \mu}{\partial r} + \rho_\psi \frac{\partial \psi}{\partial s} + \rho_\phi \frac{\partial \phi}{\partial s}\sin\psi \tag{2.32}$$

$$\frac{\partial \rho_\psi}{\partial s} = \frac{1}{r}(\frac{1}{\mu}\frac{\partial \mu}{\partial \psi} - \rho_\psi \frac{\partial r}{\partial s} + r\rho_\phi \frac{\partial \phi}{\partial s}\cos\psi) \tag{2.33}$$

$$\frac{\partial \rho_r}{\partial s} = (\frac{1}{\mu} - \rho_\phi \frac{\partial r}{\partial s}\sin\psi - r\rho_\phi \frac{\partial \psi}{\partial s}\cos\psi) \tag{2.34}$$

where r, ψ, and ϕ are the geocentric distance, colatitude $(90° - \lambda)$, and longitude, respectively. ρ_r, ρ_ψ, and ρ_ϕ are the components of the refractive index vector, which has a length μ, and s is the variable of integration in units of distance. The group time delay, t_g, gives the rate of energy travel along the ray path and is expressed as

$$\frac{\partial t_g}{\partial s} = \frac{1}{c}(1 + \frac{f}{\mu}\frac{\partial \mu}{\partial f}) \tag{2.35}$$

where f is the wave frequency. The ray tracing equations 2.29 to 2.35 determine the variation of ray path as a function of time in a slowly varying medium.

2.3.2 Diffusive Equilibrium Density Model

Diffusive equilibrium is the steady state resulting from the diffusion process. In such a state the constituent gases of the atmosphere would be distributed independently of each other. Thus, heavier ions will settle down at lower altitudes and lighter ions will be more abundant at higher altitudes [Angerami and Thomas, 1964]. So, starting from very low altitudes, say 90 km, we find oxygen ions (O^+) to be much more abundant than hydrogen ions (H^+). As the altitude increases, O^+ decreases much more rapidly than H^+ (16 times faster), and therefore H^+ increases in concentration, to satisfy the quasi-neutrality condition of the plasma which requires that

$$\alpha_{H^+} + \alpha_{He^+} + \alpha_{O^+} = 1 \tag{2.36}$$

where $\alpha_{\mathrm{H^+}} = \frac{\mathrm{N_{H^+}}}{\mathrm{N_e}}$, $\alpha_{\mathrm{He^+}} = \frac{\mathrm{N_{He^+}}}{\mathrm{N_e}}$, and $\alpha_{\mathrm{O^+}} = \frac{\mathrm{N_{O^+}}}{\mathrm{N_e}}$ are the fractional ion abundances and $\mathrm{N_e}$ $\mathrm{N_{H^+}}$, $\mathrm{N_{He^+}}$, and $\mathrm{N_{O^+}}$ are the densities of electrons, H^+, He^+, O^+ ions, respectively. At higher altitudes, H^+ is much more abundant than O^+ ions. The scale height of the ions, H_i, is given as,

$$H_i = 1.1506(T)(\frac{r_b}{7370})^2(\frac{r}{r_b})\frac{1}{4^{(i-1)}} \tag{2.37}$$

the constant value 1.1506 is obtained from $\frac{\mathrm{k_B}}{\mathrm{m_p\, g_0}}(\frac{7370}{\mathrm{r_e}})^2$, where, $\mathrm{k_B}$ is the Boltzmann constant, $\mathrm{m_p}$ is the mass of proton, $\mathrm{g_0}$ is the standard acceleration due to gravity, $\mathrm{r_e}$ is the Earth's radius, $\mathrm{r_b}$ is the geocentric distance to the base of the diffusive equilibrium density model, T is the temperature at the base of the diffusive equilibrium density model, and $i = 1, 2, 3$ represents H^+, He^+ and O^+ ions, respectively (for details refer: Burtis, 1974; Inan and Bell, 1977). The model allows flexibility in obtaining a desired density anywhere in the magnetosphere. In order to simulate the effects of field aligned density ducts, a duct density model could be added to the density model. The electron density inside a duct is given as

$$N_e(r, L) = N_{DE}(1 + \frac{\Delta N}{N_{DE}} e^{-\frac{1}{2}(\frac{L-L_0}{\Delta L})^2}) f_{rduct} \tag{2.38}$$

where

$$L = \frac{r}{r_e}(\cos\lambda_m)^{-2} \tag{2.39}$$

$$f_{rduct} = e^{-\frac{(r_{dl}-r)^2}{h_{dl}}}, r < r_{dl} \tag{2.40}$$

$$f_{rduct} = 1, r_{dl} < r < r_{du} \tag{2.41}$$

$$f_{rduct} = e^{-\frac{(r-r_{du})^2}{h_{du}}}, r > r_{du} \tag{2.42}$$

where N_{DE} is the diffusive equilibrium model density, r is the geocentric distance, $r_e = 6370$ km is the radius of the Earth, λ_m is the geomagnetic latitude, L_0 is the L shell value of the center of the duct, ΔL is the half-width of the duct, that is, the width of the duct at which the density perturbation is half its maximum value, and ΔN is the duct enhancement factor, for example, $\Delta N = 0.1$ means a 10% enhancement and $\Delta N = -0.1$ means a 10% depletion. r_{dl} is the geocentric distance (km) to the lower end of the duct. Below r_{dl}, the duct enhancement or depletion begins to merge with the background density with radial scale height (km) h_{dl}. r_{du} is the geocentric distance (in km) to the upper end of the duct. Above r_{du} the duct enhancement or depletion begins to merge with the background density with radial scale height (km) h_{du}. If the duct extends to the equator, the r_{du} is set as $r_{du} > L * 6370$ km.

2.3.3 Z Mode Inversion

IMAGE/RPI has observed a large number of echoes reflecting within the ZM cavities near and within the plasmasphere. ZM inversion of the ZM echo data allows the determination of electron density distribution along the field line up to a distance of several thousand kilometers above the satellite. Carpenter et al., (2003) have developed the ZM inversion technique to invert the ducted echo trace reflecting from above ($t_g - f$ dispersion of D or B trace) the satellite altitude to obtain the field aligned electron density profile. For the present study, the ZM inversion technique has been implemented into the MATLAB software.

The ZM inversion technique assumes that the ducted rays propagate along the geomagnetic field lines, that is, the wave normal angle is zero ($\theta \sim 0°$) and the ZM cutoff f_z is assumed to be constant along the field line. The virtual range of the reflection point of a ducted ZM signal is

related to the actual range, s, through following equation [Carpenter et al., 2003]

$$R(f) = c \int_0^s ds / V_g(f, f_{ce}(s), f_{pe}(s)) \tag{2.43}$$

where *R(f)* is the virtual range of the reflection point of the ducted ZM signal, *ds* is the differential element of the path length, $V_g(f, \mathrm{f_{ce}}(s), \mathrm{f_{pe}}(s))$ is the group velocity of the ZM signal along the duct, f is the signal frequency, $\mathrm{f_{ce}}(s)$ is the electron gyro frequency, $\mathrm{f_{pe}}(s)$ is the electron plasma frequency, and c is the free space speed of light. The refractive index of a ZM signal propagating in a duct parallel to Earth's magnetic field B_0 (assuming $\theta \sim 0$) is given as

$$\mu = [1 - f_{pe}^2/(f^2 + f f_{ce}))]^{1/2} \tag{2.44}$$

The group velocity ($\mathrm{V_g}$) for the fast ZM wave is given by equation 2.28. In the case of ZM echoes observed on IMAGE, the frequency range of the ZM echoes is small compared to the magnitude of the frequency itself, for example, for 10 July 2001, the range of frequency of the ducted D trace is only 30 kHz, while the magnitude of the propagating ZM signal is ~380-410 kHz. Thus, the expression for $\mathrm{V_g}$ can be simplified by approximating the frequency-dependent term within the square root of $\mathrm{V_g}$ using a two term Taylor series expansion about $\mathrm{f = f_{zl}}$, where $\mathrm{f_{zl}}$ is the local ZM cutoff frequency given by equation 2.21 and is a function of the local $\mathrm{f_{pe}}$ and $\mathrm{f_{ce}}$. The simplified expression of $\mathrm{V_g}$ is given as

$$V_g = c \frac{[(f - f_{zl})(2f_{zl}(s) + f_{ce}(s)) - (f_{pe}(s)^2 - f_{zl} f_{ce}(s) - f_{zl}^2)]^{1/2}}{(f_{zl}^2 + f_{zl} f_{ce}(s))^{1/2} [1 - \frac{f_{pe}(s)^2 f_{ce}(s)}{2 f_{zl}(f_{ce}(s) + f_{zl})})^{1/2}]} \tag{2.45}$$

Using the simplified expression of $\mathrm{V_g}$ equation 2.43 can be written as

$$2\delta(f')^{1/2} \int_0^{\pi/2} R(f_{zl} + (f' - f_{zl}) sin(\alpha)^2) sin(\alpha) d\alpha = \pi \int_0^{s'} t_0(s) ds \tag{2.46}$$

where the substitution of variable $\mathrm{f = f_{zl} + (f' - f_{zl})sin(\alpha)^2}$ is made and the integral is integrated over α. The integration variable α is such that $\alpha = 0$ when $\mathrm{f = f_{zl}}$ and $\alpha = \pi/2$ when $\mathrm{f = f'}$, where f' is any arbitrary frequency in the range $\mathrm{f_{zl} < f < f_{D,max}}$, and $\mathrm{f_{D,max}}$ is the maximum ducted frequency of the D trace.

A step-by-step method of ZM inversion of the ducted D trace is explained for the example of the 10 July 2001 case.

1. Measure R(f) vs. f for D trace from the plasmagram. The ducted traces have a finite time delay spread due to multipath propagation.

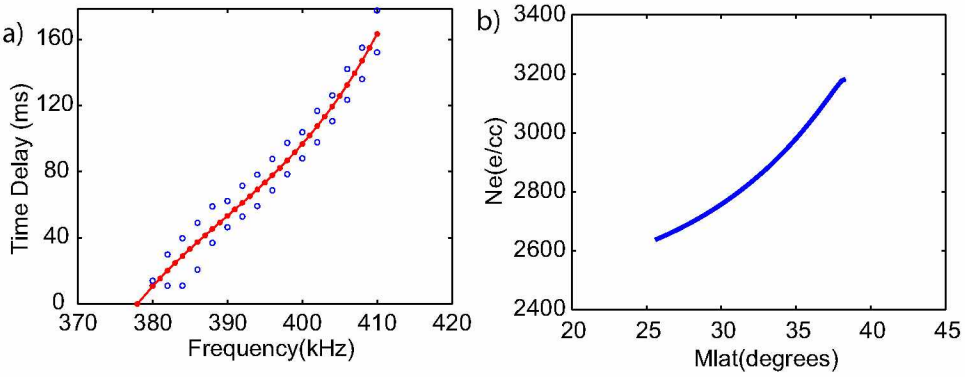

Figure 2.3 ZM inversion of 10 July 2001 case. (a) Figure showing the plot of measured values of virtual range R as a function of frequency of D trace for 10 July 2001 08:10:00 UT. A polynomial of order 3 is fitted to the data (red curve). (b) Plot of N_e obtained from ZM inversion of D trace of 10 July 2001 08:10:00 UT case.

2. A polynomial is fitted to measured R(f) vs. f. Generally, for D trace, a polynomial of order 3 is used for fitting the data. Figure 2.3(a) shows the plot of measured R(f)-f and the polyfitted values of R(f)-f (red curve). The polyfitted R(f)-f curve is extrapolated to obtain the ZM cutoff frequency (f_{zl}) such that at $R(f_{zl}) = 0$.

3. Calculate the left hand side (LHS) of equation 2.46. Variable α, corresponding to every frequency between f_{zl} and f', is calculated using equation

$$\alpha = sin^{-1}(\sqrt{\frac{f - f_{zl}}{f' - f_{zl}}}) \tag{2.47}$$

4. Calculate $R(\alpha)\sin(\alpha)$ and the integral $\int_0^{\pi/2} R(\alpha)\sin(\alpha)$

5. Calculate the LHS: $2\delta(f')^{1/2} \int_0^{\pi/2} R(f_{zl} + (f' - f_{zl})\sin(\alpha)^2)\sin(\alpha)d\alpha$, where $\delta(f') = (f' - f_{zl})/f_{zl}$

6. Calculate the right hand side (RHS) of equation 2.46 at $f = f'$. The arc distance 's' is varied along the satellite L shell such that $LHS = RHS$. This is done by varying geomagnetic latitude (λ_m) from satellite ($\lambda_{m,sat}$ corresponding to $s = 0$) up to λ'_m (corresponding to $s = s'$) such that $LHS = RHS$.

7. The λ_{m} is varied along L shell in steps of $\lambda_{\mathrm{m,step}}$ in the interval λ'_{m} to $\lambda_{\mathrm{m,sat}}$ and the following values are calculated

   (a) $\mathrm{r} = \mathrm{Lcos}^2(\lambda_{\mathrm{m}})$

   (b) $\mathrm{f_{ce}}(s)$ using the dipole field model

$$f_{ce}(s) = f_{ce,Equ}(1/r)^3\sqrt{1+3sin^2(\lambda_m)} \tag{2.48}$$

   where r is given in Earth radius ($\mathrm{R_E}$).

   (c) Calculate t(s)

$$t(s) = 0.5\frac{\sqrt{f_{ce}(s)+2f_{zl}}}{\sqrt{f_{ce}(s)+f_{zl}}} \tag{2.49}$$

8. Calculate the RHS integral $\int_0^{\mathrm{s}'}$ t(s)ds. The variable s is such that $\mathrm{s} = 0$ at $\lambda_{\mathrm{m}} = \lambda_{\mathrm{m,sat}}$ and $\mathrm{s} = \mathrm{s}'$ at $\lambda_{\mathrm{m}} = \lambda'_{\mathrm{m}}$

9. Compare the LHS and RHS. If $LHS \neq RHS$, then λ_{m} is increased in step size and the above steps are repeated until $LHS = RHS$.

10. When $LHS = RHS$, the arc distance s′ and $\mathrm{f_{ce}}(s)$ are calculated. s' is the distance from the satellite to the point of reflection of the wave. To calculate the arc length along the field line between geomagnetic equator and geomagnetic latitude λ_{m1} the following formula [Helliwell, 1965] has been used

$$s_1 = 0.5\frac{r_e}{\sqrt{3cos(\lambda_0)^2}}[x_1 + sinh(x_1)cosh(x_1)] \tag{2.50}$$

    where, r_e is Earth radius, λ_0 is invariant latitude, $\sinh(\mathrm{x_1}) = \sqrt{3}\sin(\lambda_{\mathrm{m1}})$, and $\cosh(\mathrm{x_1}) = \sqrt{1+3\sin^2(\lambda_{\mathrm{m1}})}$. The arc distance along the field line between two points λ_{m1} and λ_{m2} is then calculated as $\mathrm{ds} = |\mathrm{s_1} - \mathrm{s_2}|$.

11. The electron plasma frequency at $\mathrm{f} = \mathrm{f}'$ is then calculated as

$$f_{pe}(s) = \sqrt{g(s)(f_{zl}f_{ce}(s)+2f_{zl}^2)+(f_{zl}f_{ce}(s)+f_{zl}^2)} \tag{2.51}$$

where $g(s) = (f' - f_{zl})/f_{zl}$

12. The electron density ($N_e(s)$) at reflection point is then calculated as $N_e(s) \approx \frac{f_{pe}(s)^2}{80.6}$ (equation 2.17). Figure 2.3(b) shows the plot of N_e, inverted from the ducted D trace of 10 July 2001 08:10:00 UT, as a function of geomagnetic latitude.

2.3.4 Optimization of Diffusive Equilibrium Density Model Input Parameter r_b, T, α

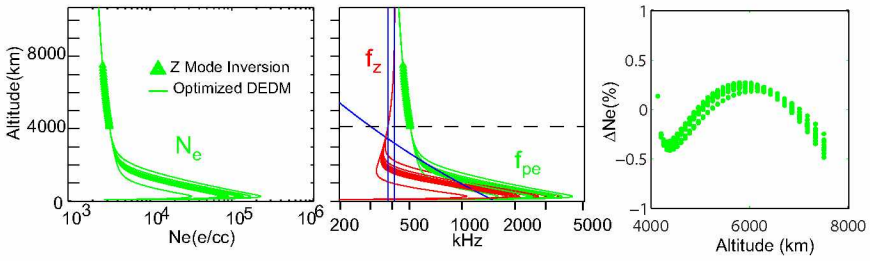

Figure 2.4 (a) Electron density and (b) characteristic plasma frequencies f_z, f_{pe}, and f_{ce} for 10 July 2001 08:10:00 UT case obtained from ZM inversion and density model optimization. (c) Plot of percentage difference of N_e obtained from density model optimization and the ZM inversion.

An automated optimization routine using the MATLAB optimization toolbox to optimize the density model parameters viz., Rbase (r_b), Temperature(T), and normalized ion composition α_i, where i=1, 2, 3 corresponds to H^+, He^+, O^+, respectively, has been developed. The program uses a MATLAB in-built function, **'fmincon()'**, which attempts to find a constrained minimum of a scalar function of several variables starting at an initial estimate. The function that is being minimized is the sum of the squares of the normalized difference in calculated density model parameters with the corresponding measured or estimated parameters. The measured/estimated parameters are $N_{e,ZMinv}$, $N_{e,in-situ}$, $f_{z,local}$, $f_{z,max}$, and $R_{f_{z,min}}$, where, $N_{e,ZMinv}$ is the N_e values obtained from ZM inversion of each trace reflecting from above the satellite altitude (B or D trace), $N_{e,in-situ}$ is the in-situ N_e measurements available from the IMAGE RPI at the satellite altitude, and $f_{z,local}$ is the value of f_z at the satellite. Value of $f_{z,max}$ is taken such that $f_{z,equ} > f_{z,max}$, and $R_{f_{z,min}}$ is the guessed altitude of the minimum f_z. $f_{z,max}$ is the maximum frequency of the observed D trace (or B trace), $f_{z,equ}$ is the model value of field aligned ZM cutoff frequency (f_z) at the equator, and $R_{f_{z,min}}$ is the altitude of minimum f_z. We note that the value of $R_{f_{z,min}}$ could not be measured experimentally, but it can be set at values higher (lower) than R_{sat} to get the desired density model for the AB type

(CD type) fast ZM case. This is required as the ducted fast ZM have been classified as echoes that are observed when satellite altitude is above $R_{f_{z,min}}$ (CD type) and when satellite altitude is below $R_{f_{z,min}}$ (AB type). The optimization program starts with initial values of r_b, T, and α_i. A lower and upper bound on these parameters is provided. The typical values of lower and upper bounds on r_b, T, and α are given as 800-1200 km, 1600-3500 K, and [(0.001-1),(0.001-1),(0.001-1)], respectively. The optimization program then calculates the density model and compares the model values with the aforementioned parameter values. The program then iterates to minimize the function.

$$f(x) = [(\frac{Ne_{DE} - Ne}{Ne})^2 + (\frac{Rf_{z,minDE} - Rf_{z,min}}{Rf_{z,min}})^2 + (\frac{f_{z,maxDE} - f_{z,max}}{f_{z,max}})^2] \tag{2.52}$$

The optimization is subject to following constraints:

$$f_{z,model} = f_{z,sat} \tag{2.53}$$

$$f_{z,Equ}(model) > f_{z,max} \tag{2.54}$$

$$R_{f_{z,min}} > R_{sat}(forAB - type) \tag{2.55}$$

$$R_{f_{z,min}} < R_{sat}(forCD - type) \tag{2.56}$$

$$\alpha_{H^+} + \alpha_{He^+} + \alpha_{O^+} = 1 \tag{2.57}$$

Figure 2.4(a) shows the plot of electron density (N_e) along $\mathbf{B_0}$ from the optimized density models. The $N_{e,ZMinv}$ is shown by green triangles. We find that the optimized values of density parameters r_b, T, and α range from 800-1200 km, 2750-3200 K, and [(0.005-0.443),(0.001-0.034),(0.556-0.994)], respectively. Figure 2.4(b) shows the plot of f_z, f_{pe}, and f_{ce} along $\mathbf{B_0}$ obtained from the optimized density models. Figure 2.4(c) shows the comparison of N_e obtained from optimized density models with the $N_{e,ZMinv}$ showing a relative difference of $\leq 0.5\%$.

A step-by-step method to obtain a density model from density model optimization - ZM inversion technique is as follows:

1. Measure the $t_g - f$ dispersion of D trace (or B trace) and use ZM inversion to obtain N_e profile along the field line.

2. Obtain the density model parameters using the density model optimization program.

3. Modify the optimized density model to obtain a density model which lies within the lower and upper range of the optimized density models.

4. Carry out ray tracing to calculate the t_g for C and D traces (A and B traces) echoes.

5. Ray tracing calculations provide t_g as a function of frequency for C and D traces (A and B trace). If there is any discrepancy between the calculated and measured t_g, then fine-tune the density model by changing the model parameters r_b, T, and α such that the time delays of C and D trace (A and B trace) lie within the range of observed time delays.

2.3.5 Automatic Ray Tracing Code for Z Mode Echoes

Another important tool developed for this thesis is the integration of Stanford 2-D ray tracing simulation code with MATLAB for automated calculation and detection of ZM echoes. As a semester project, we have modified the Stanford 2-D ray tracing code extensively to run on a standalone PC. The ray tracing code was originally written as a 3-D code by Kimura, (1966) for Stanford IBM-7090 machine. This code was later modified as 2-D code to improve speed and/or accuracy and has undergone several modifications to be in the present form [Burtis, 1974]. Earlier the code was compiled and run through FORTRAN f77 compiler on University of Alaska's unix based Nanook server. The input and output files were transferred through SSH (Secure Shell). This process was inefficient in terms of data storage and time taken in computation and data transfer. The large output files generated on the server was restricted by the memory (~200 MB) allocated to each user on the server. So, the ray tracing was performed such that the output files generated were not larger than the allocated quota of 200 MB. This process was inefficient to run large number of rays at a time. Moreover, the SSH takes lot of time to transfer the input and output files from the PC to the server and back. The ray tracing code was written in the older version of FORTRAN, so, it was not compatible with the newer version of the FORTRAN compilers. We have identified several sources of error in the code while compiling it with newer version of FORTRAN compilers (Intel visual FORTRAN 10.1, 11.1), for example, (1) the variables and constants were declared as implicit, (2) single precision functions were used with double precision numbers, (3) logical operations involved two double precision numbers, (4) counter variables were declared as double precision instead of integers, and (5) arithmetic expression using single and double precision numbers. We have then modified the code accordingly so that it is now compatible with the newer versions of FORTRAN compilers. We have integrated the code with MATLAB for increased

efficiency, portability, and storage capacity. This program was integrated into MATLAB using MEX files. This tool has been extremely useful in the ray tracing analysis of both Whistler and Z mode echoes. We have developed an automated ray tracing program, which uses the aforementioned programs along with MATLAB m-files to automatically search for the echoes given the input density model and input frequency. The main input parameters that can be given in an input file are: (1) frequency or a range of frequencies; (2) integration step size; (3) duct parameters (if ray tracing is for ducted echoes); and (4) echo trace for which echoes have to be found. The output parameters consist of: (1) echo wave normal angle(s) and (2) echo group time delay(s) and are written into an output text file. The automated program has been developed for both the Whistler mode and the Z mode. The steps involved in the automation are briefly described as follows:

1. Give frequency range ([f1,f2,...]), ducted traces ([C,D,C+D,..]), and duct parameters (ΔL, ΔN/N), for which echoes have to be found, in an input file.

2. Automated program performs ray tracing calculations using a given density model over a wide range of wave normal angles and duct parameters (ΔL, ΔN/N).

3. Echoes are found at each frequency for each trace when the reflected rays pass on both sides of the satellite. Ray parameters are interpolated at the satellite location to find the parameters for the echo ray. The echo wave normal angles and echo group time delay are written into an output file for further analysis.

Chapter 3 Experiment Description and Observations

This chapter provides an introduction to the IMAGE/RPI satellite, its data format, and data analysis. As a part of the data analysis of this dissertation, a total of ∼72,000 plasmagrams have been surveyed, out of which ∼5000 nonducted and ducted fast ZM echoes have been observed. Examples of different types of these echoes, occurrence patterns, and statistics have been discussed in this chapter.

3.1 Experiment Setup

3.1.1 The IMAGE Satellite Overview

The Imager for Magnetopause-to-Aurora Global Exploration (IMAGE) mission was the first mission dedicated to imaging the Earth's magnetosphere, the region of space controlled by the terrestrial magnetic field and containing tenuous plasma of both solar and terrestrial origin. IMAGE employed neutral atom, ultraviolet, and radio imaging techniques to produce the first comprehensive global images of the plasma populations in the inner magnetosphere [$http://image.gsfc.nasa.gov/$; Burch, 2000]. IMAGE was launched from Vandenberg AFB on 25 March 2000 at 20:34:43 UT into a highly elliptical polar orbit with an initial apogee of ∼8 Earth radii (6378 km) at 40° in the northern hemisphere and a perigee of 1000 km in the southern hemisphere [Figure 3.1]. The orbital period was ∼14 hours and the spin period was 2 minutes (spin rate of 0.5 ± 0.01), with spin axis perpendicular to the orbital plane.

3.1.2 Radio Plasma Imager(RPI)

The Radio Plasma Imager (RPI) on the IMAGE satellite was designed to use the radio sounding technique at distances of ∼1000 km to ∼8 R_E. It has an operating frequency range of 3 kHz to 3 MHz, with a receiver bandwidth of 300 Hz covering plasma densities from $< 10 - 10^5 cm^{-3}$, to

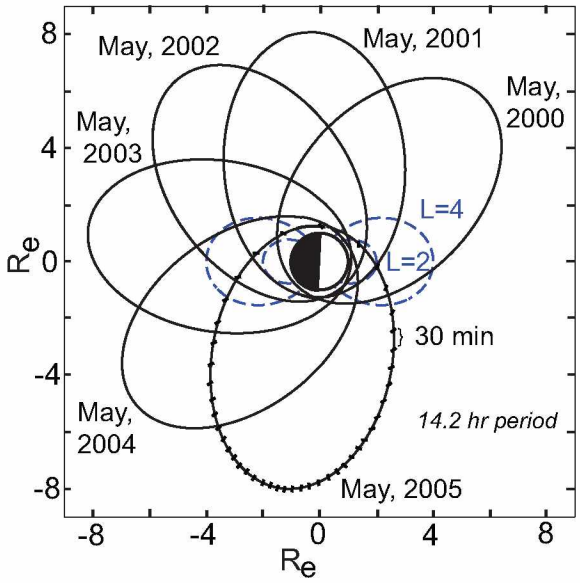

Figure 3.1 The IMAGE satellite orbit for 5 years (2000-2005). The IMAGE orbit has an apogee of 8 R_E altitude and a perigee of 600 km altitude. The initial inclination is 40°, and changes by 100° every 2 years. The tick marks labeled on the orbit show the satellite's position every thirty minutes. The spin period of the satellite is two minutes.

probe remote regions of the magnetosphere, magnetopause, plasmasphere, plasmapause and topside ionosphere [Reinisch et al., 2000]. RPI has located regions of various plasma density by observing radar echoes that are reflected from plasmas where the radio frequency meets the cutoff or reflection conditions for various propagating cold plasma wave modes, viz., ordinary, extraordinary, Whistler, and Z modes. RPI has observed echoes in all four cold plasma wave modes under various plasma conditions (f_{pe}/f_{ce}; f_{pe} is electron plasma frequency and f_{ce} is electron gyro frequency). It has three orthogonal thin wire antennas, two 500-m tip-to-tip long dipole antennas in the spin plane (X and Y) for near omni-directional transmissions, and a third antenna, a 20-m dipole along the spin axis (Z) [Reinisch et al., 2001]. In the frequency range of 3 kHz to 3 MHz, RPI omni-directionally transmitted 10 W radio pulses from X and Y antennas and received reflected echoes on all three antennas [Reinisch et al., 2000]. The 300-Hz receiver bandwidth, matched to the bandwidth of the transmitted waveform, provides a range resolution of 480 km. Echo reflections occur at plasma structures where the density gradients are parallel to the wave normal angle of the incident waves, and where the wave frequency equals the characteristic plasma frequencies. Under conditions of free space propagation, the radiated power varied from 0.1 mW at low frequencies (~10 kHz) to 10 W per dipole at 200 kHz or higher frequencies [Reinisch et al., 2001]. The nominal radiated power was reduced by 3 dB on May 8, 2000 due to the failure of the power supply of Y-antenna.

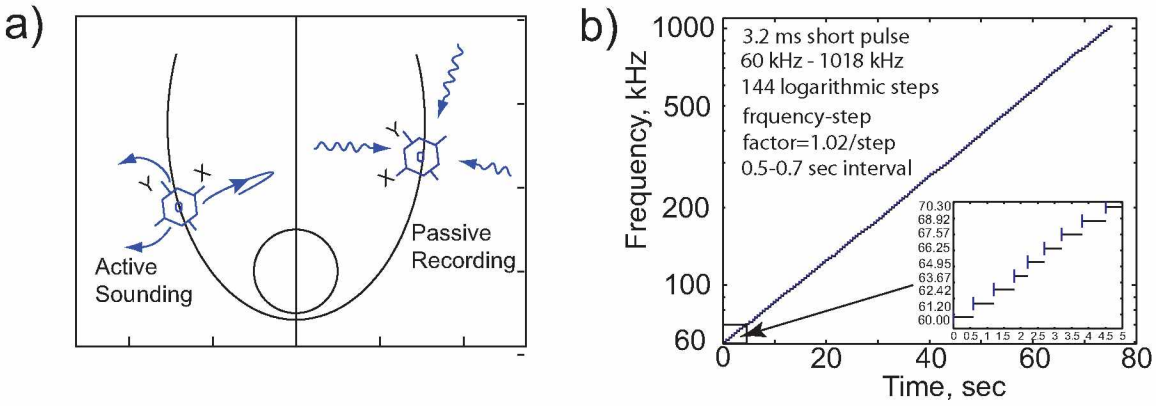

Figure 3.2 (a) Active sounding and passive recording of Radio Plasma Imager onboard IMAGE satellite. (b) A typical program schedule.

When one of the X-antenna monopoles was partially broken by a micro-meteorite, the dipole length reduced to 340 m. On 18 September 2001, an unknown part of the Y antenna was lost and again on 30 September 2004, the signal strength received by the Y antenna was reduced substantially as a result of an unknown failure of the Y antenna/receiver system. In spite of the difficulties with antennas, excellent radio sounding data and passive recording of natural emissions were acquired over the lifespan of the IMAGE satellite mission [Carpenter et al., 2003; Sonwalkar et al., 2004; 2011a]. RPI operated in active sounding and passive recording modes.

3.1.3 Plasmagram (Active Sounding)

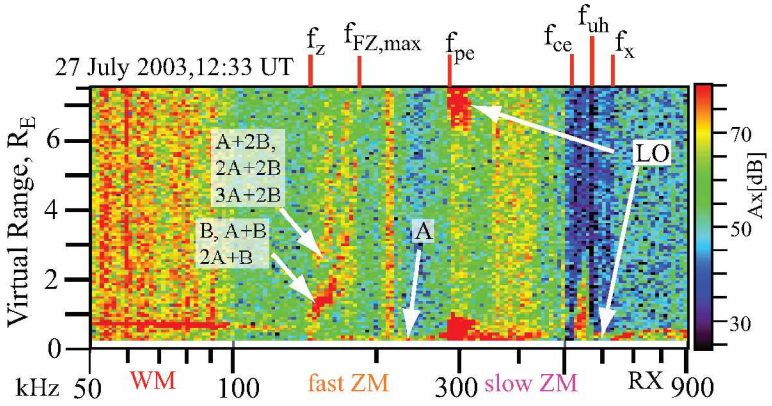

Figure 3.3 IMAGE/RPI plasmagram for 27 July 2003. The x-axis of the plasmagram is the frequency in kHz; y-axis is the virtual range in R_E. The color bar on the right hand side shows the amplitude of the electric field in dB. The observed echoes of ducted fast ZM and other modes are shown.

In active sounding mode, RPI sends out a pulse and listens for the echoes. RPI employed

stepped radio frequency sounding interleaved with listening periods or passive recording mode. The RPI radio sounding data are multidimensional plots of RPI amplitudes in the frequency vs. virtual range frame called plasmagrams. The plasmagrams have echo propagation virtual range R = 0.5ct in Earth radii on the vertical axis and sounder frequency in kHz on the horizontal axis, where R is the virtual range, c is the free-space speed of light, and t is the echo propagation delay time in seconds. Each amplitude value has information about (a) phase, (b) sounding frequency, (c) Doppler frequency, (d) echo range, (e) angle of arrival, and (f) wave polarization [Reinisch et al., 2000; Galkin 2004]. The plasma responds to the RPI transmitter signal in two basic ways, (a) reflecting the signal from a remote location back to its origin, called an echo; and (b) sustaining short range plasma waves at characteristic frequencies, called resonances. To interpret the echoes correctly in terms of the plasma characteristics of the reflector, it is necessary to determine the wave polarizations of the echoes i.e., the $O-$ and $X-$ wave components [Reinisch et al., 2000] with respect to propagation perpendicular to the ambient geomagnetic field $\mathbf{B_0}$ and R− and L− mode components with respect to propagation parallel to $\mathbf{B_0}$ [Benson, 2006; Galkin, 2004]. A train of echoes received on a plasmagram is called a trace. Echo traces in various wave propagation modes viz., Whistler, Z-, L-O, and R-X modes can be determined from the local plasma characteristics (f_{pe}/f_{ce}), wave amplitude, and frequency cutoffs observed on the plasmagrams. Figure 3.3 shows a typical IMAGE/RPI plasmagram. Echoes in various cold plasma wave modes can be identified, e.g., Whistler mode (50-135 kHz), ducted fast ZM (145 - 280 kHz), slow ZM (285-570 kHz), LO mode (285-600 kHz), and RX mode (630-900 kHz). Cutoffs are observed at ZM cutoff frequency (f_z), LO mode cutoff frequency (f_{pe}), and RX mode cutoff frequency (f_x). Resonances at f_{pe} and upper hybrid resonance frequency (f_{uh}) are also observed. The RPI transmitter stimulates short range plasma wave echoes and plasma emission, both known as local plasma resonances, that are detected in the plasmagrams. The resonance signatures appear as a spike (strong echoes covering the entire range on vertical axis but occupying only one or two frequency bins) at a characteristic frequency. The resonances are produced due to the resonant interaction of the local plasma due to the transmitter excitation. Plasma resonances observed on the plasmagrams are used to provide the local electron density N_e and magnetic field strength $|\mathbf{B_0}|$ [Benson et al., 2003]. Resonances at f_{ce} and its harmonics (nf_{ce}), f_{Qn} (Qn resonance) and f_{Dn} (Dn resonance) have been observed on IMAGE/RPI data [Benson et al., 2004]. The color bar on the right of the plasmagram shown in Figure 3.3 shows the amplitude of the electric field in decibels (dB). The electric field is calculated by dividing the measured amplitude of voltage on the antenna by the antenna effective length. The

antenna effective length is assumed to be half the physical length of the antenna [Sonwalkar et al., 2001]. Under this assumption, the effective lengths of the X, Y, and Z antennas are 250 m, 250 m, and 10 m, respectively [Reinisch et al., 2001].

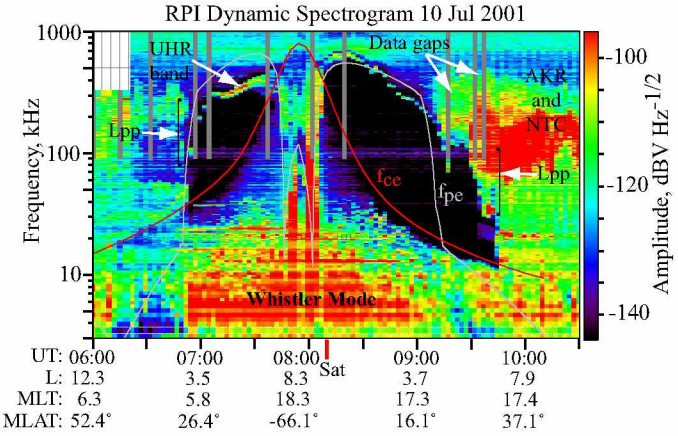

Figure 3.4 IMAGE/RPI dynamic spectrogram for 10 July 2001. x-axis represents time in UT; y-axis is the frequency (3-1000 kHz). Natural background emissions viz., WM, AKR and Non Thermal Continuum radiation are observed. Signals from ground transmitters, upper hybrid emissions, and plasmapause are shown.

3.1.4 Dynamic Spectrogram (Passive Recording)

In passive recording mode, RPI sweeps through the sequence of frequencies and listens to the background noise. In-situ measurements of electron density and temperature were performed by RPI using thermal noise spectroscopy. Figure 3.4 shows a dynamic spectrogram observed on 10 July 2001. A dynamic spectrum displays intensity (voltage in dB per unit square root frequency) as a function of frequency and time [Reinisch et al., 2000]. The color bar on the right shows the amplitude of the voltages measured on the RPI antennas in dBV/$\sqrt{Hz}$, which is simply the voltage divided by the square root of the 300 Hz bandwidth. The record of a dynamic spectrogram is obtained by the RPI receiver sweeping 300 Hz bandwidth through 243 frequency steps between 3 kHz and 1 MHz. The interval of 3 kHz to 20 kHz is from the thermal noise program 23, covered by 44 steps of 400 Hz increment at each step. The interval of 20 kHz to 1 MHz is from thermal noise program 26, covered by 199 logarithmic steps with 2% increment at each step. At each of the frequency steps, RPI samples the received signal 36 times with a 3.2 ms sampling period and calculates a series of eight 25.6 ms running averages. In Figure 3.4, the solid red curve indicates the f_{ce} calculated from the TSY96 magnetic field model [Tsyganenko and Stern, 1996]. The intense emissions below the electron cyclotron frequency are Whistler mode emissions. The ground VLF

transmitter signals in 10-40 kHz range are observed as horizontal lines on the spectrogram. The narrow banded emissions observed from ~07:00-10:00 UT in the frequency range of 40-500 kHz are the upper hybrid resonance (UHR) band emissions (Z mode emissions). The UHR band emissions are observed in the region where $f_{pe} > f_{ce}$ and are used to determine the magnetospheric electron density Ne [Benson et al., 2004]. The upper frequency edge of the UHR band is identified as the upper hybrid resonance frequency (f_{uh}). f_{uh} is related to f_{pe} and f_{ce} frequencies by the following formula:

$$f_{pe} = \sqrt{f_{uh}^2 - f_{ce}^2} \tag{3.1}$$

UHR emissions are often observed during the plasmapause crossings of the satellite and are therefore used to identify and measure the plasmapause. In Figure 3.4, the plasmapause signature could be identified at ~07:00 UT by a sudden drop in the UHR emission band. Above the UHR band, auroral kilometric radiation (AKR) and non-thermal continuum radiation are also observed [Gurnett, 1974; Hashimoto et al., 2006].

Table 3.1 List of RPI programs and their transmission format that were used for data survey.

Program	**Frequency**	**Virtual Range**	**Format** [databin, freq steps, range steps, waveform, duration]	**Year**	**Echo Type**
1	60-125 kHz	0.3-4.2 R_E	LTD, 0.9 kHz linear, 55 range steps, one 3.2 ms short pulse, 24 s	2001, 2002	ZM Ducted, Non ducted
2	180-245 kHz	0.3-4.2 R_E	LTD, 0.9 kHz linear, 55 range steps, one 3.2 ms short pulse, 21 s	2001, 2002	ZM Ducted, Non ducted
3	350-480 kHz	0.3-4.2 R_E	LTD, 2.0 kHz linear, 55 range steps, one 3.2 ms short pulse, 17 s	2001, 2002	ZM Ducted, Non ducted
5	60-1018 kHz	0.3-7.5 R_E	LTD, 2% log, 96 range steps, one 3.2 ms short pulse, 77 s	2001, 2002	ZM Ducted, Non ducted
	50-900 kHz	0.3-7.5 R_E	LTD, 2% log, 96 range steps, one 3.2 ms short pulse, 77 s	2003, 2004, 2005	ZM Ducted, Non ducted
21	14-500 kHz	0.3-4.5 R_E	LTD, 2% log, 69 range steps, one 3.2 ms short pulse, 78 s	2001, 2002	ZM Non ducted
43	50-900 kHz	0.3-7.5 R_E	LTD, 2% log, 100 range steps, one 3.2 ms short pulse, 73 s	2003	ZM Ducted, Non ducted
56	50-1014 kHz	0.3-4.2 R_E	LTD,2% log, 56 range steps, one 3.2 ms short pulse, 52 s	2003, 2004	ZM Ducted, Non ducted
57	20-326 kHz	0.3-4.2 R_E	LTD, 1.2 kHz linear, 56 range steps, one 3.2 ms short pulse, 77 s	2003, 2004	ZM Ducted, Non ducted
	20-326 kHz	0.3-3.6 R_E	LTD, 1.2 kHz linear, 56 range steps, one 3.2 ms short pulse, 77 s	2005	ZM Ducted, Non ducted

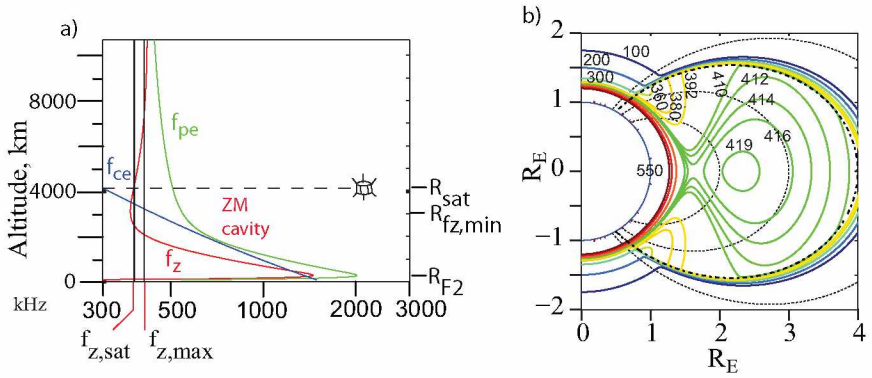

Figure 3.5 (a) Typical variation of plasma parameters f_{pe} (green), f_{ce} (blue), f_z (red) along the geomagnetic field line passing through the satellite with respect to the altitude. (b) Contours of the ZM cutoff frequency in a magnetic meridional plane with field lines at $L = 2$, 3, 4 and 5. Plasmapause is located at $L = 4$.

3.1.5 Measurement Programs and Schedules

To optimize the scientific output, different measurement programs and schedules were designed based on the operating modes, frequency range and waveforms, and databin format. Each measurement program can be completely specified by parameters, viz., frequency limits, frequency steps, waveform, pulse repetition rate, range, and data formats [Reinisch et al., 2000]. At different parts of the IMAGE orbit plasma densities varied over 6 orders of magnitude, signal powers by 12 orders of magnitude, and velocities by 4 orders of magnitude. To optimize the scientific output, RPI was pre-programmed to execute specific measuring programs on a cyclical schedule. A 'Measurement Program' (MP) was specified by a set of 21 selectable control parameters, and a total of 64 MPs could be stored. Out of the 64 MPs, few programs have been chosen for this research. Programs such as 1, 2, 3, 5, 21, 43, 56, and 57 were transmitted in the frequency range of 14 kHz to 1000 kHz in the altitude range of <10,000 km and were appropriate for observations of ZM echoes. Table 3.1 lists these programs and their transmission format. In the equatorial region, ZM cutoff frequency (f_z) can vary from ∼20 kHz - ∼10 MHz, and in the polar region f_z can vary from ∼10 kHz - ∼500 kHz [Gurnett and Inan, 1988]. Thus, all programs were chosen such that frequency range of the transmitted programs lie in the range ∼10 kHz-∼3000 kHz. However, most of the programs were transmitted up to a maximum frequency of only ∼1000 kHz.

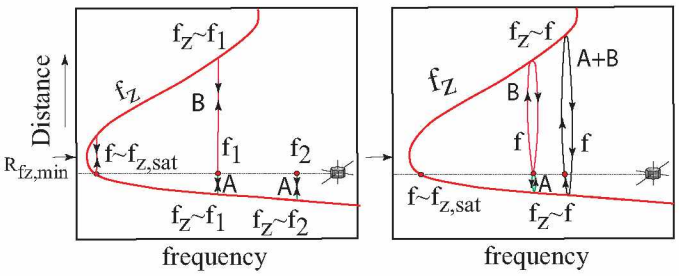

Figure 3.6 Schematic representations of the reflections of fast ZM waves when the satellite is below $Rf_{z,min}$ within the ZM cavity. (a) When no duct is present, (b) when a duct is present. (Adapted from Carpenter et al., [2003]).

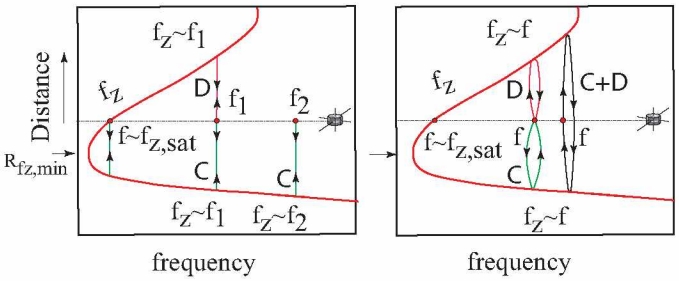

Figure 3.7 Schematic representations of the reflections of fast ZM waves when the satellite is above $Rf_{z,min}$ within the ZM cavity. (a) When no duct is present, (b) when a duct is present. (adapted from Carpenter et al., [2003]).

3.2 Interpretation of ZM Echoes and Principles of Echo Generation

In the magnetosphere, plasma is primarily composed of electrons (Ne), H^+, He^+, and O^+ ions. The expression for ZM cutoff frequency (f_z) plays an important role in the discussion of ZM wave propagation, reflection and echo formation,

$$f_z = \frac{f_{ce}}{2}[-1 + \{1 + 4(\frac{f_{pe}}{f_{ce}})^2\}^{\frac{1}{2}}] \tag{3.2}$$

where f_{pe}, f_{ce} are electron plasma frequency and electron cyclotron frequency respectively. We assume that up to 10,000 km altitude, the magnetosphere can be described by a diffusive equilibrium density model [Angerami and Thomas, 1964] and a dipole geomagnetic field model. Figure 3.5(a) shows the variation of typical plasma parameters f_{pe}, f_{ce} and f_z along the geomagnetic field line B_0 passing through the satellite (the specific plasma density model shown in this figure is the density model chosen for ray tracing analysis of fast ZM echoes observed on 10 July 2001). As is evident from equation 3.2, f_z is a function of f_{pe} and f_{ce}. f_z decreases with increasing f_{ce} and increases with increasing f_{pe}. With decreasing altitude, f_{ce} increases more rapidly than f_{pe}, therefore, f_z decreases

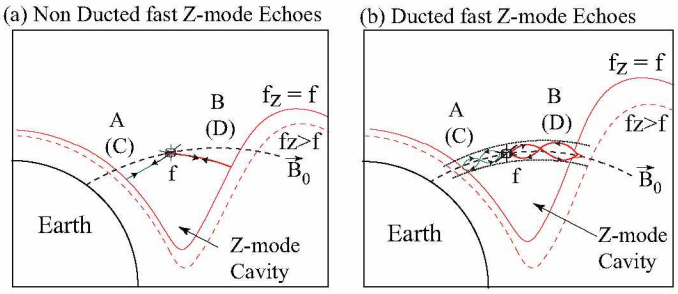

Figure 3.8 Schematic representations of the reflections of fast ZM waves in the magnetic meridional plane when the satellite is within the ZM cavity. (a) When no duct is present, (b) when a duct is present.

with decreasing altitude. At some altitude, e.g., ~3000 km, f_{pe} starts to increase more rapidly than f_{ce}. Therefore, there is a counter balancing effect of both the parameters viz., f_{pe} and f_{ce} on f_z. This counter balancing effect produces a minimum in f_z at some altitude $R_{fz,min}$. At lower altitudes (below R_{F2}), $f_{pe} \gg f_{ce}$, therefore, the f_z profile follows the f_{pe} profile. Due to this variation in the f_z profile, a cavity, called the ZM cavity, is formed in the f_z profile. If the satellite is within this cavity, then a narrow range of frequencies in the range $f_{z,sat} < f < f_{z,max}$ can be trapped within the cavity, where $f_{z,sat}$ and $f_{z,max}$ are f_z at the satellite and the upper frequency limit of the ZM cavity (figure 3.5(a)). Fast ZM rays transmitted from the satellite in the frequency range $f_{z,sat} < f < f_{z,max}$ can reflect, while propagating upwards or downwards from the satellite, from the region where $f \sim f_z$. Carpenter et al., (2003) presented the first observations of ducted fast ZM echoes within the ZM cavities and have discussed the trapping phenomena.

Figure 3.5(b) shows the contours of the ZM cutoff frequency in the magnetic meridional plane (with the same plasma density model as in Figure 3.5(a)). The black dash-dot field line represents the plasmapause (L_{pp}) at L=4. Contours have been plotted from 100 kHz - 550 kHz. A density model is chosen such that we get a ZM cavity inside L_{pp}. The magnetosphere is horizontally stratified. At lower altitudes, $f_{pe} \gg f_{ce}$, therefore, the f_z curve follows the f_{pe} curve. Along an L-shell with increasing altitude, the ZM cutoff frequency first decreases, then reaches a minimum at some altitude, and then increases again, thus forming a cavity. The length of the cavity increase with decreasing L shell, as is evident from the figure. It is also evident that the contours of f_z follow the L_{pp} field lines. This is because at L_{pp}, the plasma density decreases very sharply, therefore, there is a large gradient in the f_{pe} across L_{pp}. On the other hand, f_{ce} has no dependence upon L_{pp}, and is continuous across L_{pp}, i.e., there is no sharp decrease in the levels of f_{ce} across L_{pp}. Thus, across L_{pp}, the value of f_{ce} is constant. Therefore, the gradient in the f_{pe}/f_{ce} ratio depends only

upon the gradient of f_{pe} values. Due to this, there is a sharp decrease in the level of f_{pe}/f_{ce} at L_{pp}, and thus the f_z level shows a sharp decrease at L_{pp}.

Figure 3.6(a) shows a schematic of the interpretation of the ZM echoes when the satellite is below the altitude minimum of f_z i.e., $R_{fz,min}$. The red curve is the geomagnetic field aligned profile of f_z. The solid horizontal line represents the altitude of the satellite while it traverses the ZM cavity. Ray path propagation along the 'short' path (rays propagating towards Earth) are labeled as 'A' trace, while ray path propagation along the 'long' path (rays propagating towards the equator) are labeled 'B' trace. A, B, and other higher traces are observed for frequencies $f > f_{z,sat}$. Trace A corresponds to a single traversal of the ray propagating downward and reflecting back. For frequencies close to $f_{z,sat}$, the propagation path of the ray from the satellite to its reflection point in the downward path is very small. Therefore, for an initial frequency range close to $f_{z,sat}$, the virtual range of A trace starts apparently from a zero virtual range (on plasmagrams it is observed starting from the lowest virtual range limit of the transmitted program), gradually increases up to few ms above the lower cutoff, and then becomes constant. Trace B is formed due to a single traversal of the ray path propagating upwards with respect to the satellite altitude.

Figure 3.6(b) shows the schematics for ducted fast ZM echoes. The A and B traces are formed due to single traversals of rays guided along the geomagnetic field aligned ducts present within the ZM cavity. The second and third elements viz., trace A+B and trace 2A+B, etc., are formed due to multiple hops back and forth between the echoing points within the cavity. The presence of multiple traces led Carpenter et al., (2003) to suggest that these echoes are guided along the geomagnetic field aligned ducts, analogous to the X- and O- mode echoes that were observed by the IMAGE from regions on opposite sides of the magnetic equator. Ducted fast ZM echoes within the cavity are observed in reflections from the same hemisphere.

Figure 3.6(a) represents an ideal profile of f_z in distance versus frequency format along the geomagnetic field line passing through IMAGE. Consider three transmitted frequencies, $f \sim f_{z,sat}$, f_1, and f_2. f_1 and f_2 are frequencies above $f_{z,sat}$. When $f \sim f_{z,sat}$, only an upward propagating wave could be launched along path B. Path A is not excited. The wave propagating upwards passes through the minimum and is reflected at a region where $f \sim f_z$. The wave undergoes multiple reflections back and forth and forms echoes at $f \sim f_{z,sat}$. At f_1, waves can propagate both downwards (path A) and upwards (path B). The waves returning after one reflection can propagate back and forth within a duct and form higher traces. At f_2, only path A can be illuminated, as the wave propagating upwards (path B) does not return back to the satellite. This phenomena has been

discussed in detail by Carpenter et al., (2003). From the cold plasma dispersion diagram, we know that the group velocity of fast ZM should increase as frequency increases above the local f_z and therefore, the virtual range should decrease. From the plasmagram, it is observed that within a few kHz above the observed cutoff ($f_{z,sat}$), the virtual range of B trace decreases. Above that frequency, due to the gradual slope of the f_z curve, the increase in distance to the echoing points more than compensates for the effects of increasing group velocity, and therefore, the virtual range increases again.

Figure 3.7 shows schematics of the interpretation of the ZM echoes when the satellite is above $R_{fz,min}$. This schematic is similar to Figure 3.6. Ray paths propagating 'downward' (rays propagating towards the Earth) are labeled as 'C' trace, while ray paths propagating 'upward' (rays propagating towards the equator) are labeled as 'D' trace. C, D, and other higher traces are observed for frequencies $f > f_{z,sat}$. The same argument as for AB type follows for the propagation and reflection of CD type echoes. Figure 3.8 shows the propagation scenario for (a) nonducted and (b) ducted echoes in the magnetic meridional plane. Red curves represent the contours of f_z, the dashed black curve is the L-shell of the satellite, and the solid green and red ray paths represent the propagation of fast ZM waves within the ZM cavity in the downward and upward directions, respectively. The figure illustrates that the propagation mechanisms for both AB type and CD type fast ZM echoes are fundamentally the same.

3.3 Observations of ZM Echoes

This work presents observations of fast Z mode echoes on the IMAGE satellite during years 2001 to 2005. We have surveyed about 72,000 plasmagram for both nonducted and ducted fast Z mode echoes. We have used a special software called 'BinBrowser' developed especially for browsing and downloading the RPI plasmagrams and dynamic spectrogram by Galkin et al., (2001). This software is available for download from the University of Massachusetts Lowell Center for Atmospheric Research (UMLCAR) website [http://ulcar.uml.edu/Installation/BinBrowser/install.htm]. The RPI data is available online and could be accessed through BinBrowser software. Carpenter et al., (2003) have presented the first observations of ducted fast Z mode echoes within the trapping region or the ZM cavity. They surveyed the IMAGE data from 28 June 2001-31 July 2001 obtained from the RPI operating at low altitudes of ~1000-5000 km. Carpenter et al., (2003) categorized the ducted fast Z mode echoes (~75 cases observed in 34 days studied) as AB or CD type ducted

fast Z mode echoes. Using the same categorization as Carpenter et al., (2003), we have surveyed and expanded the data set to observation from year 2001-2005 of the IMAGE mission and from ~1000-10,000 km altitude range. Besides finding the categories of ducted echoes as described by Carpenter et al., (2003), we have found several new observations and features of nonducted and ducted ZM echoes which are presented in subsequent sub-sections. We have found observations of nonducted fast ZM echoes that were reflected from altitudes below as well as above the IMAGE satellite within the Z mode cavities. We also present the first observations of nonducted and ducted fast ZM echoes reflecting from above the satellite altitude outside the plasmasphere. We have discovered a new phenomenon: a frequency gap in echo traces reflecting from below the satellite altitude. This phenomenon is important as it is a direct manifestation of the presence of ducts in the magnetosphere and is important to study the dispersion relations and wave properties in the vicinity of characteristic plasma frequency (f_{pe}).

In the 5.8 year mission of the IMAGE satellite, operating in the frequency range 14 kHz- 1000 kHz at altitudes 600-10,000 km, RPI has detected a variety of ducted and nonducted ZM echoes at all latitudes, altitudes, and MLTs at frequencies up to ~800 kHz. Three basic types of ZM activities have been observed on IMAGE/RPI, namely (1) ducted or trapped echoes; (2) nonducted or direct echoes; and (3) diffuse or scattered echoes. A total of ~1500 cases of ducted and ~3500 cases of nonducted echoes have been observed out of a total transmission of ~72,000 plasmagrams, i.e., fast ZM echoes have been observed for ~6.5% of the total transmissions made. Ducted echoes have been observed in the altitude range of ~600-10,000 km, at $30° - 70°$ invariant latitudes, and at all MLTs. About 50% of ducted fast ZM cases are CD type, ~35% are AB type, and ~15% are AB type ducted from both hemispheres. Nonducted echoes have been observed in the altitude range of ~600-10,000 km at all invariant latitudes and Magnetic Local Times (MLT).

About 370 best cases of nonducted and ducted fast ZM echoes (105 cases of AB type, 147 cases of CD, 45 cases of conjugate ducted and 75 cases of non ducted) have been selected for a detailed survey. These cases were chosen on the following criteria: (1) all traces are distinct; (2) cutoffs are distinct; and (3) time delay versus frequency dispersion is measurable. The results of the detailed survey of these cases revealed some typical features of the ducted echoes. An atlas of echoes, based on this survey, is presented to demonstrate different types of nonducted and ducted echoes that were observed by IMAGE/RPI and have been surveyed for this work. The propagation of ZM waves is affected by the relative position of the satellite with respect to the ZM cavity, the plasmapause, and also by the presence of ducts and small scale irregularities. These effects are manifested in the

echo traces recorded by the IMAGE/RPI. The following subsections discuss different types of fast ZM echo signatures observed by the IMAGE satellite and their significance. Table 3.4, provided at the end of this section, contains the summary of each case presented in this section, viz., satellite position, characteristic frequencies, types of echo traces observed, and special features of the echoes.

3.3.1 AB Type Ducted ZM Echoes

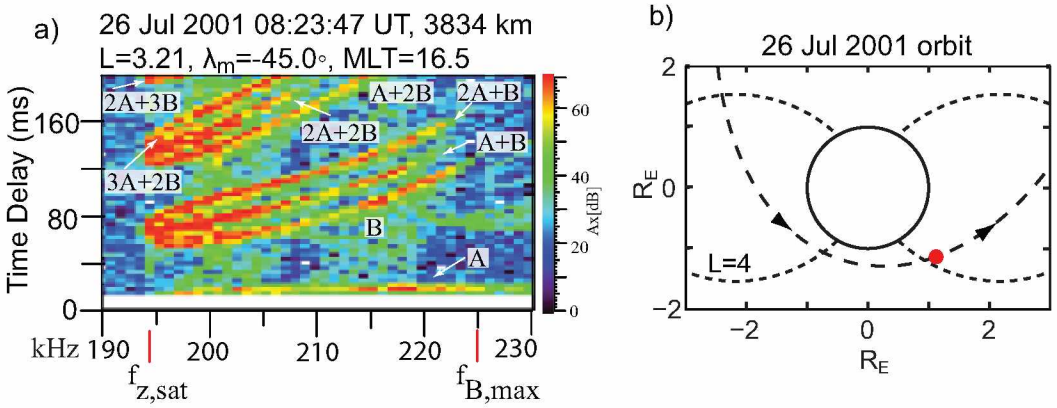

Figure 3.9 (a) Plasmagram showing discrete traces of AB type ducted fast ZM echoes observed on 26 July 2001. (b)IMAGE orbit plot for 26 July 2001 with satellite position (red dot)(regenerated from Carpenter et al., 2003).

Figure 3.9(a) shows plasmagrams of AB type ducted fast ZM (FZM) echoes received by the X antenna on RPI/IMAGE on 26 July 2001 at 08:23:47 UT inside the plasmasphere. Figure 3.9(b) shows the IMAGE orbit plot for 26 July 2001 with satellite position (red dot) at 08:23 UT. Details of satellite position, plasmapause location, and characteristic frequencies have been listed in Table 3.4. Figure 3.9(a) shows 3 sets of echo traces (total 8 echo traces) all beginning at 194.4 kHz. These echo traces are A, B, A+B, 2A+B, A+2B, 2A+2B and 3A+2B. These traces have time delay integral relationships among themselves and are formed after one, one, two, three, three, four and five reflections, respectively, while propagating within the duct between two reflection points inside the ZM cavity. Each of the traces has multiple echoes at each frequency (multipath propagation; 2-4 bins of time delay spread). The time-integral relationship and multiple echoes at each frequency indicate that these echoes are formed due to ducted propagation inside a field aligned duct. The epsilon signature of the echoes is similar to the RX-mode echoes observed by RPI/IMAGE that are thought to propagate along the geomagnetic field line inside a duct and reflect from conjugate hemispheres [Fung et al., 2003, Fung and Green 2005]. The epsilon signature in the present case indicates that IMAGE was within a duct at an altitude below $R_{f_{z,min}}$ within

the ZM cavity, and the echoes were formed due to reflection from above and below the satellite in the same local hemisphere (see Figure 3.8). A total of ∼500 cases of AB type ducted fast ZM echoes have been observed, in the altitude range of ∼600-10,000 km and invariant latitude range of $18° - 68°$, and are available for measurements of field aligned electron density, ducts, and ZM cavity. A detailed ray tracing analysis for this case has been presented in Chapter 5 of this thesis.

3.3.2 AB Type Nonducted ZM Echoes

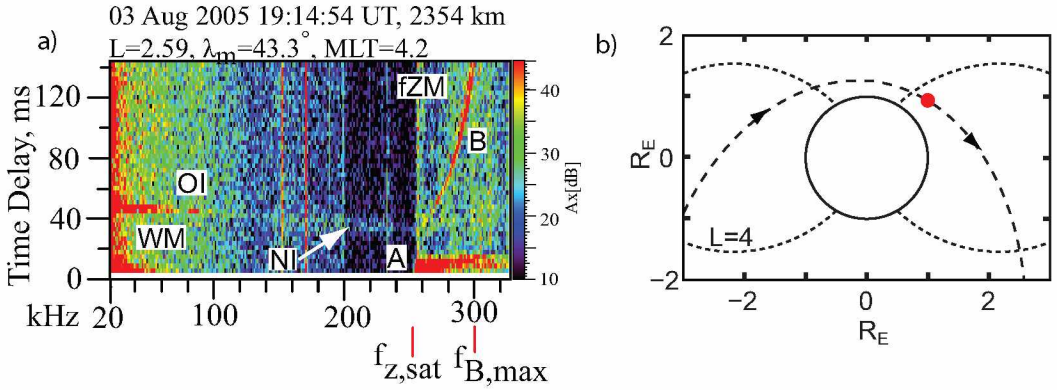

Figure 3.10 (a) Plasmagram showing discrete traces of AB type nonducted fast ZM echoes observed on 03 August 2005. The ZM cutoff frequency (f_z) at the satellite, $f_{z,sat}$, is 254 kHz and the highest nonducted frequency for B trace, $f_{B,max}$, is 300.8 kHz. (b) Orbit plot with satellite position (red dot) for 3 August 2005.

Figure 3.10(a) shows a plasmagram of AB type nonducted fast ZM echoes received by the X antenna on RPI/IMAGE on 3 August 2005 at 19:14:54 UT. Figure 3.10(b) shows the IMAGE orbit plot for 3 August 2005 with satellite position (red dot) at 19:14 UT. Refer to Table 3.4 for satellite position and other details. Figure 3.10(a) shows two traces of nonducted fast ZM echoes viz., trace A and trace B. The first echo trace (trace A) starts from an apparent zero range cutoff near 254 kHz and then rises to a time delay of ∼12 ms at higher frequencies up to the upper frequency limit of the plasmagram. Trace B starts at 261.2 kHz, slightly higher than $f_{z,sat}$, from a time delay of ∼40 ms and rises to an upper virtual range limit of ∼150 ms at 303.2 kHz. The absence of higher traces (A+B, 2A+B etc.) that are present in ducted cases suggests that the fast ZM echoes are non ducted. Figure 3.10(a) also shows two traces of Whistler mode echoes viz., obliquely-incident (OI) and normally-incident (NI) specularly reflected(SR) Whistler mode (WM) echoes (verified with ray tracing analysis) [Sonwalkar et al., 2011a, 2011b]. The WM echoes are observed over a frequency range of 20-237.2 kHz. The SR-WM echoes are patchy and the upper cutoff is not

clear. In the frequency range of 256.4-326 kHz and in the time delay range of ∼30-45 ms, there is a continuation of SR-WM echo trace to overlap with fast ZM echoes. The AB type signature of the fast ZM echoes indicates that IMAGE was within the ZM cavity at an altitude below $R_{f_{z,min}}$ and that the echoes were formed due to reflection from above and below the satellite in the same local hemisphere (see Figure 3.8). A and B trace echoes travel close to the field lines and therefore can provide information about the field aligned electron density distribution. A total of ∼200 cases of AB type nonducted fast ZM echoes have been observed, in the altitude range of ∼1100-10,000 km and invariant latitude range of $28° - 69°$, and are available for measurement of field aligned electron density distribution. A detailed ray tracing analysis for this case has been presented in Chapter 5 of this thesis.

3.3.3 CD Type Ducted ZM Echoes

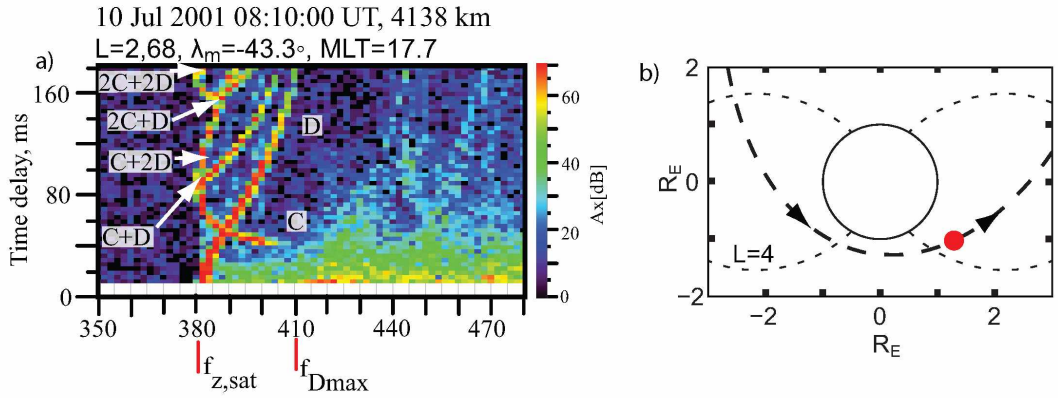

Figure 3.11 (a) Plasmagram showing discrete traces of CD type ducted fast ZM echoes observed on 10 July 2001. The ZM cutoff frequency (f_z) at the satellite, $f_{z,max}$, is 380 kHz and the highest ducted frequency, $f_{D,max}$, is 410 kHz. (b) IMAGE orbit plot for 10 July 2001 with satellite position (red dot).

Figure 3.11(a) shows a plasmagram of CD type ducted fast ZM echoes received by the X antenna on RPI/IMAGE on 10 July 2001 at 08:10:00 UT inside the plasmapshere. Figure 3.11(b) shows the IMAGE orbit plot for 10 July 2001 with satellite position shown as a red dot. Figure 3.11(a) shows 3 sets of echo traces (6 echo traces total), all beginning at 380 kHz. These echo traces are D, C, C+D, C+2D, 2C+D, and 2C+2D. These traces have a time delay integral relationship among themselves and are formed after one, one, two, three, three, and four reflections, respectively, while propagating within the duct between two reflection points inside the ZM cavity. Each of the traces has multiple echoes at each frequency. The time delay integral relationship and multiple echoes

at each frequency indicate that these echoes are formed due to ducted propagation inside a field aligned duct. The IMAGE was within a duct at an altitude above $R_{f_{z,min}}$ the ZM cavity and the echoes were formed due to reflection from above and below the satellite in the same local hemisphere (see Figure 3.8). A total of ∼800 cases of CD type ducted fast ZM echoes have been observed, in the altitude range of ∼1100-10,000 km and invariant latitude range of $30° - 68°$, and are available for measurements of field aligned electron density distribution, ducts, and ZM cavity. This case has been studied in detail and a detailed ray tracing analysis for this case has been presented in Chapter 4 of this thesis.

3.3.4 CD Type Nonducted ZM Echoes

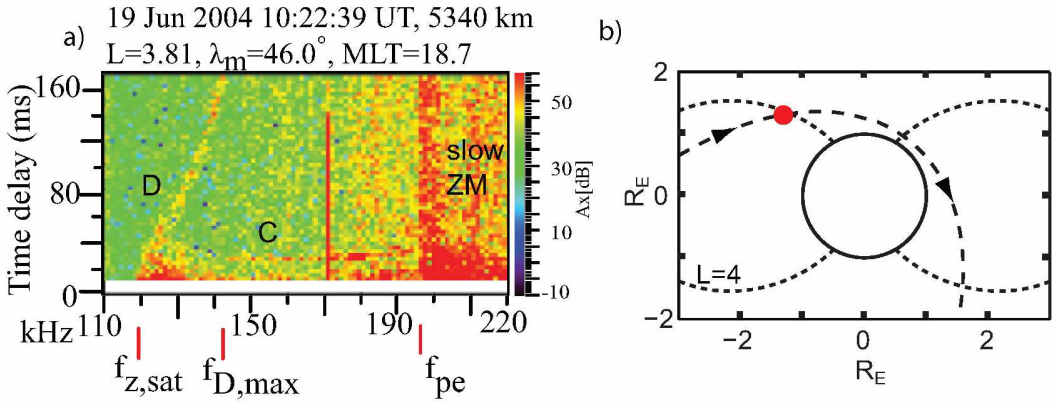

Figure 3.12 (a) Plasmagram showing discrete traces of CD type nonducted fast ZM echoes observed on 19 June 2004. The ZM cutoff frequency (f_z) at the satellite, $f_{z,sat}$, is 119.6 kHz and the highest frequency for D trace is, $f_{D,max}$, is 142.4 kHz. (b) shows IMAGE orbit plot for 19 Jun 2004 with satellite position (red dot).

Figure 3.12(a) shows a plasmagram of CD type nonducted fast ZM (fast ZM) echoes received by the X antenna on RPI/IMAGE on 19 June 2004 at 10:22:39 UT inside the plasmasphere. Figure 3.12(b) shows the IMAGE orbit plot for 19 June 2004 with satellite position at 10:22:39 UT shown as a red dot. Figure 3.12(a) shows two traces of nonducted fast ZM echoes viz., trace C and trace D. The first echo trace (trace D) starts from an apparent zero range cutoff near 119.6 kHz and then rises to a time delay of ∼178 ms at 143.6 kHz. Trace C starts at 143.6 kHz, higher than $f_{z,sat}$, from a time delay of ∼30 ms. The higher traces viz., C+D, C+2D, etc., that are present in ducted cases suggest that the fast ZM echoes are non ducted. The CD type signature of the fast ZM echoes indicate that IMAGE was within the ZM cavity at an altitude above $R_{f_{z,min}}$ and the echoes were formed due to reflection from above and below the satellite in the same local hemisphere (see Figure

3.8). Trace C and D echoes travel close to the field lines and therefore can provide information about field aligned density distribution. A total of ∼300 cases of CD type nonducted fast ZM echoes have been observed, in the altitude range of ∼1800-10,000 km and invariant latitude range of 30° – 65°, and are available for measurements of field aligned electron density distribution. A detailed ray tracing analysis for this case has been presented in Chapter 5 of this thesis.

3.3.5 Conjugate Ducted ZM Echoes in Equatorial Region

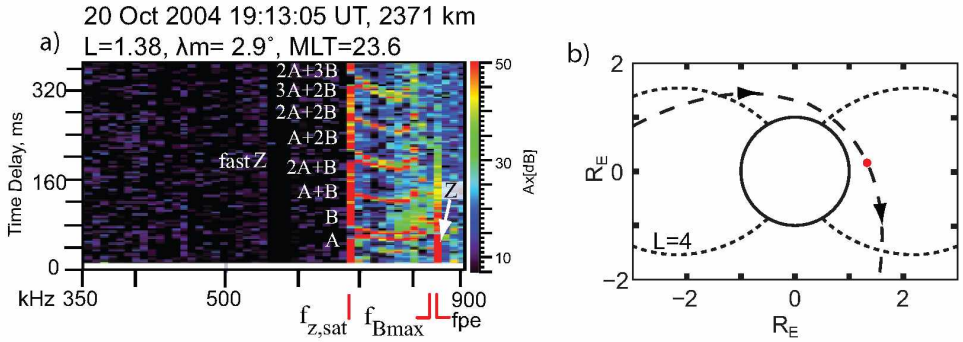

Figure 3.13 (a) Plasmagram showing discrete traces of conjugate ducted fast ZM echoes observed on 20 October 2004. The ZM cutoff frequency (f_z) at the satellite, $f_{z,sat}$, is 682.6 kHz and the highest ducted frequency is 832 kHz. (b) IMAGE orbit plot for 20 Oct 2004 with satellite position (red dot).

Figure 3.13(a) shows a plasmagram of conjugate ducted fast ZM (fast ZM) echoes received by the X antenna on RPI/IMAGE on 20 October 2004 at 19:13:05 UT inside the plasmasphere. Figure 3.13(b) shows the IMAGE orbit plot for 20 October 2004 with satellite position at 19:13:05 UT. The satellite was moving through the northern polar region towards the plasmasphere. Figure 3.13(a) shows 4 sets of echo traces (8 ducted echo traces total), all beginning at a lower cutoff of $f_{z,sat}$=682.6 kHz and a nonducted normal ZM trace that is observed to rise from zero time delay range (∼12 ms) at 696.3 kHz to 883.1 kHz. The fast ZM echo traces starting at time delay ∼60 ms are named B, A+B, and 2A+B. These traces have a time delay integral relationship among themselves and the A trace and are formed after one, two and three reflections, respectively, while propagating within the duct between reflection points in the conjugate hemispheres. Each of the traces has multiple echoes, ranging from 1-2 bins, at each frequency (multipath propagation). Echo elements A+2B, 2A+2B, and 3A+2B of the third set and 2A+3B of the fourth set are also visible starting at 682.6 kHz lower cutoff. The other higher set of echoes are not observed due to limitations of the virtual range of the sounding program. From the cutoff frequency of the 682.6 kHz and model (IGRF-2005) value of

f_{ce}=371.6 kHz, we find the local f_{pe}=848.3 kHz. This value is in close agreement with the observed f_{pe}=848.8 kHz. Trace A results from waves reflecting from the local hemisphere and trace B results from the waves reflecting from the conjugate hemisphere. The virtual range of trace A is slightly lower than that of trace B, suggesting that the length of the wave propagation paths for trace A is only slightly smaller than that of trace B. A large spread in time delay is observed at a lower cutoff $f_{z,sat}$. Time delay vs. frequency dispersion of all the traces shows a nose frequency (frequency at which time delay is minimum) midway between $f_{z,sat}$ and f_{pe}, i.e., the time delay (t_g) first decreases with frequency (at low frequency portion), attains a minimum at midway between $f_{z,sat}$ and f_{pe} (similar to nose frequency of whistlers [Heliwell, 1965]), and then starts to increase again with frequency (at high frequency portion). At frequencies near f_{pe}, t_g increases very sharply. From the cold plasma dispersion diagram, the group velocity of the ZM should increase as frequency increases above local f_z, therefore, we expect the time delay to decrease with frequency. The group velocity increases up to midway between $f_{z,sat}$ and f_{pe} and then decreases very sharply with frequency up to f_{pe} (see Chapter 4 Figure 4.28). This variation of group velocity with frequency easily explains the dispersion of the aforementioned echo traces.

The conjugate ducted echo traces are similar in appearance but different in characteristics than the ducted AB type fast ZM echoes observed inside a ZM cavity: (1) the AB-type fast ZM ducted echoes are formed due to reflections within the same local hemisphere in contrast to conjugate echoes, where reflections take place from local as well as conjugate hemispheres; (2) for conjugate ducted echoes, all the traces exhibit nose frequencies which lies midway between $f_{z,sat}$ and f_{pe}, whereas, in the case of AB type ducted echoes inside the ZM cavity, the nose frequency for B trace is observed close to $f_{z,sat}$; and (3) for conjugate ducted echoes, the upper cutoff frequency of all the traces lie very close to the f_{pe}, in contrast, for the AB type echoes, the upper cutoff of B trace is $f_{B,max} \ll f_{pe}$. We have found from ray tracing results that the upper cutoff of all the traces for a given duct is $\sim f_{pe}$ (see ray tracing discussion for 10 July 2001 case in Chapter 4). A total of ~250 cases of conjugate ducted fast ZM echoes have been observed, in the altitude range of ~600-10,000 km and invariant latitude range of $18° - 60°$, and are available for measurements of field aligned electron density distribution, and ducts.

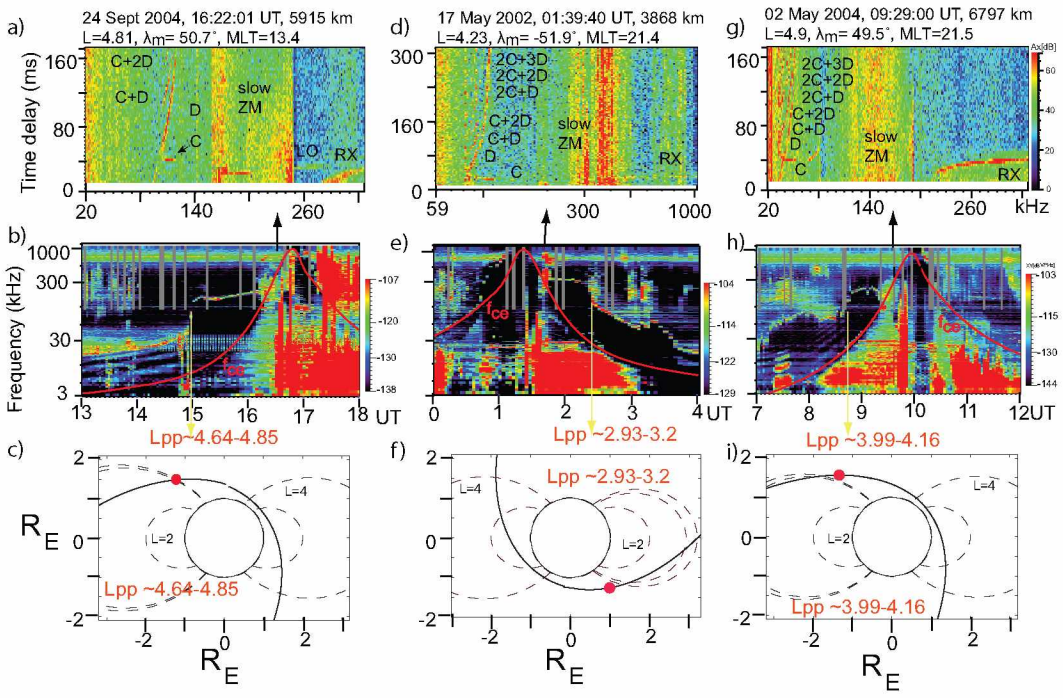

Figure 3.14 Examples of fast ZM echoes observed within the plasmapause and outside the plasmasphere. First row shows examples of fast ZM echoes reflecting in the ZM cavity (a) in the plasmapause, (d), (g) outside the plasmasphere. Second row shows corresponding dynamic spectra with plasmapause, and third row shows IMAGE orbit on that day with satellite position shown by red dot.

3.3.6 Z Mode Echoes Observed Within the Plasmapause and Outside the Plasmasphere

Figure 3.14 (a) shows an example of ducted fast ZM echoes received by the X antenna on RPI/IMAGE on 24 September 2004 at 16:22:01 UT. The echoes shown in Figure 3.14(a) are observed within the plasmapause. The plasmapause, as determined from dynamic spectra shown in Figure 3.14(b), is located at L ~4.64-4.85 on dayside, i.e., for MLT=13.4. The electron density, determined from the f_{uh} emissions, drops from 223 e/cc to 16 e/cc within a span of ~0.2L. Figure 3.14(c) shows the IMAGE orbit plot for 24 September 2004 with the position of the satellite at 16:22:01 UT. Figure 3.14(a) shows 2 sets of echo traces (4 echo traces total). These traces are D, C, C+D, and C+2D. Slow ZM, LO- and RX- mode echoes are also observed. From the cutoff frequency of 94.4 kHz and model (IGRF-2005) value of f_{ce} =188 kHz, we find the local f_{pe} =162 kHz. The local f_{pe} measured from resonance is 158 kHz. From the observed upper hybrid resonance frequency f_{uh} = 249 and RX mode cutoff $f_x = 280$, f_{pe} is calculated as 151.4 kHz and 150.4 kHz, respectively.

Figure 3.14(d) shows an example of ducted fast ZM echoes received by the X antenna on

RPI/IMAGE on 17 May 2002 at 01:39:40 UT. The echoes shown in Figure 3.14(d) are observed outside the plasmapause. The plasmapause, as determined from dynamic spectrogram shown in Figure 3.14(e), is located at L ~2.93-3.20 on nightside, i.e., for MLT=21.4. The electron density, determined from the f_{uh} emissions, drops from 996 e/cc to 157 e/cc within a span of ~0.27 L. Figure 3.14(f) shows the IMAGE orbit plot for 17 May 2002 with the position of the satellite at 01:39:40 UT (red dot). Figure 3.14(d) shows at least 3 sets of echo traces (7 echo traces total), all beginning at the same lower cutoff, f_z=82.4 kHz. Slow Z- and RX-mode echoes are also observed. From the observed cutoff frequency f_z=82.4 kHz and model (IGRF-2005) value of f_{ce}=338 kHz, we find the local f_{pe}=186 kHz.

Figure 3.14(g) shows an example of ducted fast ZM echoes received by the X antenna on RPI/IMAGE on 02 May 2004 at 09:29:00 UT. The echoes shown in Figure 3.14(g) are observed outside the plasmapause. The plasmapause location, determined from the dynamic spectrogram shown in Figure 3.14(h), lies at L ~3.99-4.16 on nightside, i.e., for MLT=21.5. The electron density, determined from f_{uh} emissions on the dynamic spectra, drops from 456 e/cc to 94 e/cc within a span of ~0.17 L. Figure 3.14(i) shows the IMAGE orbit plot for 02 May 2004 with satellite position at 09:29:00 UT (red dot). Figure 3.14(g) shows at least 3 sets of echo traces (7 echo traces total) all beginning at the same lower cutoff f_z=32 kHz. The plasmagram also shows an upper hybrid resonance signature at f_{uh}=190.4 kHz. f_{pe} resonance is observed at 81.2 kHz. From the observed cutoff frequency f_z=32 kHz and model (IGRF-2005) value of f_{ce}=163 kHz, we find the local f_{pe}=79 kHz. From the observed upper hybrid resonance frequency f_{uh}=190.4 kHz and free space RX mode echo cutoff f_x = 212 kHz, f_{pe} is calculated as 81.6 kHz and 90.6 kHz, respectively.

From the occurrence patterns of fast ZM echoes, it is observed that a majority of fast ZM echoes are inside the plasmasphere. This suggests that the ZM cavity exists mostly within the plasmasphere. Out of 370 best cases chosen for detailed analysis, 10 cases were observed outside the plasmasphere, and 5 cases within the plasmapause. Observations of few cases outside the plasmasphere suggest that the cavity occurs outside the plasmasphere only rarely. ZM cavity regions may play an important role in the propagation of natural ZM emissions in the magnetosphere, for e.g., Gurnett et al., (1983) have presented observations of trapped ZM radiation in the polar region and have suggested that once trapped in the cavity, the radiation should be subject to very little attenuation and could build up to large intensities. As suggested by Carpenter et al., (2003), the trapped ZM waves observed near the plasmapause region is important in order to investigate this poorly known region of the magnetosphere.

3.3.7 Fast ZM Reflected from Below Satellite Altitude and Slow ZM Echoes

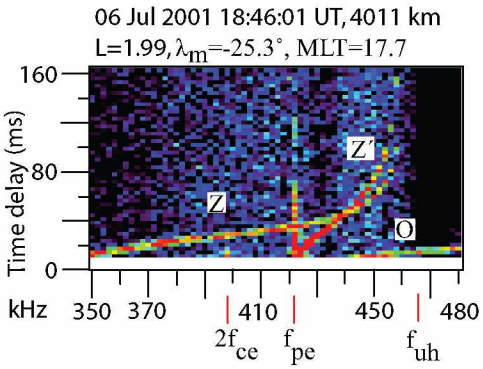

Figure 3.15 Plasmagram showing discrete traces of normal Z(Z) and slow Z(Z') ZM echoes observed on 06 July 2001 (regenerated from Carpenter et al., 2003).

Figure 3.15 shows an example (the same example as shown in Figure 4 of Carpenter et al., 2003) of normal-Z (Z) and slow-Z (Z') mode echoes received by the X antenna on RPI/IMAGE on 06 July 2001 at 18:46:01 UT. Figure 3.15 shows a well defined Z trace that begins at f_z ~350 kHz and extends upward towards a maximum frequency f_{zI} ~458 kHz, where f_{zI} is called Z-infinity [Benson, 2006] and is the upper frequency limit on vertical incidence propagation [Jackson, 1969]. The value of this limiting frequency depends upon f_{pe}, f_{ce}, and the angle between the vertical and the direction of Earth's magnetic field. The propagation time delay at f_{zI} becomes infinite [Hagg et al., 1969]. The normal Z trace results from the radio waves that propagate vertically downward from the satellite, reflect at ZM cutoff level f_z, and retrace their path back to the satellite [Hagg et al., 1969]. There is an additional ZM trace labeled as Z' that begins at local f_{pe} = 422 kHz and approaches the infinite range at the same frequency, f_{zI}, as the normal Z trace. The Z' trace was interpreted by Calvert, (1966) as the trace that propagates obliquely with respect to the geomagnetic field B_0, reflects at O-mode reflection level $f = f_{pe}$, and propagates back to the satellite. The echo trace marked as O in Figure 3.15 is the O-mode trace observed between frequencies 422-480 kHz. In Figure 3.15, the value of f_{pe} is found to be ~422 kHz and f_{ce} = 199 kHz. The lower cutoff of the normal Z trace f_z extends beyond the lowest limit (350 kHz) of the transmitted program. From the observed values of f_{pe} and f_{ce}, the values of f_z and f_{uh} are found to be ~334 kHz and ~466 kHz, respectively.

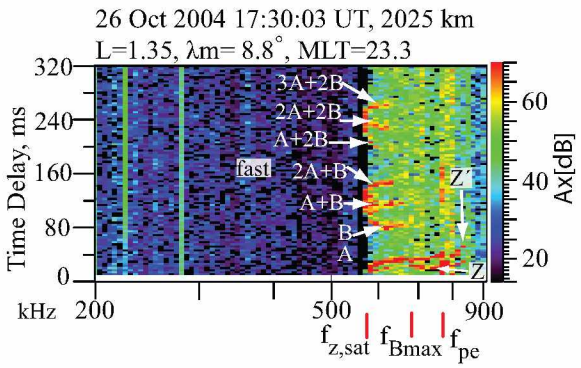

Figure 3.16 Plasmagram showing discrete traces of conjugate ducted fast ZM echoes and nonducted normal Z(Z) and slow Z(Z') ZM echoes observed on 26 October 2004. The ZM cutoff frequency (f_z) at the satellite, $f_{z,sat}$, is 571.2 kHz.

3.3.8 Fast ZM Reflected From Above the Satellite Altitude and Slow ZM Echoes

Figure 3.16 shows an example of ducted fast ZM and nonducted normal-Z (Z) and slow-Z (Z') mode echoes received by the X antenna on RPI/IMAGE on 26 October 2004 at 17:30:03 UT. The ducted fast ZM echoes are formed due to reflections from conjugate hemispheres. Figure 3.16 shows 3 sets of echo traces (7 ducted echo traces total), all beginning at lower cutoff $f_{z,sat}$=571.2 kHz. The echo trace labeled A starts at apparently zero time delay at cutoff $f_{z,sat}$=682.6 kHz and then rises to ~35 ms at higher frequencies up to the maximum frequency limit f_{pe}=772 kHz. A discrete trace is observed just below trace A that is the normal Z trace. A nonducted normal ZM trace is observed to rise from zero time delay (0.3 R_E) at cutoff f_z=571.2 kHz and extend upwards toward a maximum frequency f_{zI} ~849 kHz. The Oblique ZM trace (Z') is observed to rise from ~4 ms time delay at cutoff f_{pe} ~769 kHz and extend upwards toward a maximum frequency f_{zI} ~849 kHz. In Figure 3.15, the value of f_{pe} is found to be ~768.8 kHz. The IGRF-2005 model value of f_{ce}=472 kHz. From the observed values of cutoff f_z and f_{ce}, the values of f_{pe} is found to be ~772 kHz.

Figure 3.17 shows an example of ducted fast ZM and nonducted normal-Z (Z) and slow-Z (Z') mode echoes received by the X antenna on RPI/IMAGE on 09 October 2004 at 12:13:20 UT. Figure 3.17 shows 4 sets of echo traces (11 ducted echo traces total), all beginning at lower cutoff $f_{z,sat}$=196.1 kHz. The echo trace labeled D starts at apparently zero virtual range at cutoff $f_{z,sat}$=196.1 kHz and then rises steeply to a time delay of ~276 ms up to a maximum frequency of 229.7 kHz. A nonducted normal Z trace is observed to rise from ~4 ms time delay and extend upwards towards a maximum frequency f_{zI} ~355 kHz. An Oblique Z trace (Z') is observed to rise from ~4 ms time delay at cutoff f_{pe} ~291 kHz and extend upwards toward a maximum frequency f_{zI} ~355 kHz.

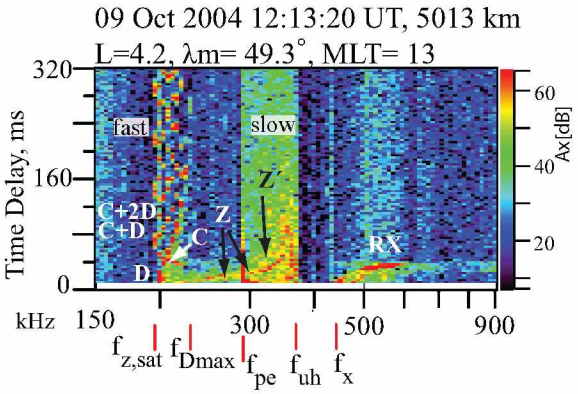

Figure 3.17 Plasmagram showing discrete traces of ducted CD type fast ZM echoes and non-ducted normal Z(Z) and slow Z(Z') ZM echoes observed on 09 October 2004.

The observation of normal Z trace echoes overlapping with ducted echoes indicates that only a small portion of the injected wave (injected at a small range of wave normal angles) can be guided by the ducts. The waves may leak from the ducts and propagate in downward vertical directions to form nonducted normal ZM echoes. The analysis of this type of cases may be important to understand the variation of plasma density in different directions in the magnetosphere, e.g., along the field line as well in the vertical direction.

3.3.9 Simultaneous Ducted and Nonducted Fast ZM Echoes

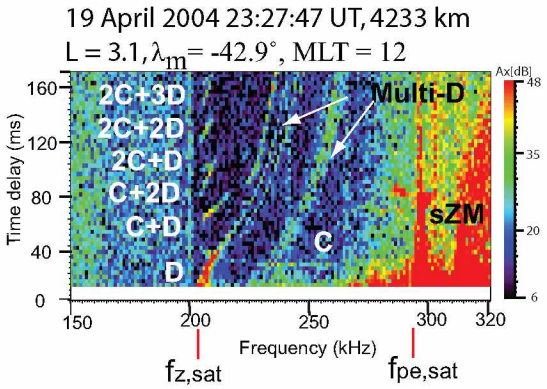

Figure 3.18 Plasmagram showing discrete traces of ducted CD type fast ZM echoes and non-ducted D trace echoes observed inside the ZM cavity.

Figure 3.18 shows an example of discrete traces of ducted fast ZM and nonducted D trace echoes received by the X antenna on RPI/IMAGE on 19 April 2004 at 23:27:47 UT. Figure 3.18 shows 2 sets of echo traces (7 ducted echo traces total). The D trace echoes start at 4 ms time delay at cutoff $f_{z,sat}$=203.6 kHz and then rises steeply to time delay of ~170 ms up to a maximum frequency of

240.8 kHz. The C trace starts at a slightly higher frequency (204.8 kHz) than the cutoff $f_{z,sat}$=203.6 kHz at a time delay of ∼42 ms and continue up to a maximum frequency of 292.4 kHz at a time delay ∼30 ms. The C+D trace is patchy starting at 206 kHz at time delay ∼64 ms up to a maximum frequency of 237.2 kHz at time delay ∼175 ms. The frequency gap is observed from 216.8 kHz to 222.8 kHz. All the other higher traces viz., C+2D, 2C+D, 2C+2D, and 2C+3D start at a slightly higher frequency than the cutoff $f_{z,sat}$ and terminate at ∼210 kHz. In addition to ducted traces, we also observe multiple D trace echoes. One of the traces, visible just below the ducted D trace starts at 221.6 kHz at time delay ∼50 ms and goes up to a maximum frequency of 245.6 kHz at time delay ∼175 ms. The other D trace echoes start at 226.4 kHz at time delay ∼12 ms and rise steadily up to a maximum frequency of 264.8 kHz at time delay ∼175 ms. Nonducted D trace echoes are formed when the satellite is above $R_{f_{z,min}}$ and when radio waves propagate upward (but are not guided by the duct) from the satellite to its reflection level, f_z, and then either retrace their path or make a loop and return back to the satellite to form an echo (see Figure 3.8). The observation of nonducted ZM echoes overlapping with ducted echoes indicates that only a small portion of the injected wave energy (injected at a small range of wave normal angles) was guided by the ducts and some portion of the wave energy may have leaked from the ducts and propagated outside the ducts to form nonducted ZM echoes. From the ray tracing analysis discussed in chapter 4 of this thesis, it is confirmed that both nonducted as well as ducted echoes are observed in the presence of ducts. There are ∼300 cases of ducted and nonducted fast ZM echoes observed by the IMAGE satellite.

3.3.10 Ducted Fast ZM and Specularly Reflected Whistler Mode Echoes

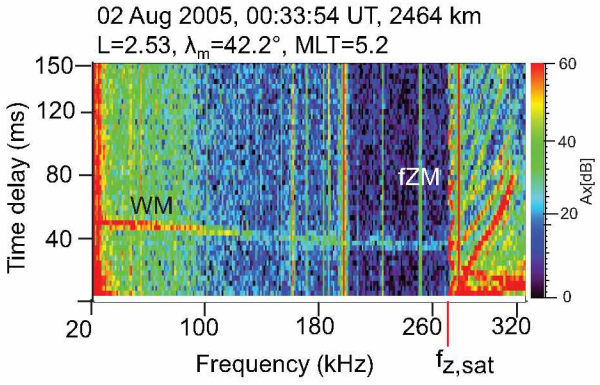

Figure 3.19 Plasmagram showing discrete traces of ducted CD type fast ZM and specularly reflected Whistler mode echoes.

Figure 3.19 shows an example of discrete traces of ducted fast ZM and specularly reflected Whistler mode echoes received by the X antenna on RPI/IMAGE on 02 August 2005 at 00:33:54 UT. Figure 3.19 shows 4 sets of echo traces (total 11 ducted echo traces) all beginning at cutoff f_z=272 kHz. The D trace echoes start at cutoff f_z=272 kHz and then rises steeply to time delay of ∼85 ms up to maximum frequency of 320 kHz. The C trace echoes start at the cutoff f_z=272 kHz at an apparent range of time delay ∼42 ms and then exhibit time delay of ∼12 ms at frequencies extending to the upper limit of the record. All the other higher traces viz., C+D, C+2D, 2C+D, 2C+2D, 2C+3D, 3C+2D, 3C+3D, 3C+4D, and 4C+3D start at the same cutoff f_z=272 kHz. Discrete SR-WM echoes are observed over a frequency range of 20-270.8 kHz, ie., up to the adjacent frequency bin of 272 kHz from which the fast ZM echoes start.

About 650 cases of fast ZM echoes (non ducted and ducted) and specularly reflected Whistler mode echoes have been observed in the altitude range of ∼650-5,000 km and invariant latitude range of 18°-90°. Whistler mode waves propagate below the satellite altitude and reflect from the Earth-Ionosphere boundary to form the specularly reflected echoes [Sonwalkar et al., 2011b] and the fast ZM waves propagate below as well as above the satellite altitude and reflect from a region where $f \sim f_z$ to form echoes (as discussed in previous section). Thus, using Whistler- and fast ZM echoes, we can remotely sense the electron density (Ne) distribution along B_0 from ∼10,000 km down to the Earth-Ionosphere boundary (90 km).

3.3.11 Ducted C Trace Echoes with Upper Cutoff at f_{pe}

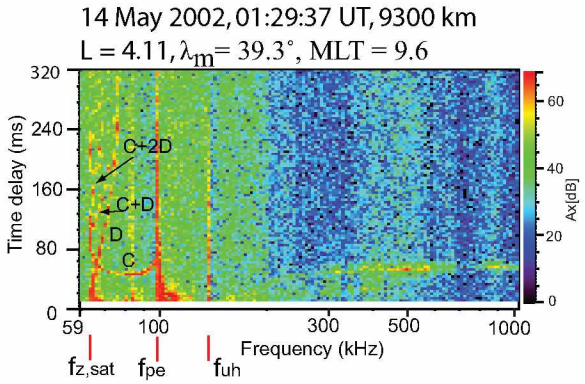

Figure 3.20 Plasmagram showing discrete traces of CD type ducted fast ZM echoes with C trace extending up to the f_{pe} observed on 14 May 2002. The C trace echoes are observed from lower cutoff f_z up to local plasma frequency f_{pe}.

Figure 3.20 shows an example (same example as shown in Figure 11 of Carpenter et al., 2003) of

ducted fast ZM echoes received by the X antenna on RPI/IMAGE on 14 May 2002 at 01:29:37 UT. Figure 3.20 shows 2 sets of echo traces (4 echo traces total) all beginning at 93.7 kHz. Each of the traces has multiple echoes at each frequency (multipath propagation). Carpenter et al., (2003) have noted that the U-shaped loop formed by the echo component C has been observed on many records but has not been analyzed in detail. The C trace starts from the lower cutoff f_z=63.7 kHz and extends to a maximum frequency f_{pe}. The t_g-f dispersion of the C trace is such that the time delay first decreases with frequency (at the low frequency portion), attains a minimum at midway between f_z and f_{pe} (similar to the nose frequency of whistlers) and then again starts to increase with frequency (at the high frequency portion). At frequencies near f_{pe}, t_g increases very sharply. The t_g-f dispersion of C trace and the 'nose' frequency have been explained in terms of the variation of group velocity with frequency and wave normal angles in Chapter 4. From the ray tracing results, we have found that the upper cutoff frequency of the C and other traces depends upon the duct parameters viz., duct half-width and density perturbation. If the duct is strong enough, then we obtain C trace echoes in the frequency range from lower cutoff f_z up to f_{pe}. At frequencies close to f_{pe}, the waves are partially ducted. From the cutoff frequency of 93.7 kHz and model (IGRF-2005) value of f_{ce}=92 kHz, we find the local f_{pe}=98 kHz. The observed value of f_{pe}=96.5 kHz. From the observed values of f_{uh} = 137.8 kHz and the RX mode cutoff frequency f_x = 168 kHz, we find the f_{pe} = 101.1 kHz and 111.5 kHz, respectively.

3.3.12 Ducted Fast ZM with Frequency Gap in 'C' Trace

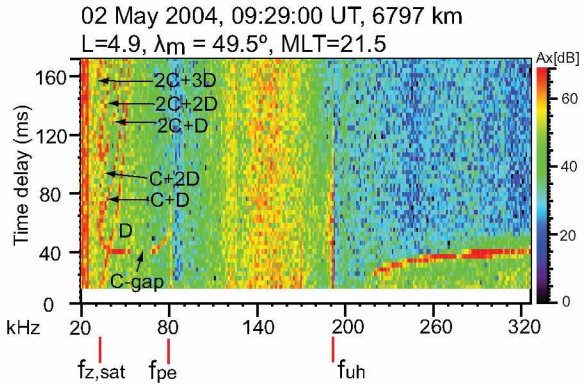

Figure 3.21 Example of CD type ducted fast ZM echoes with a frequency gap in C trace observed on 02 May 2004.

Figure 3.21 shows an example of ducted fast ZM echoes received by the X antenna on RPI/IMAGE on 02 May 2004 at 09:29:00 UT. Figure 3.21 shows 2 sets of echo traces (7 echo traces total) all

beginning at 32 kHz. An interesting observation is the gap in the C trace. C trace echoes are observed at lower frequencies from 32-52.4 kHz, then no echo is observed for the frequency range 54.8-66.8 kHz, and then they appear again at 68-80 kHz. From the ray tracings of the 10 July 2001 case, we find that the ducted C trace has peculiar behavior. For a given duct, the ducted C trace echoes are formed for two frequency ranges separated by a frequency gap, ie., C trace echoes are observed at lower frequencies, then they disappear at middle frequencies and appear again at higher frequencies. It is found that the first upper cutoff frequency of the C trace decreases with increasing duct half-width and decreasing depletions. This happens because when the frequency increases (at some frequency f $>= f_{uc1}$, where f_{uc1} is first upper cutoff frequency) the rays can no longer be guided and escape the duct. Thus, the first upper cutoff frequency of C trace will terminate at frequencies f $<< f_{pe}$. The ray tracings also show that at higher frequencies, f close to f_{pe}, the C trace is ducted again. This happens due to the peculiar structure of the refractive index surface of the fast ZM for frequencies near f_{pe}. For the frequency range close to f_{pe}, the refractive index surface has a dimple-like structure for wave normal angle close to 0° for f$\sim<$ f_{pe}, and nipple-like structure for wave normal angle close to 0° for f$>\sim f_{pe}$. This peculiar structure of the refractive index surface combined with the plasma density gradient due to the ducts bends the rays so that a ray could reflect and return back to the satellite to form an echo. An explanation of this phenomenon is given in Chapter 4 of this thesis. The observed value of f_{pe}=81.2 kHz. The cutoff frequency f_z =32 kHz and model value of f_{ce}=163 kHz, the local f_{pe}=79 kHz. From the observed values of f_{uh} = 190.4 kHz and RX mode cutoff frequency f_x = 212 kHz, f_{pe} is found to be 81.6 kHz and 90.6 kHz, respectively.

3.3.13 Ducted Fast ZM Echoes with Frequency Gaps in all Traces

Figure 3.22 shows an example of ducted fast ZM echoes received by the X antenna on RPI/IMAGE on 26 July 2001 at 22:06:17 UT. In this example, 2 sets of ducted echoes are observed viz., set 1 (C, C+D, C+2D), set 2 (2C+D, 2C+2D, 2C+3D). Echo elements within each set start at the same lower cutoff f_z=197.1 kHz, but at different time delays. From the cutoff frequency of 197.1 kHz and model (IGRF-2005) value of f_{ce}=496 kHz, we find the local f_{pe}=370 kHz. The interesting observation in this case is that all the echo elements are patchy i.e., there are one or more sets of intermediate frequency range at which echoes for all the traces are absent. No echo is observed in the frequency ranges of 203.4-204.3 kHz and 215.1-219.6 kHz. The absence of echoes may be due

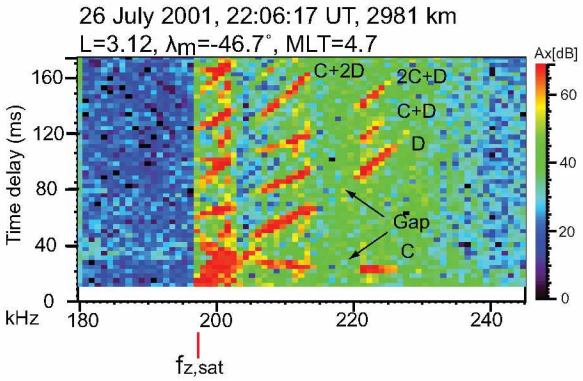

Figure 3.22 Example of ducted fast ZM echoes with frequency gaps in all trace observed on 26 July 2001.

to the presence of small scale irregularities within the density duct.

3.3.14 Ducted Fast ZM Echoes with Large Time Delay Spread of the Order of 40-80 ms

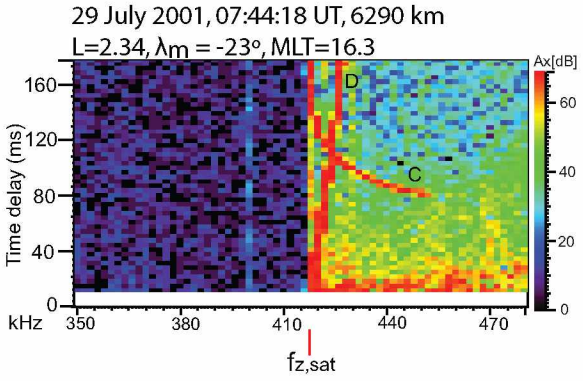

Figure 3.23 Example of ducted fast ZM echoes with time delay spread of the order of 40-80 ms observed on 29 July 2001.

Figure 3.23 shows an example of ducted fast ZM echoes received by the X antenna on RPI/IMAGE on 29 July 2001 at 07:44:18 UT. The D trace starts from an apparent zero range at cutoff f_z=418 kHz and then rises steeply to time delay of ~168 ms up to maximum frequency of 428 kHz. The C trace starts from an apparent range of ~150 ms at cutoff f_z=418 kHz and then falls slowly to time delay of ~8 ms up to maximum frequency of 452 kHz. Each of the traces shows multipath propagation. The time delay (t_g) spread of the D trace is on the order of ~50-60 ms. Normally, a t_g spread of ~10-20 ms for D trace and ~4-10 ms for C trace is observed. From ray tracing analysis (Chapter 4) it is found that the t_g spread of traces increases with increasing density depletion

of the duct. At small depletions (∼2-3%), a smaller t_g spread is obtained. At higher depletions (∼5%-10%) a t_g spread of several 10s of ms is obtained. Thus, ducts with smaller depletions of the order of few % is generally present in the magnetosphere and the large spread in t_g indicates that depletions of the order of ∼10% are occasionally present. We observe that the effects of the properties of the ducts viz., duct width and density perturbation, are directly manifested in the ducted echo traces, and from the characteristics of the ducted echo traces (upper frequency cutoffs, t_g spread) one can infer the properties of ducts.

3.3.15 Ducted Fast ZM Echoes with Overlapping Time Delays

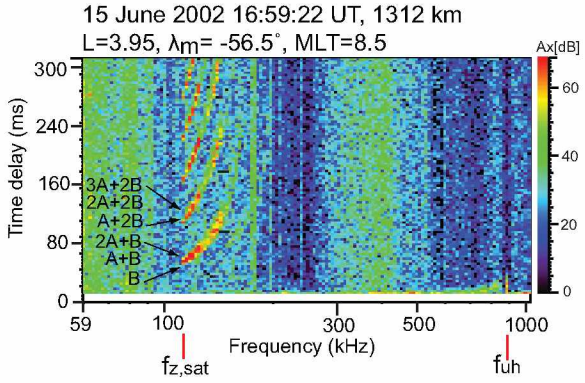

Figure 3.24 Example of ducted fast ZM echoes with overlapping time delays observed on 15 June 2002.

Figure 3.24 shows plasmagrams of AB type ducted fast ZM echoes received by the X antenna on RPI/IMAGE on 15 June 2002 at 16:59:22 UT. The IMAGE was within a duct at an altitude below $R_{f_{z,min}}$ in the ZM cavity, and the echoes were formed due to reflection from above and below the satellite in the same local hemisphere (see Figure 3.8). Figure 3.24 shows 5 sets of echo traces all beginning at cutoff f_z=113.1 kHz. Echoes for trace A are not visible because the satellite was at a low altitude (∼1300 km) and the time delay accumulated was less than the lowest time delay recorded by the plasmagram, i.e., ∼12 ms. The usual epsilon signature, which is generally observed for ducted AB type cases, is not observed in this case. The fast ZM echo traces in Figure 3.24 starting at an apparent t_g of ∼55 ms have a lower cutoff frequency, $f_{z,min}$=113.1 kHz. Normally, this set of echoes has three echo trace elements viz., B, A+B, and 2A+B. However, in this case, these traces are not distinct and they seem to overlap. If the spread of these traces (B, A+B, 2A+B) exceeds by a value equal to the t_g of A trace, then the echoes of B, A+B, and 2A+B traces may overlap, since the t_g gap between these traces is on the order of t_g of A.

3.3.16 Ducted Fast ZM Echoes with Resonance Signature at the f_z Cutoff

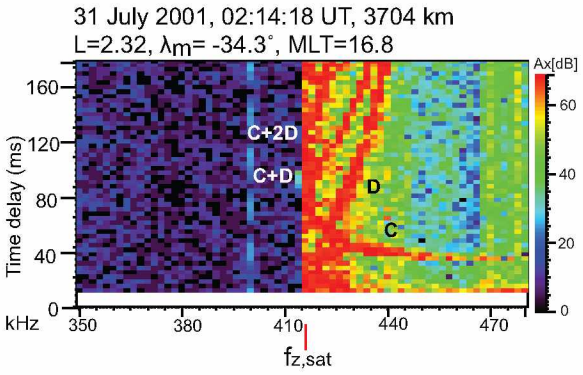

Figure 3.25 Example of ducted Fast ZM echoes with resonance signature at cutoff f_z observed on 31 July 2001.

Figure 3.25 shows plasmagrams of CD type ducted fast ZM (FZM) echoes received by the X antenna on RPI/IMAGE on 31 July 2001 at 02:14:18 UT. Figure 3.25 shows 2 sets of echo traces (5 echo traces total) all beginning at cutoff f_z=416 kHz. The interesting observation in this case is the resonance-like signature observed at the ZM cutoff frequency. This signature occupies the entire range of the plasmagram. Dougherty and Monaghan (1966) have shown theoretically that resonance can be observed at cutoff frequencies f_z and f_x. These resonances are called zero range resonance. Physically, they arise from magneto-ionic waves traveling along the geomagnetic field ($\mathbf{B_0}$), or from extraordinary waves traveling perpendicular to $\mathbf{B_0}$ with the wave number $\mathbf{k} \rightarrow 0$. The electric field of zero range waves is very weak, however, any slight non-uniformities in electron density would have a pronounced effect, e.g., if the satellite were in a slight local minimum in the electron density, strong resonances might arise from trapped electromagnetic waves. Resonances at X- and Z- mode cutoff frequencies have been observed on topside sounders [Calvert and Goe, 1963; Muldrew, 1972]. These resonances might be caused by electromagnetic waves trapped in the local minima of ionization resulting from outgassing of the rocket. Thus, for these observations, it is possible that the observed resonances are due to the trapping of electromagnetic waves in a slight (~1%) local minimum of electron density. These fine structures may be present inside the larger ducts.

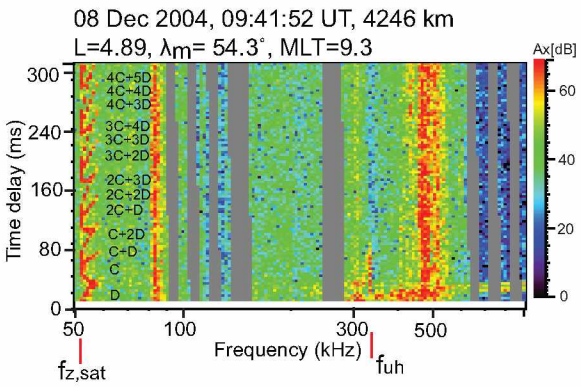

Figure 3.26 Example of ducted fast ZM Echoes up to 7^{th} order observed on 08 December 2004.

3.3.17 Ducted Fast ZM Echoes up to 7^{th} Order

Figure 3.26 shows plasmagrams of CD type ducted fast ZM echoes received by the X antenna on RPI/IMAGE on 08 December 2004 at 09:41:52 UT outside the plasmasphere. The plasmapause, as determined from the passive plasma density measurements along the IMAGE orbit, is located at L∼4.3-4.7 on dayside, i.e., for MLT=9.3. Figure 3.26 shows an unusually large number of echo traces. There are 5 sets of echo traces (15 total) all beginning at cutoff f_z=52 kHz. All of the cases are discrete (time delay spread of only 2-3 bins). The D trace starts from an apparent range of ∼4 ms time delay at cutoff frequency of 52 kHz and then abruptly stops at 59.8 kHz at a time delay of ∼35 ms. In fact, all the traces are observed to have an abrupt upper cutoff at 59.8 kHz. This abrupt upper cutoff may be due to the presence of finite ducts. From the cutoff frequency of 52 kHz and model (IGRF-2005) value of f_{ce}=297 kHz, we find the local f_{pe}=135 kHz. We also observe f_{uh} resonance at 335 kHz. The observation of a large number of multiple traces suggests that the magnetospheric ducts can sustain and guide waves without or with very little propagation loss of the wave energy.

3.3.18 Ducted Fast ZM Echoes Reflecting from ZM Cavity as well as from Conjugate Hemisphere

Figure 3.27(a) shows plasmagrams of CD type ducted fast ZM case with echoes reflecting from ZM cavity as well as from the conjugate hemisphere received by the X antenna on RPI/IMAGE on 25 July 2004 15:13:07 UT. The echoes shown in Figure 3.27 are observed inside the plasmapshere. Figure 3.27 (b) shows the IMAGE orbit plot for 25 July 2004. The red dot shows the position of

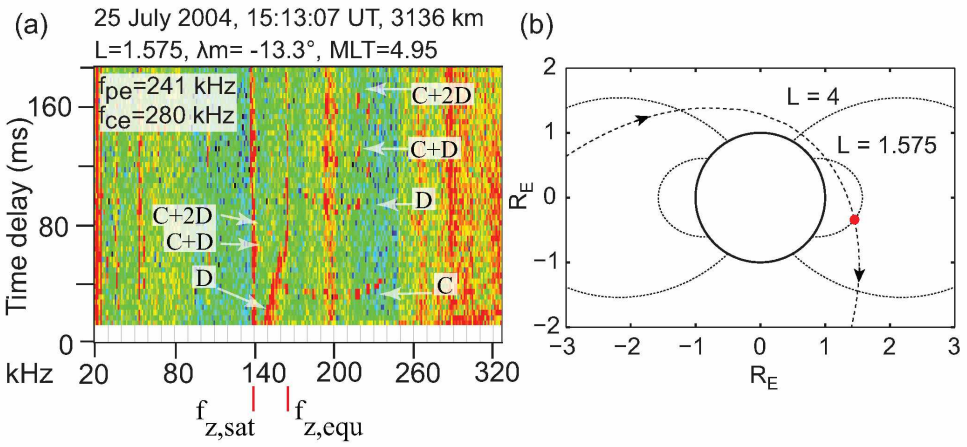

Figure 3.27 (a) Example of CD type ducted fast ZM case with echoes reflecting from ZM cavity as well as from the conjugate hemisphere observed on 25 July 2004. (b) Satellite orbit plot with position of the satellite shown by a red dot.

the satellite at 15:13:07 UT. The satellite was moving through the northern polar region towards the plasmasphere. Figure 3.27 shows a total of 4 echo traces, all beginning at $f_{z,sat}$ = 138.8 kHz. From the cutoff frequency of 138.8 kHz and model (IGRF-2005) value of f_{ce}=280 kHz, we find the local f_{pe}=241 kHz. In the plasmagram, the C trace is observed in the frequency range of 138.8 kHz - 237.2 kHz. The time delay - frequency (t_g-f) dispersion of the C trace exhibits a nose frequency at ∼202.40 kHz. D, C+D, and C+2D traces are observed in the frequency ranges of 138.8 kHz-237.2 kHz, 138.8 kHz-228.8 kHz, and 138.8 kHz-222.8 kHz, respectively. For D, C+D, and C+2D traces, two distinct t_g-f dispersions are observed in the frequency range of 138.8-165.2 kHz ($f_{z,equ}$) and 165.2-237.2 kHz ($f_{D,max}$). In the frequency range of 138.8-165.2 kHz, the D trace starts from apparent zero range cutoff near 138.8 kHz and then rises steeply to the upper range limit of 4.0 R_E (time delay of ∼170 ms) of the plasmagram at 165.2 kHz. The time delay spread for the D trace varies in the range of 3-6 range bins (10-20 ms) for $138.8kHz \leq f < 165.2kHz$. At $f_{z,equ}$ = 165.2 kHz, the echo has an exceptionally large time delay spread on the order of ∼114 ms, starting from an apparent time delay of ∼56 ms to ∼170 ms. For the C+D trace, the time delay starts at apparent time delay ∼57 ms at lower cutoff frequency f_z=138.8 kHz and increases steeply to 165.2 kHz. the C+2D trace echoes are faintly visible against the noisy background. The t_g starts at ∼57 ms at the lower cutoff frequency f_z=138.8 kHz. From the $f_{z,equ}$ and f_{ce}(IGRF) at the equator along the L-shell of the satellite ∼226.2 kHz, the $f_{pe,equ}$ =254.3 kHz.

In the frequency range of 165.2 kHz-237.2kHz, 3 echo traces are observed above ∼75 ms apparent range. The upper frequency cutoffs of the D, C+D and C+2D are limited by the transmitted program. For the D trace, echoes are clearly visible in the frequency range of 177.2 kHz - 237.2

kHz. The t_g decreases from ~90 ms at 177.2 kHz to ~80 ms at 202.4 kHz and then increases very sharply to ~170 ms at 237.2 kHz. The t_g-f dispersion of the D trace thus exhibits a 'nose' frequency at ~202.4 kHz. The t_g spread in this frequency range is small and it varies from 3-6 ms. The C+D trace echoes are clearly visible in the frequency range of 194 kHz - 237.2 kHz and C+2D trace echoes are visible in the frequency range of 201.2 kHz to 222.8 kHz. It should be noted that the D, C+D, and C+2D traces are patchy in the frequency range of 165.2 kHz-237.2 kHz, which indicates the presence of field aligned irregularities.

The peculiar t_g-f dispersion of the D, C+D and C+2D traces could be explained in terms of the ZM wave propagation in the magnetosphere in the presence of ducts inside a ZM cavity extending to the conjugate hemisphere. From the ray tracing analysis, it has been found that if the satellite is in a density depleted duct inside the ZM cavity in the magnetosphere, such that the duct extends to the conjugate hemisphere, then frequencies in the range $f_{z,sat} \leq f < f_{z,equ}$ are guided within the duct, and reflection takes place from above and below the satellite. For $f \sim f_{equ}$, rays injected at large initial wave normal angles reflect within the ZM cavity (in the local hemisphere), whereas rays injected at small initial wave normal angles propagate to the conjugate hemisphere and reflect back. Thus, for $f \sim f_{equ}$, echoes reflecting from local as well as conjugate hemispheres are formed, and the t_g spread is very large compared to the t_g spread at other frequencies. For $f > f_{z,equ}$, all the rays propagate to the conjugate hemispheres and reflect back to form echoes. Due to the large path length of the rays, the echoes exhibit large time delays. Since the propagation path of the rays traveling to the conjugate hemisphere is about the same for rays injected at various initial wave normal angles, the time delay spread is small and an 'U' shaped t_g-f dispersion is obtained. For a detailed discussion refer to the ray tracing analysis of 10 July 2001 at 08:10:00 UT in Chapter 4.

3.3.19 Fast Z Mode Echoes on Three Antennas

RPI (Radio Plasma Imager) had three orthogonal antennas, two in the spin plane (X and Y), and one along the spin axis (Z). The X and Y antennas were used for transmissions, and all three antennas were used for reception. The nominal radiated power from RPI varied from 0.1 mW at low frequencies to ~10 W per dipole at 200 kHz or higher frequencies. The failure of the power supply of Y-antenna on 8 May 2000 led to a reduction in the radiated power by 3 dB. The length of X-antenna was also reduced on 3 October 2000 due to collision with a micro-meteorite. A small section of Y antenna was lost on 18 September 2001 and as a result of an unknown failure of the

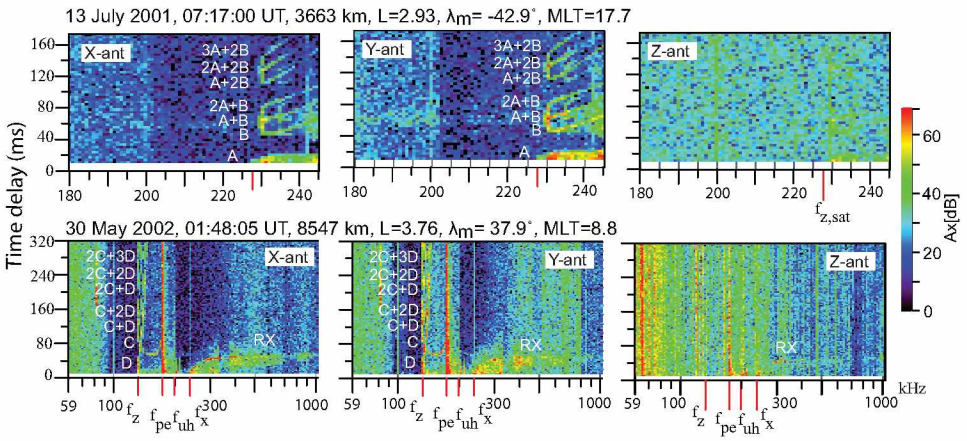

Figure 3.28 Plasmagrams showing traces of ducted fast ZM echoes observed on X, Y, and Z antennas. The echo traces are clearly visible on X, Y antennas but are not observed on Z antenna..

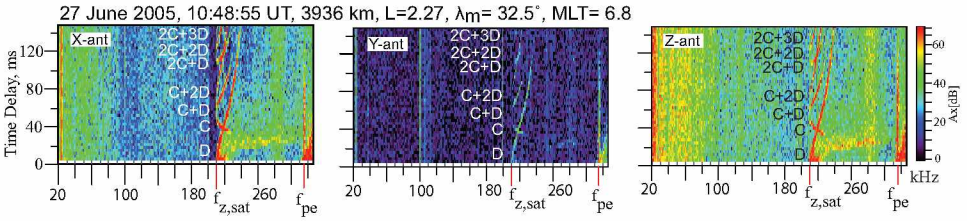

Figure 3.29 Example of ducted fast ZM echoes observed on 27 June 2005. Strong echoes are observed on X and Z antennas, and weak echoes on Y antenna.

Y-antenna/ receiver system on 30 September 2004 the signal strength received by the Y antenna was reduced substantially [Sonwalkar et al., 2004, 2011a].

Even though a small section of the Y antenna was lost on 18 September 2001, the received signal on the Y antenna was stronger than on the X and Z antennas in the majority of cases from 2001 to September 2004. From October 2004 to December 2005, the signal received on the Y antenna was weakest. Signals received on the Z antenna were weaker than those on X and Y, except after September 2004, when the Y antenna was weakest. In some cases, as shown in Figure 3.28, no ducted fast ZM echoes were observed on the Z antenna, even though the echoes were clearly defined on the X and Y antennas. In about 17 cases for CD type and 24 cases for AB type, we found that the amplitude of ducted echoes observed on the Z antenna is much weaker than that observed on the X and Y antennas and is barely recognizable. It is to be noted that after October 2004, Y antenna echoes were much weaker compared to before October 2004, so in some cases, we observe ducted traces only on the X and Z antennas (shown in Figure 3.29) and faintly on the Y antenna.

3.3.20 Lower and Upper Cutoff Frequencies of Ducted Fast Z Mode Echoes

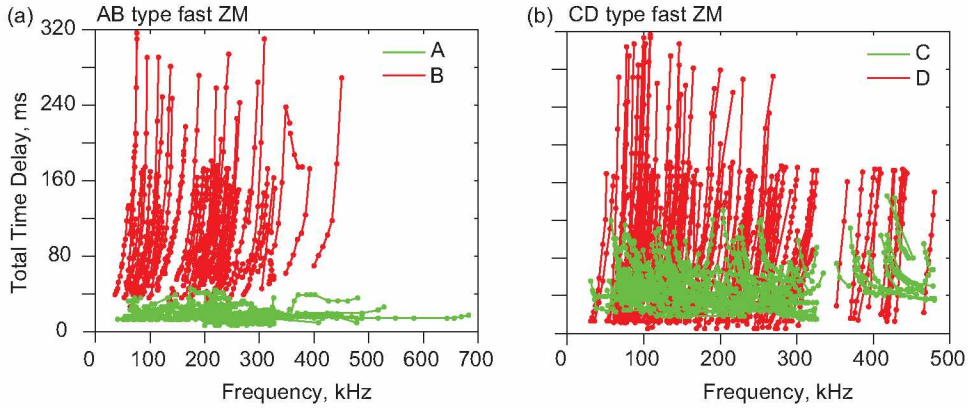

Figure 3.30 Time delay-frequency dispersion curve of (a) AB type ducted fast ZM and (b) CD type ducted fast ZM echo traces.

The cold plasma theory predicts that the fast ZM exists in the frequency range between ZM cutoff frequency and f_{pe}. For conditions $f_{pe} < f_{ce}$, fast and slow ZM can co-exist in a region termed CMA6a in the frequency regime $f_{pe} < f < f_{ZI}$ (Z-infinity cutoff) [Benson, 2006]. At ZM cutoff frequency, the refractive index goes to zero and reflection of the wave occurs.

3.3.20.1 Lower and Upper Cutoff Frequency of Ducted AB-Trace

Figure 3.30 shows time delay-frequency dispersion of AB and CD type ducted fast ZM echoes, respectively. On the plasmagram, the A trace generally starts from zero baseline on the time delay axis at $f = f_z$ and increases up to few 10s of ms. The B trace is detached from the zero time delay baseline. Figure 3.30(a) shows that the t_g of A trace varies from ~6 ms to ~40 ms and the t_g of B trace varies from ~40 ms to ~320 ms. The t_g-f curve for the A trace becomes constant with frequency at mid frequencies, and at higher frequencies, the t_g increases with increasing frequency. For the A trace, the reflection altitude is about the same for all frequencies, but for the B trace, the reflection altitude increases sharply with increasing frequency. For the B trace, the time delays depend upon the length of the propagation path and variation of group velocity along the ray path. Therefore, the A trace accumulates smaller time delays than the B trace.

Table 3.2 Lower and upper cutoff frequency of AB type fast ZM echoes. The numbers represent number of cases.

	Lower Cutoff	**Upper Cutoff**
$A < B$	14(13.3%)	7(6.7%)
$A = B$	50(47.6%)	8(7.6%)
$A > B$	15(14.3%)	70(66.7%)
Undetermined	26(24.8%)	20(19.0%)
Total	105	105

The lower cutoff of the B trace lies at f_z. For the initial 2-3 frequency bins of B trace, the time delay decreases, attains a minimum, and then increases with increasing frequency (e.g., the 26 July 2001 case). In some cases, the time delay at higher frequencies rises very steeply. In the majority of cases, the lower cutoff of B trace and other higher traces is equal to that of A trace (∼48% total cases chosen). However, there are some exceptions in which the lower cutoff of B trace is either greater than or less than that of A trace. Salient points of observation of the lower and upper cutoff frequency of AB type traces are:

1. In some cases the {B, A+B and 2A+B},{A+2B, 2A+2B, 3A+2B} traces merge at $f = f_z$, i.e., these traces have nearly same time delays at $f = f_z$. This is consistent with the ray tracing results which shows that for f very close to f_z, the time delay for A trace is ∼0, and therefore, the time-delays of (A+B)∼B, (2A+B)∼B and so on. This behavior of echoes could be attributed to very small group velocity for frequencies close to f_z. This is also due to the fact that since the satellite is below the altitude of minimum f_z, the ZM reflection level lies very close to the satellite. Therefore, the rays propagating downwards travel a smaller distance and accumulate smaller time delays.

2. The time delay for B trace decreases very sharply for the first few (1-2) frequency bins, becomes constant, and then starts to increase. For A+B trace, it increases steadily. For 2A+B trace, t_g increases very sharply for the first few frequency bins, and then increases gradually. Because of this, the first frequency bin from which the echoes start appears like a band.

3. In some cases, the B, A+B, and 2A+B traces do not merge at f_z. This may be due to the experimental limitation on the frequency resolution of the transmitted programs. Most of the

programs had frequency stepping of 0.9 kHz-2 kHz linear or 2% logarithmic. The bandwidth of the receiver is 0.3 kHz. If the falling or rising part of the t_g-f curve do not lie within 0.15 kHz of the transmitted frequency, then the echoes close to f_z will not be recorded on the $f = f_z$ frequency bin of the plasmagram. Thus, these echoes may not appear to merge at f_z.

4. In most of the cases, the upper cutoff frequencies of higher traces viz., B, A+B, 2A+B etc. are less than that of A trace. The cutoffs of individual traces viz., B, A+B, and 2A+B may or may not be the same. In some cases, the upper cutoffs are distinct, i.e., the B, A+B, and 2A+B traces terminate at frequencies and time delays lower than the experimental limitations, e.g., a case of ducted fast ZM observed on 26 July 2001 08:23:47 UT (Figure 3.22). In these cases it can be said that the upper cutoff is limited by the duct parameters (duct width, density depletions, and the extent of the duct along B). In other cases, the upper cutoff of B trace is not distinct as the time delays of higher frequencies exceed the experimental t_g limit.

3.3.20.2 Lower and Upper Cutoff Frequency of Ducted CD-Trace

On the plasmagram, the C trace is generally observed to be detached from the zero t_g baseline like the B trace. It starts from higher time delay (~40-160 ms) at $f = f_z$ and decreases to few 10s of ms. It then attains a minimum in time delay at mid frequencies and increases with increasing frequency. Figure 3.30(b) shows that the t_g of C trace varies from ~160 ms to ~15 ms and for D trace, t_g varies from ~6 ms to ~320 ms.

Table 3.3 Lower and upper cutoff frequency of CD type fast ZM echoes. The numbers represent number of cases.

	Lower Cutoff	**Upper Cutoff**
$C < D$	5(3.4%)	37(25.2%)
$C = D$	123(83.7%)	18(12.2%)
$C > D$	19(12.9%)	92(62.6%)
Undetermined	-	-
Total	147	147

D trace, on the other hand, starts from the zero time delay baseline at f_z and increases very

sharply with frequency. This is due to the fact that since the satellite is above the altitude of minimum f_z, the ZM reflection level lies very close to the satellite. Therefore, the rays propagating upwards travel a smaller distance and accumulate smaller time delays. At some point in frequency and time delay, the C and D traces intersect each other, and then as the frequency increases, the t_g of the D trace increases monotonically. Salient points of observation of the lower and upper cutoff frequency of CD type trace are:

1. In some cases the individual traces of sets {C, C+D, and C+2D}, {2C+D, 2C+2D, and 2C+3D}, and other sets of higher traces merge at $f = f_z$, i.e., these C, C+D, and C+2D traces have nearly identical time delays at $f = f_z$. This is consistent with the ray tracings, which show that for f very close to f_z, the time delay for D trace is ~0 and therefore, the time-delays of (C+D)~C, (C+2D)~C and so on.

2. For some cases, the individual traces of sets {C, C+D, and C+2D}, {2C+D, 2CA+2D, 2C+3D}, and other sets of higher traces do not merge at $f = f_z$, i.e., these C, C+D, and C+2D traces have different time delays at $f = f_z$. This may be due to the experimental limitation on the frequency resolution of the transmitted programs, as discussed earlier.

3. The upper cutoff of C trace has been observed to vary from frequency less than the upper cutoff frequency of D trace up to f_{pe}. In some cases, the C trace stops at mid frequencies, and then again appears at f close to f_{pe} (analogous to patchy SR-WM echo traces). This behavior may be attributed to the propagation effect of ZM waves in the presence of ducts. This propagation behavior has been confirmed for 10 July 2001 through ray tracings (Chapter 4).

3.4 Occurrence Pattern of Ducted and Nonducted Fast ZM Echoes

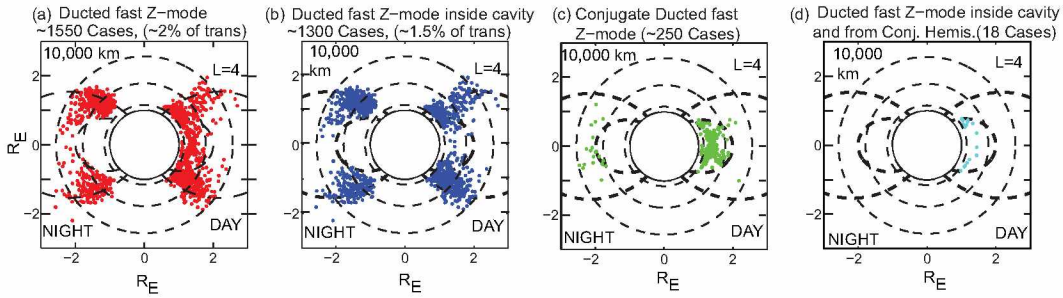

Figure 3.31 Occurrence pattern of ducted fast ZM echoes in the magnetic meridional plane. (a) Total ducted fast ZM echoes, (b) ducted fast ZM echoes inside ZM cavity, (c) ducted fast ZM with echoes reflecting from conjugate hemisphere, (d) ducted fast ZM with echoes reflecting within ZM cavity as well as from conjugate hemisphere.

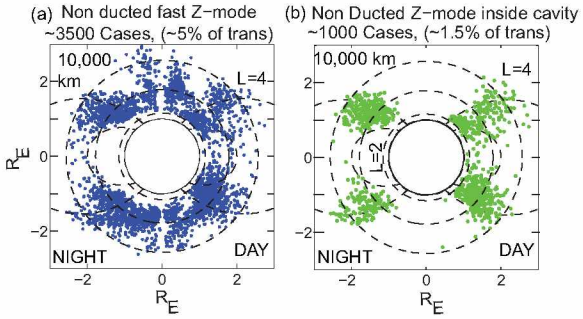

Figure 3.32 Occurrence pattern of nonducted fast ZM echoes in the magnetic meridional plane. (a) Total nonducted fast ZM echoes, (b) nonducted fast ZM echoes inside ZM cavity.

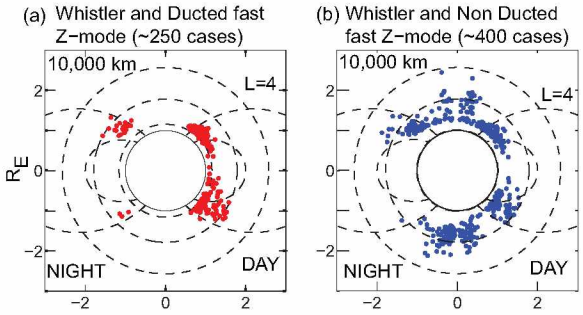

Figure 3.33 Occurrence pattern of (a) Whistler mode and ducted fast ZM echoes and (b) Whistler mode and nonducted fast ZM echoes in the magnetic meridional plane.

Figure 3.31-3.33 shows the occurrence pattern and Figure 3.34 shows the occurrence histogram of ducted and nonducted fast ZM echoes, respectively, observed by IMAGE/RPI during the transmission of programs 2, 3, 5, 21, 43, 56, 57 from 2001-2005. Ducted fast ZM echoes have been observed in the altitude range of ∼600-10,000 km, invariant latitude range of $18° - 70°$, and at all MLTs. The occurrence pattern of ducted fast ZM echoes shows that these echoes have been observed during ∼2% of the total transmissions. About 50% of ducted fast ZM cases are CD type, ∼ 35% are AB type, and ∼15% are epsilon-shaped signatures reflecting from conjugate hemispheres. The conjugate ducted echoes were detected when the satellite was within 20° of geomagnetic latitude. The majority of AB type ducted echoes have been observed at lower altitudes compared to CD type ducted fast ZM echoes, e.g., ∼65% of AB type ducted echoes have been observed in the altitude range of 1000-3000 km and ∼78% of CD type ducted echoes have been observed in the altitude range of 3000-8000 km. ∼74% of ducted AB type and ∼80% of ducted CD type echoes have been observed in the geomagnetic latitude ranges of $40° - 60°$ and $30° - 50°$, respectively. This suggests

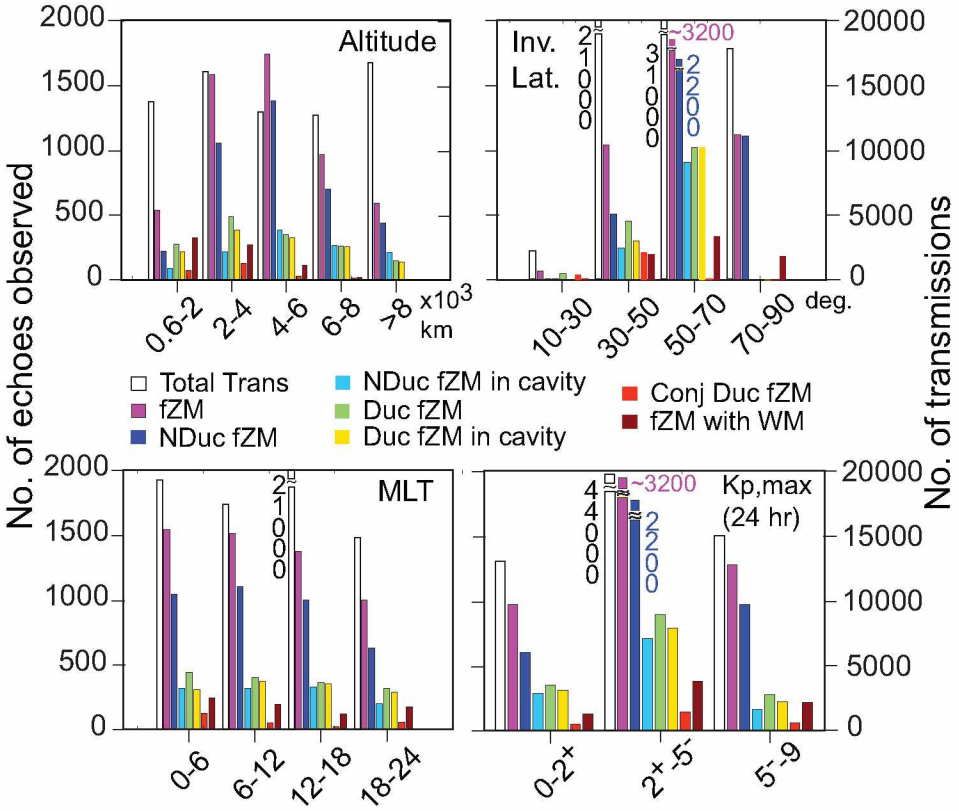

Figure 3.34 Histograms showing the occurrence of ducted and nonducted fast ZM echoes and fast ZM echoes accompanied with Whistler mode echoes. Histogram as a function of (a) altitude, (b) invariant latitude, (c) magnetic local time (MLT), and (d) $K_{p,max}$ in the past 24 hours.

that the ZM cavity is most prevalent in the geomagnetic latitude range of $30° - 60°$. Observations of fast ZM in the altitude range of ~600-10,000 km suggest that the altitude range of minimum in ZM cutoff frequency profile can vary from < 1000 km to as high as ~10,000 km. 18 interesting cases of echoes reflecting within the ZM cavity and also from the conjugate hemisphere have been observed in the altitude range of $1300 - 3000$ km and geomagnetic latitude range of $0° - 40°$. All of these echoes have been observed for $L \leq 2$. This limit on the L-shell and altitude could be attributed to the upper virtual range limitations of 7.5 R_e or ~320 ms of the transmitted programs on the IMAGE/RPI. Lower L-shell and altitude range implies a smaller propagation path for fast ZM echoes along the field line, and thus smaller time delays recorded on the plasmagrams. The occurrence of the ducted ZM echoes seems to be localized on the L-shell range of L > 1 to 5 especially between L =2 to 4 where about two-thirds of the total ducted echoes are observed. Past observations have shown the presence of field aligned irregularities within the plasmasphere and plasmapause region especially during periods of enhanced magnetic convection activity or in its

aftermath with plasmapause being especially active in the formation of density structures [Horwitz et al., 1990; Carpenter et al., 1993, 2002; LeDocq et al., 1994; Moldwin et al., 1995]. Past observations have also shown the evidence of Whistler mode ducts extending from L < 2 to beyond the plasmasphere [Carpenter and Sulic, 1988; Helliwell, 1965; Inan and Bell, 1977; Strangeways and Rycroft, 1980] therefore it seems reasonable that the conditions that generate Whistler mode ducts can also produce the ducting conditions for Z modes.

Non ducted echoes have been observed in the altitude range of ∼600-10,000 km, $18° - 88°$ invariant latitudes, and at all MLTs (Figures 3.32 and 3.34). Nonducted echoes have been found at all latitudes, but were most common poleward of the plasmasphere. Cases in which no higher ducted traces are observed, are considered non ducted, e.g., cases in which only two traces are observed (A and B traces or C and D traces) and cases in which only one trace (only A, only B, only C and only D) is observed. About 30% (∼1100 cases) of the nonducted echoes have been observed within the ZM cavities. A large fraction (∼ 2500 cases out of 3500 cases) of nonducted fast ZM cases are A-only type. B-only cases have been observed the least number of times (56 cases out of 3500 cases). AB-only cases have been observed in 200 of 3500 cases, CD-only in 300 of 3500, C-only in 300 of 3500 and D-only in 300 of 3500 cases.

Figure 3.33 shows the occurrence pattern of fast ZM echoes accompanied by specularly reflected Whistler mode (SR-WM) echoes. SR-WM echoes have been observed in ∼250 cases with ducted and ∼400 cases with nonducted fast ZM echoes. About 98% of ducted fast ZM accompanied with SR-WM cases have been observed in the altitude range ≤ 5000 km in the geomagnetic latitude range of $0° - 60°$, and only 5 cases have been observed above 5000 km. Similarly, ∼90% cases of nonducted fast ZM accompanied with SR-WM have been observed in the altitude range ≤ 5000 km for the entire geomagnetic latitude range ($0° - 90°$), and only 16 cases have been observed above 5000 km.

Echoes reflecting from above the satellite altitude were observed mostly inside the plasmasphere. This indicates that in the vast majority of cases, ZM cavities have been observed within the plasmasphere. However, in 10 out of 370 best cases of fast ZM echoes, echoes reflecting from above the satellite altitude have been observed outside the plasmapause. The location of the plasmapause was determined from the upper hybrid resonance f_{uh} band emissions recorded on the dynamic spectrograms.

Figure 3.34 shows the histogram plot of the occurrence of ducted and nonducted fast ZM echoes with respect to altitude, invariant latitude, magnetic local time (MLT), and maximum

K_p index in the preceding 24 hours ($K_{p,max}$). The planetary K-index ('p' stands for planetary), is a global geomagnetic storm index, is used to indicate the magnitude of geomagnetic storm on a scale of 0-9 with $K_p < 4$ indicating quiet days and $K_p > 4$ indicating a geomagnetic storm [http://www.swpc.noaa.gov/products/planetary-k-index]. The $K_{p,max}$ histogram shows no dependence of the occurrence of nonducted and ducted fast ZM echoes on the K_p index. The ducted echoes have been observed from very quiet to very disturbed geomagnetic periods indicating that ducts exist in the magnetosphere during all times of geomagnetic activity. A majority of ducted fast ZM echoes are observed in the altitude range of 2,000-8,000 km indicating the presence of ducts at higher altitude. The occurrence of fast ZM and ducts do not show any dependence on MLT. A majority of ducted ZM echoes have been observed in the L-shell range of $L > 1$ to $L = 5$ with about two-third of the cases concentrated in L-shell range of 2 to 4. This is consistent with the past observations of the ducts near the plasmapause region [Carpenter et al., 1993; LeDocq et al., 1994; Fung et al., 2003; Darrouzet et al., 2004]. The average occurrence frequency of ducted echoes is only few percent which is consistent with the past observations [Muldrew, 1980b; Fung et al., 2003]. Relatively low occurrence frequency of conjugate ducted fast ZM echoes are consistent with past observation of magnetospheric ducts in case of RX mode ducted echoes [Fung et al., 2003] and indicate that wave-guiding conditions may be difficult to maintain along the field line between conjugate hemisphere as compared to over partial field lengths. The higher frequency of occurrence of ducted and nonducted ZM echoes inside the ZM cavities underlines the importance of the ZM cavity region as the ubiquitous magnetospheric phenomenon whose occurrence near and within the plasmasphere and plasmapause facilitates the radio sounding of the ducts and field aligned electron density distribution in this poorly known region of space.

Figure 3.35(a) shows the plot of ZM cutoff frequency measured at the satellite ($f_{z,sat}$) and the upper cutoff of the B or D trace echoes ($f_{z,max}$) as a function of f_{pe}/f_{ce}. The black curve is the theoretical curve representing the lower ZM cutoff frequency, f_z, as a function of f_{pe}/f_{ce}. The fast ZM echoes (ducted and non ducted) have been observed for a wide range of f_{pe}/f_{ce} ratios ($0.25 - 6$). Figure 3.35(b) plots $f_{z,sat}$ and $f_{z,max}$ as a function of invariant latitude. Both $f_{z,sat}$ and $f_{z,max}$ decreases with increasing invariant latitude.

Figure 3.36 shows (a) ZM cutoff frequency ($f_{z,sat}$) and (b) upper cutoff frequency ($f_{z,max}$) as a function of altitude. The data is shown for three different ranges of invariant latitude of $10° - 30°$, $30° - 50°$, and $50° - 70°$. At any given altitude, the $f_{z,sat}$ decreases with increasing invariant latitude. As $f_{z,sat}$ is a function of electron density N_e, and N_e decreases with invariant latitude at the same

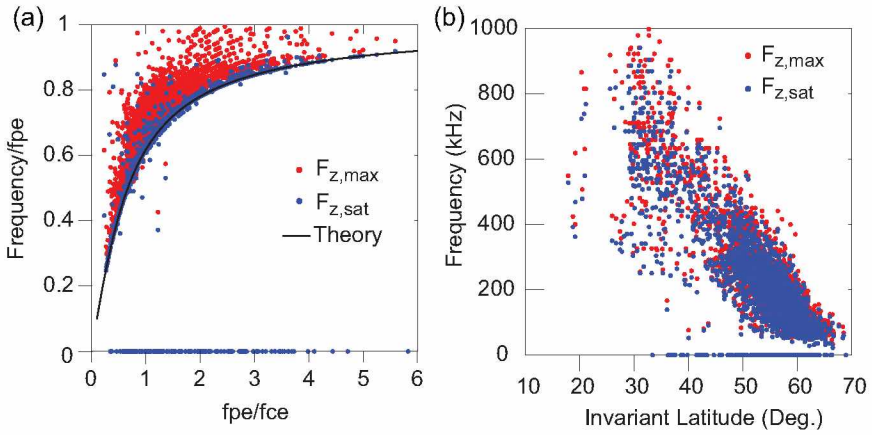

Figure 3.35 Plot of the measured ZM cutoff frequency. $f_{z,sat}$ shown as blue dots and upper frequency cutoff of B or D trace, $f_{z,max}$ as a function of (a) f_{pe}/f_{ce} and (b) as a function of invariant latitude. The black curve shown in (a) is the theoretical curve of f_z as a function of f_{pe}/f_{ce}.

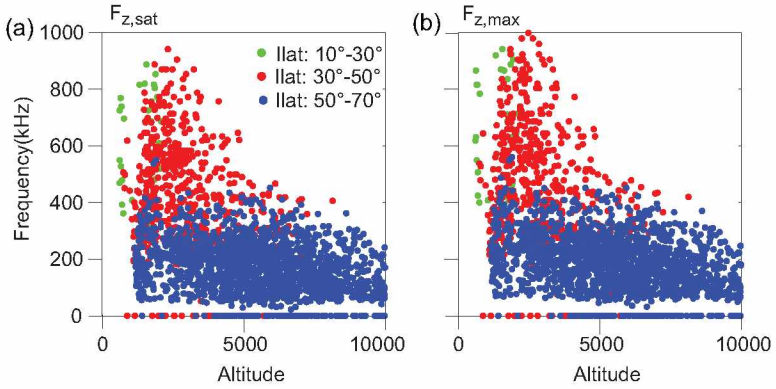

Figure 3.36 Plot of (a) Local ZM cutoff frequency ($F_{z,sat}$), and (b) upper cutoff frequency of B or D trace ($F_{z,max}$) as a function of altitude binned in three different ranges of invariant latitude.

altitude, the variation of $f_{z,sat}$ is consistent with the variation of N_e.

Figure 3.37 shows the plot of in-situ N_e obtained from the RPI. The Ne has been calculated from (1) ZM cutoff frequency f_z, (2) upper hybrid resonance frequency f_{uh}, (3) R-X mode cutoff frequency f_x, and IGRF-2005 model values of f_{ce} calculated with motion of the satellite taken into consideration. The other source of Ne measurement is the resonance observed at the local f_{pe}. The data are shown for three ranges of invariant latitude viz., $10° - 30°$, $30° - 50°$, and $50° - 70°$. It is clearly evident from the figure that (a) at any given invariant latitude, the electron density decreases with increasing altitude, and (b) at any altitude, N_e decreases with increasing invariant latitude. This trend is consistent with past measurements [Gallagher et al., 2000; Reinisch et al., 2001; Denton et al., 2002, 2004, 2006; Tu et al., 2005].

Figure 3.38 shows the plot of (a) ZM bandwidth $(f_{uh} - f_z)/f_{uh}$, and (b) fast ZM bandwidth

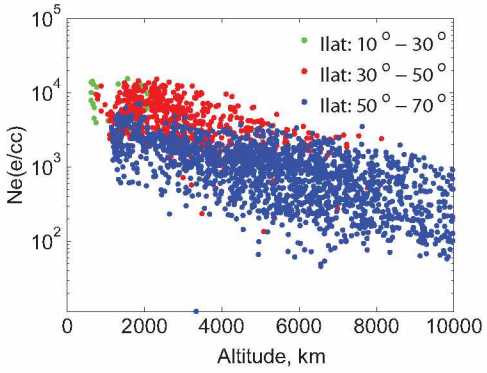

Figure 3.37 Plot of electron density as a function of altitude binned in three different ranges of invariant latitude.

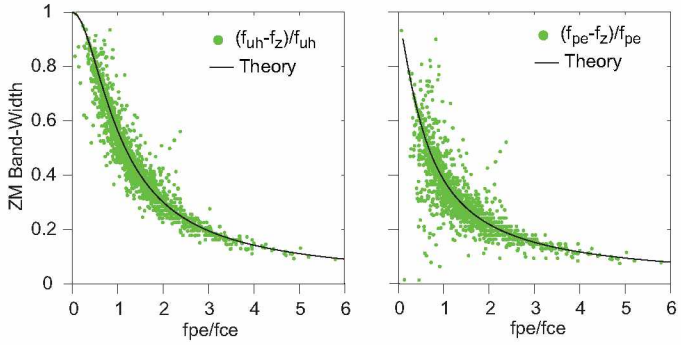

Figure 3.38 Plot of the measured ZM bandwidth. (a) $(f_{uh} - f_z)/(f_{uh})$ and (b) $f_{pe} - f_z)/(f_{pe})$ as a function of f_{pe}/f_{ce}. The black curve is the theoretical curve of bandwidth as a function of f_{pe}/f_{ce}. Both the plots show that ZM bandwidth depends strongly upon the f_{pe}/f_{ce} ratio, as predicted by the theory.

$(f_{pe} - f_z)/f_{pe}$ versus f_{pe}/f_{ce}. The black curve in both the figures represents the theoretical curve of the bandwidth as a function of f_{pe}/f_{ce}. The plots show that the bandwidth of the ZM is very sensitive to the ratio of electron plasma frequency to electron gyro frequency (f_{pe}/f_{ce}). When $f_{pe}/f_{ce} > 1$, the bandwidth is very narrow, whereas when $f_{pe}/f_{ce} < 1$, the bandwidth is very broad. In the magnetospheric regions of high plasma density ($f_{pe} > f_{ce}$), for example, near equatorial regions, the ZM emissions appear in a narrow band near f_{uh}, called upper hybrid emissions. In contrast, ZM has a broad frequency range in the auroral region where the plasma condition $f_{pe} < f_{ce}$ is prevalent.

Table 3.4: Summary Table of fast ZM echo examples. The parameters listed in the Table are figure number, Date and Time, L-shell, altitude and geomagnetic latitude, plasmapause location from dynamic spectra(DS) or from model, local ZM cutoff frequency($f_{z,sat}$, gyro frequency from IGRF-2005 model (f_{ce}), electron plasma frequency calculated from $f_{z,sat}$(@$f_{z,sat}$) or from observed resonance (@sat), combination of echoes observed, and comments noting special or unusual feature(s) of echoes

Figure #	Date-Time	L, Altitude, λ_m	L_{pp}	$f_{z,sat}$ (kHz)	f_{ce} (kHz)	f_{pe}[@$f_{z,sat}$] [@Res.] (kHz)	Combination of Echoes	Comments
Fig. 3.9	26 July 2001-08:23:47 UT	3.21, 3834 km, −45.0°	3.93-3.97 (DS)	194.4	364.2	[329.5] []	Duc. fZM-AB	$R_{sat} < R_{f_{z,min}}$; Case Study
Fig. 3.10	03 August 2005 19:14:54 UT	2.59, 2354 km, 43.3°	3.7-4.0 (DS)	254	575.1	[458.9] []	Non duc. fZM-AB	$R_{sat} < R_{f_{z,min}}$; Case Study
Fig. 3.11	10 July 2001 08:10:00 UT	2.68, 4138 km, −38.2°	5.3-6.0 (DS)	380	300.6	[508.5] []	Duc. fZM-CD	$R_{sat} > R_{f_{z,min}}$; Case Study
Fig. 3.12	19 June 2004 10:22:39 UT	3.81, 5340 km, 46.0°	6.6-6.9 (DS)	119.6	239	[207.1] [197.6]	Non duc. fZM-CD	$R_{sat} > R_{f_{z,min}}$; Case Study
Fig. 3.13	20 Oct 2004, 19:13:05 UT	1.38, 2371 km, 2.9°	3.91 (model)	682.6	371.6	[848.3] [848.8]	Conjugate duc. fZM	Sat. near the equator, 'ϵ' shaped echo signature from conj. hemisphere; diff. than fZM-AB;

continued on next page

Table 3.4 continued from previous page

Figure #	Date-Time	L, Altitude, λ_m	L_{pp}	$f_{z,sat}$ (kHz)	f_{ce} (kHz)	f_{pe}[@$f_{z,sat}$] [@Res.] (kHz)	Combination of Echoes	Comments
Fig. 3.14(a)	24 Sept 2004, 16:22:01 UT	4.81, 5915 km, 50.7°	4.64-4.85 (DS)	93.2	187.7	[161.8] [158.0]	Duc. fZM-CD	Duc. echoes from above the sat., observed within the L_{pp}
Fig. 3.14(d)	17 May 2002, 01:39:40 UT	4.23, 3868 km, −51.9°	2.93-3.20 (DS)	82.4	337.6	[186.0] []	Duc. fZM-CD	Duc. echoes from above the sat. observed outside the L_{pp}
Fig. 3.14(g)	02 May 2004, 09:29:00 UT	4.9, 6797 km, 49.5°	3.99-4.16 (DS)	32	162.8	[79.0] [81.2]	Duc. fZM-CD	Duc. echoes from above the sat. observed outside the L_{pp}
Fig. 3.15	06 Jul 2001, 18:46:01 UT	1.99, 4011 km, −25.3°	4.22 (model)	329.6	210.7	[] [422.0]	Normal(fZM) and Oblique(sZM) non duc. ZM	Fast and Slow ZM reflecting from below the sat. altitude
Fig. 3.16	26 Oct 2004, 17:30:03 UT	1.35, 2025 km, 8.8°	4.53 (model)	571.2	471.8	[771.8] [768.8]	Conjugate duc. fZM with Normal and Oblique non duc. ZM	Simultaneous observation of duc. fZM from conjugate hemispheres and non duc. Fast and Slow ZM echoes
Fig. 3.17	09 Oct 2004, 12:13:20 UT	4.2, 5013 km, 49.3°	4.07 (model)	196.1	232.8	[290.0] [291.3]	Duc. fZM-CD with Normal and Oblique non duc. ZM	Simultaneous observation of duc. fZM within the ZM cavity and non duc. Fast and Slow ZM echoes

continued on next page

Table 3.4 continued from previous page

Figure #	Date-Time	L, Altitude, λ_m	L_{pp}	$f_{z,sat}$ (kHz)	f_{ce} (kHz)	f_{pe}[@$f_{z,sat}$] [@Res.] (kHz)	Combination of Echoes	Comments
Fig. 3.18	19 Apr 2004, 23:27:47 UT	3.1, 4233, $-42.9°$	4.37 (model)	203.6	289.4	[316.8] [293.6]	Duc. fZM-CD with non duc. D trace	Simultaneous observation of duc. and non duc. fZM echoes
Fig. 3.19	02 Aug 2005, 00:33:54 UT	2.53, 2464 km, 42.2°	3.86-4.4 (DS)	272	544.7	[471.3][]	SR-WM and duc. fZM-CD	Simultaneous observations of WM and fZM echoes
Fig. 3.20	14 May 2002, 01:29:37 UT	4.11, 9300 km, 39.3°	2.48-2.84 (DS)	62.4	92.4	[98.3] [96.5]	Duc. fZM-CD	Duc. echoes from above the sat. altitude with duc. C trace extending upto fpe exhibits a nose frequency
Fig. 3.21	02 May 2004, 09:29:00 UT	4.88, 6797 km, 49.5°	3.99-4.16 (DS)	32	162.8	[79.0] [81.2]	Duc. fZM-CD	A gap in the C trace. The gap is a direct manifestation of propagation of ZM waves in presence of ducts
Fig. 3.22	26 Jul 2001, 22:06:17 UT	3.16, 2959 km, $-47.1°$	3.49-4.23 (DS)	197.1	496.4	[369.7] []	Duc. fZM-CD	Gap in C, D, C+D and other higher traces;
Fig. 3.23	29 Jul 2001, 07:44:18 UT	2.34, 6290 km, $-23.0°$	4.68 (model)	418	146.3	[485.7] []	Duc. fZM-CD	Large t_g spread of 40-80 ms indicating higher depletion level of ducts

continued on next page

Table 3.4 continued from previous page

Figure #	Date-Time	L, Altitude, λ_m	L_{pp}	$f_{z,sat}$ (kHz)	f_{ce} (kHz)	f_{pe}[@$f_{z,sat}$] [@Res.] (kHz)	Combination of Echoes	Comments
Fig. 3.24	15 Jun 2002, 16:59:22 UT	3.95, 1312 km, −56.5°	5.14 (model)	113.1	877.2	[334.7] []	Duc. fZM-AB	Duc. fZM echoes with overlapping t_g of B, A+B, 2A+B and other higher duc. traces
Fig. 3.25	31 Jul 2001, 02:14:18 UT	2.32, 3704 km, −34.3°	3.91 (model)	416	303.3	[547.0] []	Duc. fZM-CD	Resonance signature at cutoff frequency, fz
Fig. 3.26	08 Dec 2004, 09:41:52 UT	4.89, 4246 km, 54.3°	4.3-4.7 (DS)	52	296.7	[134.7] []	Duc. fZM-CD	Duc. echoes with large number of echo traces upto 7th order
Fig. 3.27	25 Jul 2004, 15:13:07 UT	1.57, 3136 km, −13.3°	2 (model)	138.8	280	[241.1] []	Duc. fZM-CD	Duc. fZM echoes reflecting from ZM cavity as well as from conjugate hemisphere
Fig. 3.28(a)	13 Jul 2001, 07:17:00 UT	2.93, 3663 km, −42.9°	3.91-4.51 (DS)	227.7	352.9	[363.6] []	Duc. fZM-AB	Comparison on X, Y, Z ant.; No echo is observed on Z ant
Fig. 3.28(b)	30 May 2002, 01:48:05 UT	3.76, 8547 km, 37.9°	3.97-4.57 (DS)	132.5	106.5	[177.9] [174.8]	Duc. fZM-CD	Comparison on X, Y, Z ant.; No echo is observed on Z ant
Fig. 3.29	27 Jun 2005, 10:48:55 UT	2.27, 3936 km, 32.5°	4.19-4.65 (DS)	209.6	255.5	[312.2] [315.2]	Duc. fZM-CD	Comparison on X, Y, Z ant. After Y ant was severed; Echoes are weakest on Y ant.;

Chapter 4 Z Mode Sounding and Theory of Propagation, Reflection and Guidance of Z mode Waves: 10 July 2001 Case Study

In this chapter, the ZM sounding technique has been developed to measure (1) field aligned electron density (N_e) distribution; (2) duct parameters (ΔL and $\Delta N/N$); and (3) ZM cavity parameters (cavity bandwidth and cavity length) in context of the case study of 10 July 2001 ducted fast Z mode (ZM) echoes. The case of 10 July 2001 of the ducted fast ZM echoes was chosen because: (1) it is a representative case of a large set of ducted and nonducted ZM echoes (CD type fast ZM), and (2) the ducted echoes are well defined for taking measurements of the time delay and frequency dispersion. This research presents a first detailed study of the propagation, reflection and guidance of ZM nonducted and ducted waves within the ZM cavity in the magnetosphere. From ray tracing analysis several new findings have been reported and have been confirmed with the actual observations of such phenomena in the data. The propagation, reflection, and guidance of fast ZM waves in the magnetosphere have been discussed in detail with the aid of refractive index surfaces, Poeverlein's construction and Snell's Law. The refractive index surface diagrams are studied along the ray paths and at reflection points to understand how the rays propagate and reflects and are guided by the density ducts in the magnetosphere.

The study of ZM echoes on the IMAGE satellite is important because the IMAGE satellite was the first long range magnetospheric radio sounder to inject radio waves into the magnetosphere in all directions [Reinisch et al., 2000]. The injected radio waves propagates in all the four plasma wave modes including the ZM and the echoes have been recorded on the IMAGE satellite. IMAGE has recorded both the ducted and nonducted ZM echoes within the ZM cavity in the magnetosphere in the low to mid-latitude region in the altitude range of ~1000-10,000 km. In the past, the ZM echoes have been observed on the topside sounders (Alouette 1, 2, ISIS 1, 2) at low altitude (~1000-3500 km). Topside sounders observed the nonducted oblique (slow) and normal (fast) ZM echoes [Calvert, 1966; Hagg et al., 1969]. Ducted Z mode echoes were observed on the topside sounding ionograms in the equatorial and polar regions of the magnetosphere [Muldrew, 1969; Benson, 1982;

Benson 1985] but no evidence of the ZM cavity was found. Carpenter et al., (2003) discovered the ducted ZM echoes within the ZM cavity observed on the IMAGE satellite. Carpenter et al., (2003) have provided a ZM inversion method to measure the field aligned electron density distribution above the satellite altitude but no attempt was made by the authors to measure the duct parameters. The magnetospheric ducts are important to study because they play an important role in the generation and propagation of natural wave emissions, and wave-particle interactions and therefore influence the radiation belt dynamics. The radiation belts (or "Van Allen Radiation Belts") are magnetospheric region of space which contains highly energetic particles trapped in the Earth's magnetic field [Van Allen and Frank, 1959]. Modeling the radiation belt is an important part of the space weather program because the energetic particles can adversely affect the spacecraft electronics and endanger human life in space. In this work ducted ZM echoes have been used to measure the magnetospheric duct parameters, instantaneous field aligned electron density distribution both below and above the satellite altitude and ZM cavity parameters. This is a first direct measurement of magnetospheric ducts obtained from ducted ZM echoes observed inside the ZM cavities and also the first quantitative measurement of the ZM cavities in the low to mid-latitude region of the magnetosphere in the altitude range of ~1000-10,000 km. Instantaneous measurements of field aligned electron density distribution is important in order to test theoretical and numerical models of magnetospheric density distribution and study the plasma loss and refilling processes. Measurement of electron density is important to develop and improve the physics based empirical models of the Earth's ionosphere and the magnetosphere. These models are necessary for optimum performance of communication and navigational satellite systems and space weather forecast. Through this case study, we have demonstrated that the ZM cavity is a real phenomenon that occurs inside the plasmasphere and rarely outside the plasmasphere. ZM cavity is important to explain the observations of natural ZM emissions in the magnetosphere. This case study demonstrate that ZM sounding is a powerful new technique of measuring the field aligned electron density distribution, magnetospheric duct parameters and ZM cavity parameters.

4.1 Case I: 10 July 2001 08:10:00 UT Ducted CD Type Fast Z Mode Echoes

Figure 4.1(a) shows plasmagrams (pr#3) of CD type ducted fast ZM echoes received by the X antenna on RPI/IMAGE on 10 July 2001 at 08:10:00 UT. Figure 4.1(a) shows 3 sets of echo traces (6 echo traces total), all beginning at 380 kHz but having different time delay spreads. The lower

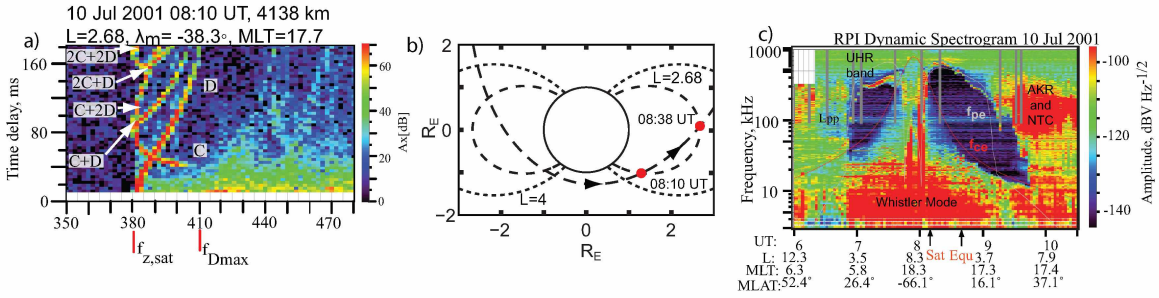

Figure 4.1 (a) Plasmagram showing discrete traces of CD type ducted fast ZM echoes observed on 10 July 2001. (b) IMAGE orbit plot for 10 July 2001 with satellite positions (red dot). (c) Dynamic spectrogram observed by IMAGE on 10 July 2001 with position of the satellite (black arrow).

and upper cutoff frequencies of these echoes are given in Table 4.1. The D trace starts from time delay(t_g)$\sim$12 ms at lower cutoff $f_{z,sat}$ =380 kHz and then rises steeply to $t_g\sim$178 ms at the upper cutoff $f_{D,max}$ =410 kHz. Three echo traces start at $t_g\sim$80 ms at lower cutoff frequency $f_{z,sat}$, namely, C, C+D, and C+2D, and two echo traces, 2C+D and 2C+2D (partial) of the third set, start at $t_g\sim$175 ms at $f_{z,sat}$. 2C+2D is only partially visible over the frequency range 380-382 kHz. This set of traces is limited by the virtual range limit of the sounding program. These traces are formed after one, two, three, three and four reflections, respectively, while propagating within the duct between two reflection points inside the ZM cavity. The higher order traces have a time delay integral relationship with C and D traces. Each of the traces has multiple echoes at each frequency. The time integral relationship and multiple echoes at each frequency indicate that these echoes are formed due to ducted propagation inside a field aligned duct.

The t_g-f dispersion of the C trace has a decreasing trend with t_g decreasing from $\sim$70 ms at 380 kHz to $\sim$40 ms at upper cutoff $f_{C,max}$ =408 kHz. The upper cutoff of C trace may extend up to higher frequencies, but the amplitude is not large enough to be distinguishable from the noise signals. For the C trace, the t_g spread varies from $\sim$15 ms at 382 kHz to $\sim$3 ms at 408 kHz. The t_g spread of the D trace ranges from 12-25 ms. At 380 kHz, the time delays of the C, C+D, and C+2D traces are indistinguishable. For the C+D, C+2D, 2C+D, and 2C+2D traces, the t_g spread is $\sim$9-12 ms, $\sim$15-22 ms, $\sim$6-20 ms, and $\sim$9-20 ms, respectively.

It is observed that for all traces, except the C trace, upper cutoff frequency is limited by the virtual range limit of the sounding program. Gyro frequency at the satellite (calculated from the International Geomagnetic Reference Field (IGRF) model) is f_{ce} $\sim$301 kHz. Electron plasma frequency, f_{pe}, calculated from $f_{z,sat}$ and $f_{ce,IGRF}$ is $\sim$509 kHz. We observe strong noise signals in the frequency range from $\sim$386-480 kHz, starting from zero apparent range up to $\sim$80 ms. These noise

Table 4.1 Lower and upper cutoff frequency of ducted traces.

Trace	Lower Cutoff	Upper Cutoff
C	380 kHz	408 kHz
D	380 kHz	410 kHz
C+D	380 kHz	406 kHz
C+2D	380 kHz	392 kHz
2C+D	380 kHz	398 kHz
2C+2D	380 kHz	382 kHz

Table 4.2 Minimum and Maximum time delays and time delay spread of ducted traces for 392 kHz.

Trace	Minimum Tg (ms)	Maximum Tg (ms)	ΔTg (ms)
C	46.6	49.5	2.9
D	56	68.6	12.6
C+D	107.3	116.5	9.2
C+2D	155.3	177.6	22.3
2C+D	155.3	177.6	22.3
2C+2D	No Echo	No Echo	

signals could be sounder-generated, as we do not see any background emissions on the dynamic spectra in the frequency range 380-480 kHz. Two rising diffuse traces are also observed above the noise signals in the frequency ranges from 422 kHz (~50 ms) to 444 kHz (~170 ms) and 452 kHz (~60 ms) to 470 kHz (~180 ms).

Figure 4.1(b) shows the IMAGE orbit plot for 10 July 2001. The red dot shows the position of the satellite at 08:10 UT and 08:38 UT. The satellite was moving through the southern polar region towards the plasmasphere. The satellite orbit then crossed the same L-shell (L =2.70) at which the ducted echoes were observed near the equator at $\lambda_m = 2.36°$ ~30 minutes later (shown by the black arrow in Figure 4.1(c) near 08:38 UT). The f_{pe} at this location could be determined from the f_{uh} emission band and the $f_{ce,IGRF}$ ~47 kHz. f_{pe} is found to lie in the range of ~483-492 kHz, which gives the ZM cutoff frequency near the equator $f_{z,equ}$ ~460-470 kHz. The observed upper cutoff of the D trace $f_{D,max}$ is, thus, ~10-13% smaller than the $f_{z,equ}$. Figure 4.1(c) shows the

dynamic spectrogram recorded by IMAGE on 10 July 2001 from 06:00 - 10:30 UT. The upper hybrid resonance band is observed from 06:45-07:35 UT on the dayside (MLT∼6) and from 08:20-09:15 UT on the duskside (MLT∼17). The red curve is the TSY96-model [Tsyganenko and Stern, 1996] electron gyro frequency. The grey curve is the model f_{pe} values. Natural background emissions such as Whistler mode emissions, auroral kilometric radiation (AKR), and non-thermal continuum (NTC) radiation are also observed. Plasmapause measurements were made from N_e measurements obtained from f_{uh} emissions [Benson et al., 2004] and from the lower cutoff of the NTC radiation [Hashimoto et al., 2006]. The plasmapause is observed around 09:30 UT between L=5.3 to L=6 on the duskside (MLT∼17). The N_e decreased from ∼165 e/cc at L=5.3 to ∼13 e/cc at L=6. The satellite was inside the plasmasphere on L-shell 2.67-2.68 when the ducted echoes were observed.

4.2 Time Delay Integral Relationship

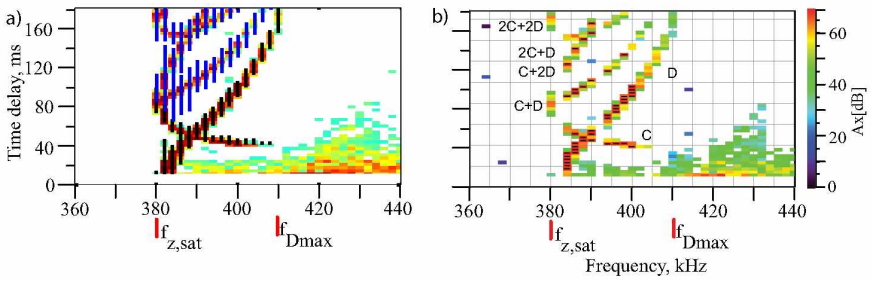

Figure 4.2 (a) Plasmagram of 10 July 2001 08:10:00 UT showing time delay integral relationship of higher order (blue vertical lines) traces with the principal traces C and D (black vertical lines). (b) Same plasmagram is represented in uncalibrated raw display with data being presented in minimum to maximum value. The red bins show strong signal saturation. The saturated echo bins (amplitude $\geq$ 64 dB) have been marked with black dash line.

The time delay spread of each trace at each frequency is attributed to the multipath propagation of waves in a duct. Waves at different wave normal angles travel along different paths and accumulate different time delays. This gives rise to multipath propagation. Figure 4.2(a) shows the plot of measured time delays of principal traces C and D (black vertical lines overlapping with the echo bins) and time delays of higher order traces (blue vertical lines overlapping with the echo bins) calculated from the time delays of principal traces. This figure has been plotted using MATLAB and the databin text file downloaded from the BinBrowser. The BinBrowser settings are as follows: (1) X antenna; (2)Color scale: 0-69 dB; (3)Representation: Amp[dB] uncalibrated; (4)No MPA threshold cleaning. The background has been suppressed by plotting only those databins which are above 30 dB threshold so that only the echo bins are seen and the background bins are discarded. For the time

integral relationship to hold, the sum of the time delays of the principal traces C and D should add to overlap with the time delay range of the next higher trace, C+D, i.e., $t_g(C) + t_g(D) = t_g(C + D)$. Similarly, the sum of time delays of C and the next higher trace C+D should add to overlap with the time delay range of the next higher trace 2C+D, i.e., $t_g(C) + t_g(C + D) = t_g(2C + D)$, and the sum of the time delay of D and the next higher trace C+D should add to overlap with the next higher trace C+2D, i.e., $t_g(D) + t_g(C + D) = t_g(C + 2D)$, and so on.

Figure 4.2(b) shows the 10 July 2001 plasmagram represented in an uncalibrated raw display. Each echo bin of each trace represents at least one echo. When the plasmagram is represented in an uncalibrated raw display, the data are presented in minimum to maximum values of 0-69 dB. We observe the echo bins of the C, D, C+D, C+2D, and 2C+D traces to be saturated, that is, the amplitude of the echo bin $\geq$ 64 dB. Each echo bin with signal saturation has been marked with a black dash line. We observe that for principal traces C and D, the majority of echo bins exhibit signal saturation at a lower frequency range. A strong signal in a higher order trace is related to a strong signal in at least one of the principal traces. Each echo bin of the C and D traces represents a different ray path. The time delay integral relationship of the higher trace C+D with that of lower traces suggests that the C+D echo has traveled a path similar to the C and D traces. Also, the time delay relation between each trace indicates that ZM waves propagate along the geomagnetic field line.

4.3 Physical Principle of Propagation, Reflection, and Guidance of Z Mode Waves

In this section we will discuss nonducted and ducted fast ZM wave propagation inside the ZM cavity in the magnetosphere. Fast ZM waves can propagate at wide range of wave normal angles, i.e., in all directions, because of closed refractive index surfaces. A wave normal angle (θ) at which the echo is formed is such that $\theta_1 < \theta < \theta_2$, where θ_1 and θ_2 are the wave normal angles for which the ray passes on either side of the satellite. Thus, for an echo to form, the condition is $\Delta\theta \rightarrow 0$, where $\Delta\theta = \theta - \theta_1 = \theta_2 - \theta$.

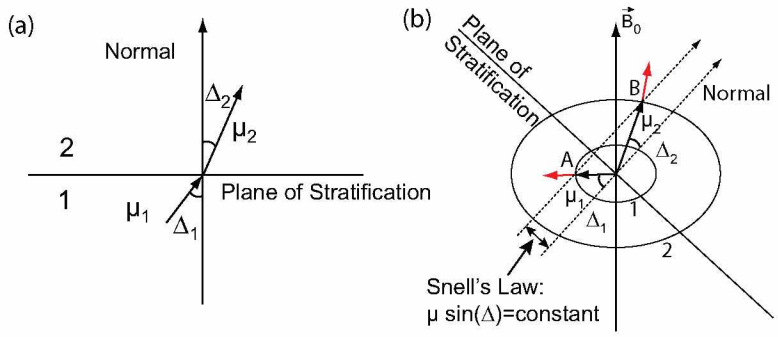

Figure 4.3 (a) Snell's Law for a simple case at a plane boundary between two different regions. (b) Poeverlein's construction illustrating the conservation of refractive index component along the plane of local stratification.

4.3.1 Snell's Law and Poeverlein's Construction

According to Snell's Law the refractive index surface component along the plane of local stratification should be conserved. The quantitative form of Snell's Law states that

$$\mu_1 \sin(\Delta_1) = \mu_2 \sin(\Delta_2) \tag{4.1}$$

where the angles Δ_1, Δ_2 are measured from the normal to the plane of stratification and μ_1 and μ_2 are the refractive indices in medium 1 and medium 2, respectively, as shown in Figure 4.3. The plane of stratification for a given wave normal direction is the locus of points which have the same phase refractive index, holding the direction of wave normal constant [Edgar, 1972]. The wave normal angle direction at each altitude is given by joining the origin of the refractive index surface to the point of intersection of the normal to the plane of stratification and the refractive index surface. Figure 4.3(a) shows the application of Snell's Law across a plane boundary between two different regions. Figure 4.3(b) shows the Poeverlein's construction. The Poeverlein's construction is a general method of finding the ray path in a stratified ionosphere or magnetosphere [Poeverlein, 1949; Budden, 1985]. The cross-section of the refractive index surface by a plane parallel to the plane of incidence is drawn at various levels of stratification encountered by the ray along its path. A vertical line is drawn perpendicular to the plane of stratification at a distance of $\mu \sin(\Delta)$ from the origin. This line is called the reference line. As shown in the Figure 4.3(b) the reference line cuts the refractive index surface 1 at two points. One of these points corresponds to the incident wave and the other to reflected wave. A line of length μ_1 joining the origin to the point of intersection and making an angle Δ_1 with the axis along the normal to plane of stratification is called the

refractive index for the wave whose wave-normal is along the direction of $\hat{\mu_1}$. The reference line intersects another refractive index surface 2. This refractive index surface corresponds to a different level of stratification. At this level the wave has refractive index μ_2 and makes an angle Δ_2 with the normal axis. In accordance with the Snell's Law, the ray propagates such that $\mu \sin(\Delta) = \text{constant}$. In an anisotropic medium such as the Earth's magnetosphere, the direction of energy propagation (ray direction) is different than the wave-normal direction [Helliwell, 1965; Budden, 1985]. The ray direction is normal to the refractive index surface [Budden, 1985]. Hence, the possible ray direction is given by the normal to the refractive index surfaces at the point of intersection of the reference line with the refractive index surfaces. The ray direction is shown as red arrows in Figure 4.3(b).

4.3.2 Mechanisms of Nonducted Propagation and Reflection of Fast ZM Waves by Ray Tracing Simulation and Snell's Law

This section uses ray tracing calculations to discuss the physical mechanisms of fast ZM echo formation based on the ZM refractive index surfaces and application of Snell's Law. A nonducted echo, as the name suggests, is not confined within the duct boundaries, but propagates smoothly in the magnetosphere and reflects at the location where $f \sim f_z$. If the wave normal angle is appropriate, then the ray may return back to the satellite to form an echo. This section discusses quantitative results of echo properties like initial wave normal angle, variation of refractive index surfaces with altitude, wave normal angle, and ray properties near the reflection point, excursion of the rays in L-shell, altitude, and the wave normal direction of the returning ray at the satellite.

Figure 4.4 shows the ray tracings of 392 kHz in the ZM cavity. In absence of the ducts, four nonducted echoes are formed C, D1, D2, and D3 (D3-1, D3-2). Three echoes (C, D1, and D2) are retracing echoes, while D3 is a looping echo. The downward propagating ray close to the satellite field line ($\mathbf{B_0}$) is termed C, and the upward propagating ray close to $\mathbf{B_0}$ is termed D1. The D2 and D3 echoes are formed when rays are launched at large initial wave normal angles towards lower L shells. The D3 ray travels toward the lower L shell, away from $\mathbf{B_0}$, and return back to the satellite forming a loop. The D2 ray travels toward the lower L shell, away from $\mathbf{B_0}$, and retraces its path after reflection to form an echo at the satellite. Rays that propagate toward L-shells higher than the satellite escape the cavity. Only those rays which are injected towards lower L-shells can reflect from a region where $f \sim f_z$, while traveling upwards or downwards, and return back to the satellite to form nonducted echoes.

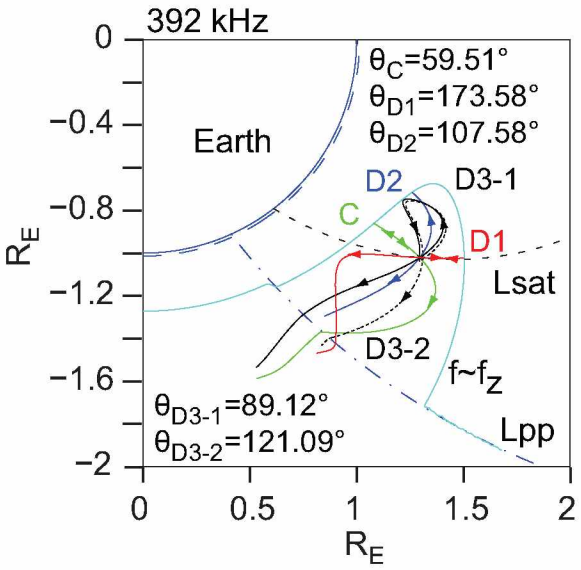

Figure 4.4 Nonducted echo ray path in magnetic meridional plane for 392 kHz in a smooth magnetosphere. Four nonducted echoes, C, D1, D2 and D3, are obtained .

4.3.2.1 Explanation of C Retracing Echo

The retracing echo, C, is formed when a ray is injected at a moderate wave normal angle $\theta_{i,C} = 59.51°$ (with respect to the satellite geomagnetic field $\mathbf{B_0}$) towards lower L-shells. The ray propagates downward from the satellite towards lower L-shells and reflects from a region where $f \sim f_z$. Figure 4.5(b) shows the ray paths of the C retracing echo and two adjacent rays injected at $\theta_i = 54°$ and 65° (dotted ray paths). The adjacent rays diverge away from the satellite.

Figure 4.5(a) shows the altitude variation of refractive index surfaces along the ray path in the vertical direction. The geomagnetic field ($\mathbf{B_0}$) is taken to be oblique (shown by the slanted black arrow line pointing downwards) and the plane of stratification is shown by the horizontal line. The red arrows indicate ray direction for the retracing ray (C echo trace) and the blue and green arrows represent the ray direction for adjacent rays. Key altitudes have been noted at satellite altitude (R_{sat}), altitude of minimum in f_z profile ($R_{f_{z,min}}$), altitude at which $\theta = 0°$, $\theta = 90°$, and the reflection point. Two vertical dotted lines are plotted at a horizontal distance $\mu \sin(\Delta)$ from the center to determine the wave normal angle and the ray angle as the ray propagates downward or upward.

From Figure 4.5(a) we note that the refractive index surface (μ-surface) is closed and oval in shape. With decreasing altitude, the size of the μ-surface first increases down to $R_{f_{z,min}}$ and then shrinks in size down to the reflection point. The C echo ray injected towards lower L shells at

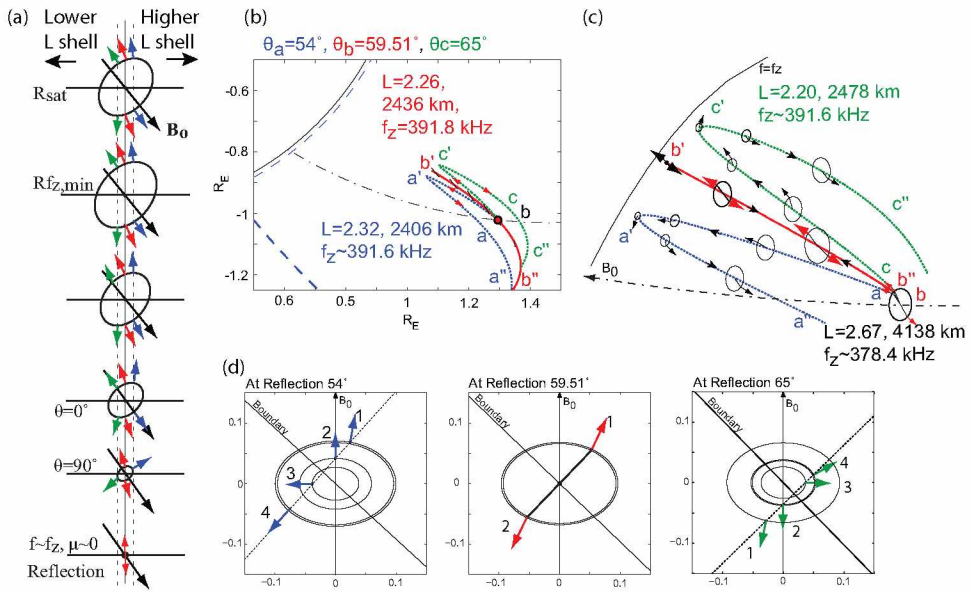

Figure 4.5 (a) Plot of the variation of refractive index surface and ray angle with altitude along the C trace echo ray path. (b) Ray path of C trace echo launched at initial wave normal angle 59.51° and adjacent ray paths at 54° and 65°. Refractive index surfaces along the ray path are shown in (c). (d) Poeverlein's construction at the reflection point.

$\theta_{i,C} = 59.51°$ must propagate such that $\mu \sin(\Delta)$ is conserved. In a hypothetical condition when there is no bending of the magnetic field line, the initial wave normal vector should be parallel to the normal so that $\mu \sin(\Delta) = 0$. This condition should hold along the ray path for a ray to reflect and retrace its path. In a real situation, when a ray is injected at an initial wave normal angle such that the wave normal vector makes a small angle with the normal, then, as the ray propagates downward, the refractive index surface shrinks in size and the wave normal angle decreases due to the bending of magnetic field lines. Due to this, the wave normal vector becomes parallel to the normal such that $\mu \sin(\Delta) = 0$ just before reflection. At the point of reflection, the refractive index surface shrinks to a point, and the refractive index goes to zero. At this point, reflection of the wave takes place. Just after reflection, the wave normal vector is aligned in the same direction as the incoming wave normal vector, but in opposite sense, and the reflected ray retraces its path after reflection. Figure 4.5(c) shows the refractive index surfaces along the echo ray path and two adjacent ray paths. Figure 4.5(d) shows the Poeverlein's construction at the point of reflection for three rays. Ray parameters along the ray path of the C retracing echo and two adjacent rays have been listed in Table A.3.

Figure 4.6 shows the plot of group velocity(V_g) and group time delay(t_g) as a function of altitude for the nonducted C trace echo at 392 kHz. The group velocity first increases with decreasing

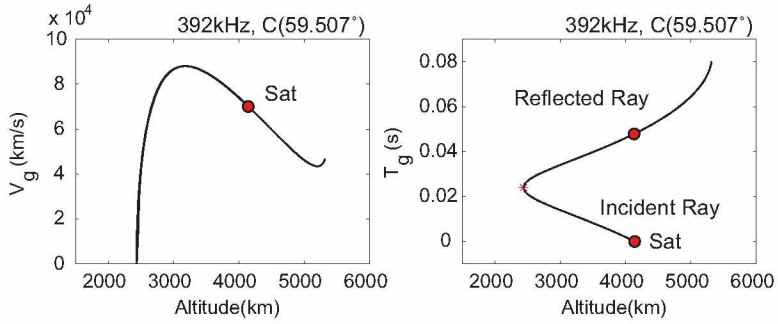

Figure 4.6 Plot of group velocity and time delay as a function of altitude for nonducted C trace retracing echo for 392 kHz.

altitude down to $R_{f_{z,min}}$ and then decreases to ∼0 at the reflection point. The time delay accumulated during the onward journey (∼24 ms) is the same as that during the return journey. The C ray reflects from an altitude of 2436 km and the maximum excursion of the ray from the L-shell of the satellite is ∼0.4, which shows that the ray propagates close to the field line of the satellite.

4.3.2.2 Explanation of D1 Retracing Echo

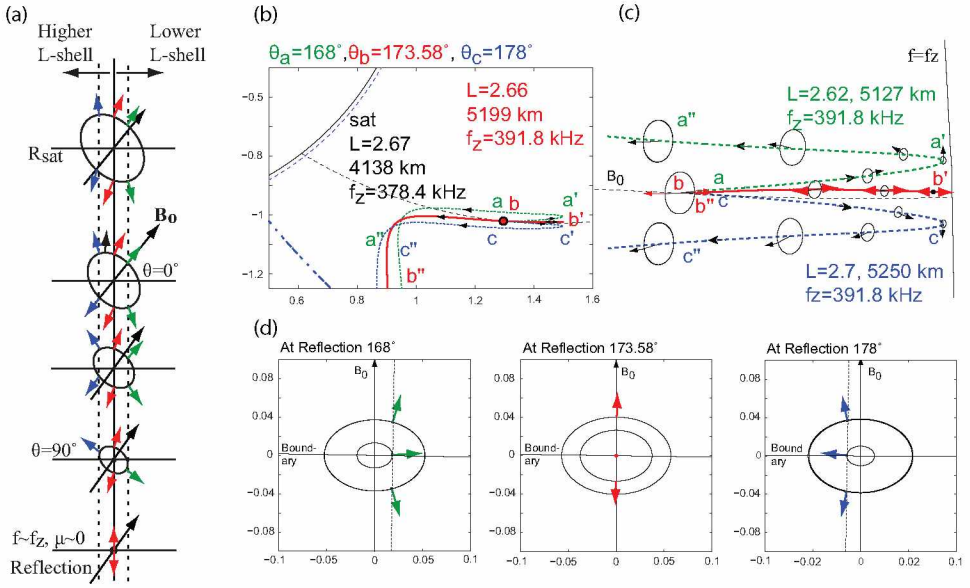

Figure 4.7 (a) Plot of the variation of refractive index surface and ray angle with altitude along the D1 retracing echo ray path. (b) Ray path of D1 trace echo launched at initial wave normal angle 173.58° and adjacent ray paths at 168° and 178° are shown. Refractive index surfaces along the ray path are also shown in (c). (d) Poeverlein's construction at the reflection point.

The retracing echo, D1, is formed when the ray is injected at a small initial wave normal angle $\theta_{i,D1} = 173.583°$ with respect to the geomagnetic field $\mathbf{B_0}$. The ray propagates close to the

geomagnetic field line upwards from the satellite towards lower L-shells and reflect from a region where $f \sim f_z$. Figure 4.7(b) shows the ray paths of the D1 retracing echo and two adjacent rays injected at $\theta_i = 168°$ and 178° (dotted ray paths). The adjacent rays diverge away from the satellite.

Figure 4.7(a) shows the altitude variation of the refractive index surfaces along the ray path in the vertical direction. The geomagnetic field ($\mathbf{B_0}$) is taken to be oblique (shown by the slanted arrow line pointing upwards) and the plane of stratification is shown by a horizontal line. The red arrows indicate ray direction for the retracing ray (D1 echo trace) and the blue and green arrows represent the ray directions for adjacent rays. Rays injected towards lower (higher) L shells are shown by green (blue) arrows. The echo ray is shown by red arrows.

From Figure 4.7(a), we note that the μ-surface of the fast ZM wave is a closed oval shape. With increasing altitude, the size of the μ-surface decreases up to the reflection point. The D1 ray propagates along the field line such that $\theta_i \sim 0°$ along the ray path. Thus, the condition $\mu \sin(\Delta) = 0$ holds along the ray path for the D1 ray to reflect and retrace its path. At the point of reflection, the refractive index surface shrinks to a point and the refractive index goes to zero. At this point, reflection of the wave takes place. Just after reflection, the wave normal vector is aligned in the same direction as the incoming wave normal vector, but in opposite sense, and the reflected ray retraces its path. Figure 4.7(c) shows the refractive index surface along the ray path. Figure 4.7(d) shows the Poeverlein's construction at the point of reflection for three rays.

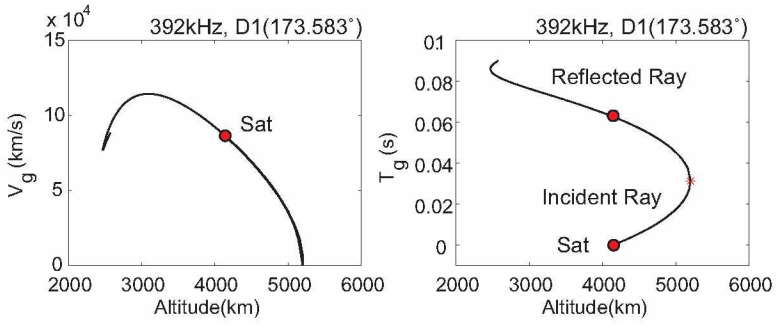

Figure 4.8 Plot of group velocity and time delay as a function of altitude for nonducted D1 trace retracing echo for 392 kHz. The echo ray reflects from above the satellite altitude in a smooth magnetosphere.

Figure 4.8 shows the plot of V_g and t_g as a function of altitude for the nonducted D1 trace echo at 392 kHz. The group velocity decreases from ~86,000 km/s at the satellite to ~0 km/s at the reflection point. The time delay accumulated during the onward journey (~31 ms) is same as that during the return journey of the ray. Table A.4 lists the important ray parameters along the D1 ray path from the satellite altitude to the reflection point. The D1 ray reflects from an altitude of

~5200 km above the satellite and from the location where f ~ f_z, and the maximum excursion of the ray from the L-shell of the satellite is ~0.01, which shows that the ray propagates along the field line of the satellite to the reflection point and back.

4.3.2.3 Explanation of D2 Retracing Echo

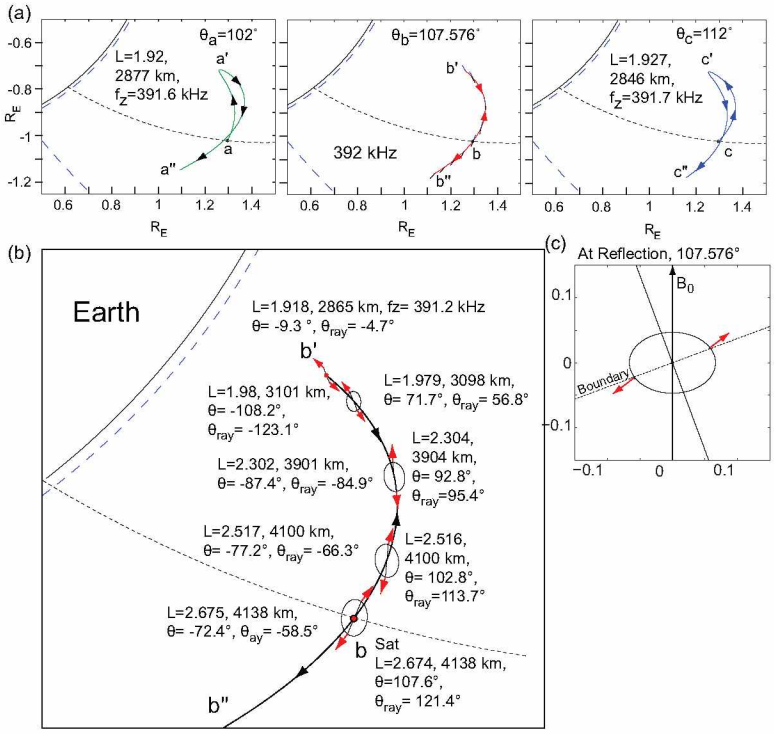

Figure 4.9 Plot of refractive index surfaces for nonducted D2 retracing echo. (a) Ray path of D2 trace echo launched at initial wave normal angle 107.6° and adjacent ray paths at 102° and 112°. (b) Refractive index surfaces along the ray path is also shown. (c) Poeverlein's construction at the reflection point.

The retracing echo, D2, is formed when the ray is injected at a large initial wave normal angle $\theta_{i,D2} = 107.576°$ towards lower L-shells. The ray then propagates downward, away from the satellite, reflects from a region where f ~ f_z, and retraces its path after reflection. Figure 4.9(a) shows the ray paths of the D2 retracing echo and two adjacent rays injected at $\theta_i = 102°$ and 112°. The 102° ray passes slightly below the satellite, while the 112° ray passes slightly above the satellite.

Figure 4.9(b) shows the altitude variation of refractive index surfaces along the ray path for the 107.576° ray. As the D2 ray is launched at a large initial wave normal angle, the ray propagates toward lower L-shells. It encounters a region of increasing f_z, f_{pe}, and f_{ce}. As the ray approaches the region where f ~ f_z, the refractive index shrinks in size, and at f ~ f_z, reflection takes place.

At the point of reflection, the refractive index goes to zero. Figure 4.9(c) shows the Poeverlein's construction at the point of reflection for the D2 ray.

Figure 4.10 shows the plot of V_g and t_g as a function of altitude for the nonducted D2 trace echoes at 392 kHz. The group velocity decreases from ~64,000 km/s at the satellite to ~0 km/s at the reflection point. The time delay accumulated during the onward journey (~51 ms) is the same as that during return journey of the ray. Table A.6 lists the important ray parameters along the D2 ray path from the satellite altitude down to the reflection point. The D2 ray reflects from an altitude of 2865 km below the satellite from the location where $f \sim f_z$, and the maximum excursion of the ray from the L-shell of the satellite is ~0.76, which shows that the ray propagates far away from the satellite field line to the reflection point and back.

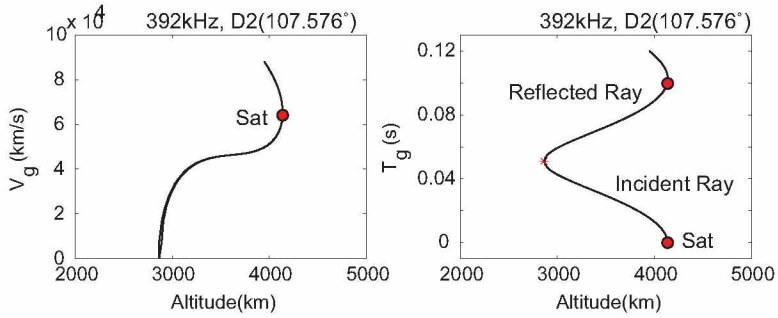

Figure 4.10 Plot of group velocity and time delay as a function of altitude for nonducted D2 trace retracing echo for 392 kHz. The echo ray reflects from below the satellite altitude in a smooth magnetosphere.

Figure 4.9(d) shows the Poeverlein's construction at the point of reflection for the 107.576° ray.

4.3.2.4 Explanation of D3 Looping Echo

The looping echo, D3, is formed when the ray is injected at a large initial wave normal angle $\theta_{i,D3-2} = 121.086°$ toward lower L-shells. Figure 4.11(a) shows the ray paths of the D3 looping echo and two adjacent rays injected at $\theta_i = 115°$ and 125°. The 115° ray passes slightly above the satellite while the 125° ray passes slightly below the satellite. Figure 4.11(b) shows the plot of the refractive index surface along the ray path for the 121.086° ray. The D3 echo ray first propagates upwards above the satellite altitude towards lower L-shells. It encounters a region of decreasing f_{pe} and f_{ce} but increasing f_z, and the refractive index surface shrinks in size. The wave normal angle decreases rapidly towards 90°, and at this point, the wave normal angle changes from greater than 90° to less than 90°. The ray then changes direction (from going upwards to going downwards

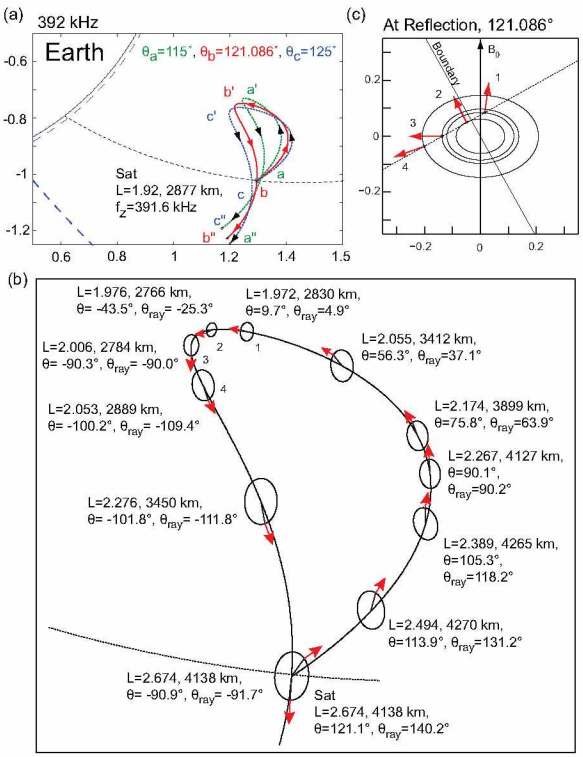

Figure 4.11 Plot of refractive index surfaces for nonducted D3 looping echo. (a) Ray path of D3 trace echo launched at initial wave normal angle 121.1° and adjacent ray paths at 115° and 125°. Refractive index surfaces along the ray path is also shown in (b). (c) Poeverlein's construction at the reflection point.

at first reflection point) from an altitude of 4127 km. The ray then propagates down, where the wave normal angle changes from less than 90° to greater than 90°. As the ray approaches the region where f $\sim$ f_z, the refractive index shrinks in size and reflection takes place. At the reflection point, the ray reverses direction from downward to upward. Figure 4.11(c) shows the Poeverlein's construction at the point of reflection for the 121.086° ray. The ray then propagates towards higher L-shells towards the satellite, thus forming a looping echo. For the looping echo, there is another ray injected at a large initial wave normal angle $\theta_{i,D3-1} = 89.119°$, which traverses the same path but in opposite sense.

Figure 4.12 shows the plot of V_g and t_g as a function of altitude for the nonducted D3 trace echo at 392 kHz. The group velocity decreases from ~70,600 km/s at the satellite to ~22,700 km/s at the reflection point. The total time delay accumulated during the onward and return journey is ~97 ms. Table ?? lists the important ray parameters along the D3 ray path. The maximum excursion of the ray from the L-shell of the satellite to its second reflection point is ~0.67 L, which shows that the ray propagates far away from the satellite field line to the reflection point and back.

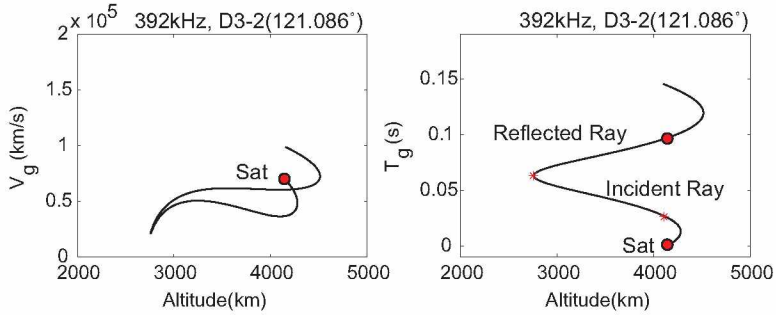

Figure 4.12 Plot of group velocity and time delay as a function of altitude for nonducted D3 trace looping echo for 392 kHz. The echo ray reflects from below the satellite altitude in a smooth magnetosphere.

4.3.2.5 Higher Order Non Ducted Fast ZM Echoes

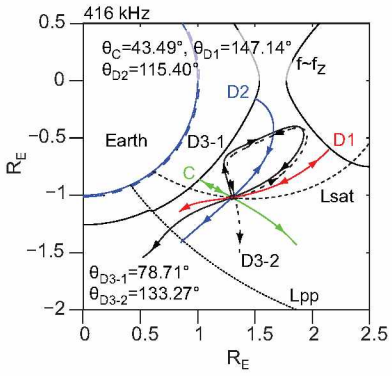

Figure 4.13 Nonducted echo ray path in magnetic meridional plane for 416 kHz in a smooth magnetosphere. Three echoes (C, D1, D2) retrace its path after reflection while one (D3) forms a loop.

From ray tracing analysis we have found that higher order nonducted echoes(D4, D5 D6-1, D6-2) are obtained at higher frequencies closer to $f_{z,equ} = 418.5$ kHz, for a very narrow band of frequencies (416 kHz $\leq f \leq$ 419 kHz), in addition to four nonducted echoes (C, D1, D2, D3). Figure 4.13 shows the four nonducted echoes for 416 kHz that are usually observed in the frequency range $f_{z,sat} \leq f \leq f_{z,equ}$.

Figure 4.14 shows the higher order nonducted echoes that are observed only for a narrow band of frequencies close to $f_{z,equ}$. These higher order traces are formed after multiple reflections. The retracing echo, D4, is formed when the ray is injected at a large initial wave normal angle $\theta_{i,D4} = 89.841°$ towards lower L-shells. The ray first propagates downward, away from the satellite, and then refracts upward. The ray then propagates and reflects from a region where $f \sim f_z$ and retraces its path after reflection. A looping echo, D5, is formed when the ray is injected at a

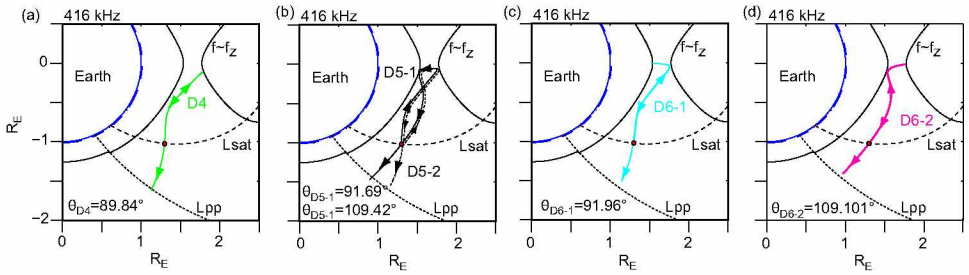

Figure 4.14 Higher order nonducted echo ray paths in magnetic meridional plane for 416 kHz in a smooth magnetosphere. Three echoes (D4, D6-1, D6-2) retrace its path after reflection while one (D5) forms a loop.

large initial wave normal angle $\theta_{\mathrm{i,D5-2}} = 109.421°$ towards lower L-shells. After reflection, the ray follows a double looping path and forms an echo at the satellite. For the looping echo, there is another ray injected at a large initial wave normal angle $\theta_{\mathrm{i,D5-1}} = 91.687°$, which traverses the same path as D5-2 but in opposite sense (shown as a solid ray path in Figure 4.14(b)). The retracing echoes, D6-1 and D6-2, are formed when the rays are injected at large initial wave normal angles ($\theta_{\mathrm{D6-1}} = 91.958°$ and $\theta_{\mathrm{D6-2}} = 109.101°$) towards lower L-shells (shown in Figure 4.14(c)-(d)). The ray propagates away from the satellite and retraces its path back to the satellite after reflection.

4.3.2.6 Explanation of t_g-f Dispersion of Non Ducted Traces

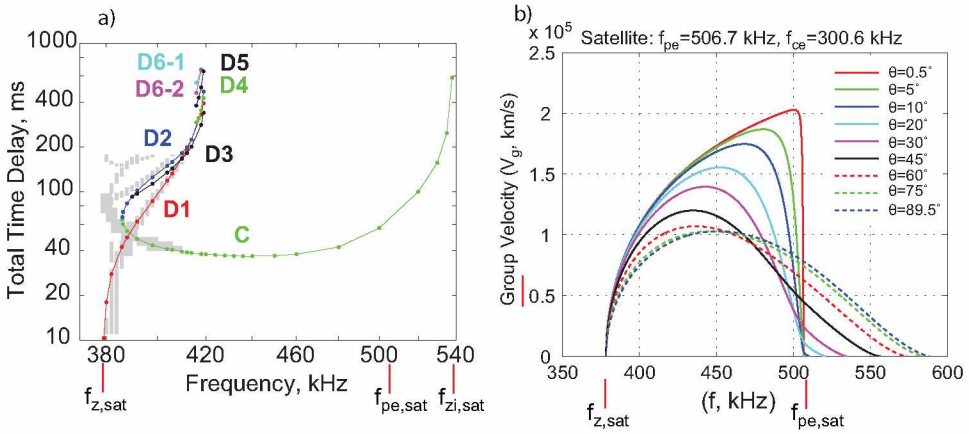

Figure 4.15 (a) Time delays versus frequency plot for nonducted echoes. C, D1, D2 and D3 echoes are observed alongside higher order nonducted traces D4, D5, D6-1 and D6-2. (b) Plot of the group velocity as a function of frequency for various wave normal angles for plasma condition at the satellite..

Figure 4.15(a) shows the plot of time delay (t_g) as a function of frequency for the nonducted echoes. The observed t_g are shown as grey bars. All the nonducted echo traces are shown in different colors. The maximum t_g of the observed traces is 180 ms. The y-axis (t_g) is shown in

Table 4.3 Frequencies at which maximum V_g is obtained at various wave normal angles for plasma condition near the satellite, f_{pe} = 506.7 kHz, f_{ce} = 300.7 kHz.

$\theta(°)$	f(kHz)	$V_{g,max}$(km/s)
0.5	500.3	2.03×10^5
5	480.3	1.87×10^5
10	468.1	1.75×10^5
20	452.8	1.56×10^5
30	442.7	1.40×10^5
45	434.8	1.20×10^5
60	436.4	1.07×10^5
75	446.4	1.03×10^5
90	451.2	1.03×10^5

logarithmic scale up to 1000 ms, as the maximum calculated t_g of nonducted traces goes up to ~670 ms. The C trace (green) is observed to be detached from the zero t_g baseline. The t_g-f dispersion of the C trace is 'U' shaped and exhibits a minimum at 'nose frequency' $f_{z,nose}$ ~440 kHz. The t_g decreases with increasing frequency, and at 440 kHz, the t_g is ~37 ms for $\theta_i = 38.79°$. Time delay for C trace then increases with increasing frequency up to the upper cutoff frequency at Z-infinity f_{zI} =538 kHz. The calculated lower cutoff frequency of the C trace has been found to be 386.2 kHz, which is greater than the observed local ZM cutoff frequency $f_{z,sat}$ =380 kHz, and the calculated time delay is ~64 ms for $\theta_i = 84.04°$. For the C trace echo at 386.2 kHz, group velocity is small and the ray has to travel a relatively longer path length. Therefore, the time delay accumulated is larger for frequencies close to $f_{z,sat}$ than at frequencies close to $f_{z,nose}$.

Figure 4.15(b) shows group velocity plotted as a function of frequency for various wave normal angles for the plasma conditions f_{pe} =~507 kHz and f_{ce} =~301 kHz at the satellite. V_g has been calculated numerically using the formula $V_g = d\omega/dk$, where ω is the angular wave frequency and k is the wave vector. From Figure 4.15(b), we observe that for $f \sim f_{z,sat}$ ~380 kHz, the group velocity is very small and close to zero. At any given wave normal angle, V_g increases with increasing frequency and attains a maximum value at the 'nose' frequency, $f_{z,nose}$. Group velocity then decreases very sharply as the frequency increases beyond $f_{z,nose}$. From the V_g-f graph, it is also evident that V_g decreases very sharply with frequencies above the 'nose' frequency for smaller wave normal angles compared to large wave normal angles. This is due to the occurrence of a dimple in

the refractive index surface near f_{pe} at small wave normal angles. It can also be discerned from the graph that at smaller frequencies, the group velocity at any given frequency is larger for small wave normal angles (direction parallel to geomagnetic field) than for large wave normal angles (direction perpendicular to geomagnetic field). This implies that the total time delays accumulated for the echoes propagating at small wave normal angles (C and D1) are smaller than the time delays for echoes propagating at large wave normal angles (D2, D3 and other higher order nonducted traces).

For frequencies greater than $f_{pe,sat}$, V_g has a larger value at large wave normal angles and vice-versa. From the graph, we observe that, for the V_g-f curve for $30° - 45°$ wave normal angles, the maximum V_g is obtained for f ~435-443 kHz. The 'nose' frequency of 440 kHz of the C trace obtained from ray tracings, lies within this range of frequencies. As the C trace echo rays in the frequency range $f_{z,sat} \leq f \leq f_{pe,sat}$ travel close to the geomagnetic field line, they encounter about the same plasma conditions during their onward and return journeys. Therefore, the minimum time delay is accumulated for frequencies close to the 'nose' frequency for the given plasma conditions.

Table 4.4 Group velocity V_g, in km/s, for ZM waves at various initial wave normal angles and at various frequencies for plasma condition near the satellite, $f_{pe} = 506.7$ kHz, $f_{ce} = 300.7$ kHz.

f / $\theta(°)$	~0	10	30	45	60	~90
378.23	2.29×10^3	779	754	714	655	554
392	8.79×10^4	8.74×10^4	8.37×10^4	7.82×10^4	7.10×10^4	6.13×10^4
410	1.27×10^5	1.26×10^5	1.18×10^5	1.08×10^5	9.65×10^4	8.58×10^4
420	1.42×10^5	1.40×10^5	1.29×10^5	1.16×10^5	1.03×10^5	9.37×10^4
432	1.57×10^5	1.54×10^5	1.37×10^5	1.20×10^5	1.07×10^5	9.97×10^4
440	1.65×10^5	1.61×10^5	1.39×10^5	1.20×10^5	1.07×10^5	1.02×10^5
480	1.94×10^5	1.69×10^5	9.61×10^4	8.30×10^4	8.73×10^4	9.59×10^4
507	2.91×10^3	3.18×10^3	2.43×10^4	4.49×10^4	6.27×10^4	7.81×10^4

For frequencies greater than the local electron plasma frequency f_{pe}, the t_g increases very rapidly to the upper cutoff at 538 kHz, at which point the t_g is ~585 ms at a wave normal angle of $\theta = 35.28°$. The upper cutoff of the C trace is obtained at Z-infinity frequency (f_{zI}) [Benson 2006]. From the V_g-f graph, we observe that the upper cutoff frequency of V_g-f curve, that is, the frequency at which V_g ~0, is obtained between f ~535 kHz for 30° to f~556 kHz for 45°. Thus, Z-infinity of ~538 kHz lies in the range of 535-556 kHz.

The D1 trace (as shown in Figure 4.15(a) as red curve), on the other hand, starts from a zero

range baseline at $f_{z,sat}$ and increases very rapidly with frequency. As the satellite is above the altitude minimum in the f_z profile, $R_{f_{z,min}}$, the ZM reflection level for rays propagating upwards lies very close to the satellite for $f \sim f_{z,sat}$. Therefore, for $f \sim f_{z,sat}$, the rays propagating upwards travel smaller distances, which compensates for the effect of smaller group velocity V_g near $f \sim f_{z,sat}$. Thus, the ray accumulates smaller time delays.

From Figure 4.15(a), we see that the t_g of the D1 trace increases steeply with increasing frequency up to the upper cutoff frequency at 419 kHz, which is close to the upper cutoff frequency of the ZM cavity (model) $f_{z,equ} = 418.5$ kHz. From the V_g-f graph, we observe that V_g increases steeply from $f_{z,sat}$ ~380 kHz to $f_{z,equ}$ ~419 kHz at any given wave normal angle. Thus, an increase in the path length from satellite to the reflection point compensates for the increase in group velocity from $380 - 419$ kHz resulting in greater time delays. At higher frequencies ($f > f_{z,equ}$) the rays do not encounter a region of $f \sim f_z$ necessary for reflection, and therefore escape the cavity. Thus, for $f > f_{z,equ}$, only C trace echoes are obtained.

The t_g-f dispersion of other traces could be explained in a similar manner with the aid of the V_g-f graph. From Figure 4.15(a), we observe that the D2 trace (blue) echoes are in the frequency range of 386.2 kHz $\leq f \leq$ 419 kHz. The D3 trace (black) echoes are observed in the frequency range of 390 kHz $\leq f \leq$ 419 kHz. The higher order nonducted traces, D4, D5, D6-1, and D6-2 are observed in frequency ranges of 416 kHz $\leq f \leq$ 419 kHz, 416 kHz $\leq f \leq$ 419 kHz, 416 kHz $\leq f \leq$ 418 kHz, and 416 kHz $\leq f \leq$ 418 kHz, respectively.

From the t_g-f plot of Figure 4.15(a), we observe that: (1) the lower cutoff of the D1 trace is always lower than the lower cutoffs of the C, D2, D3, and other higher traces (D4, D5, D6-1 and D6-2); (2) the lower cutoffs of the C and D2 traces are equal and the echoes have equal time-delays at this frequency; (3) the lower cutoff of D3 is greater than that of the C, D1, and D2 traces, but lower than that of the D4, D5, D6-1, and D6-2 higher order traces; (4) the lower cutoffs of all the higher order traces are equal and are greater than those of the C, D1, D2 and D3 traces, (5) the upper cutoff of the C trace is always greater than the upper cutoff of the D1, D2, D3 and higher order traces (D4, D5, D6-1 and D6-2); (6) the upper cutoff of D1, D2, D3, D4, and D5 are equal to $\sim f_{z,equ}$; and (7) the upper cutoffs of the D6-1 and D6-2 traces are lower than the cutoffs of all the traces C, D1, D2, D3, D4, and D5 traces.

4.3.3 Mechanisms of Ducted Propagation and Reflection of ZM Waves by Ray Tracing Simulation and Snell's Law

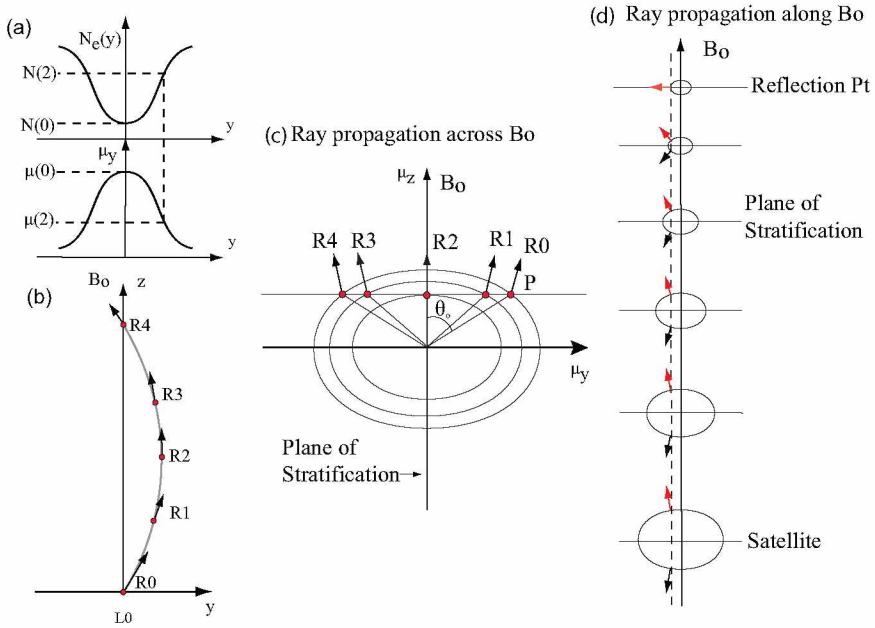

Figure 4.16 Fast ZM refractive index surfaces and application of Snell's Law for ducted ray propagation. (a) The N_e profile of a density depleted duct and refractive index profile of fast ZM across a depletion duct are shown. (b) ZM ray path along the depletion duct.(c) Application of Snell's Law for ray propagation across duct (transverse propagation) using family of refractive index surfaces obtained from Appleton-Hartree equation. (d) Application of Snell's Law for ray propagation along the duct (longitudinal propagation).

If waves are guided along the field aligned density depletions or enhancements, they are called ducted waves. The propagation and reflection of waves inside a duct can be understood in terms of superposition of wave propagation in (a) transverse (perpendicular to geomagnetic field line) and (b) longitudinal (parallel to geomagnetic field line) directions, as shown in Figure 4.16(c)-(d).

In *Transverse Propagation*, waves in any given mode can be confined in a duct if the refractive index decreases from the center towards the edge of the duct. Figure 4.16(a) shows the N_e profile across a field aligned density duct with density varying perpendicular to $\mathbf{B_0}$. The corresponding refractive index profile is also shown. In the cross-$\mathbf{B_0}$ direction, the N_e profile decreases towards the center of a density depleted duct, while the refractive index increases towards the center. The decreasing refractive index profile from the center towards the edge of the duct provides the condition for total internal reflection of waves.

From a given N_e profile, a family of refractive index surfaces can be constructed using the

Appleton-Hartree equation as shown in Figure 4.16(c). Snell's Law defines the wave normal directions and ray direction. Assuming that inside a duct the boundary lies parallel to the geomagnetic field direction, the projection of the refractive index along this boundary must be the same for different strata of the media. Assuming an initial wave normal angle of θ_0, the normal to the plane of stratification (shown by a horizontal line in Figure 4.16(c)) intersects the refractive index surface at point P. The direction from the center to the point of intersection 'P' with the refractive index surface represents the possible wave normal direction for the ducted ray. At the intersection, the direction of energy of the wave, or the ray direction, is perpendicular to the refractive index surface shown by an arrow 'R0'.

Figure 4.16(b) shows the ducted ray path as a ray, which starting with an initial wave normal angle θ_0 at the center of the duct (point R0 in Figure 4.16(b)), propagates from the center towards the edge of the duct (point R2 in Figure 4.16(b)). The direction of the ray at each point, R0 through R4 in (b), is shown at the point of intersection in Figure 4.16(c). The wave normal angle always rotates in a direction of increasing refractive index, and the ray rotates in the same sense as the wave normal angle. As the ray moves towards the edge of the duct, it encounters shrinking refractive index surfaces. Its wave normal angle decreases until it becomes 0°, at which point the ray reaches a point of maximum lateral excursion from the center of the duct (point R2 in Figure 4.16(b)), where the wave normal and ray angle become parallel to the magnetic field $\mathbf{B_0}$. The relation between the maximum initial wave normal angle (θ_0) and the density perturbation N(2)/N(0) required to trap the waves is obtained by applying Snell's Law, $\mu(0)\cos(\theta_0) = \mu(2)$, where $\mu(0)$ and $\mu(2)$ are the refractive index at the center of the duct and at the point of reflection of ray near the edge of the duct, respectively, and θ_0 is the initial wave normal angle. After this point, the ray moves back towards the center of the duct following a ray path (R2 through R4 in Figure 4.16(b)) that is a mirror image of the lower half of the path about a horizontal line due to the symmetry of the refractive index surface. Following the same argument as above, the ray path on the other side is similar to ray paths R0 through R4 but in opposite sense. The ray path shows that ZM waves are trapped within the depletion duct as the rays propagate close to the magnetic field line in a zig-zag path.

Figure 4.16(d) shows *Longitudinal propagation*. From the profile of the refractive index inside a duct, it can be deduced that the plane of stratification inside a duct is approximately parallel to $\mathbf{B_0}$ near the edges, while it is perpendicular to $\mathbf{B_0}$ at the center. As a ray propagates along the geomagnetic field line, it encounters shrinking refractive index surfaces. In contrast to transverse

propagation, the wave normal angle increases with shrinking refractive index surfaces. The ray reflects from a point where the wave normal angle becomes perpendicular to $\mathbf{B_0}$, as shown in Figure 4.16(d). When we superpose the transverse and longitudinal propagation, then we get the complete ducted propagation of waves along the field aligned density depleted duct.

If the satellite is inside a density depleted duct, then fast ZM rays injected at a range of wave normal angles (varying from $0° - 90°$) may be confined inside the duct and propagate along the geomagnetic field line. Only a small range of wave normal angles can be guided in a given duct and the range increases with increasing density depletion. Ducted rays reflect inside the duct at a location where $f \sim f_z$ and return back to the satellite to form ducted echoes. From ray tracing analysis it is found that both looping as well as retracing ducted echoes are formed. A looping ducted echo is defined as an echo which, after reflection at $f \sim f_z$, does not travel along the same path as an incident ray. Instead, it forms a zig-zag loop before intercepting the satellite to form an echo. There are two looping echoes that follow the same path but in opposite directions and therefore have identical time delays. A retracing ducted echo is defined as an echo, which after reflection at $f \sim f_z$, travels along the same path as an incident ray and form an echo at the satellite.

4.3.3.1 Propagation and Reflection of Ducted Z Mode Echoes: $f_{z,sat} \leq f < f_{z,equ}$

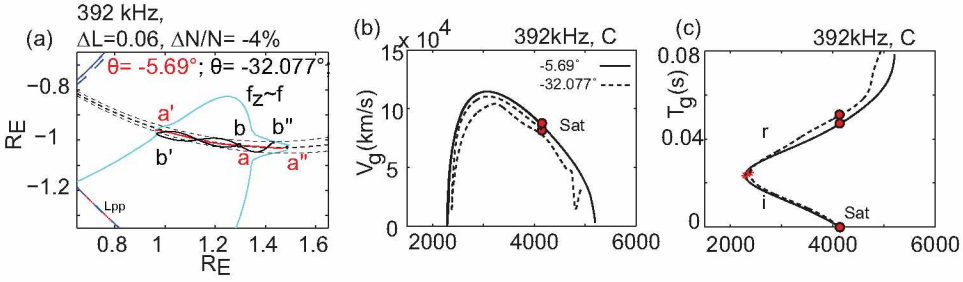

Figure 4.17 Ray path of 392 kHz ducted C trace echo and plot of group velocity and time delay as a function of altitude. (a) Ray launched at an initial wave normal angle -32.077° and -5.69° in density depleted duct of ΔL =0.06 L and depletion of 4%. Plot of group velocity and time delay as a function of altitude for ducted C trace are shown in (b), and (c) respectively.

Figure 4.17(a) shows the ducted C trace echoes at θ_i of -5.69° and -32.077°. Ducted C trace echoes propagate below the satellite along the duct, reflect at $f \sim f_z$, and return back to the satellite. From ray tracings for the C trace, both the looping- and retracing-ducted echoes have been obtained. Rays injected at different θ_i have different travel paths and therefore accumulate different time-delays. This is called multi-path propagation. The reflection altitude of the C trace at all wave

normal angles is about the same, i.e., rays propagating towards Earth at different initial wave normal angles reflect at about the same altitude as can be seen in Figures 4.17(a)-(b). The ray injected at a small $\theta_i = -5.69°$ travels a lesser distance and accumulates a lesser time delay than the ray injected at a large $\theta_i = -32.077°$. Figures 4.17(b)-(c) shows V_g and t_g as a function of altitude for ducted C trace echoes for 392 kHz. Table A.8 lists the ray parameters along the ray path for ducted C trace echoes at $\theta_i = -32.077°$.

Figure 4.18 shows the ray path for the -32.077° ray. Figure 4.18(b)-(c) shows the plot of $\mu-$surfaces along the vertical direction and along the ray path, respectively. Corresponding to each point along the ray path (R1-R6), a $\mu-$surface has been plotted along the vertical direction. As the ray is launched, it deviates from the center of the duct (L = 2.674) towards higher L-shells to L =2.721 and undergoes total internal reflection at a location (3714 km) where the wave normal angle is $\theta \sim 0°$. At this point, the ray refracts inwards toward the center of the duct. As the ray propagates down, the size of the refractive index increases and becomes maximum at $R_{f_{z,min}}$. The group velocity increases from ~82,000 km/s at the satellite to 110,000 km/s at $R_{f_{z,min}}$. The ray further propagates downward and the wave normal angle increases steadily towards 90° near the reflection point, where the ray reverses direction from going downward to going upward. The reflection occurs at an altitude of ~2380 km at L =2.768. At the reflection point, the refractive index (μ) and the group velocity (V_g) have finite values of $\mu \sim 0.05$ and V_g =15,000 km/s, respectively. After reflection, the ray follows a looping path during its return journey. The time delay accumulated during the onward journey (~23 ms) is the same as that during the return journey, as can be seen from Figure 4.17(c).

Figure 4.19(a) shows the ducted D trace echoes at θ_i of 161.071°, 138.544°, and 126.242°. Ducted D trace echoes propagate above the satellite along the duct, reflect at $f \sim f_z$, and return back to the satellite. Both the looping- and retracing-ducted echoes have been obtained from ray tracings for the D trace. From Figure 4.19(a), it is evident that, for D trace, the reflection altitude of rays is different at different θ_i. The ray propagation path is shorter for the ray injected at a large $\theta_i = 126.242°$ and the ray reflects from a lower altitude. Ray injected at a smaller $\theta_i = 161.071°$ has a higher reflection altitude and longer propagation path. The deviation of rays from the center of the duct is large for large θ_i and vice versa. Thus, a ray injected with small θ_i accumulates a larger time delay than a ray with a large θ_i.

Figure 4.19(b)-(c) shows V_g and t_g as a function of altitude for ducted D trace echoes for 392 kHz. Figure 4.20 shows the ducted D ray path launched at 138.544° anti parallel to the geomagnetic

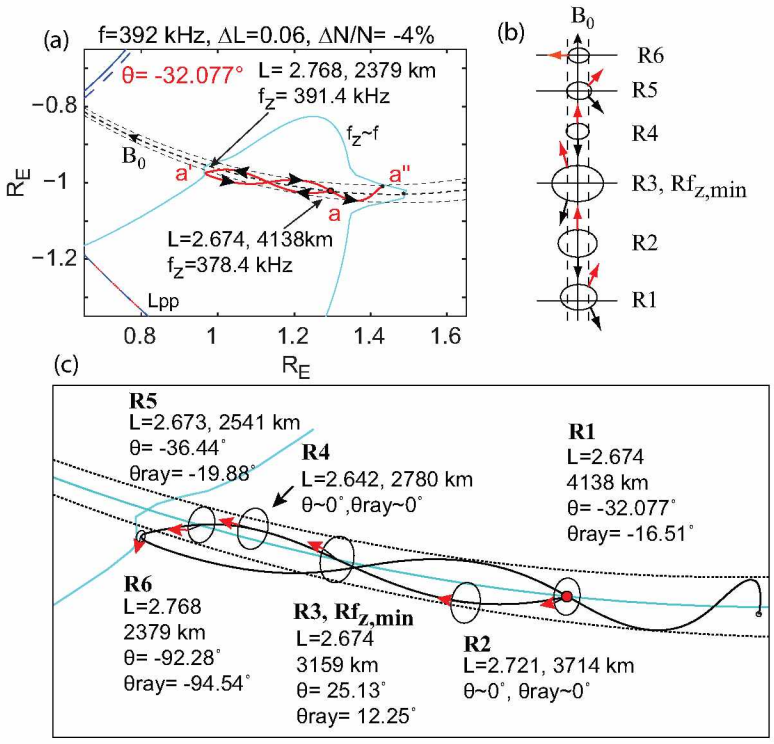

Figure 4.18 Poeverlein's construction explaining 392 kHz ducted C trace echo ray propagation. (a) Ray path of ducted C trace echo launched at an initial wave normal angle -32.077°. (b) Simplified Poeverlein's construction schematic of the propagation and reflection of C trace rays inside the duct. (c) Refractive index surfaces along the ray path..

field line (ray tracing convention takes the direction of the geomagnetic field going from North to South). Figure 4.20(b)-(c) shows $\mu-$surfaces along the vertical direction and along the ray path, respectively. Corresponding to each point along the ray path (R1-R7), a $\mu-$surface has been plotted along the vertical direction. The ray deviates away from the center of the duct (L = 2.674) towards lower L-shells to L =2.623 and undergoes total internal reflection at a location (4420 km) where the wave normal angle is $\theta \sim 0$. At this point the ray refracts inwards towards the center of the duct. As the ray propagates upward, the size of the refractive index shrinks and the group velocity decreases from $\sim 79,000$ km/s at the satellite to $\sim$ 29,000 km/s at the reflection point.

Near the reflection point, the wave normal angle increases steadily towards 90° and the ray reverses direction from up to down. The reflection occurs at an altitude of ~4951 km at L =2.671. At the reflection point the refractive index (μ) and group velocity (V_g) have finite values of $\mu \sim 0.16$ and $V_g \sim$29,000 km/s, respectively. After reflection, the ray follows a looping path during its return journey. The time delay accumulated during the onward journey (~27 ms) is the same as that during the return journey, as can be seen from Figure 4.19(c).

From the above discussion, we find that: (1) rays injected at larger (smaller) initial wave normal

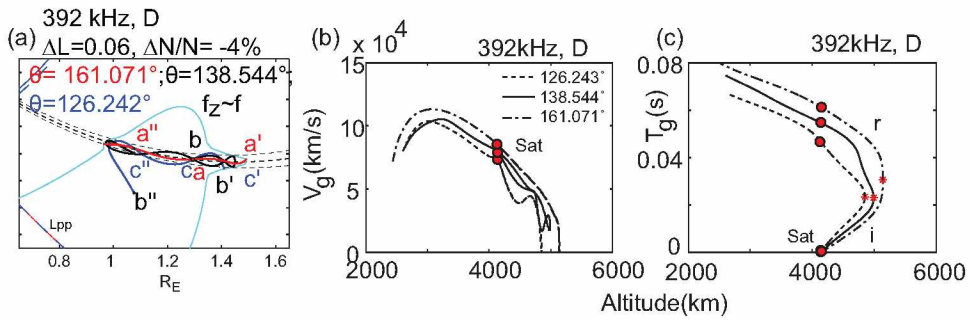

Figure 4.19 Ray path of 392 kHz ducted D trace echo and plot of group velocity and time delay as a function of altitude. (a) Ray launched at an initial wave normal angle 161.071°, 138.544° and 126.242° in density depleted duct of half width 0.06 L depletion of 4%. Plot of group velocity and time delay as a function of altitude for ducted D trace are shown in (b), (c) respectively.

angles have largest (smallest) L-shell excursions from the center of the duct; (2) rays injected with larger (smaller) θ_i have smaller (larger) group velocities; and (3) retracing and looping ducted echoes are observed. For retracing ducted echoes, specular (mirror-like) reflection takes place at a location where $f \sim f_z$, whereas for looping echoes, refraction rather than reflection of the wave takes place at the reflection point $f_z < f$. It should be noted that for looping echoes, the wave frequency (f) may be larger than f_z at the reflection point. Higher order ducted echoes, e.g., C+D traces (not shown in the ray tracing figures), are formed when (1) rays travel above (below) the satellite and reflect at $f \sim f_z$, then travel downwards (upwards) and reflect at $f \sim f_z$ and then return back to the satellite to form an echo.The wave normal angles at which the C+D echoes are formed are different than the wave normal angles at which the C or D trace echoes are formed. A similar argument follows for the higher traces (C+2D, 2C+D, and 2C+2D). The rays propagate back and forth within the duct to form higher order ducted echoes.

4.3.3.2 Propagation and Reflection of Ducted Z Mode Echoes: $f \sim f_{z,equ}$

Figure 4.21 shows the raypaths of 420 kHz ducted C and D trace echoes. Figure 4.22(a)-(d) plots V_g and t_g as a function of altitude for ducted C trace echoes for 420 kHz. Table A.10 lists the ray parameters along the ray path for 420 kHz C trace echoes at $\theta_i = -1.481°$ and 13.610°. Figure 4.23(a)-(f) plots V_g and t_g as a function of altitude for ducted D trace echoes for 420 kHz. Table A.11 list the ray parameters along the ray path for D trace echoes at 136.395°, 152.584°, and 175.364° wave normal angles. D trace rays injected at large initial wave normal angles ($\theta = 136.395°$ and $\theta = 152.584°$) reflect within the ZM cavity, as can be seen from Figure 4.21(b), whereas rays injected at a relatively smaller wave normal angle ($\theta = 175.364°$) propagate to the conjugate hemisphere and

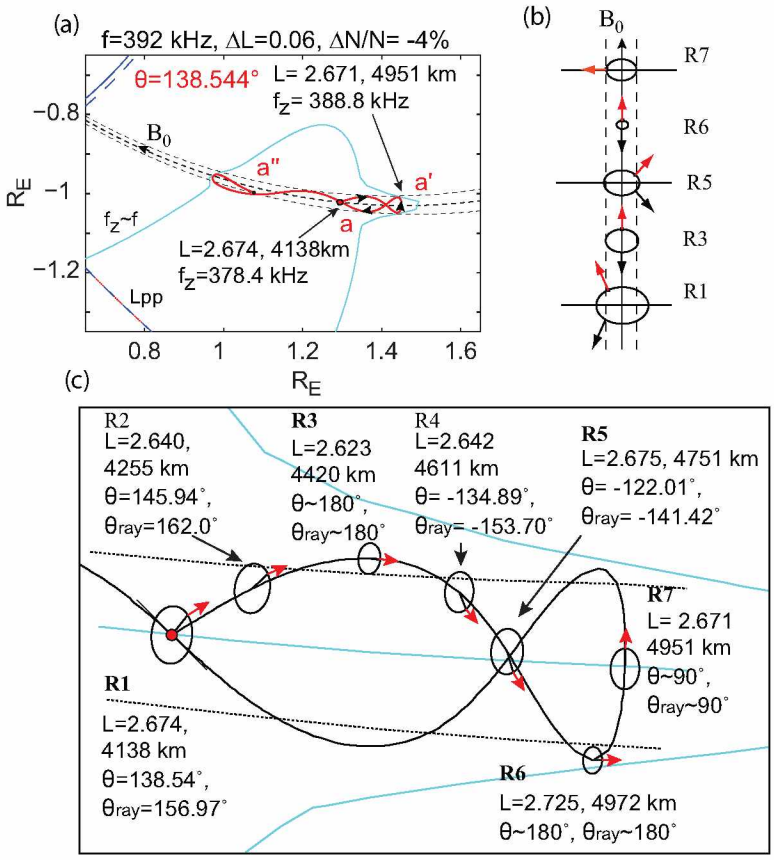

Figure 4.20 Poeverlein's construction explaining ducted D trace echo ray propagation. (a) Ray launched at an initial wave normal angle of 138.544°. (b) simplified Poeverlein's construction schematic of the propagation and reflection of D trace rays inside the duct. (c) Refractive index surfaces along the ray path.

reflect back to form an echo. The echoes propagating and reflecting from within the local hemisphere accumulate relatively smaller time delays compared to echoes propagating and reflecting from the conjugate hemisphere. Thus, the t_g-f dispersion at $f \sim f_{z,equ} = 420$ kHz shows a very large time delay spread (see Figure 4.27).

4.3.3.3 Propagation and Reflection of Ducted Z Mode Echoes: $f > f_{z,equ}$

Figure 4.24 shows the raypaths of 432 kHz ducted C and D trace echoes. Figure 4.25(a)-(d) shows the plot of V_g and t_g as a function of altitude for ducted C trace echoes for 432 kHz. Table A.12 lists the ray parameters along the ray path for C trace echoes at $\theta_i = 6.415°$ and -19.926°. The time delay accumulated during the onward journey (~19 ms) is the same as that during return journey (Figure 4.25).

Figure 4.26(a)-(d) shows V_g and t_g as a function of altitude for ducted D trace echoes for 432

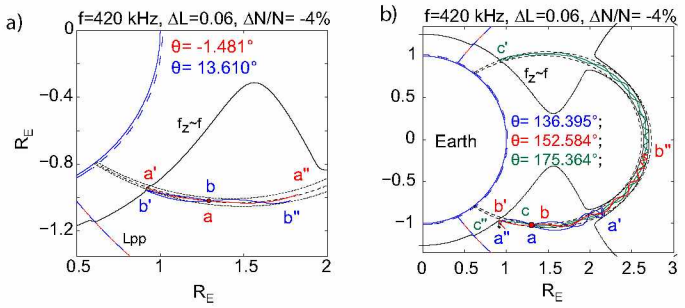

Figure 4.21 Ray paths of 420 kHz ($f \sim f_{z,equ}$) ducted C and D trace echoes in a duct of $0.06L$ half width and 4% depletion. (a) Rays reflecting from below the satellite altitude. (b) Rays reflecting from above the satellite altitude. For D trace, rays at large wave normal angles (blue and red rays in (b) reflect within the ZM cavity whereas for small wave normal (green ray in (b)) the ray propagates to the conjugate hemisphere and reflects back to form an echo.

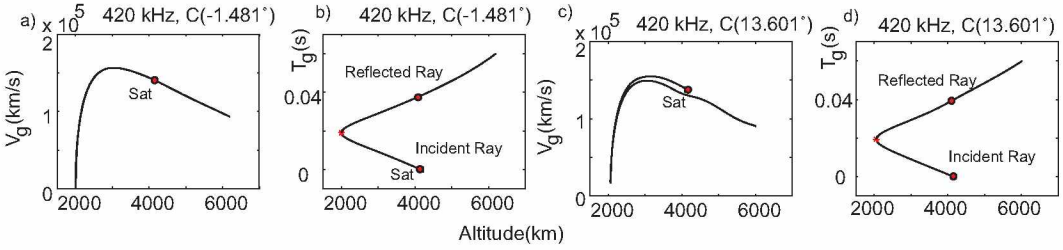

Figure 4.22 Plot of group velocity and time delay as a function of altitude for ducted C for 420 kHz.

kHz. The rays injected at different θ_i towards the equator propagate to the conjugate hemisphere and reflect back to form echoes. Table A.13 lists the ray parameters along the ray path for D trace echoes at $\theta_i = 155.695°$ and -168.421°. The time delay accumulated during the onward journey (~335 ms) is about the same as during the return journey (Figure 4.26(b) and (d)). Thus, for both rays, t_g is large due to a large path length, but the spread in time delay is small, as can be seen in the Figure 4.27.

4.3.3.4 Explanation of t_g-f Dispersion of Ducted Traces

Figure 4.27 shows t_g-f plot for ducted echoes calculated from an average density model of the 10 July 2001 case. The duct model is chosen such that the half-width $\Delta L = 0.06$ (126 km at satellite altitude) and the density depletion is 4%. The average density model parameters are $f_{z,sat}$ ~380 kHz, $f_{z,equ}$ ~419 kHz, and electron plasma frequency at the equator, $f_{pe,equ}$ ~442 kHz. The ducted traces are color-coded in the figure. The black triangles in the figure represent the nonducted echoes. Figure 4.27 shows interesting features:

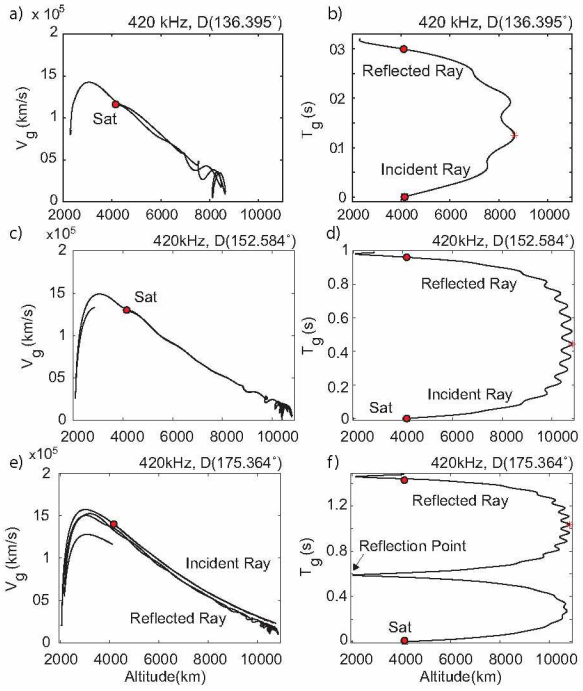

Figure 4.23 Plot of group velocity and time delay as a function of altitude for ducted D for 420 kHz.

1. Non ducted echoes are observed in addition to ducted echoes.

2. The lower cutoffs of all the ducted traces are the same, i.e., ∼380 kHz.

3. The time delay spread of all the traces (except the C trace) increases with increasing frequency and is maximum at $f(= 420\,\text{kHz}) \sim f_{z,equ}$.

4. The average time delay decreases at $f > 420$ kHz, attains a minimum at f ∼432 kHz (f_{nose}), and then increases to f ∼440 kHz, which is close to $f_{pe,equ}$(∼442 kHz).

5. The frequency at which the minimum t_g occurs (432 kHz) depends not on the duct parameters but on the value of $f_{pe,equ}$, and is called as the 'nose' frequency (f_{nose}).

6. The time delays of the nonducted D trace (D1) and the ducted D trace with small initial wave normal angles are similar. This is because both rays travel close to the field line, reflect from about the same altitude, and have similar group velocities (see figures 4.8 and 4.19(b)). The t_g-f dispersion of the D trace and other higher traces could be explained simply in terms of the variation of V_g with θ and frequency, and variation of f_z and f_{pe} along the L-shell of the satellite (L_{sat}).

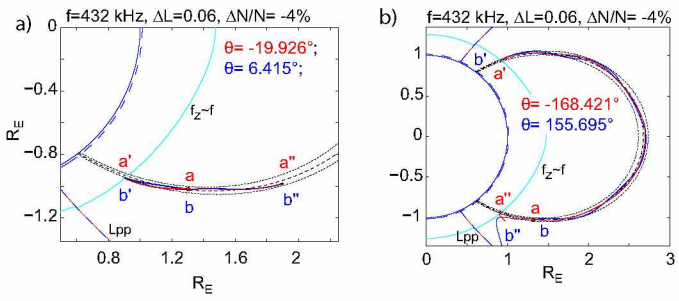

Figure 4.24 Ray paths of 432 kHz ($f > f_{z,equ}$) ducted C and D trace echoes in a duct of $0.06L$ half width and -4% depletion. (a) Rays reflecting from below the satellite altitude. Retracing and looping ducted C trace echoes are obtained. (b) Rays reflecting from above the satellite altitude. For D trace, rays propagates to the conjugate hemisphere and reflect back to form an echo. Retracing and looping ducted C as well as D trace echoes are obtained.

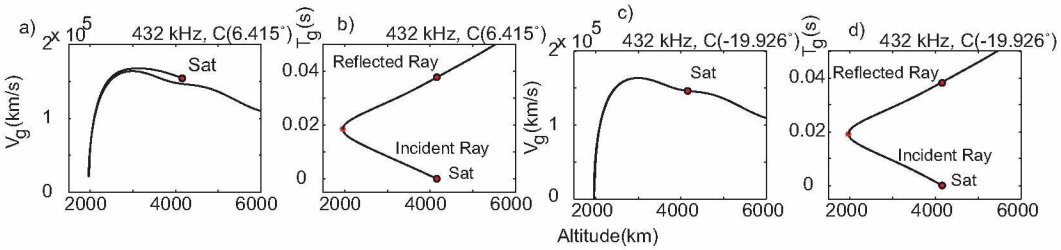

Figure 4.25 Plot of group velocity and time delay as a function of altitude for ducted C trace echoes for 432 kHz.

7. A frequency gap in the C trace is observed in the frequency range of 439 - 496 kHz. For this frequency range, only nonducted echoes are obtained. For the frequencies 380 - 438 kHz, the ducted C trace echoes are obtained. For the frequencies 497 - 522 kHz, the wave propagation is affected by the presence of density gradients and multiple partially ducted echoes are obtained.

Figure 4.28(a)-(b) shows the contours of f_z and f_{pe} for 350-550 kHz. The f_{pe} contours are concentric, suggesting that the magnetosphere obtained from the diffusive equilibrium density model is horizontally stratified. At lower altitudes where $f_{pe} \gg f_{ce}$, f_z contours follow the f_{pe} contours. Along an L-shell with increasing altitude, the f_z first decreases, then reaches a minimum at some altitude $R_{f_{z,min}}$, then increases again, forming a ZM cavity.

Figure 4.28(c) shows V_g versus frequency (f) in the range of $f_z \leq f \leq f_{uh}$ at various wave normal angles. The curves have been plotted for plasma conditions at the equator on the L-shell of the satellite, $f_{pe} = 441.8$ kHz and $f_{ce} = 47.9$ kHz. The f_z and f_{uh} are 418.5 kHz and 444.4 kHz, respectively. V_g has been calculated numerically using the formula $V_g = d\omega/dk$, where ω is the angular wave frequency and k is the wave vector. For longitudinal propagation ($\theta \sim 0°$), V_g increases

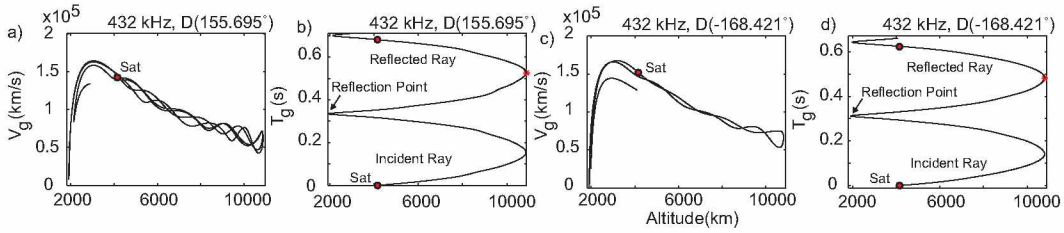

Figure 4.26 Plot of group velocity and time delay as a function of altitude for ducted D trace echoes for 432 kHz.

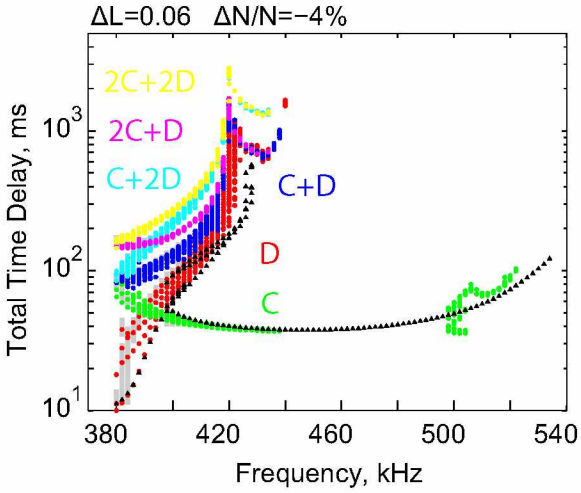

Figure 4.27 Time delays versus frequency plot for the duct width $\Delta L = 0.06$ and density depletion $\Delta N/N = -4\%$.

with increasing f, becomes maximum just before $f \sim f_{pe}$, decreases very sharply, and attains a minimum at $f = f_{pe}$. For $\theta > 0°$, V_g shows the same trend and attains a minimum at $f_{pe} < f < f_{uh}$. The frequency at which V_g attains its maximum value decreases with increasing wave normal angle. For example, for $\theta = 0.5°$, V_g attains maximum value of ~95,000 km/s at f~441 kHz, and for $\theta = 60°$, the maximum value of V_g ~37,000 km/s is at f~427 kHz. Table 4.5 lists the values of frequencies at which V_g maxima occur at various wave normal angles.

For ducted propagation, a ray travels along the geomagnetic field line. As the ray propagates towards the equator, it encounters regions of increasing f_z and decreasing f_{pe} along its travel path, as can be seen from the f_z and f_{pe} contours in Figure 4.28(a)-(b). If f is such that $f \sim f_{z,equ}$, then from the contour plot of f_z, we observe that near the equator, f_z contours follow the field line. Therefore, a ray of frequency $f \sim f_{z,equ}$ sees a region of low group velocity for large part of its travel path near the equator and accumulates most of its travel time in that region (see Figure 4.23(d)). Thus, for $f \sim f_{z,equ}$, the ray accumulates large time delays compared to when $f < f_{z,equ}$. Figure 4.23(c)-(d) shows group velocity versus altitude and group time delay versus altitude for the 420

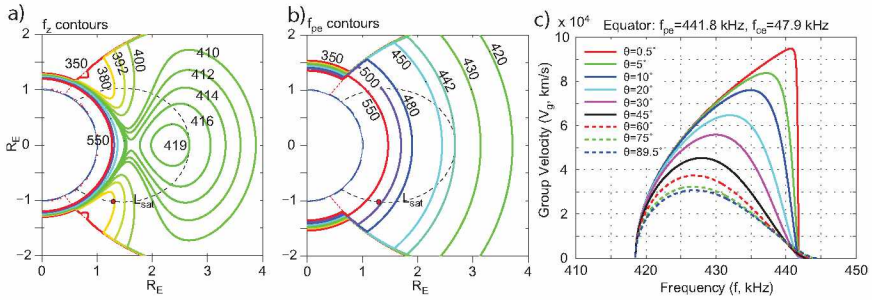

Figure 4.28 Contours of f_z and f_{pe}. The black dotted curve is the L-shell of the satellite (L_{sat}). Plot of the group velocity versus frequency for various wave normal angles for plasma condition at the equator.

Table 4.5 Frequencies at which maximum V_g is obtained at various wave normal angles for plasma condition near the equator, f_{pe} = 441.8 kHz, f_{ce} = 47.9 kHz.

$\theta(°)$	f(kHz)	$V_{g,max}$(km/s)
0.5	440.7	9.49×10^4
5	437.2	8.39×10^4
10	434.9	7.61×10^4
20	432.0	6.48×10^4
30	430.0	5.59×10^4
45	428.0	4.54×10^4
60	426.9	3.74×10^4
75	426.9	3.24×10^4
90	426.9	3.08×10^4

kHz ray injected at an initial wave normal angle of $\theta = 152.584°$. It is evident from the graph that the group velocity decreases from ~130,000 km/s to ~930 km/s at the reflection point near the equator (10390 km, -3.7°). At the reflection point, the value of f_{pe} ~445 kHz, f_{ce} ~51 kHz, and f_z ~420 kHz. It is also found that the ray accumulated most of its time delay near the equator. The total time delay accumulated when the ray was within 10° geomagnetic latitude of the equator is 0.52 seconds, ~54% of the total echo time delay (0.96 sec), while the ray traveled only ~27% of the total echo path length (~27000 km).

The 'nose' frequency at 432 kHz in the t_g-f dispersion for frequency range $f_{z,equ} < f < f_{pe,equ}$ could be explained in terms of the variation of V_g with f at a given θ. For the condition when $f > f_{z,equ}$, rays travel to the conjugate hemisphere and reflect where $f \sim f_z$. We observe from the contour plot of f_z that the reflection altitude of rays transmitted in the frequency range of

$f_{z,equ} < f < f_{pe,equ}$ is about the same in the conjugate hemisphere. Therefore, the travel path length of rays for $f > f_{z,equ}$ is about the same. This means that the total time delay accumulated for $f > f_{z,equ}$ will depend upon the variation of group velocity (V_g) as a function of f and θ. As shown in the plot of V_g in Figure 4.28(c), V_g at any given θ increases with increasing frequency, attains a maximum at frequency close to but less than f_{pe}, and then decreases as f approaches f_{pe}. From ray tracing we found that for $f > f_{z,equ}$, the minimum t_g is obtained for f in the range of 430-434 kHz (Figure 4.27). From the plot of V_g versus frequency in Figure 4.28(c), it is evident that the maximum in V_g at 430 kHz - 434 kHz is obtained when the wave normal angle is in the range of $10° - 30°$. From ray tracing analysis, we found that for frequencies in the range of 430-434 kHz, rays are guided for wave normal angles $\leq 26°$. Rays injected at higher initial wave normal angles escape the duct. Therefore, a wave of frequency in the range of 430 kHz - 434 kHz propagating at moderate wave normal angles ($10° - 30°$) will have maximum V_g near the equator and therefore minimum time delay.

Table 4.6 Group velocity V_g, in km/s, for ZM waves at various initial wave normal angles and at various frequencies for plasma condition near the equator $f_{pe} = 441.8$ kHz, $f_{ce} = 47.9$ kHz.

f / θ(°)	∼0°	10°	30°	45°	60°	∼90°
418.5	3.11×10^3	671	649	615	564	477
420	2.59×10^4	2.58×10^4	2.48×10^4	2.32×10^4	2.10×10^4	1.76×10^4
426	5.75×10^4	5.68×10^4	5.11×10^4	4.43×10^4	3.72×10^4	3.06×10^4
432	7.61×10^4	7.30×10^4	5.43×10^4	4.01×10^4	3.13×10^4	2.62×10^4
436	8.60×10^4	7.54×10^4	3.90×10^4	2.53×10^4	1.98×10^4	1.76×10^4
441.8	3.41×10^3	1.35×10^2	8.94×10^2	1.77×10^3	2.64×10^3	3.50×10^3

It has been found from ray tracing that for density depleted ducts, the upper cutoff frequency is always $f \leq f_{pe,equ} =$∼442 kHz. Calvert (1995) has discussed the theory of ducting of the four plasma wave modes in troughs (depletion) and crests (enhancements). The wave normal angle inside a duct depends upon the density deviation of the duct (ΔN), the longitudinal refractive index, the rate of change of the longitudinal refractive index with density and the refractive index radius of curvature. When the refractive index radius of curvature changes sign, the ducting in a wave mode changes from crest (trough) to trough (crest). This is known as curvature reversal. For fast ZM the ducting occurs in troughs from the ZM cutoff (f_z) to curvature reversal at halfway between the ZM cutoff and plasma frequency (f_{pe}) [region Z_1], in crests up to f_{pe} [region Z_2], and in crests between f_{pe}

and f_{ce} if $f_{pe} < f_{ce}$ [region Z_3]. Calvert, (1995) has shown that for ZM, the strongest ducting occurs near the ZM cutoff frequency and near the curvature reversal. The weakest ducting occurs near f_{pe}, at which point the radii of curvature become quite small and the duct strength decreases to zero.

4.3.3.5 Explanation of Frequency Gap in C trace in presence of Ducts

A peculiar behavior is observed for the ducted C trace. For a given duct, the ducted C trace echoes are obtained for two frequency ranges separated by a frequency gap. From the ray tracings it is found that C trace echoes are observed at lower frequencies ($f_{lc1} \leq f \leq f_{uc1}$), disappear at middle frequencies, and reappear at higher frequencies ($f_{lc2} \leq f \leq f_{uc2}$) closer to electron plasma frequency f_{pe}. From the t_g-f plot shown in Figure 4.27, for a typical duct of half-width ΔL =0.06 and density depletion of 4%, C trace echoes are observed in the frequency range of f_{lc1} =380 kHz to f_{uc1} =438 kHz and then from f_{lc2} =497 kHz to f_{uc2} =522 kHz. When the frequency is increased beyond f_{uc1}, the rays are no longer guided and escape the duct. The upper cutoff frequency of the C trace terminates at frequency $f_{uc1} \ll f_{pe}$. The waves are not ducted for a range of frequencies $f_{uc1} < f < f_{lc2}$. At higher frequencies $f_{lc2} < f < f_{uc2}$, C trace echoes are obtained again. These echoes are partly ducted and partly non ducted. This behavior can be explained in terms of the peculiar shape of refractive index surfaces for small θ_i for frequencies lying close to the f_{pe}. The refractive index surface has a dimple-like structure for wave normal angles close to 0° for $f <\sim f_{pe}$ and an inverted cone-like structure for wave normal angles close to 0° and $f >\sim f_{pe}$ (see Figure 2.2).

Figure 4.29 shows the ray path of the 497 kHz C trace echo launched at $\theta_i = 8.07°$. Refractive index surfaces have been plotted along the ray path explaining the formation of C trace echoes in the presence of density ducts. Refractive index surfaces along the ray path in the vertical direction are shown in Figure 4.30. The geomagnetic field is taken to be vertically down and the plane of stratification is shown by horizontal lines. The red arrows in Figure 4.30(a) indicate ray direction. f_{pe} and f_{ce} at the satellite are ∼507 kHz and ∼294 kHz, respectively. We know that for the plasma conditions $f_{pe} > f_{ce}$ and a small wave normal angle direction, the refractive index surface exhibits dimple-like structure for frequencies lying close to f_{pe}. The transmitted frequency 497 kHz lies close to f_{pe}, and therefore, the refractive index surface at the satellite altitude exhibits a dimple-like structure (Figure 4.30(a) and (b)).

During the initial part of the ray path as the ray moves toward the center of the duct, the

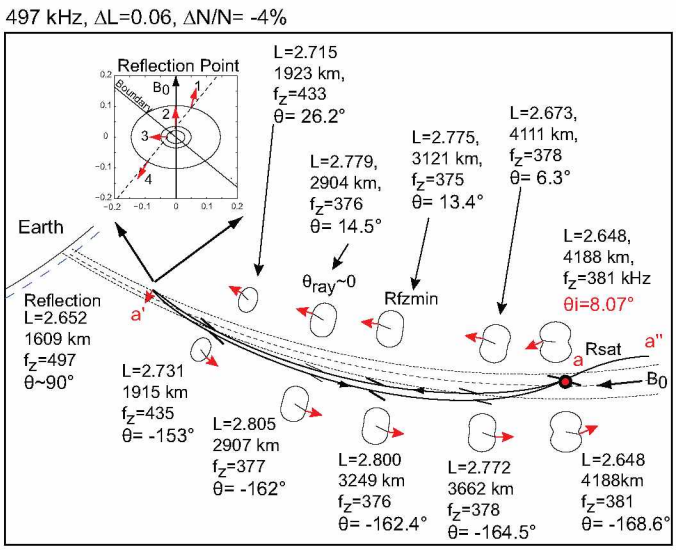

Figure 4.29 Figure showing propagation of C trace echo ray for 497 kHz in presence of duct of half width 0.06 L and density depletion of 4%.

refractive index surface increases in the parallel direction ($\mu(0°)$) and decreases in the perpendicular direction ($\mu(90°)$). Small portions of the dimples in the refractive index surfaces are shown in Figure 4.30(b), depicting the change in ray direction. Due to this typical variation in the μ-surface, as the ray moves toward the center of the duct, the ray angle decreases (in contrast to the change in ray direction when the refractive index surface is elliptical, as shown in Figure 4.30(c)). As the ray moves outward from the center of the duct, the dimple structure of the refractive index surface becomes flatter, i.e., the dimple starts to disappear. As the ray is also moving in a downward direction, f_{pe} and f_{ce} increase and the refractive index surface shrinks in size and the dimple becomes flatter. The shrinking refractive index causes the wave normal angle to increase and the flatness of the dimple structure causes the ray angle to decrease.

At the altitude close to $R_{f_{z,min}}$, the μ-surface becomes oblate in shape (the dimple structure has now disappeared) and the ray angle changes direction from moving outward towards higher L shells to moving inward towards lower L shells (Figure 4.29). As the ray propagates further, the refractive index surface (μ-surface) shrinks and changes shape from oblate to elliptical. Due to a shrinking μ-surface, the wave normal angle and the ray angle increase more and more towards the lower L shells and the ray starts to move towards the duct again. At ~1923 km, the ray enters the duct (Figure 4.29). As the ray moves further into the duct, the wave normal angle starts to decrease due to total internal reflection (Figure 4.30(c)). Near ~1610 km, the reflection takes place. Near this point, the ray angle changes direction very rapidly, as shown in the inset of Figure 4.29.

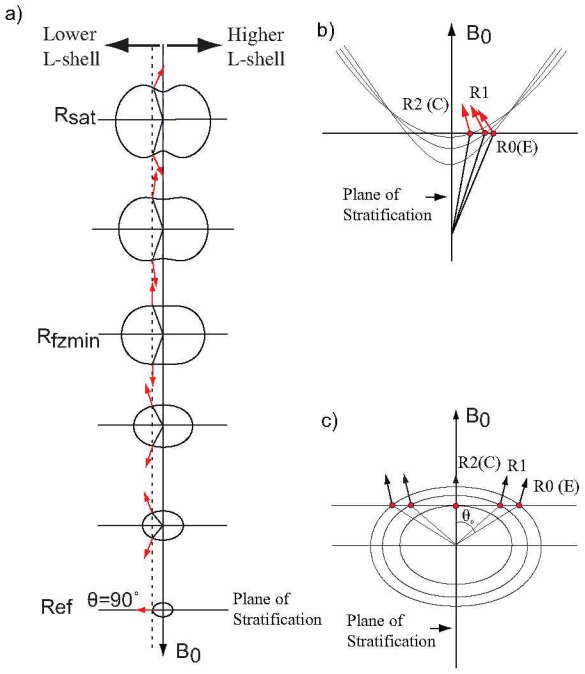

Figure 4.30 Poeverlein's construction explaining 497 kHz ducted C trace echo ray propagation. (a) Variation of refractive index surfaces with altitude assuming vertical B. (b) Enlarged portion of refractive index surfaces at the satellite altitude for wave normal angles close to 0°. (c) Variation of refractive index surfaces before the reflection point of the ray.

In the returning phase of the ray path, just after reflection the μ-surface increases in size and the wave normal angle and ray angle decrease. At the midpoint of its propagation path, i.e., at ~3000 km altitude, the refractive index surface changes from elliptical to oblate and the ray angle changes direction. As the ray propagates further upward, the dimple in the refractive index surface starts to reappear. At the same time, the refractive index surface also increases in size. As the wave normal angle is small and due to the presence of dimple, the ray starts to bend inward toward the satellite and forms an echo. Calvert (1995) has pointed out that for strong ducts and large wave normal angles, the adjoining regions of trough ducting also extend into the region of crest ducting across the curvature reversal, that is, trough ducting occurs in region Z_2. Such ducting occurs at oblique wave normal angles as a result of off-axis maxima of the longitudinal refractive index. However, the aforementioned echoes for wave frequency close to f_{pe} are partially ducted and occur at small wave normal angles due to the peculiar variation of the refractive index surface for small wave normal angles (dimple or nipple).

4.4 Effect of Duct Half-Width and Density Perturbation on Ducted Echoes

Ducted echoes are characterized by: (1) average time delay (t_g); (2) time delay spread (Δt_g); (3) time integral relationship of higher order ducted traces with the principal traces (C and D); (4) lower cutoff (f_{lc}) and upper cutoff (f_{uc}) frequencies of ducted traces; and (5) a frequency gap in the C trace. The ducted echoes of the 10 July 2001 case were observed when the satellite was within a duct. However, the duct parameters are unknown, so, to determine the range of duct parameters, ducted echoes are calculated through ray tracing simulations and the variation of Δt_g and f_{uc} with duct half-width ΔL and density perturbation $\Delta N/N$ is studied. Ray tracing calculations have been performed for the average density model obtained for the 10 July 2001 case. To be consistent with the observations, the plasma condition at the satellite, the reference electron density ($N_{e,ref}$), has been kept constant. This ensures that the lower cutoff (f_{lc}) frequency of the ducted traces are the same as that of the observations. Therefore, when a duct is introduced the $N_{e,ref}$ is same whereas the N_e in the background medium is changed accordingly. This approach is more appropriate because the ducted waves propagate along the geomagnetic field line and therefore can sense the electron density along the field line. The ΔL and $\Delta N/N$ are then varied over a range of values and the ray tracings are performed at each frequency for each trace to obtain the ducted echoes. The t_g-f dispersion thus obtained is compared with the observations and the range of ΔL and $\Delta N/N$ are found. This gives the range of final duct parameters that can explain the observations.

The problem of the variation of the Δt_g and f_{uc} with the duct parameters ΔL and $\Delta N/N$ can be studied using another approach, the direct problem approach. In this approach the background electron density of the magnetosphere is kept constant and the electron density at the satellite location is changed for every duct introduced in the model. This is a totally different approach than that mentioned in previous paragraph. According to direct problem approach, when the electron density at the reference point ($N_{e,ref}$) is changed then the density profile along the geomagnetic field line is changed. Reducing the electron density at the reference point will change the Z mode cavity parameters such as (i) the upper frequency limit of the ZM cavity ($f_{D,max}$) will decrease, (ii) the cavity length at any given frequency will increase, and(iii) the lower and upper cutoff frequency of the traces will decrease. The average time delay of the ducted traces depend upon the length of the Z mode cavity, therefore, with decreasing $N_{e,ref}$ the Z mode cavity length will increase and the time delays will increase. This can be understood from the Figures 3.6 and 3.7. The red curve in the figure is the plot of Z mode cutoff frequency (f_z) with altitude along the geomagnetic field line. The

horizontal black line represent the satellite altitude. As can be seen from the figure that f_z forms a cavity such that when the satellite is within this cavity, then the rays that are injected upwards as well as downwards will propagate and reflect back from region where transmitted frequency, f, is equal to the Z mode cutoff frequency ($f \sim f_z$). The path length which a ray travels determines the total time taken for the ray to travel from satellite to its reflection point and back (called as time delay). The reference point is the point at which the horizontal line cuts the f_z curve at which point $f_z = f_{z,sat}$ and corresponding electron density is equal to reference electron density($N_{e,ref}$). Now if $N_{e,ref}$ is decreased, then the whole f_z profile will shift towards left, which means that at any given frequency, the path length will increase and therefore average time delays will increase.

The lower cutoff frequency (f_{lc}) of the ducted traces depends upon the Z mode cutoff frequency at the satellite, $f_{z,sat}$. At a frequency equal to the Z mode cutoff frequency, the refractive index of the wave goes to zero, therefore, a ray with frequency less than the Z mode cutoff frequency would not propagate at all. So, changing the reference electron density every time a duct is introduced changes the $f_{z,sat}$ and this in turn will change the f_{lc} of all the traces. The upper cutoff of D and higher traces depends upon the f_z at the equator ($f_{z,equ}$) along the geomagnetic field line of the satellite, therefore, by decreasing the $N_{e,ref}$, the $f_{z,equ}$ will decrease and this will decrease the upper cutoff frequency f_{uc} of the ducted traces.

Therefore, with the direct problem approach the characteristics of the ducted echoes viz., lower and upper cutoff frequencies of the ducted traces, time delay spread and average time delays will change for each duct parameter. Thus, the results obtained from completely different density models could not be compared. The direct problem approach is a separate problem altogether and has not been presented in this thesis as it is beyond the scope of this work. In the current approach, to study the effect of duct width and density perturbation on the characteristics of the ducted echoes, the density model is kept constant and duct width and density perturbation are varied so that the results obtained for a range of duct parameters can be compared to obtain an inference about the effects of duct parameters on the ducted echoes. Next subsections discusses the effect of duct parameters ΔL and $\Delta N/N$ on time delay spread Δt_g and upper cutoff frequency f_{uc}.

4.4.1 Effect of ΔL and $\Delta N/N$ on Time Delay Spread (Δt_g)

In this section the variation of Δt_g with ΔL and $\Delta N/N$ is discussed. The time delay spread has been calculated for one frequency at 392 kHz for all the ducted traces. Figure 4.31 shows the

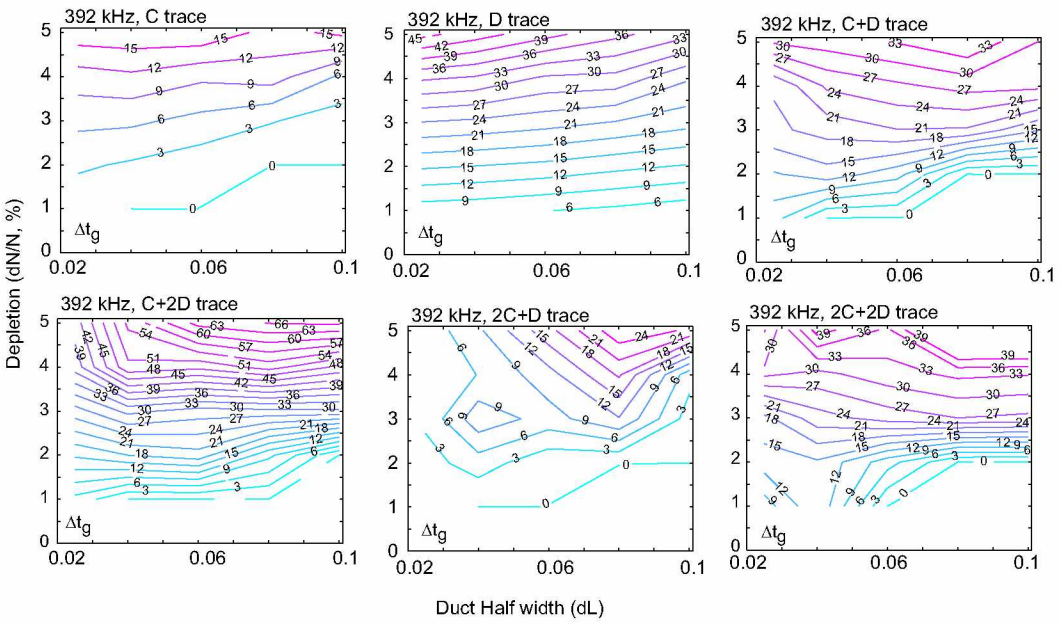

Figure 4.31 Contour plot of time delay spread of ducted traces for varying duct half-width (ΔL) and density depletions (ΔN/N) .

contour plots of the time delay spread (Δt_g) of ducted traces varying with duct half-width and density depletions. Density depletion varies from 1% to 5% and duct half-width varies from 0.025L to 0.1L (~53 to ~210 km at satellite altitude, see Table A.15). The duct half-width varies along the x-axis and density depletion varies along the y-axis. From the figure it can be noted that:

1. At constant ΔL, Δt_g increases with increasing depletion for most of the traces.

2. At constant depletion, Δt_g for C and D traces decreases slightly with increasing ΔL. For example, at 4% depletion, the time delay spread of the C trace decreases from ~12 ms at $\Delta L = 0.025$ to ~9 ms at $\Delta L = 0.1$. For D trace, Δt_g changes from ~33 ms at $\Delta L = 0.025$ to ~27 ms at $\Delta L = 0.1$.

3. For the higher traces ($C + D$, $C + 2D$, $2C + D$, and $2C + 2D$) the Δt_g decreases slightly with increasing ΔL at lower depletion levels e.g., 1% to 2%. At higher depletion levels, the Δt_g increases with increasing ΔL.

4.4.2 Effect of ΔL and ΔN/N on Upper Cutoff Frequency(f_{uc})

This section discusses the variation of f_{uc} with ΔL and ΔN/N. Figure 4.32 shows contour plots of the upper cutoff frequency of ducted traces with varying duct half-width and density depletions.

ΔN/N is varied from 1% to 5% and ΔL is varied from 0.025L (~53 km) to 0.1L (~210 km). The ΔL varies along the x-axis and ΔN/N varies along y-axis. From the figure it can be noted that:

1. At constant ΔL, f_{uc} increases with increasing depletion for almost all the traces.
2. At constant depletion, f_{uc} decreases with increasing ΔL for almost all the traces.
3. For D and higher traces ($C + D$, $C + 2D$, $2C + D$, and $2C + 2D$), the upper limit of the frequency cutoff is 440 kHz. This frequency is close to the electron plasma frequency at the equator, $f_{pe,equ}$ ~442 kHz. This is in accordance with Calvert (1995), who states that, for ZM waves, ducting is weakest at $f \sim f_{pe}$.

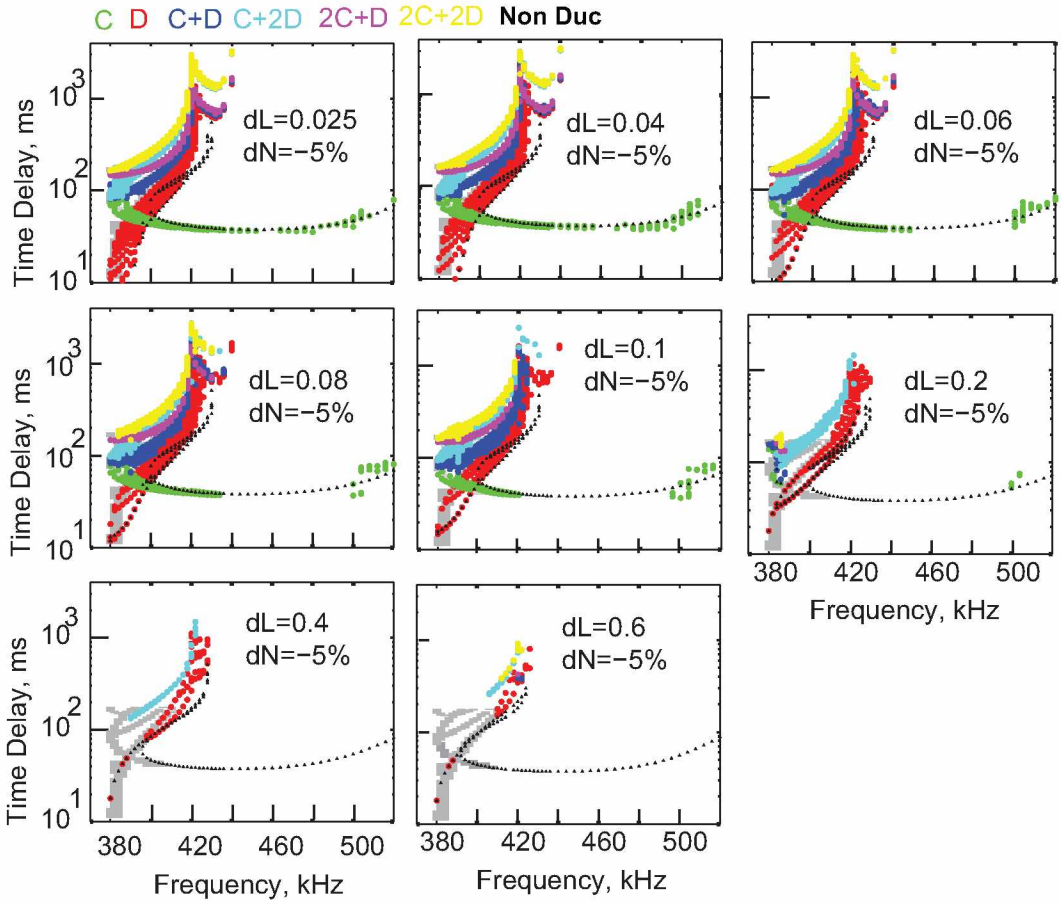

Figure 4.34 Plot of time delay vs frequency for varying duct half-width at constant depletions (ΔN/N) of 5%. The black dots represents the nonducted echoes. The ducted echoes are color coded as shown on the top of the figure.

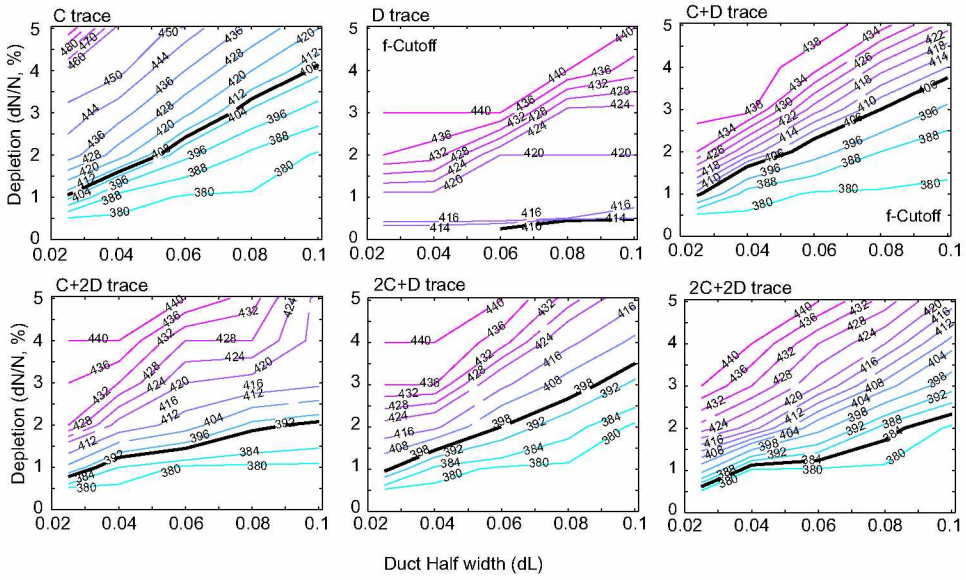

Figure 4.32 Contour plot of upper cutoff frequency(f_{uc}) of ducted traces for varying ΔL and ΔN/N.

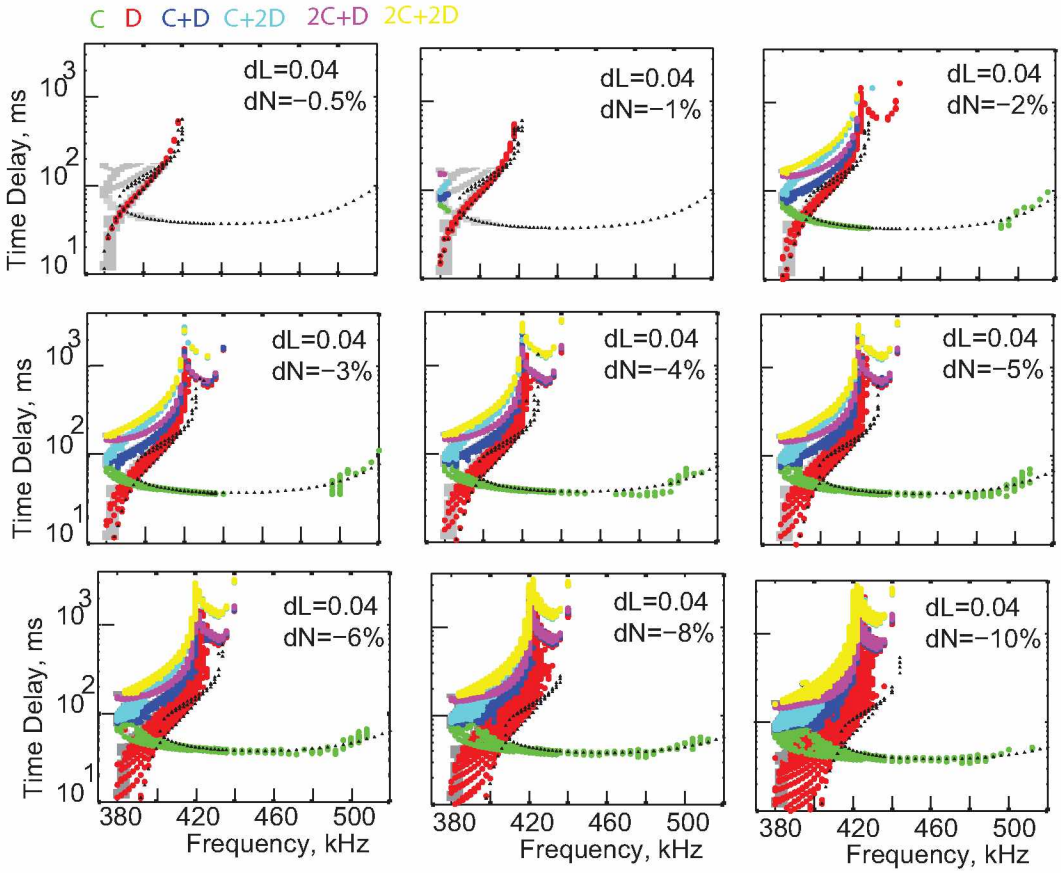

Figure 4.33 Plot of time delay vs frequency for varying depletions (ΔN/N) at ΔL = 0.04 (∼84 km at R_{sat}). The black dots represents the nonducted echoes. The ducted echoes are color coded as shown on the top of the figure.

4.4.3 Effect of ΔL and ΔN/N on Time Delay-Frequency(t_g-f) Dispersion

Figure 4.33 shows the t_g-f plot at a constant ΔL of 0.04 L ($\sim$84 km) and depletion varying from 0.5% to 5%. t_g is plotted on the y-axis on a logarithmic scale and frequency is plotted on the x-axis. It can be observed that:

1. Non ducted echoes are obtained even in the presence of ducts.
2. At a small depletion of 0.5%, only ducted D trace echoes are obtained. C trace and other higher traces ($C + D$, $C + 2D$, $2C + D$, and $2C + 2D$) are not obtained.
3. As the density depletion increases to 1%, C and other higher trace ducted echoes start to appear at lower frequency ranges.
4. The f_{uc} of all the traces increases with increasing depletion.
5. The Δt_g of all the traces increases with increasing depletion.
6. For larger depletions 2%-5%, a frequency gap in the C trace is observed. C trace echoes are obtained for two frequency ranges separated by a frequency gap. Only nonducted echoes are obtained in this frequency range. The second frequency range, for which C trace echoes are obtained, lies close to the f_{pe} at the satellite ($f_{pe,sat}$ $\sim$507 kHz). See Table A.16.
7. The first upper cutoff frequency (f_{uc1}) of the C trace increases with increasing depletions. For frequencies $f > f_{uc1}$, the rays can no longer be guided and thus escape the duct.
8. The second lower cutoff frequency (f_{lc2}) of the C trace decreases with increasing depletion for ducts ΔL =0.025, 0.04 (Table A.16). For relatively wider ducts, e.g., $\Delta L = 0.06 - 0.1$, it is observed that the f_{lc2} increases slightly with increasing depletion.
9. The second upper cutoff frequency (f_{uc2}) increases with increasing depletion.

Thus, it is observed that the upper cutoff frequency of C trace terminates at frequencies $f \ll f_{pe}$. The waves are not ducted for a range of frequencies $f_{uc1} < f < f_{lc2}$. At higher frequencies $f \geq f_{lc2}$, echoes are obtained. These echoes are partly ducted and partly non ducted. As the depletion level is increased, the frequency gap disappears and ducted echoes are obtained at all frequencies between the lower and upper cutoffs.

Figure 4.34 shows t_g versus f at a constant depletion ($\Delta N/N$) of 5% and ΔL varying from 0.025 L (~53 km) to 0.6 L (~1263 km). Time delays are plotted on y-axis on a logarithmic scale and frequency is plotted on the x-axis. It can be observed that:

1. Non ducted echoes are obtained even in the presence of ducts.
2. At a small ΔL of 0.025 L, ducted echoes of all traces are observed.
3. For narrower ducts (0.025-0.1 L), as the duct half-width is increased, the f_{uc} decreases with increasing ΔL.
4. For wider ducts (ΔL ~0.2-0.6), only ducted D trace echoes are obtained. The C trace and other higher trace ducted echoes are not obtained. Besides D trace echoes, only refracted echoes are obtained. The refracted echoes are obtained due to refractive effects in the presence of large density gradients in the magnetosphere. For example, for a duct half width of 0.2, the 'cyan' colored echoes are refracted echoes.
5. For refracted echoes, the lower cutoff frequency increases and the upper cutoff frequency decreases with increasing ΔL.
6. For narrower ducts (ΔL ~0.025-0.1), the frequency gap in the C trace increases with increasing ΔL.

4.5 Formulation of ZM Sounding of Field Aligned Electron Density, Duct Parameters and ZM Cavity

This section discusses the method used to find the average density model, duct parameters, and ZM cavity parameters that can explain the observations. An initial guess of the density model is obtained from ZM inversion and density model optimization. Stanford 2D ray tracing code has been used for the analysis. The ray tracing code uses a diffusive equilibrium density model to represent electron and ion densities inside the plasmasphere. An r^{-n} density variation outside the plasmasphere is assumed with the fall factor $n = 4.5$ in order to obtain a collisionless model at middle invariant latitudes [Angerami and Thomas, 1964; Sonwalkar et al., 2011b]. A dipole magnetic field model is chosen to represent the Earth's magnetic field. Dipole field parameters are chosen such that f_{ce} calculated from the model value at the satellite is equal to that obtained from

the IGRF-2005 or experimentally measured values. The ray tracing program uses a density model such that the reference point (r, λ_m) of the reference electron density ($N_{e,ref}$) can be fixed anywhere in the magnetosphere. The program then calculates the N_e at the base of the density model (N_b) and adjusts the density model such that $N_{e,ref}$ remains the same. For the 10 July 2001 case, the $f_{pe,sat}$ has been calculated from f_z and $f_{ce,IGRF}$ at the satellite location, taking into consideration the motion of the satellite in orbit. The N_e thus obtained is used as the reference N_e and the reference point is fixed at the satellite location ([R_{sat}, $\lambda_{m,sat}$]) in the density model.

Density models should be consistent with constraints on local ZM cutoff frequency, $f_{z,local}$, ZM cutoff frequency at the equator, $f_{z,equ}$, the altitude of minimum in the f_z profile $R_{f_{z,min}}$ and t_g-f dispersion of the traces observed. The density model must satisfy the following constraints:

$$f_{z,local} \simeq f_{z,sat} \tag{4.2}$$

$$f_{z,equ} > f_{D,max} \tag{4.3}$$

$$R_{f_{z,min}} < R_{sat} \tag{4.4}$$

$$\int_C ds/V_g(f,\theta,\mathbf{B},N_e) = t_g(f/C) \tag{4.5}$$

$$\int_D ds/V_g(f,\theta,\mathbf{B},N_e) = t_g(f/D) \tag{4.6}$$

where s denotes the distance along the ray path, V_g is the group velocity along the ray path, t_g(f/C) and t_g(f/D) are the measured time delays of the C and D echoes, respectively, $f_{z,sat}$ is the ZM cutoff frequency measured at the satellite, and $f_{D,max}$ is the maximum observed frequency of the D trace. If, with the initial density model, the constraints are not met, then the density model parameters r_b, T, and ion composition (α) are modified so that constraints 4.2-4.6 are satisfied.

As a first step, ray tracing calculations are performed using a density model obtained from the ZM inversion and density model optimization. The parameters of the initial density model (Model 1) are listed in Tables 4.7 and 4.8. Figure 4.35(a)-(b) shows the plot of N_e and characteristic frequency along the geomagnetic field line. It is observed that a ZM cavity is formed by the f_z profile such that $R_{f_{z,min}}$ lies below the satellite altitude. Figure 4.35(c) compares the calculated t_g of the C and D traces, from the initial density model (model 1 in Table 4.7), with the observations. The model values compare well with the observations except at higher frequencies at which the

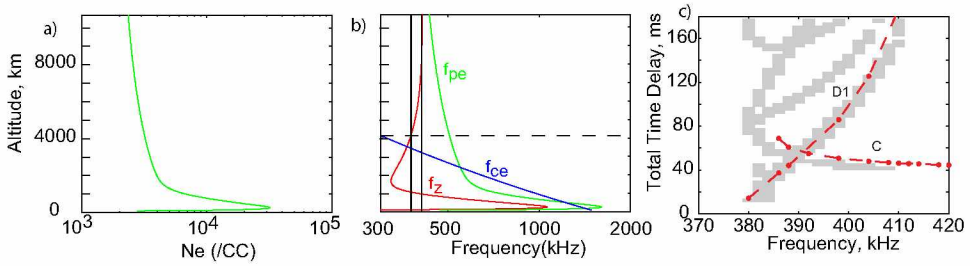

Figure 4.35 Initial density model obtained from ZM inversion and optimization method. (a) N_e , and (b) characteristic frequencies f_{pe}, f_{ce}, and f_z along geomagnetic field line for the initial density model. (c) Comparison of the ray tracing calculated time delays of C and D1 nonducted traces with the observations for initial density model.

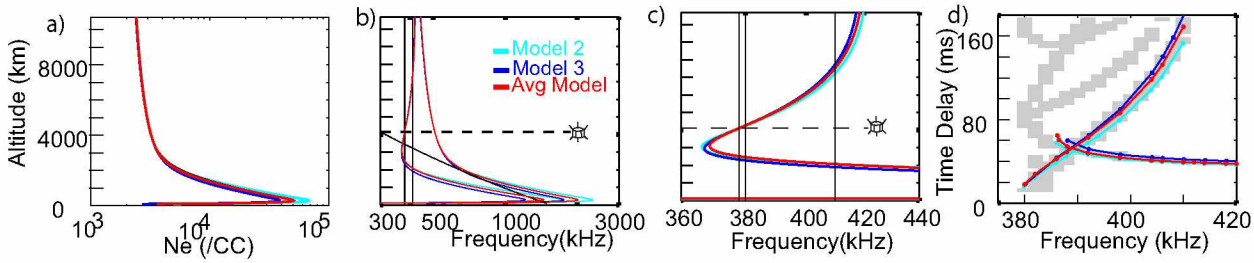

Figure 4.36 Plot of the average density model and two extreme density models (model 2 and 3). (a) N_e, and (b) characteristic frequencies f_{pe}, f_{ce}, f_z along geomagnetic field line. (c) Close-up plot of the ZM cutoff frequency, f_z. (d) Comparison of the calculated time delays of C and D traces for three density models with the observations.

time delays of D1 trace are overestimated. The initial density model is then modified to obtain an average density model which matches the observed average t_g of the C and D traces.

For finding the average density model, two extreme density models are found such that the calculated time delays of the C and D traces match the minimum and maximum t_g of the observed C and D traces. An average density is then found from these two extreme density models such that: (1) $f_{z,equ}$ of the average density model lies between the $f_{z,equ}$ of the extreme density models and (2) the calculated time delays of the C and D traces fit the average measured time delays. Figure 4.36(a) shows the N_e of the two extreme density models (models 2 and 3) and the average density model (model 4). Figure 4.36(b) shows the characteristic frequencies f_z, f_{pe}, and f_{ce} for the three models, and Figure 4.36(c) shows a close-up view of the f_z profile. Table 4.7 lists the input parameters for these models and Table 4.8 lists the model parameters along the field line. The density models have been plotted along the L-shell of L =2.677, at which the f = $f_{z,sat}$(380 kHz) was transmitted. It is evident from the figure that the average model lies between the two extreme density models. The reflection altitude of the fast ZM waves for the average density model lies in the altitude range of ~2000-7,000 km. Figure 4.36(d) shows the time delay plot of models 2 and

3 and the average model. Model 2 matches the lower t_g of the C and D traces, model 3 matches the upper t_g of the C and D traces, and the average model matches the average t_g of the C and D traces.

Table 4.7 Average density model input parameters for 10 July 2001. The parameters are r_b in geocentric distance (km), T is temperature at the base height, [H,He,O] is the ion composition at the base height, and N_e at the reference point.

Model	r_b(km)	T (K)	[H,He,O]	$N_{e,ref}$(e/cc)
1	7171	2889	[0.2279, 0.0243, 0.7478]	3186
2	7370	4000	[0.04,0.0225,0.9375]	3186
3	7370	4600	[0.065,0.0655,0.8695]	3186
4 (Avg)	7490	4400	[0.065,0.049,0.886]	3186

Table 4.8 Important parameters of the density models at key altitudes for 10 July 2001. The parameters are f_z at the satellite $f_{z,sat}$, minimum f_z along the field line $f_{z,min}$, altitude in km of $f_{z,min}$ ($R_{f_{z,min}}$), value of f_z at the equator along the field line ($f_{z,equ}$), value of f_{pe} at the equator along the field line ($f_{pe,equ}$), value of f_{pe} at F2 peak ($f_{pe,F2}$), and altitude of the F2 peak ($R_{f_{pe,F2}}$).

Model	$f_{z,sat}$	$f_{z,min}$	$R_{f_{z,min}}$	$f_{z,equ}$	$f_{pe,equ}$	$f_{pe,F2}$	$R_{f_{pe,F2}}$
1	378.3 km	325.3 kHz	1665 km	412.0 kHz	435.3 kHz	1.61 MHz	260 km
2	378.3 km	366.4 kHz	3040 km	419.7 kHz	443.1 kHz	2.32 MHz	280 km
3	378.3 km	367.2 kHz	2970 km	417.2 kHz	440.5 kHz	1.76 MHz	285 km
4(avg)	378.3 km	368.8 kHz	3110 km	418.5 kHz	441.8 kHz	2.02 MHz	285 km

Ray tracing calculations are performed using the average density model. In the present case, the experimentally measured cutoff f_z =380 kHz has an uncertainty of 2 kHz, the frequency interval of the transmitted program. Thus, the local f_z may lie between ~378-380 kHz. The f_{ce} at the satellite, calculated from the IGRF-2005 model, is ~301 kHz, which gives the range of f_{pe} at the satellite as 506.4 -508.5 kHz. This is equivalent to N_e of ~3181-3208 e/cc. This allows flexibility in setting the value of $N_{e,ref}$ at the reference point in the density model. The N_e chosen at the reference point ~3186 e/cc, lies within this range. The f_{ce} at the equator on the surface of the Earth is taken as ~918 kHz, matched to the $f_{ce,IGRF}$ at the satellite (f_{ce} ~301 kHz) when f =380 kHz frequency was transmitted. The plasmapause (L_{pp}) is taken at L ~5.9, as determined from the dynamic spectrogram. Since the satellite was well inside the plasmasphere when the echoes

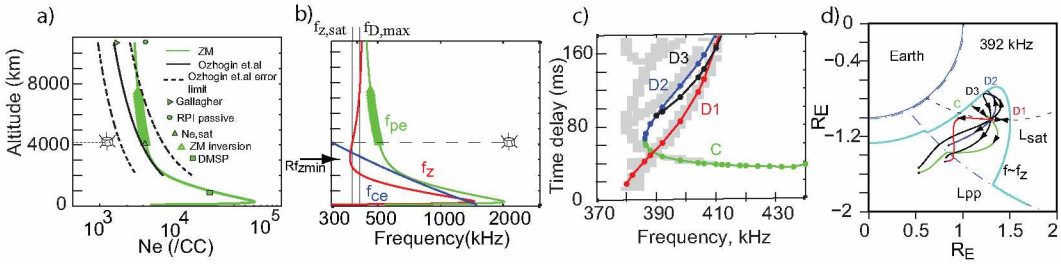

Figure 4.37 (a) Electron (N_e) density along geomagnetic field line for the average density model. Density model is compared with empirical models and in-situ measurements. (b) characteristic frequencies f_{pe}, f_{ce} and f_z along the geomagnetic field line, (c) Comparison plot of the nonducted time delays for C, D1, D2 and D3 echoes with the observations. (d) ray paths of the four nonducted echoes obtained inside the ZM cavity when no duct is present.

were observed, the ray tracing results are not sensitive to the location of L_{pp} and the exponent in the r^{-n} model.

Table 4.9 Comparison of average density model with in-situ data for 10 July 2001. The parameters are UT, altitude in km, L-shell(L), Magnetic local time (MLT), geomagnetic latitude (λ_m), N_e measured in-situ, N_e from the density model, percentage difference.

Measurement	UT	Alt (km)	L	MLT	λ_m (°)	N_e (e/cc)	$N_{e,mod}$ (e/cc)	% diff
DMSP-f13	08:03:16	864.9	2.6844	19.09	-49.4	16300.5	19980	20.3%
RPI DS	08:38:36	10829	2.6979	17.4	2.36	2889-3008	2422	17.6 - 21.6%

Figure 4.37(a) shows the field aligned N_e profile along L =2.677, obtained from the average density model, and its comparison with N_e, obtained from in-situ measurements and empirical density models. Tables 4.9 - 4.10 compare the N_e obtained from ZM sounding with in-situ measurements and empirical density models. The Ozhogin et al., (2012) model underestimates N_e obtained from average density model at 2000 km by ~10%, at the satellite altitude of 4138 km by ~11%, and at the equator by ~51%. Gallagher et al., (2000) model underestimates N_e obtained from the average density model by ~45%. The N_e measurements from passive recording (dynamic spectra) on the IMAGE satellite made along the L shell L ~2.70 near the equator at λ_m ~2.36° and ~10,829 km are also shown. The average density model differs by ~18%-22% from the passive measurement. It is important to note the N_e obtained from ZM sounding at the equator is in better agreement with the in-situ N_e from RPI compared to the empirical density models. N_e measured from the DMSP f-13 satellite agrees within ~20% with the average density model, and N_e obtained from the ZM inversion of the D trace (between ~4000-8000 km altitude) matches within ~1%.

Table 4.10 Comparison of average density model with empirical density models for 10 July 2001. The parameters are altitude in km, N_e obtained from empirical model, N_e from the density model, percentage difference.

Empirical Model	Alt (km)	N_e (e/cc)	$N_{e,model}$ (e/cc)	% diff
G2000	10680 km (Equ)	1531	2422	45.1 %
Oz2012	10680 km (Equ)	1434	2422	51.2 %
Oz2012	4138 km	2858	3184	10.8 %
Oz2012	2000 km	4995	5534	10.2 %

Figure 4.37(b) plots f_z, f_{pe}, and f_{ce} along the geomagnetic field line for the average density model. A dashed horizontal line represents the satellite altitude (4138 km). The minimum in altitude of f_z ($R_{f_{z,min}}$) occurs at an altitude lower than the satellite altitude. This condition is necessary to obtain CD type fast ZM echoes. A ZM cavity is obtained for a narrow frequency range of 380 kHz-419 kHz. Thus, the bandwidth of the ZM cavity is ~39 kHz. The altitude of the cavity ranges from ~2010-10,680 km, which gives a cavity length of ~8670 km.

Figure 4.37(c) compares the t_g-f dispersion of fast ZM echoes calculated from ray tracing with the observations. The time delays have been calculated without assuming a duct in the model. The corresponding ray paths of these traces are shown in Figure 4.37(d) for 392 kHz. In the absence of ducts, four nonducted echoes (C, D1, D2, and D3) are obtained when the satellite is within the ZM cavity. The t_g of the C and D1 fast ZM echoes matches the average observed time delays.

To simulate the ducted echoes, density depleted ducts are introduced in the average density model. The ducts are centered at L = 2.674 (L-shell lie at at the center of the L-hells of 380 kHz and 410 kHz frequencies). Duct half-widths were varied from $\Delta L = 0.025 - 0.10L$ and density depletions were varied from $\Delta N/N = 1\% - 5\%$. The time delays for each trace and frequency were calculated for a range of duct parameters. Figures 4.38 and 4.39 compare the observed time delays of the ducted echoes. Besides the ducted echoes, nonducted echoes were also obtained (shown as black triangles).

The important characteristics of the ducted echoes are: (1) average time delay (t_g); (2) time delay spread (Δt_g); (3) time integral relationship of higher order ducted traces with that of principal traces; (4) lower cutoff (f_{lc}) and upper cutoff (f_{uc}) frequencies; and (5) frequency gap in C trace echoes. The average time delay is determined from the average density model. The time delay

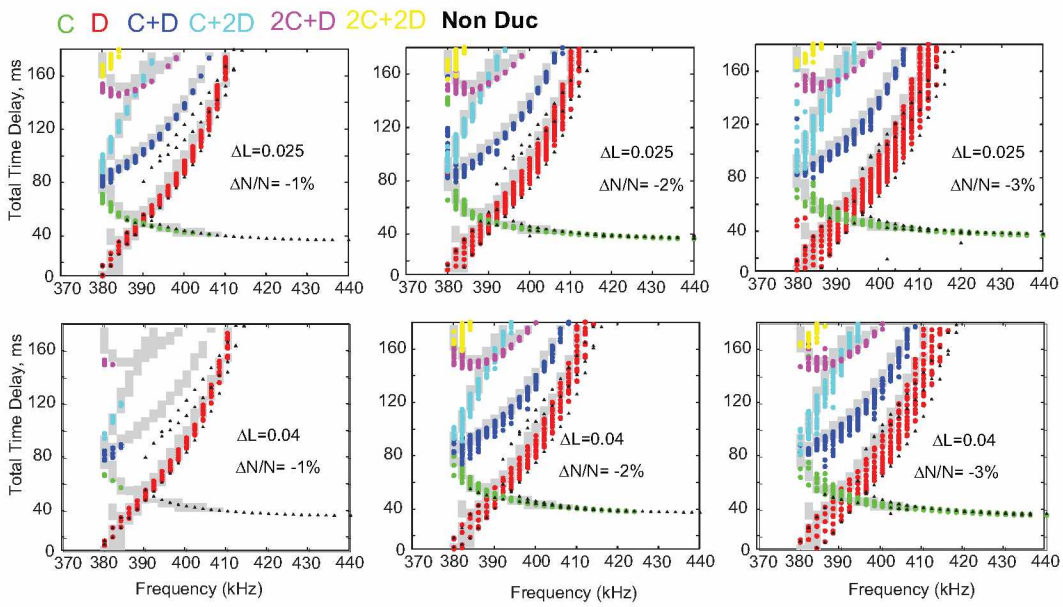

Figure 4.38 Time delays versus frequency plot for the final duct parameters that explains the observations part-1.

spread and cutoffs depend upon the duct parameters of half-width and density depletion. So, for the 10 July 2001 case, the criteria of choosing the final duct model are:

1. The duct model should give upper cutoff at least up to the observed upper cutoff.
2. The duct model should at least match the time delay spread with the observations.

Table 4.11 Duct parameters from contour plots of time delay spread (Δt_g) versus (ΔL, $\Delta N/N$).

Trace	ΔL=0.025	ΔL=0.04	ΔL=0.06	ΔL=0.08	ΔL=0.10
C	~1.5-2%	~2%	~2-2.5%	~2.5-3%	~3%
D	~1.5%	~1.5-2%	~1.5-2%	~1.5-2%	~1.5-2%
C+D	~1.5%	~1.5%	~2%	~2-2.5%	~2-2.5%
C+2D	~2.5%	~2-2.5%	~2-2.5%	~2.5%	~2.5%
2C+D	NA	NA	NA	NA	NA

The final duct parameter is a subset of duct parameters that satisfies both the criteria mentioned above. Tables Ḟor the 10 July 2001 case, the observed cutoffs of all the traces except the C trace have experimental limits. The C trace has an upper cutoff of 408 kHz due to the propagation characteristics of the ducted waves, not due to experimental limitations. Thus, in determining the

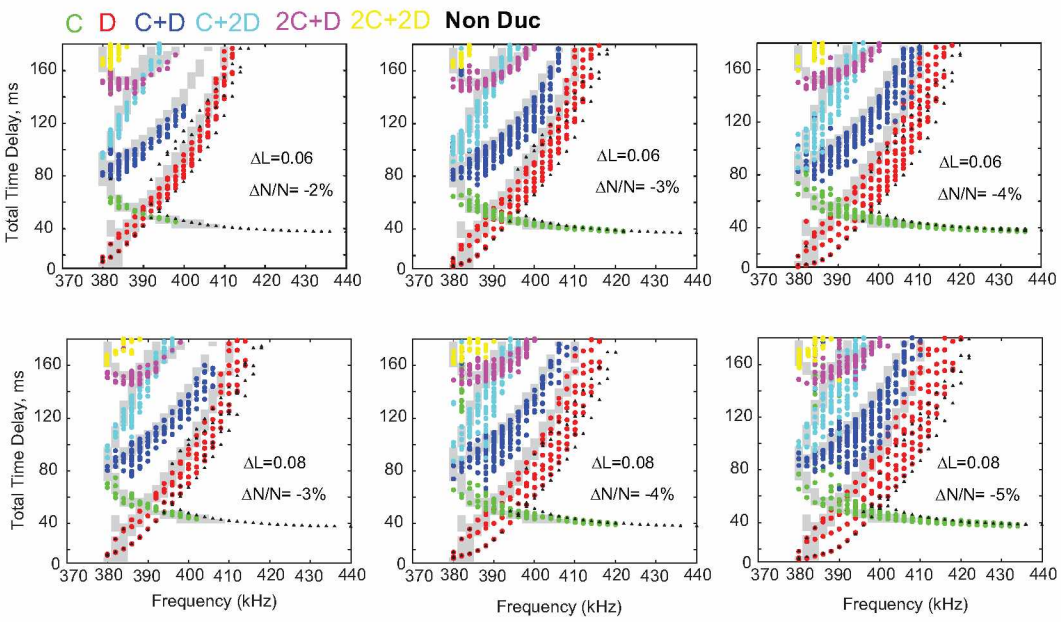

Figure 4.39 Time delays versus frequency plot for the final duct parameters that explains the observations part-2.

Table 4.12 Duct parameters from contour plots of upper cutoff frequency (f_{uc}) versus (ΔL, $\Delta N/N$).

Trace	ΔL=0.025	ΔL=0.04	ΔL=0.06	ΔL=0.08	ΔL=0.10
C	~1%	~1.5%	~2%	~3-3.5%	~3.5-4%

final duct parameters, the upper cutoff frequency of the C trace is considered. From the contour plots of time delay spread and upper cutoff frequency versus duct half-width and density depletion, the combination of duct parameters obtained are given in Tables 4.11-4.12. Table 4.13 lists the final duct parameters that could explain the observations.

4.6 Summary of Results: 10 July 2001 Case analysis

The results of the case study can be summarized as follows:

1. A density depleted duct is required to guide ZM waves.

2. A density depleted duct of half width ranging between ~160 km and 500 km in the equatorial plane and depletions of ~1% - 4% covering an altitude range of 2000-8000 km could explain the observed ducted echoes on 10 July 2001.

Table 4.13 Final duct parameters for 10 July 2001 case ducted echoes along L = 2.674. The parameters are duct half-width in L, duct half-width in km at 1000 km altitude, duct half-width in km at satellite altitude, duct half-width in km at equator, and duct depletion level.

ΔL (half-width)	ΔL @1000 km	ΔL at the satellite @4138 km	ΔL at the equator @10,660 km	ΔN/N
0.025	28 km	53 km	159 km	~1% - 2%
0.04	44 km	84 km	255 km	~1.5%-3%
0.06	66 km	126 km	382 km	~2%-3%
0.08	88 km	168 km	510 km	~3%-4%

3. Average time delays (t_g) depend upon the N_e along the geomagnetic field line and the shape of the ZM cavity.

4. The bandwidth of the ZM cavity is ~39 kHz and its length is ~8670 km.

5. The gap in the C trace is due to the propagation effects of ZM waves in the presence of ducts and the occurrence of dimple-shaped refractive index surfaces near f_{pe}. The gap frequency range depends upon the duct parameters and increases with increasing ΔL and decreases with increasing ΔN/N. Calvert (1995) has pointed out that for strong ducts and large wave normal angles, trough ducting occurs in the region above the curvature reversal (halfway between f_z and f_{pe}) up to f_{pe}. However, in the present case, for wave frequency close to f_{pe}, the waves are partially ducted and ducting occurs at small wave normal angles due to the peculiar peculiar variation of the refractive index surface (dimple or nipple) for small wave normal angles about the axis.

6. In the absence of ducts, four nonducted echoes are obtained in the ZM cavity. Three of the echoes (C, D1, and D2) retrace their path after reflection, while one forms a loop (D3).

7. Higher order nonducted traces (D4, D5, D6-1, and D6-2) are obtained for a very narrow range of frequencies close to the $f_{z,equ}$.

8. The C trace exhibits a 'nose' frequency at midway between $f_{z,sat}$ and $f_{pe,sat}$.

9. The lower cutoff of the D1 trace is always lower than the lower cutoffs of the C, D2, D3 and other higher traces (D4, D5, D6-1, and D6-2).

10. The lower cutoffs of the C and D2 traces are equal and the echoes have equal time-delays at this frequency.

11. The lower cutoff of the D3 is greater than that of the C, D1, and D2 traces, but lower than that of the D4, D5, D6-1 and D6-2 higher order traces.

12. The lower cutoffs of all the higher order traces are equal and are greater than those of the C, D1, D2, and D3 traces.

13. The upper cutoff frequency of the nonducted C trace lies in the range $f_{pe} < f < f_{uh}$. The upper cutoff of the C trace is always greater than the upper cutoffs of D1, D2, D3, and higher order traces (D4, D5, D6-1, and D6-2).

14. The upper cutoffs of the D1, D2, D3, D4, and D5 traces are equal to the $\sim f_{z,equ}$.

15. The upper cutoffs of the D6-1 and D6-2 traces are lower than those of all the other traces (C, D1, D2, D3, D4, and D5).

16. Ducted propagation of waves could be understood in terms of the superposition of wave propagation in the transverse (perpendicular to $\mathbf{B_0}$) and longitudinal (parallel to $\mathbf{B_0}$) directions.

17. In the presence of ducts, both nonducted and ducted echoes are obtained, and echoes are formed from both looping and retracing paths.

18. Rays injected at large initial wave normal angles (θ_i) have maximum L-shell excursion from the center of the duct compared to rays injected at small θ_i.

19. Rays injected at smaller θ_i towards the equator reflect from relatively higher altitudes compared to rays injected at larger θ_i.

20. The ducted C trace echoes injected at different θ_i reflect at about the same altitude Earthward of the satellite, and therefore accumulate smaller t_g spread.

21. For ducted D rays, echoes are obtained from the local and conjugate hemispheres when the duct extends to the conjugate hemisphere and $f \geq f_{z,equ}$.

22. For weaker ducts, only D trace echoes are obtained. C and other higher trace echoes are obtained for relatively higher depletions.

23. Keeping $\Delta N/N$ constant, both the upper cutoff frequency and time delay spread decrease with increasing ΔL.

24. Keeping ΔL constant, both the upper cutoff frequency and time delay spread increase with increasing $\Delta N/N$.

25. The electron density measurements from ZM sounding are in good agreement with satellite in-situ measurements and give a better estimate than the empirical density models.

4.7 Discussion

A new method of ZM sounding has been developed in this research to measure the magnetospheric duct parameters, field aligned electron density distribution and Z mode cavity parameters. The detailed study of the nonducted and ducted wave propagation, reflection, and guidance will prove to be fundamental in our understanding of the generation and propagation of natural wave emissions in the magnetosphere. Measurements of the duct parameters, field aligned electron density distribution, and ZM cavities are important to understand the wave-particle interactions and propagation of natural wave emissions, and in improving and building the empirical/theoretical density models to accurately represent the magnetospheric density profiles and density structures.

The study of ZM echoes on the IMAGE satellite is important because the IMAGE satellite was the first magnetospheric radio sounder to inject radio waves into the magnetosphere in all directions [Reinisch et al., 2000]. These waves could propagate in all the four plasma wave modes including the ZM. ZM waves plays an important role in the wave-particle interactions and are important to understand the origins of naturally occurring ZM emissions in the magnetosphere. ZM have also proved to be an important remote sensing diagnostic tool [Horne and Thorne, 1998; Summers et al., 2001; Glauert and Horne, 2005; Benson, 2006; Colpitts et al., 2010; Ye et al., 2010; Xiao et al., 2012]. In the past, free space mode sounding on the RPI has been used to remotely sense the field aligned electron density distribution [Reinisch et al., 2001, 2004; Fung et al., 2003; Fung and Green, 2005; Tu et al., 2006; Benson, 2010; Ozhogin et al., 2012]. In the free space mode sounding on the RPI, which is effective to a minimum altitude of $\sim$2000 km, the echoes reflect from region where the electron density is greater than the electron density at the satellite. This implies that if the satellite is at higher latitude, the region from the satellite to the equator could not be sensed. The equatorial electron density can only be obtained when the RPI is present in the equatorial region at

the time of sounding, or, the electron densities in the equatorial region can be interpolated from the known total electron content in that region. The total electron content can be known from the time delay of the conjugate lowest frequency echo. This may introduce a possible uncertainty in the field line dependence in the equatorial region [Tu et al., 2006]. ZM sounding on the RPI complements the free space mode sounding. Carpenter et al., (2003) have provided a ZM inversion method to measure the field aligned electron density distribution only above the satellite altitude. The ZM sounding method developed in this work provides the field aligned electron density distribution both below and above the satellite altitude. With the aid of the case study of 10 July 2001, we have demonstrated that the ZM echoes can be used to remotely sense the field aligned electron density distribution in the altitude range extending from ~1000 km altitude (and from ~90 km altitude if accompanied by Whistler mode echoes) in the denser region below the satellite up to the relatively tenuous equatorial region above the satellite and also from the conjugate hemisphere if the duct extends there and the format of the recording program is appropriate to record the large time delays of the echoes reflecting from the conjugate hemisphere. For the case study of 10 July 2001, the propagation, reflection, and guidance of the fast ZM waves in the magnetosphere have been studied with the aid of refractive index surfaces, Poeverlein's construction and Snell's Law. We have found several new phenomena which are important for the understanding of the wave propagation in the magnetosphere. The Ray tracing analysis shows that in the absence of ducts, four nonducted echoes are obtained. This result is new and important in the sense that it helped us identify the nonducted echoes in our database which have the potential to be used as a diagnostic tool for measuring the field aligned electron density distribution within the ZM cavity in the magnetosphere. In this study it is found that the two principal nonducted echoes, C and D1, propagate close to the field line and therefore can sense the field aligned electron density distribution. Another important phenomenon that was discovered and corroborated with ray tracing analysis is the phenomenon of frequency gap in echo trace reflecting from below the satellite altitude (C trace). The gap in the C trace is due to the propagation effect of ZM waves in the presence of ducts and the occurrence of dimple-shaped refractive index surfaces near the characteristic plasma frequency f_{pe}. The range of the frequency gap depends upon the duct parameters ΔL and $\Delta N/N$. It has been confirmed from ray tracings that the frequency gap could occur only in the presence of a duct and is a direct consequence of the propagation effects of fast ZM waves in the presence of ducts. This phenomenon is important as it is a direct manifestation of the presence of ducts in the magnetosphere and is important to study the dispersion relations and wave properties in the vicinity of the characteristic plasma frequency

(f_{pe}). Another interesting result of the ray tracings are the echoes that are obtained from within the ZM cavity in the local hemisphere as well as from the conjugate hemisphere when the duct extends there. This type of echo has been observed and recorded on the IMAGE/RPI plasmagrams in the low altitude region and lower L-shells. This important results can be used to design the future magnetospheric sounders such that the ZM echoes can be used to remotely sense the field aligned electron density distribution in the altitude range extending from ~1000 km below the satellite altitude up the equator in the local as well as the conjugate hemisphere.

This research provides a first direct measurement of magnetospheric ducts observed inside the ZM cavities in the magnetosphere and also the first quantitative measurement of the ZM cavities in the low to mid-latitude region of the magnetosphere in the altitude range of ~1000-10,000 km. The magnetospheric ducts are important to study because they play an important role in the generation and propagation of natural wave emissions, and wave-particle interactions and therefore influence the radiation belt dynamics [Calvert, 1982; James, 1991, 2000, 2006; Sonwalkar, 2006; Bell et al., 2009; Haque et al., 2011]. Radiation belt particles can adversely affect the spacecraft electronics and endanger human life in space. Therefore, modeling the radiation belt is an important part of the space-weather program. Duct sounding has been used successfully for measuring the field aligned electron density distribution [Reinisch et al., 2001, 2004; Fung et al., 2003; Fung and Green, 2005; Tu et al., 2006; Benson, 2010; Ozhogin et al., 2012]. In this case study, instantaneous measurement of field aligned electron density distribution have been made from the ducted fast ZM echoes. Instantaneous measurement of electron density distribution is important in the development of empirical models which provides a benchmark for testing the theoretical and numerical models of the magnetospheric density distribution and to study the wave-particle interactions, wave propagation, plasma loss and refilling processes and space weather forecast. These models are necessary for optimum performance of communication and navigational satellite systems [Kozyra et al., 1997; Reinisch et al., 2001; Horne, 2002; Reinisch et al., 2004; Tu et al., 2006; Gulyaeva and Gallagher, 2007; Smith and Gallagher 2008; Gerzen et al., 2015]. The data set of Z mode sounding obtained from the IMAGE satellite mission provides an unique opportunity to measure the instantaneous electron density measurements in low to mid-latitude region of the magnetosphere in the altitude range of ~1000-10,000 km.

Chapter 5 Measurement of Field Aligned Electron Density, Ducts, and Z Mode Cavity Parameters from Z Mode Sounding

This chapter discusses the Z mode (ZM) sounding method applied to ducted AB type echoes, non-ducted (AB, CD) echoes observed inside the ZM cavity, and seven successive cases of nonducted and ducted fast ZM echoes observed during plasmapause crossing of the IMAGE satellite, to measure field aligned electron density (N_e) distribution, ducts, and ZM cavity parameters.

5.1 Case II: 26 July 2001 08:23:47 UT Ducted AB Type Fast Z Mode Echoes

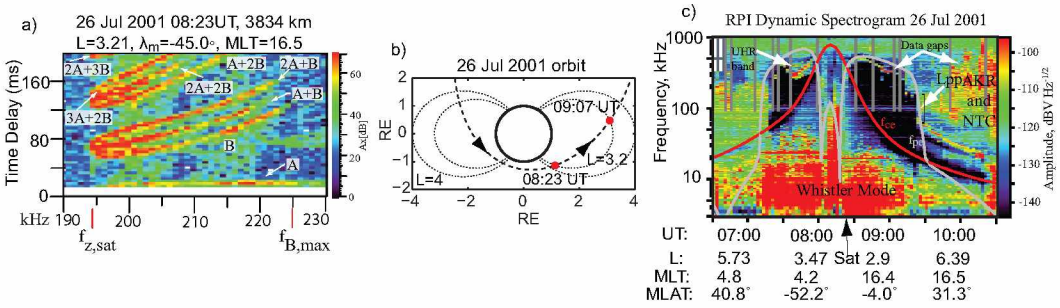

Figure 5.1 (a) Plasmagram showing discrete traces of AB type ducted fast ZM echoes observed on 26 July 2001. (b) IMAGE orbit plot for 26 July 2001. The position of the satellite at 08:2347 UT is shown by the red dot. (c) Dynamic spectrogram observed by IMAGE on 26 July 2001.

Figure 5.1(a) shows plasmagrams of AB type ducted fast ZM echoes received by the X antenna on IMAGE on 26 July 2001 at 08:23:47 UT at an altitude of 3834 km, $\lambda_m = -45.0°$, MLT=16.5, and L=3.21. The Z-mode cutoff frequency at the satellite, $f_{z,sat}$, is 194.4 kHz and the highest ducted frequency, $f_{B,max}$, is 225 kHz. These echoes were observed when the satellite was below the altitude of minimum in the f_z, $R_{f_{z,min}}$ [Carpenter et al., 2003]. The A trace represents echoes of the 'short' path of propagation below the satellite, while the B trace echoes represent 'long' path of propagation above the satellite. In the plasmagram, traces at different virtual ranges are observed. Figure 5.1 shows 8 echo traces, all beginning at 194.4 kHz and having different virtual

ranges. The A trace starts from the base of the plasmagram at a time delay (t_g) of ~10 ms and lower cutoff $f_{z,sat}$ =194.4 kHz, then rises gradually to ~20 ms at the upper cutoff $f_{A,max}$ =245 kHz. The upper cutoff of the A trace may extend to higher frequencies, but is limited by the program format. Three echo traces start at ~60 ms at lower frequency cutoff f_z =194.4 kHz, namely B, A+B, and 2A+B. Three echo traces, namely A+2B, 2A+2B, and 3A+2B, start from ~120 ms at $f_{z,sat}$ =194.4 kHz. Another trace, 2A+3B, is partially visible at ~178 ms over the frequency range 194.4-199.8 kHz. This trace is limited by the virtual range limit of the sounding program. These traces have a t_g integral relationship among themselves and are formed after one, two, three, three, four, five, and five reflections, respectively, while propagating within the duct between two reflection points inside the ZM cavity. Each of the traces has multiple echoes at each frequency (multipath propagation; 2-4 bins of t_g spread). The t_g integral relationship and multiple echoes at each frequency indicate that these echoes are formed due to ducted propagation inside a field aligned duct. The t_g-f dispersion of the B trace first decreases from ~50 ms at 194.4 kHz to ~46 at 199 kHz and then increases to ~115 ms at the upper cutoff, $f_{B,max}$ =225 kHz. The lower and upper cutoff frequencies of all the traces are listed in Table A.17. Table A.18 lists the t_g spread (Δt_g) at 208.8 kHz. From Figure 5.1(a), it is observed that at 194.4 kHz, the time delays of the B, A+B, and 2A+B traces are indistinguishable from that of A+2B, 2A+2B, and 3A+2B. We observe that for all traces except B, A+B, and 2A+B traces, the upper cutoff frequency is limited by the virtual range limit of the sounding program.

Figure 5.1(b) shows the IMAGE orbit plot for 26 July 2001 with the position of the satellite at 08:23 UT (red dot). The satellite was moving through the southern polar region towards the plasmasphere. The satellite orbit then crossed the L-shell (L ~3.24) close to the L-shell of the satellite L ~3.2 at which the ducted echoes were observed near the equator at λ ~9.4° ~42 minutes later. f_{pe} at this location calculated from the f_{uh} emission band and $f_{ce,IGRF}$ ~30 kHz lies in the range of ~312-318 kHz, which corresponds to N_e of ~1208-1258 e/cc. The f_z near the equator $f_{z,equ}$ lies in the range of ~297-304 kHz. Figure 5.1(c) shows the dynamic spectrogram recorded by IMAGE on 26 July 2001 from 06:30 - 10:30 UT. The position of the satellite is indicated by a black arrow. The plasmapause was observed around 09:20 UT between L =3.93 – 3.97 on the duskside (MLT~16).

An average density model (as discussed in detail in Chapter 4) is found that matches the average t_g of the A and B traces. This density model is used for further ray tracing simulations to find duct parameters. The parameters of the density models are listed in Tables 5.1 and 5.2.

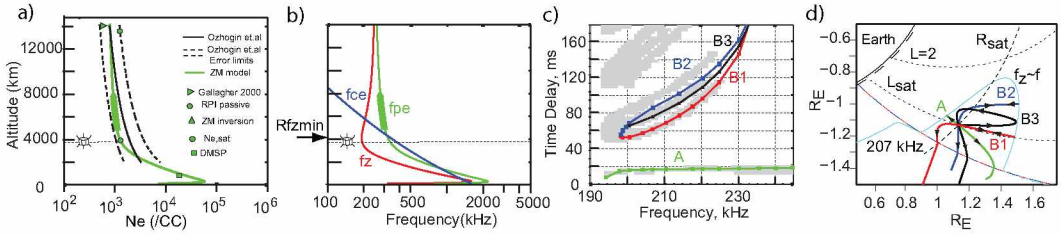

Figure 5.2 (a) Plot of electron density (N_e) along geomagnetic field line from the average density model for 26 July 2001. Density model is compared with empirical models and in-situ measurements. (b) Characteristic frequencies f_{pe}, f_{ce} and f_z along the geomagnetic field line. (c) Comparison plot of the nonducted time delays for A, B1, B2 and B3 echoes with the observations. (d) Ray paths of the four nonducted echoes obtained inside the ZM cavity when no duct is present.

Table 5.1 Average density model input parameters for 26 July 2001. The parameters are r_b in geocentric distance (km), T is temperature at the base height, [H,He,O] is the ion composition at the base height, and N_e at the reference point.

Model	r_b(km)	T(K)	[H,He,O]	$N_{e,ref}$(e/cc)
Avg	7650	4300	[0.012,0.0085,0.9795]	1341

Ray tracing calculations are performed using the average density model. In the present case, the experimentally measured cutoff $f_z = 194.4$ kHz has an uncertainty of 0.9 kHz, where 0.9 kHz is the frequency interval of the transmitted program. Thus, the local f_z lies between ~193.5 -194.4 kHz. The $f_{ce,IGRF}$ at the satellite, ~364 kHz, which gives the range of f_{pe} at the satellite as $328.5 - 329.5$ kHz. This is equivalent to N_e ~1339-1347 e/cc. The N_e chosen at the reference point, ~1341 e/cc, lies within this range. The f_{ce} at the equator is taken as ~945 kHz matched to the $f_{ce,IGRF}$ at the satellite (~364 kHz) when the $f = 194.4$ kHz was transmitted. The plasmapause is taken at $L_{pp} = 4.01$, as determined from the dynamic spectrogram. Since the satellite was well inside the plasmasphere when the echoes were observed, the ray tracing results are not sensitive to the location of the plasmapause L_{pp} and the exponent in the r^{-n} model outside the plasmasphere.

Figure 5.2(a) shows the field aligned N_e profile along L =3.207. Tables 5.3 - 5.4 compare the N_e obtained from ZM sounding with in-situ measurements and empirical density model values. The

Table 5.2 Important parameters of the density models at key altitudes for 26 July 2001. The parameters are f_z at the satellite $f_{z,sat}$, minimum f_z along the field line $f_{z,min}$, altitude in km of $f_{z,min}$ ($R_{f_{z,min}}$), value of f_z at the equator along the field line ($f_{z,equ}$), value of f_{pe} at the equator along the field line ($f_{pe,equ}$), value of f_{pe} at F2 peak ($f_{pe,F2}$), and altitude of the F2 peak ($R_{f_{pe,F2}}$).

Model	$f_{z,sat}$	$f_{z,min}$	$R_{f_{z,min}}$	$f_{z,equ}$	$f_{pe,equ}$	$f_{pe,F2}$	$R_{f_{pe,F2}}$
Avg	193.7	192.8 kHz	4090 km	243.9 kHz	257.8 kHz	2196 kHz	270 km

Table 5.3 Comparison of average density model with in-situ data for 26 July 2001. The parameters are UT, altitude in km, L-shell(L), Magnetic local time (MLT), geomagnetic latitude (λ_m), N_e measured in-situ, N_e from the density model, percentage difference.

Measurement	UT	Alt (km)	L	MLT	λ_m (°)	N_e (e/cc)	$N_{e,mod}$ (e/cc)	% diff
DMSP-f13	09:37	868.5	3.219	18.6	-53.55	19377	21910	12.2%
RPI DS	09:05	13759	3.243	16.4	9.4	1208-1258	828	37%-41%

Table 5.4 Comparison of average density model with empirical density models for 26 July 2001. The parameters are altitude in km, N_e obtained from empirical model, N_e from the density model, percentage difference.

Empirical Model	Alt (km)	N_e (e/cc)	$N_{e,model}$ (e/cc)	% diff
G2000	14060 km(Equ)	584	825	34.1%
Oz2012	14060 km(Equ)	789	825	4.5%
Oz2012	Rsat= 3834	1986	1347	38.3%
Oz2012	2000 km	3278	4460	30.6%

average density model matches with the N_e obtained from Ozhogin et al., (2012) model at 2000 km within ∼31%, at the satellite altitude of 3834 km within ∼5%, and at the equator within ∼38%. The density model matches with Gallagher et al.,(2000) model within ∼34%. Electron density measured from DMSP f-13 matches within ∼12%. The N_e measurement, ∼1208-1258 e/cc, made from passive recording (dynamic spectra) along the L shell L =3.243 near the equator at λ_m ∼9.4° and ∼13759 km, matches within ∼37%-41%. The N_e obtained from the ZM inversion of the B trace, shown in Figure 5.2(a), matches the N_e obtained from the ZM sounding within ∼2%.

Figure 5.2(b) shows f_z, f_{pe}, and f_{ce} along the geomagnetic field line. A dashed horizontal line represents the satellite altitude (3834 km). The minimum in altitude of f_z ($R_{f_{z,min}}$) occurs at an altitude higher than the satellite altitude. This condition is necessary to obtain AB type fast ZM echoes. The f_z profile forms a narrow ZM cavity within which frequencies in the range of ∼194-244 kHz can be trapped. Thus, the bandwidth of the ZM cavity is ∼50 kHz. The altitude of the cavity ranges from ∼2655-14,060 km making it ∼11,400 km long. The altitude of the minimum in f_z cavity lies above the satellite altitude $R_{f_{z,min}} = 4090$ km, as indicated by an arrow. The density model is chosen such that (i) $f_{z,local} = f_{z,sat}$, (ii) $f_{z,Equ} > f_{B,max}$, and (iii) $R_{f_{z,min}} > R_{sat}$.

Figure 5.2(c) compares the nonducted t_g-f dispersion of fast ZM echoes calculated from ray tracing with observed t_g-f values. The time delays have been calculated without any duct present in the model. The corresponding ray paths of these traces are shown in Figure 5.2(d) for 207 kHz. Four nonducted echoes, A, B1, B2, and B3 are obtained. Three of the four echoes (A, B1, and B2) retrace their path after reflection and the other (B3) forms a loop. The t_g of the A and B1 fast ZM echoes matches the average observed time delays. It is clearly observed from Figure 5.2(c) that: (1) the lower cutoff frequency of the A trace is lower than that of all the other traces; (2) the lower cutoff frequencies of the B1 and B2 traces are equal and have the same t_g at the lower cutoff; (3) the lower cutoff of B3 is larger than all the other traces; and (4) the upper cutoff frequency of the A trace is larger than that of the B1, B2, and B3 traces.

To simulate the ducted echoes, density depleted ducts were introduced in the average density model. The ducts were centered at L =3.19. Duct half-widths were varied from ΔL =0.025-0.1 L and density depletions were varied from $\Delta N/N$ = 1% - 10%. The time delays for each frequency of each trace were calculated for each combination of duct parameters. The t_g-f dispersion obtained from ray tracings is compared with that of the observations. The ranges of ΔL and $\Delta N/N$ are short listed which gives a range of final duct parameters that can explain the observations.

5.1.1 Effect of Duct Half-Width and Density Perturbation on Time Delay Spread (Δt_g)

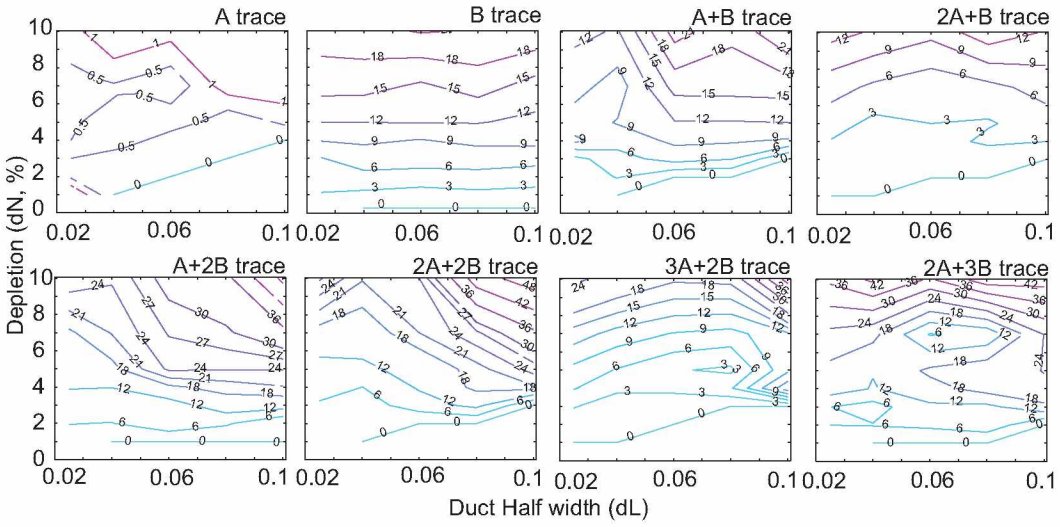

Figure 5.3 Contour plot of t_g spread of ducted traces for varying duct half-width (ΔL) and density depletions ($\Delta N/N$) .

Using the average density model, the t_g spread has been calculated for one frequency (208.8 kHz) for all the ducted traces for the 26 July 2001 case. Figure 5.3 shows the contour plots of the t_g spread (Δt_g) of the ducted traces with varying duct half-width (ΔL) and density depletions ($\Delta N/N$). ΔL varies along the x-axis and density depletion varies along the y-axis. $\Delta N/N$ varies from 1% to 10% and ΔL varies from 0.025L (~36 km at satellite altitude) to 0.1L (~143 km at satellite altitude). From the contour plot it is observed that:

1. At constant ΔL, Δt_g increases with increasing depletion for most of the traces. For the A trace, the increase in Δt_g is very small compared to other traces, for example, at $\Delta L = 0.05$, Δt_g of the A trace increases from 0 ms (representing only one echo) at 1% depletion to ~1 ms at 5% depletion, whereas for the B trace, Δt_g increases from 3 ms at 1% depletion to ~15 ms at 5% depletion.

2. At constant depletion, Δt_g for traces A,B, A+B, and 2A+B remains about constant or decreases slightly with increasing duct half-width. For higher order traces (A+2B, 2A+2B, 3A+2B, and 2A+3B), Δt_g increases with increasing ΔL.

5.1.2 Effect of Duct Half-Width and Density Perturbation on Upper Cutoff Frequency f_{uc}

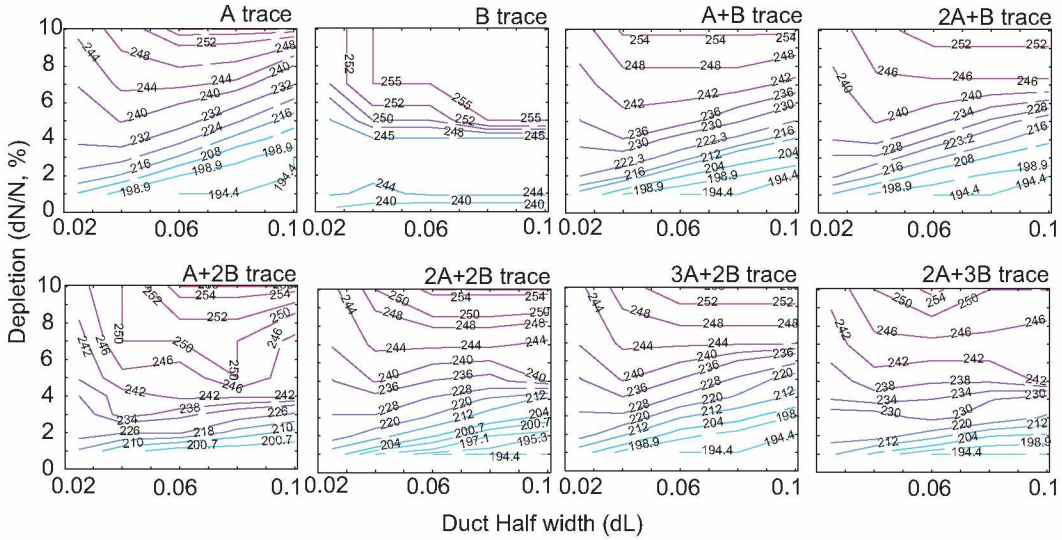

Figure 5.4 Contour plot of upper cutoff frequency(f_{uc}) of ducted traces for varying ΔL and $\Delta N/N$.

Figure 5.4 shows the contour plots of the upper cutoff frequency (f_{uc}) of ducted traces with

varying ΔL and density depletions. Duct half-width varies along the x-axis and density depletion varies along the y-axis. Density depletion varies from 1% to 10% and ΔL varies from 0.025L (∼36 km at satellite altitude) to 0.1L (∼143 km at satellite altitude). From the figure it can be noted that:

1. At constant ΔL, f_{uc} increases with increasing depletion for all the traces.

2. At constant depletion, f_{uc} decreases with increasing ΔL for smaller depletions (ΔN/N ≤ 3%). For ΔN/N > 3% the f_{uc} increases from 0.02 to ∼0.06 and then decreases with ΔN/N.

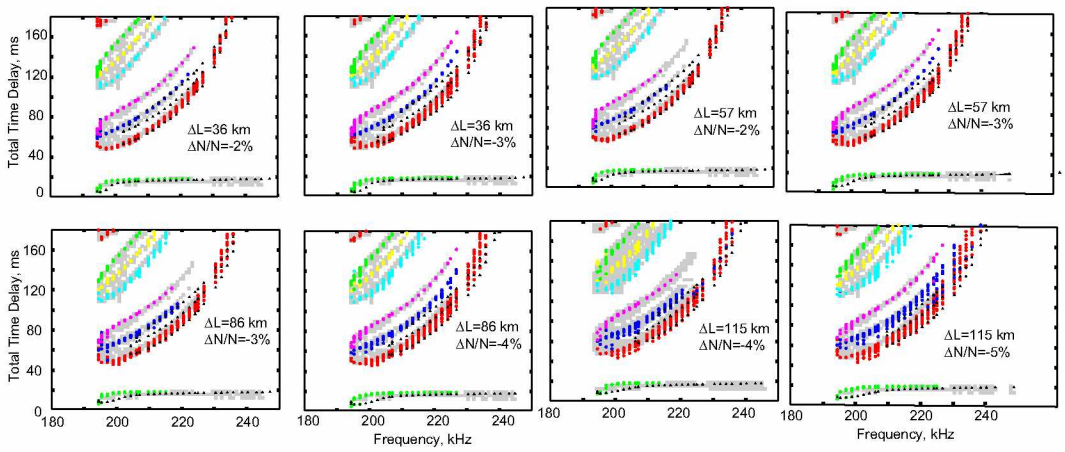

Figure 5.5 Time delays versus frequency plot for the final duct parameters that explains the observations of 26 July 2001 AB type ducted fast ZM echoes.

Table 5.5 Final duct parameters for 26 July 2001 case ducted echoes along L =3.19. The parameters are duct half-width in L, duct half-width in km at 1000 km altitude, duct half-width in km at satellite altitude, duct half-width in km at equator, and duct depletion level.

ΔL (half-width)	ΔL(km) @1000 km	ΔL(km) satellite (3834 km)	ΔL(km) Equator (13950 km)	dN/N
0.025	20	36	159	∼2% - 3%
0.04	33	57	255	∼2%-3%
0.06	49	86	382	∼3%-4%
0.08	65	115	510	∼4%-5%

Figure 5.5 compares t_g of the ducted echoes with the observed t_g. Duct half-width is given in km at the satellite altitude of 3834 km (see Table A.19). Besides the ducted echoes, nonducted echoes are also obtained (shown as black triangles). The final duct parameters are a subset of duct

parameters that satisfy the criteria for t_g spread and upper cutoff frequency. For the 26 July 2001 case, the observed upper cutoffs of all the traces except the B, $A + B$, and $2A + B$ traces have experimental limits. The B, $A + B$, and $2A + B$ traces have upper cutoffs of 225 kHz, 222.3 kHz, and 223.2 kHz, respectively, due to the propagation characteristics of the ducted waves. Thus, in determining the final duct parameters, the upper cutoff frequencies of the B, $A + B$, and $2A + B$ traces are considered. The final duct parameters are listed in Table 5.5.

5.1.3 Summary of Results: 26 July 2001 Case Analysis

1. A density depleted duct is required to guide ZM waves.

2. A density depleted duct centered at $L_{sat} = 3.19$, of half-width ranging between ~160 to 500 km in the equatorial plane, and depletions of ~2% - 5% covering an altitude range of 2800 - 8000 km could explain the ducted echoes observed on 26 July 2001.

3. The bandwidth of the ZM cavity is ~50 kHz and the length of the cavity is ~11,400 km.

4. In the absence of ducts, four nonducted echoes are obtained in the ZM cavity. Three of the echoes (A, B1, and B2) retrace their path after reflection while one forms a loop (B3).

5. In the presence of ducts, both nonducted and ducted echoes are obtained, formed from both looping and retracing paths.

6. Keeping ΔN/N constant, f_{uc} decreases with increasing ΔL. Δt_g remains about constant or decreases slightly with increasing ΔL for the A, B, A+B, and 2A+B traces, whereas for the higher order traces (A+2B, 2A+2B, 3A+2B, and 2A+3B), Δt_g increases with increasing ΔL.

7. Keeping ΔL constant, both f_{uc} and Δt_g increase with increasing ΔN/N.

8. The diffusive equilibrium density model explains the observed dispersion of the ducted fast ZM echoes. The model is in good agreement with in-situ N_e measurements from DMSP-f13 (~25%), in-situ RPI (~37-41%), and N_e from empirical density models.

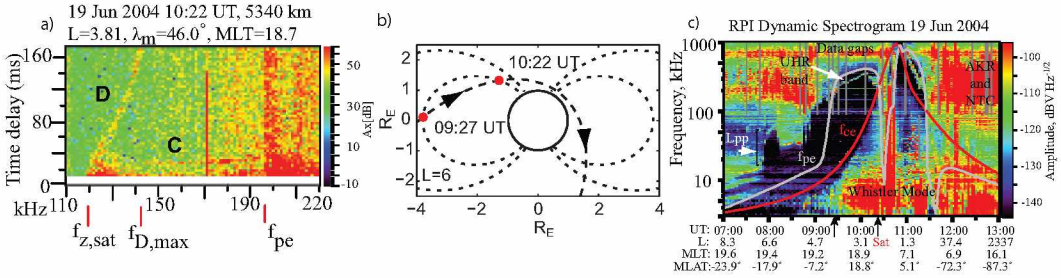

Figure 5.6 (a) Plasmagram showing discrete traces of CD type nonducted fast ZM echoes observed on 19 June 2004. (b) IMAGE orbit plot for 19 June 2004 with satellite position shown as a red dot. (c) Dynamic spectrogram observed by IMAGE on 19 June 2004 with position of the satellite shown by a black arrow.

5.2 Case III: 19 June 2004 10:22:39 UT Nonducted CD Type Fast Z Mode Echoes

Figure 5.6(a) shows a plasmagram (pr#57) of CD type nonducted fast ZM echoes received by the X antenna on RPI/IMAGE on 19 June 2004 at 10:22:39 UT inside the plasmasphere at an altitude of 5340 km, λ_m = 46.0°, L =3.808, and MLT =18.7. The plasmapause, from dynamic spectra (5.6(c)), is located at L =6.6 – 6.9 on nightside, i.e., for MLT =19.3. Figure 5.6(b) shows the IMAGE orbit plot for 19 June 2004 with the position of the satellite at 09:27:15 UT and 10:22:39 UT (red dot). The satellite was moving through the plasmasphere towards the northern polar region. The satellite crossed the L-shell (L ~3.84) near the equator (λ_m = 1.1°) close to the L-shell of the satellite (L ~3.81) ~55 minutes earlier. f_{pe} at this location calculated from the f_{uh} emission band and $f_{ce,IGRF}$ is in the range of ~206-210 kHz, which corresponds to N_e of ~528-550 e/cc. The f_z near the equator $f_{z,equ}$ lies in the range of ~199-203 kHz.

Figure 5.6(a) shows two traces of nonducted fast ZM echoes, trace C and trace D. Trace D starts from an apparent zero range cutoff near 119.6 kHz and then rises to t_g ~180 ms at 142.4 kHz up to the upper range limit of the plasmagram. The D trace is diffuse in the lower frequency range, with a t_g spread of 6-7 range bins. The lower cutoff of the C trace is not clear. The C trace is observed to start at a higher frequency of ~143.6 kHz, higher than $f_{z,sat}$, from a t_g of ~30 ms. Time delay remains constant up to the upper cutoff at 194 kHz. The C trace is discrete and occupies 1-2 range bins. It extends up to the electron plasma frequency f_{pe}. A strong resonance signature at ~198 kHz is identified as f_{pe}. The absence of higher traces (C+D, C+2D, etc.) that are present in ducted cases suggests that the fast ZM echoes are non ducted. From the cutoff frequency of 119.6 kHz and $f_{ce,IGRF}$ =237 kHz, the local f_{pe} =206 kHz.

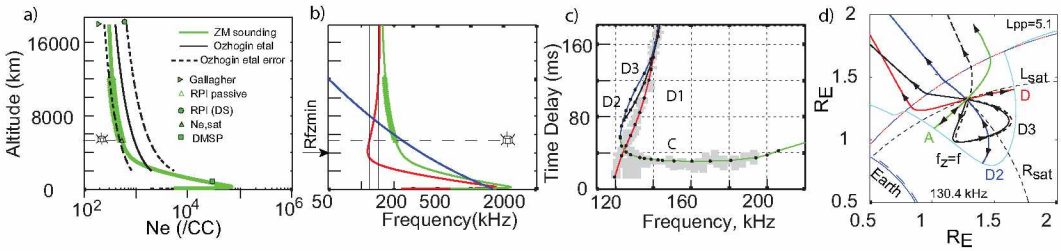

Figure 5.7 (a) Plot of electron (N_e) density along geomagnetic field line from the average density model for 19 June 2004. Density model is compared with empirical models and in-situ measurements. (b) Characteristic frequencies f_{pe}, f_{ce} and f_z along the geomagnetic field line. (c) Comparison plot of the nonducted time delays for C and D echoes with the observations. (d) Ray paths of the four nonducted echoes obtained inside the ZM cavity when no duct is present.

Table 5.6 Average density model input parameters for 19 June 2004. The parameters are r_b in geocentric distance (km), T is temperature at the base height, [H,He,O] is the ion composition at the base height, and N_e at the reference point.

Model	Rb (km)	T (K)	[H,He,O]	$N_{e,ref}$
Avg	7570	3500	[0.0026,0.0149,0.9825]	528

Ray tracing calculations are performed using the average density model with r_b = 7570 km, temperature T = 3500 K, ion composition H = 0.0026, He = 0.0149, and O = 0.9825, and N_e at the satellite N_e ~528 e/cc corresponding to f_{pe} obtained from f_z observed at 119.6 kHz. The average density model is chosen such that: (1) $f_{z,local} = f_{z,sat}$; (2) $f_{z,Equ} > f_{B,max}$; (3) $R_{f_{z,min}} < R_{sat}$; and (4) the calculated t_g of the C and D traces matches with their observed average t_g. Table 5.6 lists the input parameters for these models and Table 5.7 lists the model parameters along the field line. It should be noted that there is an uncertainty of 1.2 kHz (equal to the program frequency stepping) in the measurement of the f_z at the satellite. Thus, the local f_z may lie between 118.4 -119.6 kHz. f_{ce} at the satellite, calculated from the IGRF model, is ~239 kHz, which gives the range of f_{pe} at the satellite as 205.7-207 kHz. This is equivalent to N_e ~524-532 e/cc. The N_e chosen at the reference point ~528 e/cc, lies within this range. The f_{ce} at the equator is taken as ~928 kHz matched to the $f_{ce,IGRF}$ at the satellite (~239 kHz) when the f = 119.6 kHz frequency was transmitted.

Figure 5.7(a) shows electron density (N_e) along L =3.81. Tables 5.8 and 5.9 compare the N_e obtained from ZM sounding with in-situ measurements and empirical density model values.

Figure 5.7(b) shows plots of f_z, f_{pe}, and f_{ce} along the geomagnetic field line. The f_z profile forms a narrow ZM cavity within which frequencies in the range of $\sim 119 - 148$ kHz can be trapped.

Table 5.7 Important parameters of the density models at key altitudes for 19 June 2004. The parameters are f_z at the satellite $f_{z,sat}$, minimum f_z along the field line $f_{z,min}$, altitude in km of $f_{z,min}$ ($R_{f_{z,min}}$), value of f_z at the equator along the field line ($f_{z,equ}$), value of f_{pe} at the equator along the field line ($f_{pe,equ}$), value of f_{pe} at F2 peak ($f_{pe,F2}$), and altitude of the F2 peak ($R_{f_{pe,F2}}$).

Model	$f_{z,sat}$	$f_{z,min}$	$R_{f_{z,min}}$	$f_{z,equ}$	$f_{pe,equ}$	$f_{pe,F2}$	$R_{f_{pe,F2}}$
Avg	118.9	114.8	4165 km	148.4 kHz	156.6 kHz	2328	270 km

Table 5.8 Comparison of average density model with in-situ data for 19 June 2004. The parameters are UT, altitude in km, L-shell(L), Magnetic local time (MLT), geomagnetic latitude (λ_m), N_e measured in-situ, N_e from the density model, percentage difference.

Measurement	UT	Alt (km)	L	MLT	λ_m (°)	N_e (e/cc)	$N_{e,mod}$ (e/cc)	% diff
DMSP-f13	10:38 UT	848.2	3.807	17.08	56.94	28937	20430	34.5
RPI (DS)	09:27 UT	18124	3.843	19.1	1.11	528.1-549.6	304.4	53.7-57.4
RPI (plsmg)	10:23 UT	5250.6	3.868	18.7	46.64	484.3	533.7	9.7

Thus, the bandwidth of the ZM cavity is ~29 kHz. The altitude of the cavity ranges from ~2695-17,890 km, making the length of the cavity ~15,200 km. The altitude of minimum f_z lies below the satellite altitude, as indicated by an arrow.

Figure 5.7(c) compares the t_g-f dispersion of nonducted fast ZM echoes calculated from ray tracing with that of the observations. The corresponding ray paths of these traces for 130.4 kHz are shown in Figure 5.7(d). Four nonducted echoes (C, D1, D2, and D3) are obtained. Three of the four echoes (C, D1, and D2) retrace their path after reflection and the other (D3) forms a loop. There are two looping echoes which traverse the same path but in opposite sense (two rays are shown as solid and dashed black rays) and thus accumulate identical time delays. The t_g of the C and D1 fast ZM trace echoes matches that of the observations. It is clearly observed from Figure 5.7(c) that: (1) the lower cutoff frequency of the D1 trace is lower than that of all the other traces; (2) the lower cutoff frequencies of the C and D2 traces are equal and have the same t_g; (3) the lower cutoff of D3 is larger than that of all the other traces; (4) the upper cutoff frequency of the C trace is larger than that of the D1, D2, and D3 traces; and (5) the C trace extends beyond $f = f_{pe}$.

Table 5.9 Comparison of average density model with empirical density models for 19 June 2004. The parameters are altitude in km, N_e obtained from empirical model, N_e from the density model, percentage difference.

Empirical Model	Alt (km)	N_e (e/cc)	$N_{e,model}$ (e/cc)	% diff
G2000	17890	196	304	43.5
Oz2012	17890	400	304	27.1
Oz2012	5340	915	528	53.8
Oz2012	2000	1930	2765	35.6

5.2.1 Summary of Results: 19 June 2004 Case Analysis

1. The diffusive equilibrium density model explains the observed dispersion of the ducted fast ZM echoes. The model is in good agreement with in-situ N_e measurements from DMSP-f13 (∼35%), in-situ RPI (∼10% at the satellite), in-situ RPI (∼54-57% at the equator), and N_e from empirical density models (G2000, Oz2012).

2. The bandwidth of the ZM cavity is ∼29 kHz and the length of the cavity is ∼15,200 km.

3. Four nonducted echoes are obtained in the ZM cavity. Three of the echoes (C, D1, and D2) retrace their path after reflection, while one forms a loop (D3).

5.3 Case IV: 03 August 2005 19:14:54 UT Nonducted AB Type Fast Z Mode and Specularly Reflected Whistler Mode Echoes

Figure 5.8(a) shows a plasmagram (pr#57) of the AB type nonducted fast ZM echoes received by the X antenna on RPI/IMAGE on 03 August 2005 at 19:14:54 UT inside the plasmasphere at altitude 2354 km, $\lambda_m = 43.3°$, L =2.585, and MLT =4.2. Figure 5.8(b) shows the IMAGE orbit plot for 03 August 2005 with the position of the satellite at 19:14 UT. Figure 5.8(c) shows the dynamic spectrogram observed on 03 August 2005 for a 4 hour interval, 16:30-21:00 UT. The plasmapause is observed around 20:00 UT between L_{pp} = 3.72-4.04 on dayside, i.e., for MLT=4.8.

Figure 5.8(a) shows two traces of nonducted fast ZM echoes, trace A and trace B. Trace A starts from an apparent zero range near lower cutoff 254 kHz and then rises to a t_g ∼12 ms at higher frequencies up to the upper frequency limit of the plasmagram, 326 kHz. Trace B starts at 261.2

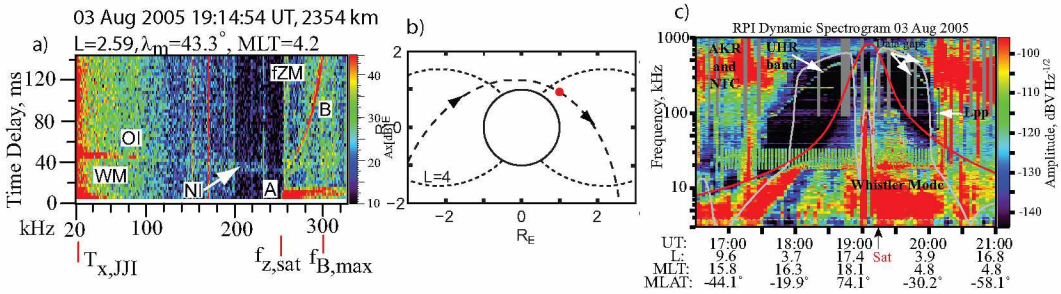

Figure 5.8 (a) Plasmagram showing discrete traces of AB type nonducted fast ZM echoes observed on 03 August 2005. (b) IMAGE orbit plot for 03 August 2005 with position of satellite at 08:23:47 shown by a red dot. (c) Dynamic spectrogram observed by IMAGE on 03 August 2005 with position of the satellite shown by black arrow.

kHz, slightly higher than $f_{z,sat}$, from a t_g ~40 ms and rises to an upper t_g limit of ~155 ms at 303.2 kHz. At an initial frequency range from 261.2-285.2 kHz, the echoes cover 1-3 range bins at each frequency. At higher frequencies, the t_g spread increases up to 5-6 range bins. This t_g spreading suggests the presence of field aligned irregularities. The absence of higher order traces (A+B, 2A+B, etc.) that are present in ducted cases suggests that the fast ZM echoes are non ducted. Figure 5.8(a) also shows two traces of obliquely-incident (OI) and normally-incident (NI) specularly reflected (SR) Whistler mode (WM) echoes. The WM echoes are observed over a frequency range of 20-237.2 kHz. The SR-WM echoes are patchy and the upper cutoff is not clear. There is, in fact, a hint of trace in the frequency range of ~250-326 kHz and in the virtual range of 0.71-1.08 R_E. The background in the frequency range of 254-326 kHz is very noisy. The initial part of this echo trace, i.e., from 264.8-275.6 kHz, is observed at the same t_g range as that of NI-SR-WM echo. The enhancement in amplitude may be due to overlapping of the SR-WM echoes with the fast ZM echoes. In the frequency range of 256.4-326 kHz and in the virtual range of 30-45 ms, there is a continuation of the SR-WM echo trace to overlap with fast ZM echoes. This trace could not be the ducted echo element, as in all observed cases, the B trace is the strongest (the prominent echo trace observed here should be B trace). The AB type signature of the fast ZM echoes indicate that the IMAGE was within the ZM cavity at an altitude below $R_{f_{z,min}}$ and the echoes were formed due to reflection from below and above the satellite in the same local hemisphere. From the cutoff frequency of 254 kHz and IGRF model value of f_{ce} =575 kHz, the local f_{pe} =459 kHz. A ground transmitter signal at 21.2 kHz from the JJI vlf transmitter (Japan, 32°N 05'; 131°E 51') is also observed.

Ray tracing calculations are performed using the average density model taking r_b = 7570 km, temperature T = 2470 K, ion composition H = 0.100, He = 0.067, and O = 0.833, and N_e at

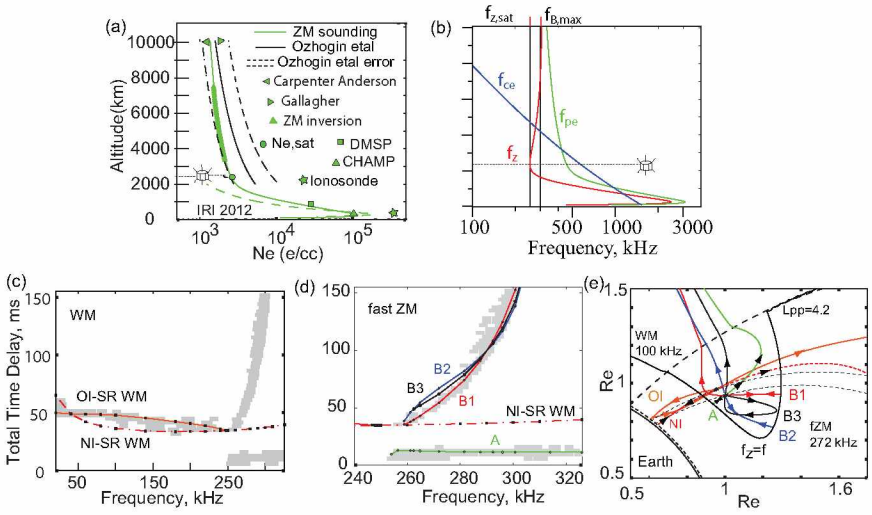

Figure 5.9 (a) Plot of electron (Ne) density along geomagnetic field line from the average density model for 03 August 2005. Density model is compared with empirical models and in-situ measurements. (b) Characteristics frequencies f_z, f_{pe} and f_{ce}. Comparison of the calculated time delays for (c) SR-WM echoes, and (d) nonducted fast ZM echoes with the observations. (e) Ray paths of SR-WM echoes and the four nonducted fast ZM echoes obtained inside the ZM cavity.

Table 5.10 Average density model input parameters for 03 August 2005. The parameters are r_b in geocentric distance (km), T is temperature at the base height, [H,He,O] is the ion composition at the base height, and N_e at the reference point.

Model	Rb (km)	T (K)	[H,He,O]	$N_{e,ref}$(e/cc)
Avg	7570	2470	[0.100, 0.067, 0.833]	2600

the satellite ∼2600 e/cc corresponding to f_{pe} obtained from f_z observed at 254 kHz. The average density model is chosen such that: (1) $f_{z,local} = f_{z,sat}$; (2) $f_{z,Equ} > f_{B,max}$; (3) $R_{f_{z,min}} > R_{sat}$; and (4) the calculated t_g of the A and B traces match their observed average t_g. The local f_z may lie between 252.8-254 kHz (uncertainty of 1.2 kHz). The f_{ce} at the satellite calculated from the IGRF model is ∼575 kHz, which gives the range of f_{pe} at the satellite as $457 - 459$ kHz. This is equivalent to N_e ∼2596-2612 e/cc. The N_e chosen at the reference point, ∼2600 e/cc, lies within this range. The f_{ce} at the equator is taken as ∼950 kHz matched to the $f_{ce,IGRF}$ at the satellite (∼575 kHz)

Table 5.11 Important parameters of the density models at key altitudes for 03 August 2005. The parameters are f_z at the satellite $f_{z,sat}$, minimum f_z along the field line $f_{z,min}$, altitude in km of $f_{z,min}$ ($R_{f_{z,min}}$), value of f_z at the equator along the field line ($f_{z,equ}$), value of f_{pe} at the equator along the field line ($f_{pe,equ}$), value of f_{pe} at F2 peak ($f_{pe,F2}$), and altitude of the F2 peak ($R_{f_{pe,F2}}$).

Model	$f_{z,sat}$	$f_{z,min}$	$R_{f_{z,min}}$	$f_{z,equ}$	$f_{pe,equ}$	$f_{pe,F2}$	$R_{f_{pe,F2}}$
Avg	253	2395	305.7	332.1	3093	255 km	2395 km

when the $f = 254$ kHz frequency was transmitted.

Table 5.12 Comparison of average density model with in-situ data for 03 August 2005. The parameters are UT, altitude in km, L-shell(L), Magnetic local time (MLT), geomagnetic latitude (λ_m), N_e measured from DMSP f-13 satellite, N_e from the density model at ~850 km, percentage difference.

Measurement	UT	Alt (km)	L	MLT	λ_m (°)	N_e (e/cc)	$N_{e,mod}$ (e/cc)	% diff
DMSP-f13	20:18	855.6	2.5879	7.02	48.55	29097	20760	33.4
CHAMP	19:51	345.7	2.6356	1.94	50.77	104000	100200	3.7

Table 5.13 Comparison of average density model with ionosonde data for 03 August 2005. The parameters are ionosonde station name, local time, Local time of the satellite, L-shell, geographic longitude, geographic latitude, Great Circle Distance, height of the F2 peak, N_e from the density model at F2 peak(255), percentage difference.

Station	LT	IMAGE	L-shell	Longitude	Latitude	GCD (km)	Nof2 (e/cc)	Ne(Mod) (e/cc)	% diff
Bear Lake (BL841)	4:10	6:45	2.358	31°42′ W	41°17′N	4427	338000	118700	64.90%

Figure 5.9(a) shows the plot of field aligned N_e along L =2.585 when 254 kHz ray was transmitted. The comparison of average density model with in-situ and empirical density models is given in Tables 5.12, 5.13, and 5.14.

Figure 5.9(b) shows the plot of f_z, f_{pe}, and f_{ce} along the geomagnetic field line for the average density model. The f_z profile forms a narrow ZM cavity within which frequencies in the range of ~254-306 kHz can be trapped. Thus, the bandwidth of the ZM cavity is ~52 kHz. The altitude of the cavity ranges from ~1615-10,100 km, making its length ~8500 km. The altitude of the minimum in f_z cavity lies above the satellite altitude (2354 km), that is, $R_{f_{z,min}} = 2395$ km.

Figure 5.9(c) compares the t_g-f dispersion of SR-WM calculated from ray tracing with that of the observations. At a lower frequency range (20-~150 kHz), the observed dispersion matches with the OI-SR and at a higher frequency range (~150-250 kHz), both the OI-SR and NI-SR echoes match the observations. The OI-SR echoes are obtained up to the upper cutoff frequency of 248 kHz, while NI-SR echoes are obtained at higher frequencies up to the upper frequency limit of the transmitted program. The corresponding ray paths of OI-SR and NI-SR echoes at 100 kHz are shown in Figure 5.9(e). Both OI-SR and NI-SR rays travel close to the field line and reflect at the

Table 5.14 Comparison of average density model with empirical density models for 03 August 2005. The parameters are altitude in km, N_e obtained from empirical model, N_e from the density model, percentage difference.

Empirical Model	Alt (km)	N_e (e/cc)	$N_{e,model}$ (e/cc)	% diff
IRI2012	290	189100	118700	45.7
CA1992	10100	1234	1368	10.3
G2000	10100	1809	1368	27.8
Oz2012	2000	5336	2968	57.0
Oz2012	2354	4696	2597	57.6
Oz2012	10100	1591	1368	15.1

Earth-Ionosphere boundary at 90 km.

Figure 5.9(d) compares the t_g-f dispersion of nonducted fast ZM echoes with that of the observations. The t_g of the A and B1 fast ZM echoes matches the observed average t_g of the A and B traces. The corresponding ray paths of these traces for 272 kHz are shown in the Figure 5.9(e). Four nonducted echoes, A, B1, B2, and B3 are obtained. Three of the four echoes (A, B1, and B2) retrace their paths after reflection and the other (B3) forms a loop. A and B1 ray paths travel close to the field line, whereas B2 and B3 rays travel farther away from the satellite. It is clearly observed from Figure 5.9(d) that: (1) the lower cutoff frequency of the A trace is lower than that of all the other traces; (2) the lower cutoff frequencies of the B1 and B2 traces are equal; (3) the lower cutoff of the B3 is larger than thst of all the other traces; and (4) the upper cutoff frequency of the A trace is larger than that of the B1, B2, and B3 traces.

5.3.1 Summary of Results: 03 August 2005 Case Analysis

1. The diffusive equilibrium density model explains the observed dispersion of the ducted fast ZM echoes. The model is in good agreement with with in-situ N_e measurements from DMSP-f13 (∼33%), CHAMP (∼4%), Ionosonde (∼65%), and N_e from empirical density models (CA1992, G2000, Oz2012).

2. The bandwidth of the ZM cavity is ∼52 kHz and the length of the cavity is ∼8500 km.

3. Four nonducted echoes are obtained in the ZM cavity. Three of the echoes (A, B1, and B2)

retrace their path after reflection, while one forms a loop (B3).

4. This case demonstrates that when fast ZM echoes are accompanied by Whistler mode echoes, ZM sounding can be performed in conjunction with Whistler mode sounding to obtain the field aligned N_e in the altitude range of 90 km- ~10,000 km [Mayank and Sonwalkar, 2012].

5.4 Case V-Successive Cases of Fast Z mode: 27 June 2005 10:36 UT - 10:54 UT

Figure 5.10 shows a series of seven plasmagrams (pr#57) of nonducted and ducted fast ZM (FZM) echoes received by the X antenna on RPI/IMAGE on 27 June 2005 as the IMAGE moved from L =13.34 outside the plasmasphere at 10:36 UT to L=2.07 inside the plasmasphere at 10:54 UT. The satellite was inside the ZM cavity (shown as blue and green f_z contours). The positions of the satellite are shown by black dots. The model value of the plasmapause [Carpenter and Anderson, 1992] is taken at L =4.68, as shown in Figure 5.10(h). Figure 5.10(i) shows the dynamic spectrogram recorded by IMAGE on 27 June 2005 from 08:00 - 13:00 UT. The upper hybrid resonance band is observed from 08:45-10:15 UT on the duskside (MLT~19) and from 10:45-12:45 UT on the dayside (MLT~7). A sharp decrease in the UHR band near 09:35 UT on the duskside (MLT~19) can be observed, indicating that the satellite crossed the plasmapause. However, the UHR band does not show any sharp decrease and is smooth on the dayside (MLT~7) of the orbit, therefore, the plasmapause measurement cannot be made. The positions of the satellite between 10:36 UT - 10:54 UT are shown by red bars.

The satellite locations and characteristic frequencies for the successive cases shown in Figures 5.10(a)-(g) are listed in Table 5.15. Considering the model plasmapause at $L_{pp} = 4.68$, we observed that the first two cases, observed at 10:36:55 UT and 10:39:55 UT, lie outside the plasmasphere, while the rest of the cases are inside the plasmasphere. The altitude of the cases increases from 1870 km outside the plasmasphere to 5057 km inside the plasmasphere. The N_e obtained from the f_{pe} resonance observed on the plasmagram shows that N_e first decreases from ~1070 e/cc to ~808 e/cc as the satellite moved from L =13.34 at 1870 km to L =5.78 at ~2200 km and then increases steadily from ~808 e/cc to ~1260 e/cc at L =2.07 as the satellite moves towards the equator. When the satellite is outside the plasmasphere or near the plasmapause, only Whistler mode and fast ZM echoes reflecting from below the satellite altitude (A trace) are observed (cases from 10:36

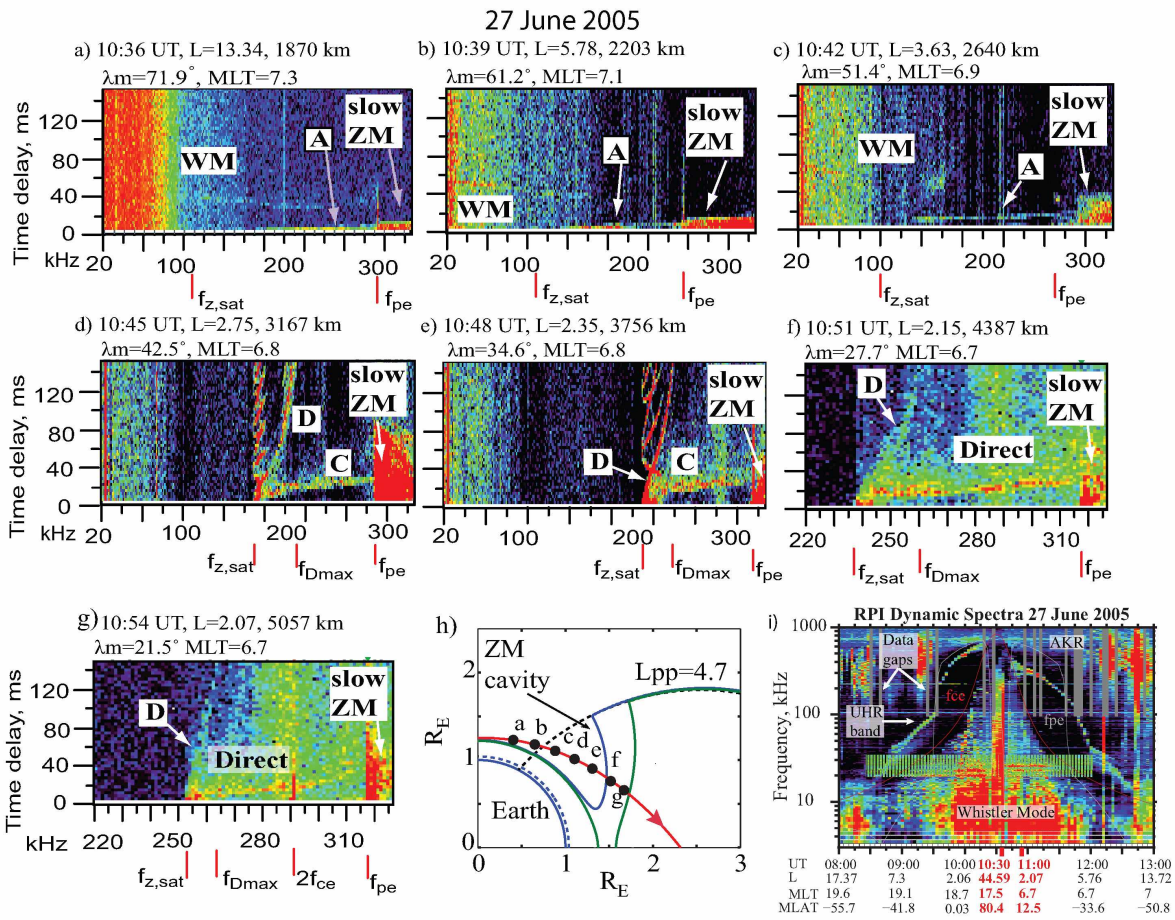

Figure 5.10 (a-g)Series of plasmagrams showing nonducted and ducted fast ZM echoes, Whistler and slow ZM echoes on seven successive soundings extending from L =13.34 outside the plasmasphere to L =2.07 inside the plasmasphere. (h) Low-altitude portion of the IMAGE orbit with satellite positions (black dots). Blue and green curves show two constant f_z contours indicating that the satellite was traversing within the ZM cavity, (i) Dynamic spectrogram recorded by IMAGE on 27 Jun 2005. The positions of the satellite are indicated at 10:36 UT - 10:54 UT by vertical red lines.

UT - 10:42 UT). As the satellite moves inward, the presence of the ZM cavity is manifested in terms of the echoes reflecting from above the satellite altitude (D trace), observed in cases from 10:45 UT to 10:54 UT. Thus, it is evident that the ZM cavity is a real phenomenon that occurs inside the plasmasphere and is less likely to be observed outside the plasmasphere.

Table 5.16 lists the satellite location, upper hybrid resonance frequency (f_{uh}), and calculated electron plasma frequency (f_{pe}) obtained from the f_{uh} band observed on the dynamic spectrogram for the time period overlapping with the time period of the successive cases, that is, from 10:44 UT - 11:02 UT. The N_e measurements show that N_e increases steadily as the satellite moves from L =2.84 to L =2.14 near the equator.

Table 5.15 Satellite location and important parameters for successive cases observed on 27 June 2005. The parameters are universal time (UT), satellite location in L-shell(L), geomagnetic latitude ($\lambda(°)$), magnetic local time (MLT), altitude (km), local f_z (f_z), IGRF model electron cyclotron frequency (f_{ce}), f_{ce} resonance, electron plasma frequency (f_{pe}) calculated from f_z and $f_{ce,IGRF}$, f_{pe} resonance observed on the plasmagram, and maximum Kp-index for the preceding 24 hours.

UT	L	λ_m (°)	MLT	Alt (km)	f_z	f_{ce} (IGRF)	f_{ce} (res)	f_{pe} (@f_z)	f_{pe} (res)	$K_{p,max}$
10:36:55	13.344	71.9	7.3	1870	-	701.6	-	-	293.6	2
10:39:55	5.781	61.2	7.0	2203	-	585	-	-	255.2	2
10:42:55	3.630	51.4	6.9	2640	-	460.6	-	-	269.6	2
10:45:55	2.752	42.5	6.8	3167	168.8	345	-	294.5	287.6	2
10:48:55	2.346	34.6	6.8	3756	209.6	255.5	-	312.2	315.2	2
10:51:54	2.152	27.7	6.7	4387	237.2	192.1	195.2	319.1	317.6	2
10:54:55	2.070	21.5	6.7	5057	252.8	145.9	152	317.5	317.6	2

Table 5.16 Electron plasma frequency measurement made from dynamic spectrogram recorded on 27 June 2005. The parameters are UT, L-shell(L), geomagnetic latitude (λ_m), magnetic local time (MLT), altitude in km, lower and upper limits of upper hybrid resonance frequency (f_{uh1}, f_{uh2}), IGRF model values of electron cyclotron frequency ($f_{ce,IGRF}$) and corresponding calculated electron plasma frequency (f_{pe1}, f_{pe2}).

UT	L	$\lambda_m(°)$	MLT	Alt(km)	f_{uh1}	f_{uh2}	$f_{ce,IGRF}$	f_{pe1}	f_{pe2}
10:44:50	2.84	43.7	6.8	3088	439.2	448.0	383.1	214.8	232.2
10:47:50	2.39	35.7	6.8	3666	413.9	422.1	289.3	296.0	307.4
10:50:50	2.17	28.6	6.7	4291	382.4	390.0	218.5	313.8	323.0
10:53:50	2.08	22.4	6.7	4950	353.2	360.3	167.0	311.2	319.3
10:56:50	2.05	17.9	6.7	5494	DATA	GAP	136.5	DATA	GAP
10:59:50	2.08	11.8	6.7	6330	332.9	339.5	103.7	316.3	323.3
11:02:50	2.14	7.4	6.7	7033	319.9	326.3	89.5	307.1	313.8

5.4.1 27 June 2005 10:36:55 UT: Discrete Specularly Reflected Whistler Mode and Non Ducted Fast Z Mode Echoes Outside the Plasmasphere

Figure 5.10(a) shows a plasmagram of nonducted fast ZM echoes reflecting from below the satellite altitude received by the X antenna on RPI/IMAGE on 27 June 2005 at 10:36:55 UT. These echoes were observed outside the plasmasphere. Figure 5.10(h) shows the IMAGE orbit plot for 27 June 2005. The red dot at position 'a' shows the position of the satellite at 10:36:55 UT. IMAGE was at an altitude of 1870 km, $\lambda_m = 71.9°$, L =13.340, and MLT =7.3. Figure 5.10(a) shows a trace of specularly reflected(SR) Whistler mode (WM) echoes observed in the frequency range of 118.4−290 kHz in the apparent t_g range of 30-60 ms. In the frequency range of 118.4 − 240 kHz, the WM echoes are discrete, with t_g spread ranging from 1-2 range bins (3-6 ms spread). For the frequency range of 275.6-292.4 kHz, the observed WM echoes are diffuse, with the time delay spread ranging from 3-6 range bins (9-18 ms spread). The SR-WM echo trace is patchy, that is, echoes are not observed for a range of frequencies, for example, for f ∼240-270 kHz. A resonance signature at $f = f_{pe}$ is observed at 293.6 kHz. Discrete nonducted fast ZM echoes reflecting from the bottom (trace A) are observed in the frequency range of 166.4-326 kHz. The echo trace A starts from an apparent zero range cutoff near 166.4 kHz and then rises to ∼0.25 R_E (t_g of ∼11 ms) at higher frequencies up to 293.6 kHz. At $f > f_{pe}$, echoes are observed in the apparent range of 0-14 ms up to the upper frequency limit of the plasmagram (326 kHz). This echo trace may contain the slow ZM echo as well as the A trace echoes. SR-WM echoes overlap with fast ZM echoes in the frequency range of 166.4 − 292.4 kHz. The local f_z calculated from f_{pe} and $f_{ce,IGRF}$ ∼681 kHz is $f_{z,sat}$ ∼109 kHz. It is important to note that lower cutoff of the A trace is not observed in this case.

Ray tracing calculations are performed assuming r_b = 7370 km, temperature T = 1850 K, ion composition H = 0.02, He = 0.02, and O = 0.96, and N_e at the satellite N_e = 1069 e/cc, corresponding to the f_{pe} observed at 293.6 kHz. A r^{-n} power law distribution with a fall factor of $n = 4.5$ is assumed outside the plasmapause. The f_{ce} at the equator is taken as ∼817 kHz matched to the $f_{ce,IGRF}$ at the satellite (∼701 kHz) when f = 166.4 kHz frequency was transmitted (166.4 kHz is the first observed frequency of the fast ZM A trace). Figure 5.11(a) shows the N_e profile along the geomagnetic field line for L =10.46, that is, when 166.4 kHz frequency was transmitted. The N_e profile obtained from WM and ZM sounding (solid green curve) is compared to the N_e profile of the IRI-2012 empirical model (dashed blue curve) and the in-situ N_e measured from DMSP f-13 satellite at ∼850 km and the CHAMP satellite at ∼350 km. The comparisons are given

in Tables 5.21-5.22.

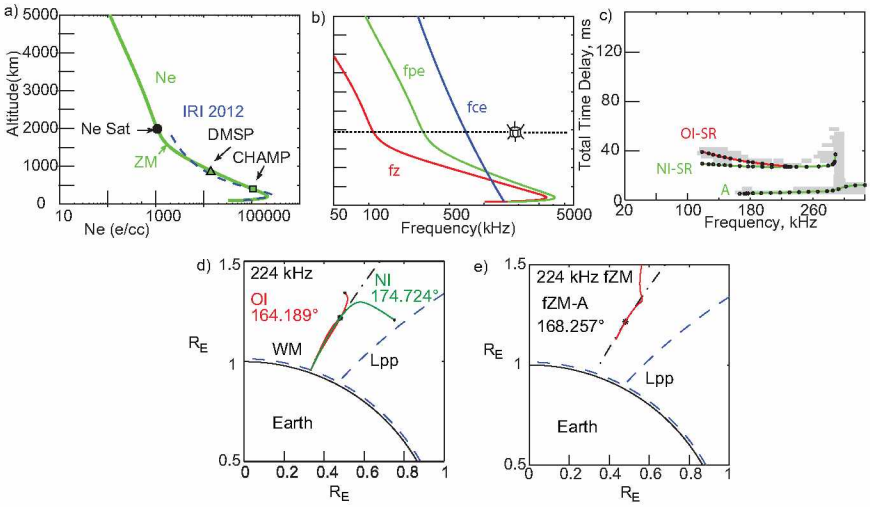

Figure 5.11 (a) N_e along the geomagnetic field line from average density model for 27 June 2005 10:36:55 UT. (b) Characteristic frequencies f_z, f_{pe} and f_{ce} along the geomagnetic field line. (c) t_g-f dispersion of Whistler and fast ZM echoes. (d)Ray paths of 224 kHz rays for OI- and NI-SR-WM echoes, (e) fast ZM A trace echo.

Figure 5.11(b) shows f_z, f_{pe}, and f_{ce} along the geomagnetic field line. Figure 5.11(c) shows the t_g-f plot of the WM and ZM echoes. OI-SR- and NI-SR-WM echoes are obtained from ray tracings that explain the observations. For fast Z mode, echoes reflecting from below the satellite altitude are obtained from ray tracing calculations. The t_g of the fast ZM A trace echoes increases gradually from ~5 ms at 166.4 kHz to ~9 ms at 292.4 kHz. This indicates that the increase in reflection altitude of a ray is compensated by the increase in the group velocity as the frequency increases from 166.4 kHz to 292.4 kHz. For frequencies greater than f_{pe}, t_g increases rapidly from ~9 ms at 292.4 kHz to ~12 ms at 326 kHz. The refractive index of ZM for $f > f_{pe}$ is greater than 1, indicating a decrease in group velocity of the waves.

Figure 5.11(d)-(e) shows the ray paths of 224 kHz rays. At 224 kHz, OI-SR- and NI-SR-WM echoes as well as fast ZM echoes are obtained. The satellite was at ~1958 km, $\lambda_m = 68.45°$ and L =9.689 when the 224 kHz rays were transmitted. The OI-SR- and NI-SR-WM rays travel close to the field line and reflect at the Earth-Ionosphere boundary at 90 km. The fast ZM ray propagates close to the field line and reflects from an altitude of ~1327 km at L =9.396. Due to its small propagation path, the fast ZM ray accumulates a smaller time delay.

5.4.2 27 June 2005 10:39:55 UT: Discrete Specularly Reflected Whistler Mode and Non Ducted Fast Z Mode Echoes Outside the Plasmasphere

Figure 5.10(b) shows plasmagrams of nonducted fast ZM echoes reflecting from below the satellite altitude received by the X antenna on RPI/IMAGE on 27 June 2005 at 10:39:55 UT at an altitude of 2202 km, $\lambda_m = 61.2°$, L =5.781, and MLT =7. The satellite location is at 'b' in 5.10(h). Figure 5.10(b)) shows a trace of SR-WM echoes observed in the frequency range of $20 - 162.8$ kHz in the apparent t_g range of 36-56 ms. The SR-WM echo trace is patchy and no echo is observed for a range of frequencies, f ~125-~156 kHz. A resonance signature at $f = f_{pe}$ is observed at 255.2 kHz. Discrete nonducted fast ZM echoes reflecting from the bottom (trace A) are observed in the frequency range of 132.8-326 kHz. The echo trace A starts from an apparent zero range cutoff near 132.8 kHz and then rises to t_g of ~11 ms at higher frequencies up to $f_{pe} = 255.2$ kHz. At $f > f_{pe}$, echoes are observed in the apparent range of 4-17 ms up to the upper frequency limit (326 kHz) of the plasmagram. This echo trace may contain the slow ZM echo as well as the A trace echoes. The A trace is discrete, with a t_g spread ranging from 1-2 range bins (3-6 ms spread). SR-WM echoes overlap with fast ZM echoes in the frequency range of $132.8 - 162.8$ kHz. The local f_z calculated from f_{pe} and $f_{ce,IGRF}$ ~564 kHz is $f_{z,sat}$ ~98 kHz. It is important to note that the lower cutoff frequency of the A trace is not observed in this case.

Ray tracing calculations are performed assuming $r_b = 7370$ km, temperature $T = 2250$ K, ion composition $H = 0.004$, $He = 0.005$, and $O = 0.991$, and N_e at the satellite, N_e ~808 e/cc corresponding to the f_{pe} observed at 255.2 kHz, and a fall factor (n) of -4.5 outside the plasmapause. The plasmapause is taken at L =4.68, as determined from the model. f_{ce} at the equator is taken as ~815 kHz, matched to the $f_{ce,IGRF}$ at the satellite (~585 kHz) when the $f = 132.8$ kHz frequency was transmitted (132.8 kHz is the first observed frequency of the fast ZM A trace echo). Figure 5.12(a) shows the N_e profile along the geomagnetic field line L =5.19, that is, when the 132.8 kHz frequency was transmitted. The N_e profile obtained from WM and ZM sounding (solid green curve) is compared to the N_e profile of the IRI-2012 empirical model (dashed blue curve) and in-situ N_e measured from the DMSP f-13 satellite at ~850 km and the CHAMP satellite at ~350 km.

Figure 5.12(b) shows f_z, f_{pe}, and f_{ce} along the geomagnetic field line. Figure 5.12(c) shows the t_g-f plot of the WM and ZM echoes. OI-SR- and NI-SR-WM echoes are obtained from ray tracings that explain the observations. For fast ZM, echoes reflecting from below the satellite altitude are obtained from ray tracing calculations. The t_g of the fast ZM A trace echoes increases gradually

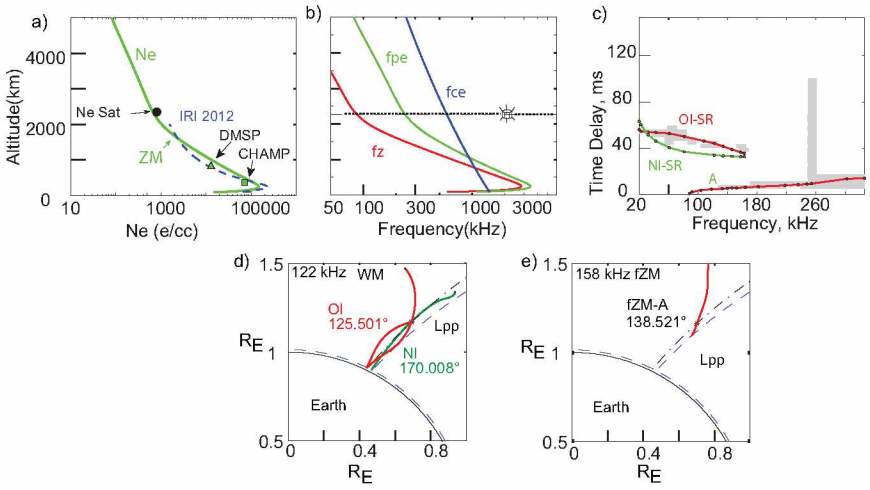

Figure 5.12 N_e along the geomagnetic field line from average density model for 27 June 2005 10:39:55 UT. (b) Characteristic frequencies f_z, f_{pe} and f_{ce} along the geomagnetic field line. (c) t_g-f dispersion of Whistler and fast ZM echoes. Ray paths of (d) OI-SR- and NI-SR-WM echoes at 122 kHz, and (e) fast ZM A trace echo at 158 kHz.

from ∼5 ms at 132.8 kHz to ∼9 ms at 255.2 kHz. For $f > f_{pe}$, t_g increases rapidly from ∼9 ms at 255.2 kHz to ∼14 ms at 326 kHz, indicating a decrease in the group velocity for $f > f_{pe}$. Figure 5.12(d)-(e) shows the ray paths of the OI-SR- and NI-SR-WM echoes at 122 kHz rays and the fast ZM echoes at 158 kHz. The 122 kHz rays were transmitted when the satellite was at ∼2272 km, $\lambda_m = 59.4°$, and L =5.23. For 158 kHz rays, the satellite was at ∼2292 km, $\lambda_m = 58.9°$, and L =5.09. OI-SR and NI-SR rays travel close to the field line and reflect at the Earth-Ionosphere boundary at 90 km. The ray path of the fast ZM echo at 158 kHz propagates close to the field line and reflects from the outer edge of the plasmapause at an altitude of ∼1809 km at L =4.6895. The total t_g accumulated by the ray is ∼5.8 ms.

5.4.3 27 June 2005 10:42:54 UT: Discrete Specularly Reflected Whistler Mode and Non Ducted Fast Z Mode Echoes Inside the Plasmasphere

Figure 5.10(c) shows plasmagrams of nonducted fast ZM echoes reflecting from below the satellite altitude received by the X antenna on RPI/IMAGE on 27 June 2005 at 10:42:54 UT inside the plasmasphere at an altitude of 2640 km, $\lambda_m = 51.4°$, L =3.63, and MLT =6.9. Satellite position is shown as 'c' in Figure 5.10(h). Figure 5.10(c) shows a trace of SR-WM echoes observed in the frequency range of 28.4 – 164 kHz in the apparent t_g range of 43-72 ms. WM echoes are discrete in the frequency range of 28.4 – 68 kHz and diffuse in the frequency range of 149.6-164 kHz. The

SR-WM echo trace is patchy and echoes are not observed for f ~69-148.4 kHz. A faint resonance signature at $f = f_{pe}$ is observed at 293.6 kHz. The upper cutoff of the WM echo trace is observed to be at 162.8 kHz, which is less than the min(f_{pe},f_{ce}). Discrete nonducted fast ZM echoes reflecting from the bottom (trace A) are observed in the frequency range of 131.6-326 kHz. The echo trace A starts from an apparent range of ~10 ms at 131.6 kHz and then rises to t_g of ~20 ms at higher frequencies up to f_{pe} = 291.2 kHz. The fast ZM echoes may extend beyond 291.2 kHz, but are indistinguishable from the diffuse slow ZM echoes that are also observed in the frequency range of 269.6 – 326 kHz. SR-WM echoes overlap with the fast ZM echoes in the frequency range of 149.6 – 164 kHz. The local f_z, calculated from f_{pe} and $f_{ce,IGRF}$ ~439, is $f_{z,sat}$ ~128 kHz. It is important to note that the ZM cutoff, f_z, is not observed in this case.

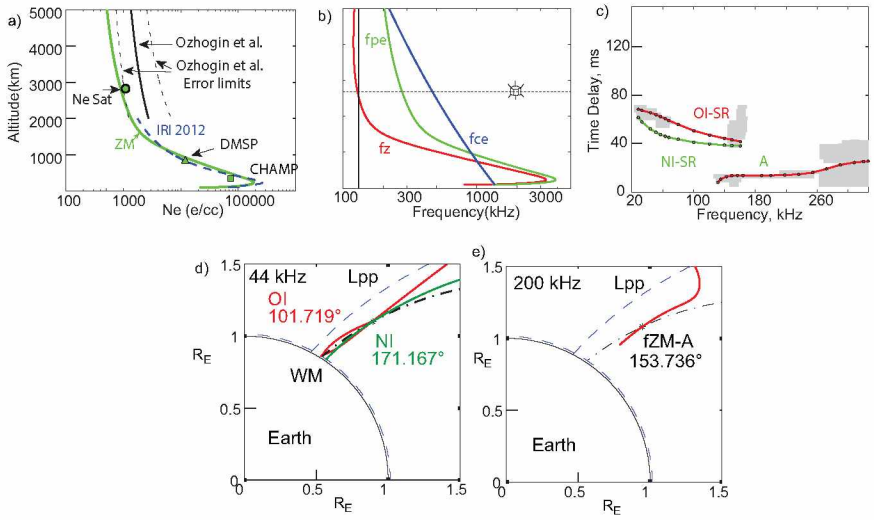

Figure 5.13 N_e along the geomagnetic field line from average density model for 27 June 2005 10:42:54 UT. (b) Characteristic frequencies f_z, f_{pe} and f_{ce} along the geomagnetic field line. (c) t_g-f dispersion of Whistler and fast ZM echoes. Ray paths of (d) OI-SR- and NI-SR-WM echoes at 44 kHz, and (e) fast ZM A trace echo at 200 kHz.

Ray tracing calculations are performed assuming r_b = 7380 km, temperature T = 1800 K, ion composition $H = 0.01$, $He = 0.09$, and $O = 0.90$, and N_e ~902 e/cc at the satellite, corresponding to f_{pe} ~269.6 kHz. The fall factor (n) outside the plasmapause does not affect the results as the satellite is inside the plasmasphere. f_{ce} at the equator is taken as ~808 kHz matched to $f_{ce,IGRF}$ at the satellite (~461 kHz) when f = 131.6 kHz frequency was transmitted (131.6 kHz is the first observed frequency of the fast ZM A trace echo). Figure 5.13(a) shows the N_e profile along the geomagnetic field line at L =3.41, that is, when the 131.6 kHz frequency was transmitted. The N_e profile obtained from Whistler and ZM sounding (solid green curve) is compared with the N_e

obtained from in-situ measurements and empirical models. Tables 5.22-5.23 compares the model N_e values with in-situ and empirical density model values.

Figure 5.13(b) shows f_z, f_{pe}, and f_{ce} along the geomagnetic field line. The f_z profile forms a very narrow cavity. However, from ray tracing we found that no echoes are obtained from the rays reflecting from above the satellite altitude, as the rays do not bend enough to form an echo at the satellite. Figure 5.13(c) shows the t_g-f plot of the WM and ZM echoes. For fast Z mode, echoes reflecting from below the satellite altitude are obtained from ray tracing calculations. The t_g of the fast ZM A trace echoes increases gradually from ~8 ms at 131.6 kHz to ~16 ms at 269.6 kHz. For frequencies greater than f_{pe}, the t_g increases rapidly from ~16 ms at 269.6 kHz to ~26 ms at 326 kHz.

Figure 5.13(d) shows the ray paths of WM echoes at 44 kHz and fast ZM echoes at 200 kHz. At 44 kHz both the OI-SR- and NI-SR-WM echoes are obtained. The 44 kHz ray was transmitted when the satellite was at ~2664 km, $\lambda_m = 50.9°$, and L =3.55. For the 200 kHz ray, the satellite was at ~2780 km, $\lambda_m = 48.8°$, and L =3.35. In Figure 5.13(e) the ray path of the fast ZM echo at 200 kHz is shown. The ray propagates close to the field line and reflects from an altitude of ~1527 km at L =3.057. The total t_g accumulated by the ray is ~13.7 ms.

5.4.4 27 June 2005 10:45:55 UT: Ducted Fast Z Mode Echoes Inside the Plasmasphere

Figure 5.10(d) shows plasmagrams of CD type ducted fast ZM echoes received by the X antenna on RPI/IMAGE on 27 June 2005 at 10:45:55 UT inside the plasmasphere at an altitude of 3167 km, $\lambda_m = 42.5°$, MLT =6.8, L =2.75. Figure 5.10(h) shows the satellite position as 'd'. $f_{z,sat}$ is 168.8 kHz and the highest ducted frequency, $f_{D,max}$, is 210.8 kHz. Table 5.17 lists the lower and upper cutoffs of the ducted traces.

Figure 5.10(d) shows 10 echo traces all beginning at 168.8 kHz and have different t_g spreads. The upper cutoff of the C trace may extend up to higher frequencies, but the strong diffuse slow ZM echoes mask the C trace echoes. All the ducted traces, except the C, D, and C+D traces, show an upper cutoff near ~180 kHz. This upper cutoff is due to the propagation effect of waves within a duct. The C+D trace shows a gap in t_g-f dispersion for the frequency range of 185-194 kHz.

An interesting observation is the direct trace that starts from ~177.2 kHz at ~8 ms and slowly rises in t_g to merge with the C trace echo near ~200 kHz. The lower cutoff of the direct trace may

Table 5.17 Lower and upper cutoff frequency of ducted traces for 27 June 2005 10:45:55 UT.

Trace	Lower Cutoff	Upper Cutoff
D	168.8 kHz	210.8 kHz
C	168.8 kHz	286.4 kHz
C+D	168.8 kHz	206 kHz
C+2D	168.8 kHz	178.4 kHz
2C+D	168.8 kHz	180.8 kHz
2C+2D	168.8 kHz	182 kHz
2C+3D	168.8 kHz	180.8 kHz
3C+2D	168.8 kHz	180.8 kHz
3C+3D	168.8 kHz	177.2 kHz
3C+4D	168.8 kHz	173.6 kHz

start from $f_{z,sat}$ but could not be distinguished from the strong signal of the D trace echo. The direct trace would appear inconsistent with the occurrence of the CD type fast ZM echoes, as the echoes reflecting from below the satellite altitude (C trace) are generally detached from apparent zero range base line as shown in Figure 5.10(d)-(e). The observation of direct echoes along with ducted CD type fast ZM echoes has been discussed by Carpenter et al., (2003). The smaller t_g and the overlap of the echo frequency range with the C trace echoes suggests that the direct echoes are formed from reflections earthward of the IMAGE. Direct echoes may be formed due to reflection of waves in vertically downward and inward directions, allowing for initial reflections close to the satellite. Ray tracing calculations have been performed to explain this phenomenon.

The t_g spread of the D trace ranges from 3 ms to ~50 ms. For the C trace, the t_g spread varies from ~3-18 ms. The C trace echoes show a large t_g spread in the frequency range of ~168.8-200 kHz and ~220-260 kHz. At 168.8 kHz, the t_g of the C, C+D, and C+2D traces are indistinguishable. For the C+D and C+2D traces the t_g spread varies from ~3-15 ms and ~6-25 ms, respectively. For the 2C+D, 2C+2D, and 2C+3D traces, the t_g spread varies from ~5-25 ms, ~3-18 ms, and ~3-22 ms, respectively. For the 3C+2D, 3C+3D, and 3C+4D traces, the t_g spread varies from ~3-25 ms, ~3-18 ms, and ~3-9 ms, respectively. Diffuse slow ZM echoes are also observed in the frequency range of 287.6 - 326 kHz. This indicates the presence of field aligned irregularities which can scatter the ZM echoes to produce a large spread in time delays. A sharp lower cutoff of diffuse

slow ZM echoes is observed at 287.6 kHz. The lower cutoff frequency of slow ZM echoes at 287.6 kHz is identified as the local electron plasma frequency.

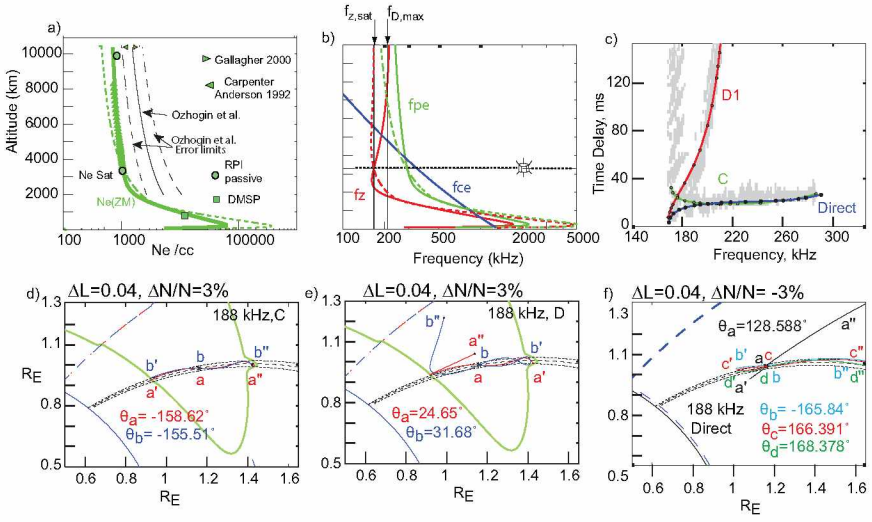

Figure 5.14 N_e along the geomagnetic field line from two density models that explains the ducted fast ZM echoes (solid curve) and direct fast ZM echoes (dashed curve) for 27 June 2005 10:45:55 UT. (b) Characteristic frequencies f_z, f_{pe} and f_{ce} along the geomagnetic field line. (c) t_g-f dispersion of fast Z mode echoes. Ray paths of 188 kHz frequency for (d) ducted C trace fast ZM echoes, (e) ducted D trace fast ZM echoes, and (f) direct fast ZM echoes.

Ray tracing calculations have been performed for this case to explain two different traces: the ducted fast ZM echoes and direct echoes. For ducted fast ZM echoes, ray tracing calculations are performed assuming r_b = 7520 km, temperature T = 2850 K, ion composition H = 0.035, He = 0.016, and O = 0.949, and N_e at the satellite, N_e ~1068 e/cc, corresponding to f_{pe} obtained from $f_{z,sat}$ = 168.8 kHz. It should be noted that there is an uncertainty of 1.2 kHz (equal to the program frequency stepping) in the measurement of the f_z at the satellite. Thus, the local f_z may lie between 167.6 -168.8 kHz. The $f_{ce,IGRF}$ at the satellite is ~345 kHz, which gives the range of f_{pe} at the satellite as $293 - 294.5$ kHz. This is equivalent to N_e ~1066-1076 e/cc. The N_e ~1068 e/cc chosen at the reference point lies within this range. The f_{ce} at the equator is taken as ~800 kHz matched to the $f_{ce,IGRF}$ at the satellite (~345 kHz) when the f = 168.8 kHz frequency was transmitted (168.8 kHz is the f_z at the satellite). The average ray tracing density model and the t_g-f plot are shown in Figure 5.14. Figure 5.14(a) shows the N_e profile along the geomagnetic field line L =2.63, that is, when the 168.8 kHz frequency was transmitted by IMAGE. The N_e profile obtained from the ZM sounding (solid green curve) is compared to the N_e obtained in-situ and from empirical density models (see Tables 5.22-5.23). It should be noted that the comparison has not been made with the IRI-2012 model and the CHAMP in-situ data as the fast ZM wave propagation

earthward reflects at higher altitudes (∼1500-2000 km).

Figure 5.14(b) shows f_z, f_{pe}, and f_{ce} along the geomagnetic field line. The f_z profile forms a narrow ZM cavity within which frequencies in the range of ∼168.8-218 kHz can be trapped. Thus, the bandwidth of the ZM cavity is ∼50 kHz. The altitude of the cavity ranges from ∼1780-10,400 km which gives the length of the cavity as ∼8600 km. Figure 5.14(c) shows the t_g-f plot of the C and D traces when no ducts are assumed in the model. The t_g of the C and D fast ZM echoes matches with the observed average t_g of C and D traces. Figure 5.14(d)-(e) shows the ray paths of the ducted C and D trace echoes (blue and red rays), respectively, in a duct of half-width $\Delta L = 0.04$ L and density depletion of 3%. It is observed that C and D echo rays injected at $\theta_{i,C} = -158.62°$, $-155.51°$, and $\theta_{i,D} = 24.65°$, $31.68°$, respectively, are guided by the duct and form retracing and looping echoes.

To simulate the direct trace echoes, we assume another density model. This is based on the assumption that the ZM cutoff profile in some other direction may not contain a ZM cavity, so the waves may reflect close to the satellite. To find the density model for direct echoes, the average density model is modified such that the altitude of the f_z profile below the satellite altitude is increased. Thus, for direct trace echoes, ray tracing calculations are performed assuming $r_b = 7520$ km,temperature $T = 1700$ K, ion composition $H = 0.02$, $He = 0.20$, and $O = 0.78$, and $N_e = 1070$ e/cc at the satellite.

Figure 5.14(a)-(b) shows N_e profile (dashed green curve), and f_z, f_{pe}, and f_{ce} (dashed curves) for the direct trace density model. The f_z profile does not form a ZM cavity or apparently a very shallow one. Figure 5.14(c) shows the t_g-f plot of the direct trace (blue curve) when no duct is assumed in the model. The t_g of the direct trace (which propagates in the fast Z mode) matches with the average time delays of the observed direct fast ZM echoes. The spread in t_g indicates the presence of field aligned irregularities in the vicinity of the satellite. Ray paths for the direct echoes density model are shown in Figure 5.14(f). Rays injected at small θ_i are guided by the duct and form ducted echoes at the satellite. The ray path of the nonducted direct fast ZM echo for a large $\theta_i = 128.588°$ reflects from below the satellite altitude. It is observed that ducted as well as nonducted rays reflect very close to the satellite and therefore accumulate smaller time delays.

To simulate the ducted echoes a density depleted duct is introduced in the average density model. A range of duct half-widths and density depletions are taken and the ducted echoes are obtained through ray tracing calculations. The duct is centered at L =2.615. The observed cutoff of all the traces except the C, D, and C+D traces are clearly observed. Thus, in determining the

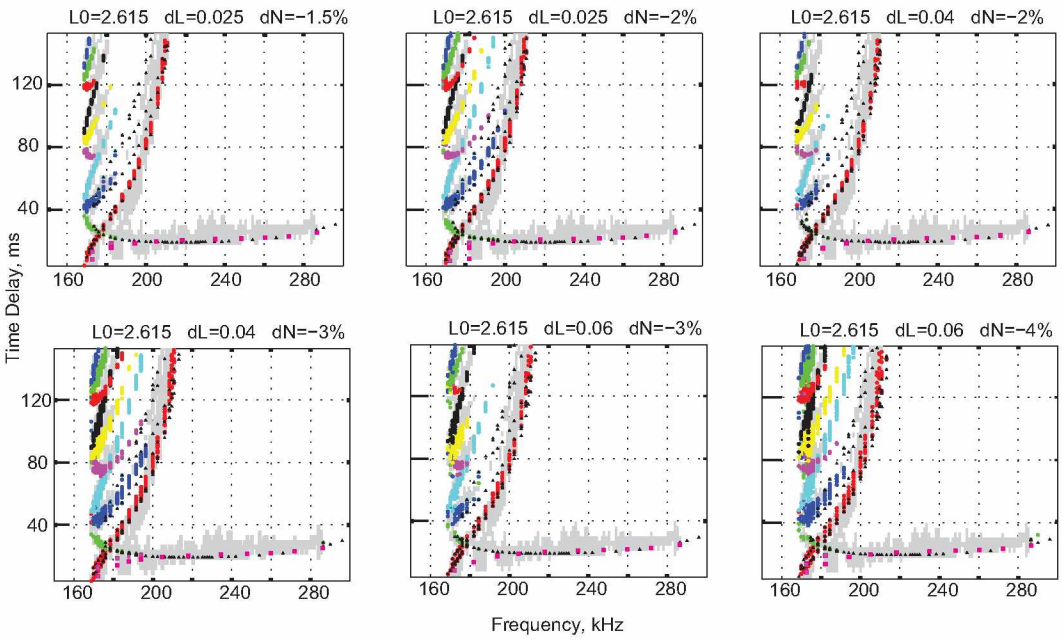

Figure 5.15 Time delays versus frequency plot for the final duct parameters that explains the ducted fast ZM echoes observed on 27 June 2005 10:45:55 UT.

Table 5.18 Final duct parameters for 27 June 2005 10:45:55 UT case along L =2.615. The parameters are duct half-width in L, duct half-width in km at 1000 km altitude, duct half-width in km at satellite altitude, duct half-width in km at equator, and duct depletion level.

ΔL (half-width)	ΔL @ 1000 km	ΔL at satellite 3300 km	ΔL at equator 10380 km	ΔN/N
0.025	29 km	47 km	159 km	∼1.5-2%
0.04	46 km	75 km	255 km	∼2-3%
0.06	69 km	112 km	382 km	∼3-4%

final duct parameters, the upper cutoff frequencies of other higher traces are considered. Thus, the final duct parameters that can explain the observations lie in the range of duct half-width of $0.025 - 0.06$ L and density depletion of $-1.5\% - 4\%$. Table 5.18 lists these final duct parameters. Figure 5.15 shows the t_g-f plots for a range of duct parameters. It is noted that both ducted and nonducted echoes are obtained in the presence of ducts. The ducted echoes are color-coded. The black triangles represent the nonducted echoes that are obtained from ray tracings with ducts present. The direct trace echoes obtained from the direct trace density model are also shown (magenta squares).

5.4.5 27 June 2005 10:48:55 UT: Ducted Fast Z Mode Echoes Inside the Plasmasphere

Figure 5.10(e) shows plasmagrams of CD type ducted fast ZM echoes received by the X antenna on RPI/IMAGE on 27 June 2005 at 10:48:55 UT inside the plasmasphere at an altitude of 3756 km, $\lambda_m = 34.6°$, MLT =6.8, and L =2.35. Satellite position is shown as 'e' in the Figure 5.10(h). $f_{z,sat}$ =209.6 kHz and the highest ducted frequency, $f_{D,max}$, is 239.6 kHz. Table 5.19 lists the lower and upper cutoffs of the ducted traces.

Table 5.19 Lower and upper cutoff frequency of ducted traces for 27 June 2005 10:48:55 UT.

Trace	Lower Cutoff	Upper Cutoff
D	209.6 kHz	239.6 kHz
C	209.6 kHz	227.6 kHz
C+D	209.6 kHz	228.8 kHz
C+2D	209.6 kHz	224.0 kHz
2C+D	209.6 kHz	228.8 kHz
2C+2D	209.6 kHz	218.0 kHz
2C+3D	209.6 kHz	212.0 kHz

The upper cutoff of the C trace may extend up to higher frequencies but the strong diffuse direct echoes reflecting from below the satellite altitude mask the C trace echoes. The direct trace starts from ~216.8 kHz at ~5 ms and slowly rises in t_g to ~30 ms at 306.8 kHz. The lower cutoff of the direct trace may start from $f_{z,sat}$ but it could not be distinguished from the strong signal of the D trace echo.

Diffuse slow ZM echoes are also observed in the frequency range of 315.2 - 326 kHz. A sharp lower cutoff of diffuse slow ZM echoes is observed at 315.2 kHz. From the cold plasma wave theory, it is known that the lower cutoff of slow ZM waves is at the local electron plasma frequency. Thus, the lower cutoff frequency of slow ZM echoes at 315.2 kHz is identified as the local electron plasma frequency. A resonance signature is also observed at 315.2 kHz.

Ray tracing calculations have been performed for this case to explain two different traces, ducted fast ZM echoes and direct echoes. For ducted fast ZM echoes, ray tracing calculations are performed assuming r_b = 7520 km, temperature T = 3200 K, ion composition H = 0.09, He = 0.05, and

$O = 0.86$, and N_e ~1201 e/cc at the satellite, corresponding to the f_{pe} obtained from f_z observed at 209.6 kHz. The local f_z may lie between 208.4 -209.6 kHz (1.2 kHz uncertainty). $f_{ce,IGRF}$ ~256 kHz at the satellite gives the range of f_{pe} as $311 - 312$ kHz. This is equivalent to N_e ~1200-1209 e/cc. The N_e chosen at the reference point, 1200.9 e/cc, lies within this range. f_{ce} at the equator is taken as ~791 kHz, matched to the $f_{ce,IGRF}$ at the satellite (~256 kHz) when $f = 209.6$ kHz frequency was transmitted (209.6 kHz is the f_z at the satellite).

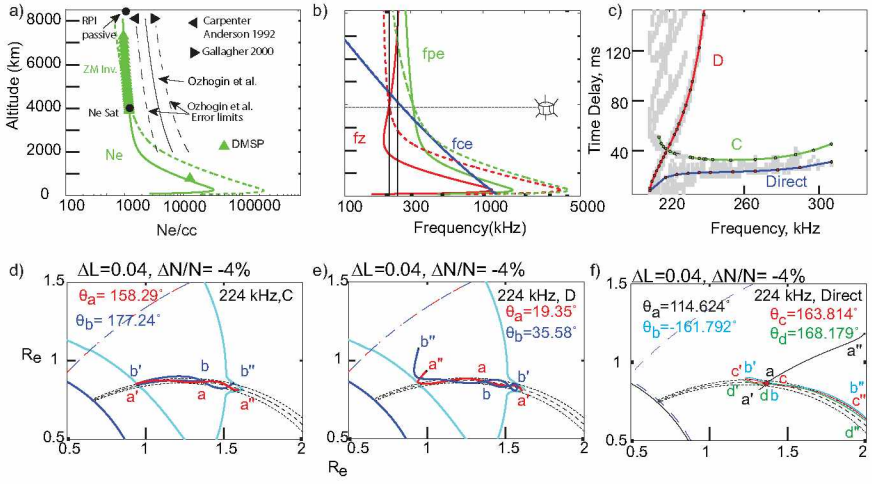

Figure 5.16 N_e along the geomagnetic field line from two density models that explains the ducted fast ZM echoes (solid curve) and direct fast ZM echoes (dashed curve) for 27 June 2005 10:48:55 UT. (b) Characteristic frequencies f_z, f_{pe} and f_{ce} along the geomagnetic field line. (c) t_g-f dispersion of fast Z mode echoes. Ray paths of 224 kHz frequency for (d) ducted C trace fast ZM echoes, (e) ducted D trace fast ZM echoes, and (f) direct fast ZM echoes.

The average ray tracing density model and the t_g-f plot are shown in Figure 5.16. Figure 5.16(a) shows the N_e profile (solid green curve) along the geomagnetic field line at L =2.273, that is, when the 209.6 kHz frequency was transmitted. The N_e profile obtained from the ZM sounding is compared to the N_e obtained from in-situ measurements and empirical density models (see comparison tables 5.22-5.23). It should be noted that the comparison has not been made with the IRI-2012 model and CHAMP in situ data as the fast ZM wave propagating earthward reflects at higher altitudes (~1500-2000 km).

Figure 5.16(b) shows f_z, f_{pe}, and f_{ce} along the geomagnetic field line (solid curves). The f_z profile forms a narrow ZM cavity within which frequencies in the range of ~209-244 kHz can be trapped. Thus, the bandwidth of the ZM cavity is ~35 kHz. The altitude of the cavity ranges from ~1560-8110 km, making the length of the cavity ~6550 km. Figure 5.16(c) shows the t_g-f plot of the C and D trace when no duct is assumed in the model. The t_g of the C and D fast ZM echoes matches with the observed average t_g of the C and D traces. Figure 5.16(d)-(e) shows

the ray paths of the ducted C and D trace echoes (blue and red rays), respectively, in a duct of half-width ΔL = 0.04 L and density depletion of 4%. It is observed that C and D echo rays injected at $\theta_{i,C}$ = 158.29°, 177.24°, and $\theta_{i,D}$ = 19.35°, 35.58°, respectively, are guided by the duct and form retracing and looping echoes.

For direct trace echoes, ray tracing calculations are performed assuming r_b = 7570 km, temperature T = 2800 K, ion composition H = 0.0015, He = 0.0300, and O = 0.9685, and N_e = 1200.9 e/cc at the satellite. Figure 5.16(a)-(b) shows the N_e profile (dashed green curve), f_z, f_{pe}, and f_{ce} (dashed curves) for the direct trace density model. The f_z profile does not form a ZM cavity. It is also observed that the f_z profile below the satellite lies at much higher altitude compared to the average density model for ducted traces. Due to this the reflection altitude of rays propagating earthward of the IMAGE lies much closer to the satellite and, therefore, the rays accumulate smaller time delays. Figure 5.16(c) shows t_g-f plot of the direct trace (blue curve) when no duct is assumed in the model. The t_g of the direct trace (which propagates in the fast Z mode) matches with the average time delays of the observed direct fast ZM echoes. The spread in t_g indicates the presence of field aligned irregularities in the vicinity of the satellite.

Ray paths for the direct echo density model are shown in Figure 5.16(f). Rays injected at small θ_i are guided by the duct and form ducted echoes at the satellite. The ray path of the nonducted direct fast ZM echo for large θ_i = 114.624° reflects from below the satellite altitude. It is observed that ducted and nonducted rays reflect very close to the satellite and therefore accumulate smaller time delays.

Table 5.20 Final duct parameters for 27 June 2005 10:48:55 UT case along L =2.27. The parameters are duct half-width in L, duct half-width in km at 1000 km altitude, duct half-width in km at satellite altitude, duct half-width in km at equator, and duct depletion level.

ΔL (half-width)	ΔL @ 1000 km	ΔL at satellite 3936 km	ΔL at equator 14460 km	ΔN/N
0.025	37 km	70 km	159 km	~3-4%
0.04	59 km	112 km	255 km	~4-5%
0.06	88 km	169 km	382 km	~5-6%

To simulate the ducted echoes, density depleted ducts are introduced in the average density model. A range of duct half-widths and density depletions are taken and the ducted echoes are obtained through ray tracing calculations. The duct is centered at L =2.27. The cutoffs of the C and C+D traces are clearly observed. The upper cutoff frequencies of the other traces are limited

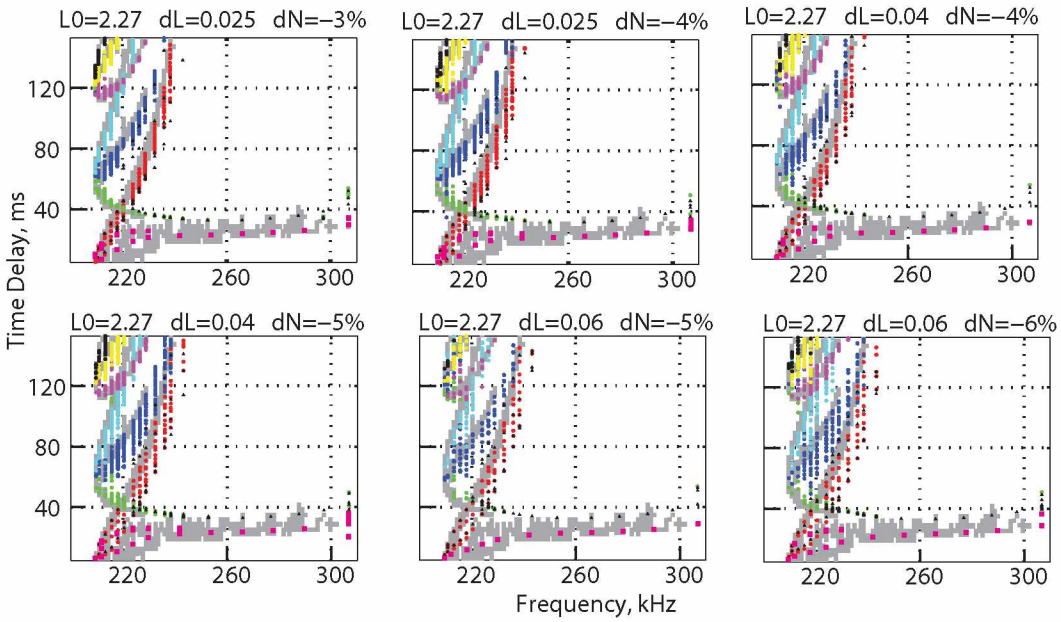

Figure 5.17 Time delays versus frequency plot for the final duct parameters that explains the ducted fast ZM echoes observed on 27 June 2005 10:48:55 UT.

by the transmitted program. Thus, in determining the final duct parameters, the upper cutoff frequencies of these traces are considered. Thus, the final duct parameters that can explain the observations lie in the range of duct half-width of $0.025 - 0.06$ L and density depletion of $3\% - 6\%$. Table 5.20 lists the final duct parameters. Figure 5.17 shows the t_g-f plots for a range of duct parameters. It is to be noted that both ducted and nonducted echoes are obtained in the presence of ducts. The ducted echoes are color-coded. The black triangles represent the nonducted echoes that are obtained from ray tracings with ducts present. The direct trace echoes obtained from the direct trace density model are also shown (magenta squares).

5.4.6 27 June 2005 10:51:54 UT: Fast Z Mode and Direct Echoes Inside the Plasmasphere

Figure 5.10(f) shows plasmagrams of fast ZM echoes received by the X antenna on RPI/IMAGE on 27 June 2005 at 10:51:54 UT inside the plasmasphere at an altitude of 4387 km, $\lambda_m = 27.7°$, MLT =6.7, and L =2.15. Satellite position is shown as 'f' in Figure 5.10(h). $f_{z,sat}$ is 237.2 kHz and the upper cutoff frequency of the D trace $f_{D,max}$ is 258.8 kHz. Echoes from the propagation path above the satellite towards the equator are labeled D. Only D trace echoes are observed.

Direct trace echoes are observed to start from ∼244.4 kHz at ∼8 ms and slowly rise in t_g to

~40 ms at 316.4 kHz. The lower cutoff of the direct trace may start from the $f_{z,sat}$, but it could not be distinguished from the strong signal of the D trace echo. Diffuse slow ZM echoes are also observed in the frequency range of 317.6 - 326 kHz. The lower cutoff frequency of slow ZM echoes at 317.6 kHz is identified as the local f_{pe}.

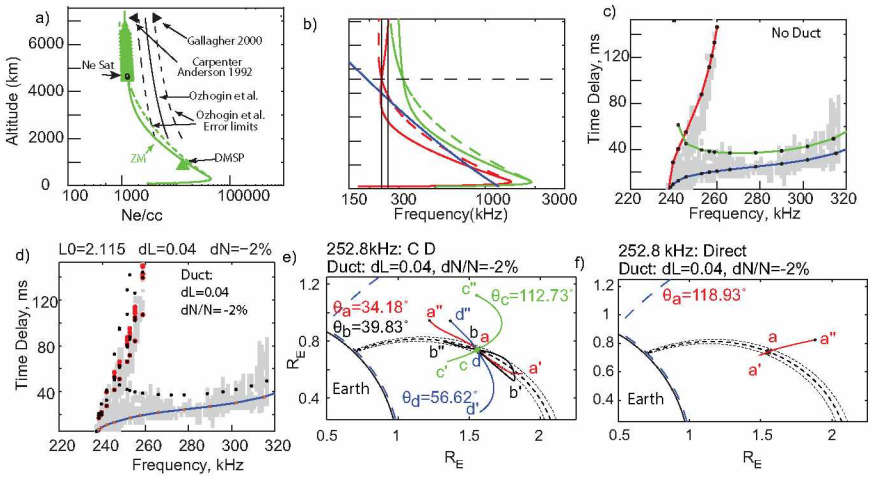

Figure 5.18 N_e along the geomagnetic field line from two density models that explain the ducted fast ZM echoes (solid curve) and direct fast ZM echoes (dashed curve) for 27 June 2005 10:51:54 UT. (b) Characteristic frequencies f_z, f_{pe} and f_{ce} along the geomagnetic field line. (c) t_g-f comparison of fast ZM echoes calculated from ray tracings with observations when no duct is present. (d) t_g-f comparison of fast ZM echoes calculated from ray tracings with observations when duct of half-width 0.04 L and depletion of 2% is present. (e) Ray paths of 252.8 kHz frequency for C and D trace fast ZM echoes, and (f) direct fast ZM echoes reflecting from bottom of the satellite.

Ray tracing calculations have been performed for this case to explain two different traces, diffuse D trace echoes, and direct echoes. For D trace echoes, ray tracing calculations are performed assuming $r_b = 7570$ km, temperature $T = 4500$ K, ion composition $H = 0.0200$, $He = 0.0001$, and $O = 0.9799$, and N_e ~1262 e/cc at the satellite, corresponding to f_{pe} obtained from f_z observed at 237.2 kHz. The range of f_{pe} at the satellite is $318 - 319$ kHz (from local f_z 236-237.2 kHz). This is equivalent to N_e ~1253-1263 e/cc. f_{ce} at the equator is taken as ~784 kHz matched to the $f_{ce,IGRF}$ at the satellite (~192.1 kHz) when the 237.2 kHz frequency was transmitted (237.2 kHz is the f_z at the satellite).

The ray tracing density model and results are shown in Figure 5.18. Figure 5.18(a) shows the N_e profile along the geomagnetic field line at L =2.116, that is, when the 237.2 kHz frequency was transmitted. The N_e profile obtained from the ZM sounding (solid green curve) is compared to N_e obtained from in-situ measurements and empirical density models (see comparison Tables 5.22-5.23).

Figure 5.18(b) shows f_z, f_{pe}, and f_{ce} (solid curves) along the geomagnetic field line. The f_z

profile forms a narrow ZM cavity within which frequencies in the range of ∼237-261 kHz can be trapped. Thus, the bandwidth of the ZM cavity is ∼24 kHz. The altitude of the cavity ranges from ∼2785-7105 km, making the length of the cavity ∼4520 km.

Figure 5.18(c) shows the t_g-f plot of the C(green) and D(red) traces when no duct is assumed in the model. The t_g of the C and D fast ZM echoes matches with the observed average t_g of the C and D traces. However, it can be seen that the observed spread in the t_g of the D trace is quite large compared to that obtained from the ray tracings. This spread in t_g indicates multipath propagation of the waves in the presence of ducts. Since higher traces (C+D, C+2D, etc.) are not observed, the depletion level should be low enough so as to obtain only the ducted D trace echoes. To simulate the ducted echoes, a density depleted duct is introduced in the density model. Figure 5.18(d) shows the t_g-f plots for a typical duct of half-width ∼0.04 (∼255 km at the equator) and density depletion of 2%. It is noted that both ducted and nonducted (shown as black dots) echoes are obtained in the presence of ducts. The ducted echoes are shown as red circles. The nonducted echoes are shown as black dots. From the figure it is observed that multiple echoes are formed, which gives the spread in t_g of the D trace. It is also observed that the t_g of the nonducted C trace matches only the upper edge of the observed echoes in the frequency range of $248 - 316$ kHz. Moreover, the C trace starts from a higher t_g range at $f_{z,sat}$, whereas the direct echoes are observed to start near the zero apparent range of the plasmagram.

To simulate the direct trace echoes, we assume another density model. This is based on the assumption that the ZM cutoff profile in some other direction may not contain a ZM cavity so that the waves may reflect close to the satellite. Thus, for direct trace echoes, ray tracing calculations are performed assuming $r_b = 7570$ km, temperature $T = 5500$ K, ion composition $H = 0.0050$, $He = 0.0051$, and $O = 0.9899$, and N_e ∼1262 e/cc at the satellite. The f_{ce} at the equator is taken as ∼784 kHz matched to the $f_{ce,IGRF}$ at the satellite (∼192.1 kHz) when the $f = 237.2$ kHz frequency was transmitted (237.2 kHz is the f_z at the satellite).

Figure 5.18(a)-(b) shows the N_e profile (dashed green curve), f_z, f_{pe}, and f_{ce} (dashed curves) for the direct trace density model. The f_z profile does not form a ZM cavity. It is also observed that the f_z profile below the satellite lies at a much higher altitude compared to the model for the D trace echoes. Due to this, the reflection altitude of rays propagating earthward of the IMAGE lies much closer to the satellite and, therefore, the rays accumulate smaller time delays. Figure 5.18(c) shows the t_g-f plot of the direct (blue) trace when no duct is assumed in the model. The t_g of the direct trace (which propagates in the fast Z mode) matches the average time delays of the observed

direct fast ZM echoes. The spread in t_g indicates the presence of field aligned irregularities in the vicinity of the satellite. Figure 5.18(d) shows the t_g-f plot of the direct fast ZM trace in presence of a duct. The t_g of the direct fast ZM echoes are shown as blue curves. From the figure it is observed that the time delays of the direct trace do not differ much from the case when no ducts were present.

Figure 5.18(e) shows the ray paths of the ducted D (black and red rays) trace echoes reflecting from above the satellite altitude and nonducted fast ZM echoes (blue and green rays) reflecting from below the satellite altitude. It is observed that D trace rays injected at θ_i ~34.18° and ~39.83° are weakly guided by the duct and form retracing and looping echoes, respectively, after propagating close to the field line of the satellite and reflecting from above. The nonducted fast ZM echoes D2(dd'd" at ~56.62°) and C(cc'c" at ~112.73°) are also observed. Figure 5.18(f) shows the ray paths of the direct fast ZM (red ray) injected at θ_i ~118.93°, which reflects from below the satellite altitude. It is observed that the ray reflects very close to the satellite and therefore accumulates a smaller time delay.

5.4.7 27 June 2005 10:54:55 UT: Fast Z Mode and Direct Echoes Inside the Plasmasphere

Figure 5.10(g) shows plasmagrams of fast ZM echoes received by the X antenna on RPI/IMAGE on 27 June 2005 at 10:54:55 UT inside the plasmasphere. Satellite position is shown as 'g' in Figure 5.10(h). IMAGE was at an altitude of 5056 km, $\lambda_m = 21.5°$, MLT =6.7, L =2.07. $f_{z,sat}$ is 252.8 kHz and the upper cutoff frequency of D trace $f_{D,max}$, is 263.6 kHz. Only D trace echoes are observed.

The direct trace starts from ~260 kHz at ~10 ms and slowly rises in t_g to ~40 ms at 315.2 kHz. The lower cutoff of the direct trace may start from $f_{z,sat}$, but it could not be distinguished from the strong signal of the D trace echoes. The D trace echoes have a large t_g spread. The t_g spread of the D trace ranges from ~9-32 ms. This large t_g spread indicates the presence of field aligned irregularities. Diffuse slow ZM echoes are also observed in the frequency range of 317.6 - 326 kHz. The lower cutoff frequency of slow ZM echoes at 317.6 kHz is identified as the local f_{pe}. f_{ce} resonances are also observed at f_{ce} = 152.0 kHz (not shown in the plasmagram) and at $2f_{ce}$ = 291.2. $f_{ce,IGRF}$ at this location is 145.3 kHz.

Ray tracing calculations have been performed for this case to explain two different traces, diffuse D trace echoes and direct fast ZM echoes. For D trace echoes, ray tracing calculations are performed

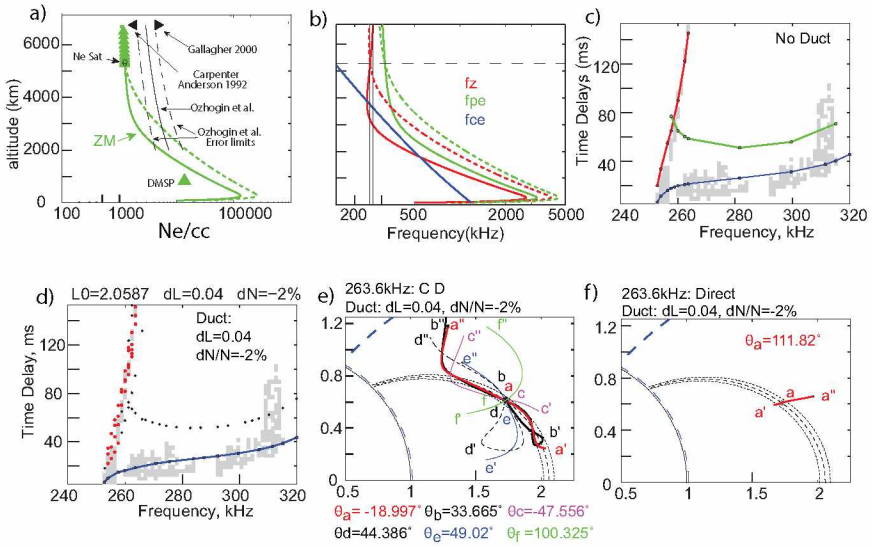

Figure 5.19 N_e along the geomagnetic field line from two density models that explain the ducted D trace echoes (solid curve) and direct fast ZM echoes (dashed curve) for 27 June 2005 10:54:55 UT. (b) Characteristic frequencies f_z, f_{pe} and f_{ce} along the geomagnetic field line. (c) t_g-f comparison of fast ZM echoes calculated from ray tracings with observations when no duct is present. (d) t_g-f comparison of fast ZM echoes calculated from ray tracings with observations when duct of half-width 0.04 L and depletion of 2% is present. (e) Ray paths of 263.6 kHz frequency for C and D trace fast ZM echoes, and (f) direct fast ZM echoes reflecting from bottom of the satellite.

assuming r_b = 7570 km, temperature T = 3500 K, ion composition H = 0.007, He = 0.001, and O = 0.992, and N_e ~1247 e/cc at the satellite, corresponding to the f_{pe} obtained from f_z observed at 252.8 kHz. The range of f_{pe} at the satellite is $317 - 318$ kHz (from local f_z of 251.6 -252.8 kHz). This is equivalent to N_e ~1244-1254 e/cc. The N_e chosen at the reference point viz., ~1247 e/cc lies within this range. The f_{ce} at the equator is taken as ~779 kHz, matched to the $f_{ce,IGRF}$ at the satellite (~147 kHz) when the f = 252.8 kHz frequency was transmitted (252.8 kHz is the f_z at the satellite).

The ray tracing density model and the t_g-f plot are shown in Figure 5.19. Figure 5.19(a) shows the N_e profile along the geomagnetic field line L =2.059, that is, when 252.8 kHz frequency was transmitted by the IMAGE. The N_e profile obtained from the ZM sounding (solid green curve) is compared to the N_e obtained from in-situ measurements and empirical density models (see comparison Tables 5.22-5.23).

Figure 5.19(b) shows f_z, f_{pe}, and f_{ce} (solid curves) along the geomagnetic field line. The f_z profile forms a narrow ZM cavity within which frequencies in the range of ~252-264 kHz can be trapped. The bandwidth of the ZM cavity is found to be ~12 kHz. The altitude of the cavity ranges from ~2975-6745 km, which makes the length of the cavity ~3770 km. Figure 5.19(c) shows the t_g-f

plot of the C(green) and D(red) traces when no duct is assumed in the model. The t_g of the D fast ZM echoes matches with the observed average t_g of the D trace. The calculated t_g of the C trace overestimates the observed t_g. It can be seen that there is a spread in t_g of the D trace. This spread in t_g indicates multipath propagation of the waves in the presence of ducts. Since higher traces (C+D, C+2D, etc.) are not observed, the depletion level should be low enough to obtain only the ducted D trace echoes. To simulate the ducted echoes, a density depleted duct is introduced in the density model. Figure 5.19(d) shows the t_g-f plots for a typical duct of half-width $\sim$0.04 ($\sim$255 km at the equator) and density depletion of 2%. It is noted that both ducted and nonducted echoes are obtained in the presence of ducts. The ducted echoes are shown as red circles. The nonducted echoes are shown as black dots. When a weaker duct is present, multiple echoes are formed, which gives the spread in t_g of the D trace. It is also observed that the t_g of the nonducted C trace does not match observed direct trace echoes.

To simulate the direct trace echoes, we assume another density model. This is based on the assumption that the ZM cutoff profile in some other direction may not contain a ZM cavity, so that the waves may reflect close to the satellite. Thus, for direct trace echoes, ray tracing calculations are performed assuming r_b = 7570 km, temperature T = 4000 K, ion composition H = 0.0008, He = 0.0001, and O = 0.9991, and $N_e \sim$ 1249 e/cc at the satellite. The ray tracing density model and results are shown in Figure 5.19. Figure 5.19(a)-(b) shows the plot of N_e profile (dashed green curve), f_z, f_{pe}, and f_{ce} (dashed curves) for direct trace density model. The f_z profile does not form a ZM cavity. It is also observed that the f_z profile below the satellite lies at a much higher altitude compared to the model for D trace echoes. Due to this, the reflection altitude of rays propagating earthward of the IMAGE lies much closer to the satellite, therefore the rays accumulate smaller time delays. Figure 5.19(c) shows the t_g-f plot of the direct(blue) trace when no duct is assumed in the model. The t_g of the direct trace matches the average t_g of the observed direct fast ZM echoes. This spread in t_g indicates the presence of field aligned irregularities in the vicinity of the satellite. Figure 5.19(d) shows the t_g-f plot of the direct fast ZM trace in the presence of a duct (blue curve). It is observed from the figure that the time delays of the direct trace do not differ much from the case when no duct is present.

Figure 5.19(e) shows the ray paths of the ducted D trace echoes (black and red rays) reflecting from above the satellite altitude and nonducted fast ZM echoes (blue, green, and black-dashed rays) reflecting from below the satellite altitude. It is observed that D trace rays injected at $\theta_i \sim -19°$ and $\sim$33.67° are guided by the duct and form retracing and looping echoes, respectively, after

propagating close to the field line of the satellite and reflecting from above. The nonducted fast ZM echoes C (ff'f" at ∼100.33°), D1(cc'c" at ∼−47.56°), D2 (ee'e" at ∼49.02°), and D3 (dd'd" at ∼44.39°) are also observed. Figure 5.19(f) shows the ray paths of the direct fast ZM (red ray), injected at θ_i ∼111.82°, which reflect from below the satellite altitude. It can be seen that the rays reflect very close to the satellite and therefore accumulate smaller time delays.

5.4.8 Summary of Results: 27 June 2005 Case Analysis

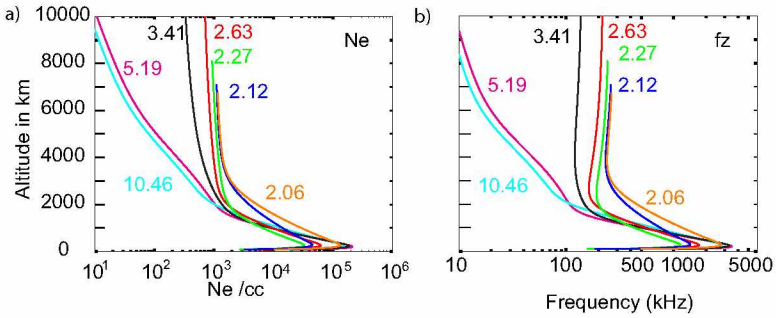

Figure 5.20 Summary of (a) field aligned N_e profile, (b) field aligned f_z profile across L-shells from 10.46 to 2.06 (along the IMAGE orbit crossing the plasmapause) for all the successive fast ZM cases observed on 27 June 2005.

Figure 5.20(a) shows field aligned N_e profiles across L-shells of 10.46-2.06 obtained from the ZM soundings of the nonducted and ducted fast ZM echoes observed on 27 June 2005. The plasmapause is at L =4.68. The profiles of N_e and f_z for L =10.46 and L =5.19 are outside the plasmapause, while the rest of the profiles are inside the plasmasphere. It is observed that for L-shells greater than 4.68, the N_e at higher altitudes (≥ 2000 km) decreases much more rapidly than that for L shells inside the plasmasphere. This is due to the assumption of r^{-n} type variation of N_e outside the plasmasphere and diffusive equilibrium distribution inside the plasmasphere. At any given altitude ≥ 2000 km, N_e increases from higher to lower L-shells. For the cases in which nonducted fast ZM echoes are observed simultaneously with WM echoes (L =10.46 − 3.41), the N_e obtained from ZM sounding compares well with the in-situ N_e measurements made at lower altitudes from the CHAMP satellite (∼25%-60%), and the DMSP f-13 satellite (∼15%-50%). At F2 peak, the N_e matches within ∼20%-50% with the IRI model values. Table 5.21 lists the duct and ZM cavity parameters obtained from the successive cases. Tables 5.22-5.23 compare ZM sounding with in-situ measurements and empirical density model values.

For cases inside the plasmasphere for which only fast ZM echoes are observed (L =2.63 − 2.06), the ZM sounding provides the N_e profile from the lowest to highest reflection altitude of the ZM

Table 5.21 Summary of the ZM sounding of ZM cavities from successive cases observed on 27 June 2005. The parameters are UT, altitude in km, geomagnetic latitude (λ_m), L-shell(L), ZM cavity band width, ZM cavity length, duct half-width (in L-shell) and duct depletion level. *Note: altitude and λ_m are taken for first observed frequency of the ZM echoes.*

UT	Altkm	λ_m	L-shell	ZM Cavity BW (kHz)	ZM Cavity Length (km)	ΔL (Equator)	ΔN/N Depletion
10:36:55 UT	1936	69.3	10.4627	-	-	-	-
10:39:55 UT	2278	59.2	5.1897	-	-	-	-
10:42:54 UT	2729	49.7	3.4139	-	-	-	-
10:45:55 UT	3299	40.6	2.6297	50	8600	160-380	1.5% - 4%
10:48:55 UT	3936	32.5	2.2733	35	6550	160-380	3% - 6%
10:51:54 UT	4598	25.6	2.1160	24	4520	250	2%
10:54:55 UT	5288	19.5	2.0589	12	3770	250	2%

Table 5.22 Summary of the comparison of N_e obtained from ZM sounding of the successive cases observed on 27 June 2005 with in-situ N_e measurements. The parameters are UT, altitude in km, geomagnetic latitude (mlat), L-shell(L), percent difference of N_e measured from CHAMP satellite (~350 km), DMSP f-13 satellite (~850 km), RPI passive experiment near the equator, and RPI active experiment (f_{pe} resonance). *Note: altitude and λ_m are taken for first observed frequency of the ZM echoes.*

UT	Alt(km)	λ_m	L-shell	CHAMP 350 km	DMSP 850 km	RPI (DS) Equator	RPI (Plsmg) Satellite
10:36:55 UT	1936	69.3	10.4627	~25%	~15%	-	~1%
10:39:55 UT	2278	59.2	5.1897	~48%	~48%	-	~19%
10:42:54 UT	2729	49.7	3.4139	~58%	~29%	-	~19%
10:45:55 UT	3299	40.6	2.6297	-	~23%	13%-17%	~4%
10:48:55 UT	3936	32.5	2.2733	-	~32%	8%-12%	~3%
10:51:54 UT	4598	25.6	2.1160	-	-	-	~1%
10:54:55 UT	5288	19.5	2.0589	-	-	-	~1%

Table 5.23 Summary of the comparison of N_e obtained from ZM sounding of the successive cases observed on 27 June 2005 with empirical models. The parameters are UT, altitude in km, geomagnetic latitude (mlat), L-shell(L), percent difference of N_e at F2 peak from IRI-2012 model, Ozhogin et al., (2012), Carpenter and Anderson, (1992) and Gallagher et al., (2000) empirical models. *Note: altitude and λ_m are taken for first observed frequency of the ZM echoes.*

UT	Altkm	λ_m	L-shell	IRI-2012 F2 peak	Oz2012 2000 km	Oz2012 Equator	CA1992 Equator	G2000 Equator
10:36:55 UT	1936	69.3	10.4627	∼22%	-	-	-	-
10:39:55 UT	2278	59.2	5.1897	∼47%	-	-	-	-
10:42:54 UT	2729	49.7	3.4139	∼35%	∼67%	∼78%	∼38%	∼85%
10:45:55 UT	3299	40.6	2.6297	-	∼101%	∼73%	∼51%	∼81%
10:48:55 UT	3936	32.5	2.2733	-	∼114%	∼83%	∼49%	∼109%
10:51:54 UT	4598	25.6	2.1160	-	∼58%	∼83%	∼43%	∼117%
10:54:55 UT	5288	19.5	2.0589	-	∼32%	∼85%	∼44%	∼121%

waves along the field line, which generally lies between ∼1500-10,000 km altitude. It is also observed that the N_e profile obtained from the empirical models of Carpenter and Anderson (1992), Gallagher et al., (2000), and Ozhogin et al., (2012) overestimate the N_e obtained from ZM sounding.

Ozhogin et al., (2012) model overestimates the N_e at 2000 km altitude by ∼32%- 114% and at the equator by ∼73%-85%. The empirical model of CA1992 and G2000 overestimate the equatorial densities by ∼38%-51% and 81%-121%, respectively. For the two cases (L =2.63 and 2.27) for which in-situ N_e measurements are available from the RPI passive experiment at the equator, the N_e obtained from the ZM sounding matches quite well, within ∼8% - 17%. For all cases, N_e from ZM sounding matches within ∼1% - 19% with in-situ N_e obtained from the RPI active experiment (obtained from the f_{pe} resonance frequency) at the satellite altitude. Thus, ZM sounding in the mid latitude region better estimates the field aligned N_e as compared to the empirical models of CA1992, G2000, and Oz2012.

From the ray tracing simulation of the ducted fast ZM cases, it is found that ducts of half-width in the range of ∼160-380 km in the equatorial plane and depletion of ∼1.5%-6% are required to guide the fast ZM waves and obtain the t_g-f dispersion that matches with the observations. Figure 5.20(b) shows field aligned f_z profiles across L-shells of 10.46-2.06. It is clearly observed from the figure that for L-shells outside the plasmapause, the ZM cavity is not formed. As the satellite moves inward toward lower L-shells, the satellite encounters the ZM cavity from L =2.63 to L =2.06. The

bandwidth of the ZM cavity decreased from ∼50 kHz at L =2.63 to ∼12 kHz at L =2.06. Cavity length decreased from ∼8600 km at L =2.63 to ∼3770 at L =2.06. Thus, it is evident that the ZM cavity is a real phenomenon that occurs inside the plasmasphere and is less likely to be observed outside the plasmasphere.

From the ray tracing calculations of direct fast ZM echoes, it is found that the f_z profile may deviate quite significantly in some other directions compared to the field aligned variation. This means that the fast ZM waves can propagate and reflect from an altitude close to the satellite and from a vertically downward and inward direction to obtain smaller time delays, while fast ZM waves can be guided along the geomagnetic field line to obtain the ducted echoes. This is a direct consequence of the three-dimensional structure of the ZM cavity within the magnetosphere.

Chapter 6 Conclusions and Future Work

6.1 Summary of Major Results and Conclusion

Z mode (ZM) sounding on IMAGE/RPI provides a powerful method for measurements of (1) field aligned electron density distribution; (2) field aligned magnetospheric ducts; and (3) ZM cavities from the ~1000-10,000 km altitude range. In its 5.8 year mission the IMAGE satellite, operating in the frequency range of 14 kHz-1000 kHz at altitudes ~600-10,000 km, has detected a variety of ducted and nonducted ZM echoes at all latitudes, altitudes and magnetic local times (MLTs) in the frequency range of ~20 kHz to ~800 kHz. Three basic types of Z-mode activities have been observed by the IMAGE/RPI, namely: (1) ducted or trapped echoes; (2) nonducted or direct echoes; and (3) diffuse or scattered echoes. For this research work, a thorough data survey has been performed for fast ZM echoes for the years 2001-2005. Carpenter et al., (2003) have studied 34 days of IMAGE/RPI soundings from 28 June 2001-31 July 2001 in the low altitude range of ~1000-5000 km and have categorized ~75 cases of the ducted fast Z mode echoes as AB or CD type ducted fast Z mode echoes on the basis of the altitude of the satellite with respect to the altitude of the minimum in ZM cutoff frequency profile along the geomagnetic field line. The AB and CD type echo traces have very distinct signatures on the plasmagram. Using the same categorization as Carpenter et al., (2003), we have surveyed and expanded the data set from year 2001-2005 of the IMAGE mission and from ~600-10,000 km altitude range. Besides finding the categories of ducted echoes as described by Carpenter et al., (2003), we have found several new observations and features of nonducted and ducted ZM echoes. We have found observations of nonducted fast ZM echoes that were reflected from altitudes below as well as above the IMAGE satellite within the Z mode cavities. We have also found the first observations of nonducted and ducted fast ZM echoes reflecting from above the satellite altitude outside the plasmasphere. We have discovered a new phenomenon: a frequency gap in echo traces reflecting from below the satellite altitude. This phenomenon is important as it is a direct manifestation of the presence of ducts in the magnetosphere.

About 5000 cases of fast ZM echoes have been observed on IMAGE/RPI out of 72,000 plasmagrams surveyed. About 30% of the cases are ducted and have been observed in the altitude range of ~600-10,000 km, invariant latitude range of 30° - 70°, and at all MLTs. Most of the ducted echoes were observed within the ZM cavity inside the plasmasphere. About 50% of ducted fast ZM cases were observed when the satellite was above $R_{f_{z,min}}$ (CD type), ~35% were observed when the satellite was below $R_{f_{z,min}}$ (AB type), and the remaining 15% are epsilon-shaped signatures reflecting from the conjugate hemispheres when the duct extends there. About 3500 cases are nonducted fast ZM echoes observed in the altitude range of ~600-10,000 km, 20°-89° invariant latitudes, and at all MLTs. Nonducted echoes have been found at all latitudes but were most common poleward of the plasmasphere. About 250 and 400 cases of ducted and nonducted fast ZM echoes have been observed with specularly reflected Whistler mode (SR-WM) echoes, respectively. About 370 best cases of nonducted and ducted fast ZM echoes were chosen for a detailed survey. Several important features have been identified for ducted and nonducted fast ZM echoes. The propagation of ZM waves is affected by the relative position of the satellite with respect to the ZM cavity and the plasmapause, and by the presence of ducts and field aligned irregularities. These effects are manifested in the echo traces recorded by IMAGE/RPI. From the occurrence pattern of fast ZM echoes, it is observed that a majority of fast ZM echoes are observed inside the plasmasphere. Out of 370 best cases of fast ZM echoes, 10 cases of new observations of echoes reflecting from above the satellite altitude outside the plasmapause and 5 cases within the plasmapause have been reported. These findings suggests that the ZM cavity mostly exists within the plasmasphere and rarely outside.

About 18 cases of new observations of ducted ZM echoes reflecting simultaneously within the ZM cavity and from the conjugate hemisphere have been observed in the L-shell range of ~1.5-2 at ~1400-3000 km. These cases are observed inside the ZM cavity when the duct extends to the conjugate hemisphere. The t_g-f dispersion of these cases suggests that the ZM waves reflect within the ZM cavity and also from the conjugate hemisphere. This important result can be used to design the future magnetospheric sounders such that the ZM echoes can be used to remotely sense the field aligned electron density distribution in the altitude range extending from ~1000 km below the satellite altitude up the equator in the local as well as the conjugate hemisphere. Another important new phenomenon of frequency gaps in echo traces reflecting from below the satellite altitude (C trace) has been observed in the data. It has been confirmed from ray tracings that the frequency gap could occur only in the presence of a duct and is a direct consequence of the

propagation effects of fast ZM waves in the presence of ducts. This phenomenon is important as it is a direct manifestation of the presence of ducts in the magnetosphere and is important to study the dispersion relations and wave properties in the vicinity of characteristic plasma frequency (f_{pe}).

A new ZM sounding technique has been developed for nonducted and ducted ZM echoes to measure the field aligned electron density distribution, duct parameters (ΔL, ΔN/N), ZM cavity parameters: $f_{z,min}$, $R_{f_{z,min}}$, ZM cavity bandwidth, and ZM cavity altitude extent. Carpenter et al., (2003) have provided a ZM inversion method to measure the field aligned electron density distribution only above the satellite altitude. The ZM sounding method developed in this work provides the field aligned electron density distribution both below and above the satellite altitude. The ZM sounding technique employs tools such as ZM inversion, density model optimization, and automatic ray tracing and echo finding programs to analyze the ZM echoes and measure the aforementioned parameters.

Ray tracing simulations have been performed for four representative cases of fast ZM echoes (two cases of nonducted and two cases of ducted each for AB and CD type) and seven successive cases of nonducted and ducted fast ZM echoes observed by the IMAGE satellite during a plasmapause crossing. A detailed ray tracing study of CD type ducted fast ZM echoes (10 July 2001 case) has been performed to demonstrate the technique of ZM sounding of field aligned electron density, ducts and ZM cavity parameters. In the absence of ducts, four nonducted echoes are obtained in the ZM cavity. Three of the echoes (C, D1, and D2) retrace their path after reflection while one (D3) forms a loop. When ducts are introduced in the density model, ray tracings show that both nonducted as well as ducted echoes are obtained. The propagation, guidance, and reflection of nonducted and ducted fast ZM waves in the magnetosphere have been studied in detail with the help of refractive index diagrams, Poeverlein's construction and Snell's Law. This is the first study to give a detailed account of the propagation and reflection of ZM waves within the ZM cavity in the magnetosphere.

The ray tracing results show that a density depleted duct is required to guide fast ZM waves and the average time delays (t_g) of the nonducted and ducted traces depend upon the electron density distribution along the geomagnetic field line and the shape of the ZM cavity. Ducted propagation of waves could be understood in terms of the superposition of waves in the transverse (perpendicular to $\mathbf{B_0}$) and longitudinal (parallel to $\mathbf{B_0}$) directions. Ducted echoes are characterized by: (1) average time delay; (2) time delay spread; (3) time integral relationship of higher order ducted traces with the principal traces; (4) lower and upper cutoff frequencies; and (5) frequency gap in C trace

echoes. The average time delay is determined from the average density model. The time delay spread, cutoffs, and frequency gap depend upon the duct parameters : duct half-width (ΔL) and density depletion (ΔN/N). It is observed that keeping depletion level (ΔN/N) constant, both the upper cutoff frequency (f_{uc}) and time delay spread (Δt_g) decrease with increasing duct half-width (ΔL). Keeping ΔL constant, both the f_{uc} and Δt_g increase with increasing ΔN/N. A frequency gap in echo trace reflecting from below the satellite altitude (C trace) has been obtained through ray tracing analysis and has also been observed in the data recorded by IMAGE/RPI. The gap in the C trace is due to the propagation effect of ZM waves in the presence of ducts and the occurrence of dimple-shaped refractive index surfaces near f_{pe}. The frequency gap range depends upon the duct parameters ΔL and ΔN/N and it increases with increasing ΔL and decreases with increasing depletion ΔN/N. Another interesting result of the ray tracings are the echoes that are obtained from within the ZM cavity in the local hemisphere as well as from the conjugate hemisphere when the duct extends there. This type of echo has been observed and recorded on the IMAGE/RPI plasmagrams.

From ZM sounding of eleven cases of nonducted and ducted fast ZM echoes (Tables 6.1 and 6.2 summarize the results of ZM sounding of the eleven cases), it is found that a density depleted duct of half width ranging between ~160-500 km in the equatorial plane, and depletions of ~1% - 6%, is required to guide ZM waves. Ray tracing simulations for seven successive cases of nonducted and ducted fast ZM echoes observed during plasmapause crossing by the IMAGE satellite have been performed to study the latitudinal variation of field aligned electron density and ZM cavity parameters. The bandwidth of the ZM cavity lies in the range of ~12-53 kHz and the length of the cavity ranges from ~3800-15,000 km. It is found that fast ZM echoes provide measurements of magnetospheric ducts and electron densities along the field lines in the altitude range of ~1000-10,000 km (and ~90-10,000 km if accompanied by Whistler mode echoes). The ZM sounding in the mid-latitude region agrees with the in-situ measurements of the RPI, DMSP, and CHAMP satellites and better estimates the field aligned N_e as compared to empirical models of Carpenter and Anderson (1992), Gallagher et al., (2000), and Ozhogin et al., (2012). It is found that for L-shells outside the plasmapause, the ZM cavity is not formed. The ZM cavity starts to form when the satellite moves inside the plasmasphere. Thus, it is evident that the ZM cavity is a real phenomenon that occurs inside the plasmasphere, but rarely observed outside the plasmasphere.

A new method of ZM sounding has been developed in this research to measure the magnetospheric duct parameters, field aligned electron density distribution and Z mode cavity parameters.

The detailed study of the nonducted and ducted wave propagation, reflection and guidance will prove to be fundamental in our understanding of the natural wave emissions in the magnetosphere. The measurement of duct parameters, and field aligned electron density distribution and ZM cavities is important to understand the wave-particle interactions and propagation of natural wave emissions, and in improving and building the empirical/theoretical density models to accurately represent the magnetospheric density profiles and density structures. In this research we have provided a first direct measurement of magnetospheric ducts obtained from ducted ZM echoes observed inside the ZM cavities and also the first quantitative measurement of the ZM cavities in the low to mid-latitude region of the magnetosphere in the altitude range of ~1000-10,000 km. The plasma density structures such as the magnetospheric ducts are important to study because they play an important role in the generation and propagation of natural wave emissions, and wave-particle interactions and therefore influence the radiation belt dynamics. The radiation belts (or "Van Allen Radiation Belts") are magnetospheric region of space which contains highly energetic particles trapped in the Earth's magnetic field [Van Allen and Frank, 1959]. Radiation belt particles can adversely affect the spacecraft electronics and endanger human life in space. Therefore, modeling the radiation belt is an important part of the space-weather program. Duct sounding has been used successfully for measuring the field aligned electron density distribution. The data set of Z mode sounding obtained from the IMAGE satellite mission provides an unique opportunity to measure the instantaneous electron density measurements in low to mid-latitude region of the magnetosphere in the altitude range of ~1000-10,000 km. Instantaneous measurement of electron density distribution is of prime importance in the development of empirical models. These empirical models provide a benchmark for testing the theoretical and numerical models of the magnetospheric density distribution and to study the wave-particle interactions, wave propagation, plasma loss and refilling processes and with forecasting of space weather. These models are necessary for optimum performance of communication and navigational satellite systems. Empirical models of the plasmapause and equatorial density distribution are well developed. Unfortunately, the global representation of the off-equatorial electron density distribution is yet to be accurately represented by the existing statistical density models. This is because of the lack of measurement of instantaneous field aligned electron density distribution in this region. The statistical models of the off-equatorial density profile were developed from the electron density measurements made in-situ along the satellite orbits at limited geophysical locations and geomagnetic conditions and therefore do not accurately represents the latitudinal variation of electron density profile along the

field line. The fast Z mode data presented in this study were obtained in the low to mid-latitude region in the ~1000-10,000 altitude range is an ideal data set to fill this gap in the measurement and it provides an unique opportunity to measure the instantaneous field aligned electron density distribution and develop accurate empirical/statistical models of this poorly known region of space. Developing the empirical models that can accurately represent the density distribution and density structures in the magnetosphere is an important part of the space weather forecasting.

This research will prove to be fundamental in understanding the generation and propagation of natural ZM emissions in the magnetosphere, developing future magnetospheric sounders, and building empirical models of ducts and electron density distribution in the low to mid-latitude region of the magnetosphere and understand the role of ducts in the radiation belt dynamics. ZM sounding will be important in building the database of field aligned electron density distribution in the low to mid latitude region of the magnetosphere in the altitude range of ~1000-10,000 km. This database will be important to build the empirical density model or improve the existing empirical models of the off-equatorial electron density profile of the plasmasphere and understand the dynamics of this poorly known transition region between the plasmasphere and plasma trough during varying geomagnetic conditions.

6.2 Suggestions for Future Work

This research provides many new contributions to the understanding of the observations of ZM echoes, magnetospheric ducts and ZM cavities and the mechanisms of propagation, reflection, and guidance of ZM waves within the ZM cavity in the magnetosphere. This research also provides opportunities for future research.

1. The cold plasma density distribution of the plasmasphere plays an important role in the generation and propagation of natural waves and the overall dynamics of the radiation belt. Thus, it is important to measure the field aligned plasmaspheric density distribution and develop reliable empirical density models. Empirical models of the equatorial electron density are well developed [Carpenter and Anderson, 1992; Sheeley et al., 2001; Denton et al., 2004; Reinisch et al., 2004; Tu et al., 2006; Larsen et al., 2007], however, the global representation of the off-equatorial electron density distribution by statistical models [Gallagher et al., 1988, 1998, 2000; Goldstein et al., 2001; Denton et al., 2002, 2004, 2006; Huang et al., 2004; Reinisch et al., 2004; Tu et al., 2006] are not accurate. The reason of this inaccuracy is because these

electron density measurements have been made in-situ along the satellite orbits and in limited locations and geomagnetic conditions. The satellite orbit crosses the same L-shell at different MLTs and local time, therefore, the assumption that density values obtained at low and high latitude crossings of a particular flux tube may not be correct. Hence, to reduce the possibility of error the results are averaged over many crossings. However, the averaging of these in situ measurements masks the latitudinal dependence of the field aligned electron density distribution [Reinisch et al., 2001, 2009].

RPI onboard the IMAGE used the radio sounding technique to remotely measure the electron density in the magnetosphere [Reinisch et al.,2000]. Since the multiple point (20-100) measurements are made almost instantaneously, these field aligned distribution provide an accurate representation of the field line dependence of the electron density [Reinisch et al., 2009]. The ZM sounding in the ZM cavity has proved to be a very important diagnostic tool for the measurement of the field aligned electron density distribution. Unlike the free space mode echoes, the ZM echoes observed within the ZM cavity, reflects from the denser region below the satellite altitude as well as from the tenuous region above the satellite altitude. This means that with ZM sounding the electron density distribution can be obtained from regions which are tenuous as compared to the region near the spacecraft. In free space mode sounding, which is effective to a minimum altitude of ~2000 km, the echoes reflect from region where the electron density is greater than the electron density at the satellite. This implies that if the satellite is at higher latitude, the region from the satellite to the equator could not be sensed. The equatorial electron density can only be obtained when the RPI is present in the equatorial region at the time of sounding, or, the electron densities in the equatorial region can be interpolated from the known total electron content in that region. The total electron content can be known from the time delay of the conjugate lowest frequency echo. This introduces a possible uncertainty in the field line dependence in the equatorial region [Tu et al., 2006]. ZM sounding on the RPI complements the free space mode sounding. Along a field line within a ZM cavity, ZM waves can propagate and reflect from ~1000 km altitude (and from ~90 km altitude if accompanied by Whistler mode echoes) below the satellite and from the equatorial region above the satellite altitude, thus, providing the electron density distribution from ~1000 km up to the equator along a field line. A majority of cases of ZM echoes have been observed in the ~1000-10,000 km altitude range in the low to mid-latitude region of the magnetosphere inside the plasmasphere and near the plasmapause region. This

dataset presents an unique opportunity to make the field aligned electron density measurements using the newly developed ZM sounding method presented in this thesis and develop or improve the off-equatorial empirical density models. For example, about 1800 cases, out of ~5000 cases, of ducted and nonducted fast ZM echoes reflecting within the ZM cavity could provide measurements of field aligned electron density distribution in the altitude range of ~1000-10,000 km. As these cases have been obtained from 2001-2005 over a large range of local time, seasons, geophysical parameters and geomagnetic activities, the database of field aligned electron density profiles can be used to study its dependence on above mentioned parameters, study the plasmasphere loss and refilling processes and to build an empirical model that could accurately represent the off-equatorial density variation along the field line.

2. The existing ionospheric empirical models are not able to connect to a plasmasphere model smoothly. For example, the comparison of satellite data and total electron content data shows shortcomings in the IRI representation of the topside electron density profile. Recent attempts have been made to construct density models that can smoothly connect a topside ionospheric profile to a plasmasphere model, there is still a need to properly describe the transition of densities from high altitude into the topside ionosphere [Reinisch et al., 2007]. Global Core Plasma Model (GCPM) of the inner magnetosphere has been developed by integrating various region specific models for the core plasma density. There is an inherent discontinuity between the ionospheric model (IRI) and the plasmaspheric models used by the GCPM. A power law function is used to interpolate between the topside ionospheric profile of IRI and plasmaspheric density profile. Thus, there is a need to bridge the gap in the representation of the density distribution in the topside ionosphere F_2 peak to ~1 R_E (6370 km) altitude extending into the plasmasphere [Gallagher et al., 2000]. Plasmasphere, besides the ionosphere, is a significant source of the total electron content (TEC) which causes the global positioning satellite inaccuracies, range errors in the global navigation satellite system, and communication problems [Gerzen et al., 2015]. In a recent study it has been found that the plasmasphere TEC contribution from the Global Core Plasma Model (GCPM) and International Reference Ionosphere (IRI) extension with plasmasphere model contribute to ~10%-60% depending upon the time of the day, season, geographic location, solar activity, and geomagnetic activity. Thus, an accurate representation of the plasmaspheric density distribution is necessary for optimal performance of the GPS-TEC applications [Gulyaeva and Gallagher, 2007]. Gerzen et al., (2015) have pointed out that there is a need of additional mea-

surements of the electron density, e.g., the IMAGE RPI active mode sounding measurements, for modeling of the upper part of the plasmasphere (L > 4). ZM sounding in conjunction with Whistler mode sounding can provide the electron density distribution from ~90 km up to the equator along a field line that is the altitude range covering the topside ionosphere to the overlying plasmasphere. There are ~650 such cases from which these measurements can be made. These measurements can help to improve the existing topside ionospheric empirical density models that can connect smoothly to a overlying plasmasphere model.

3. The IMAGE mission has provided the first opportunity to directly measure magnetospheric ducts using radio sounding by RPI [Darrouzet et al., 2009]. The magnetospheric ducts are important to study because they play an important role in the generation and propagation of natural wave emissions, and wave-particle interactions and therefore influence the radiation belt dynamics. About 370 best cases of ducted and nonducted fast ZM echoes, out of ~5000 cases, have been identified that could provide measurements of magnetospheric ducts, field aligned electron density distribution, and ZM cavities in the altitude range of ~1000-10,000 km (and ~90-10,000 km if accompanied by Whistler mode echoes) at low to mid-latitude regions of the magnetosphere. As most of the ducted ZM echoes have been observed on field lines near the plasmapause, they provide an excellent opportunity to study electron density distribution and ducts in this region of space. The measurement of ducts can be used to build empirical models of ducts in the low to mid-latitude regions of the magnetosphere.

4. About 100 cases of frequency gaps in C trace echoes have been identified in our data set. The ray tracing analysis has confirmed that this phenomenon occurs only in the presence of ducts. As the frequency gap varies with varying duct parameters, analysis of these cases can provide accurate measurements of duct parameters from ZM sounding.

5. From the survey of fast ZM echoes, it is evident that conditions for the formation of ZM cavity are more favorable inside the plasmasphere than outside, as most of the echoes observed within the ZM cavity were also inside the plasmasphere. However, relatively few cases (~10 out of 370 best cases) in which echoes were reflected above the satellite altitude have been observed outside the plasmapause. This shows that the ZM cavity exists outside the plasmapause. Analysis of these cases may provide an understanding of the plasma conditions necessary for the formation of ZM cavities outside the plasmapause.

Table 6.1 Summary of measured duct and ZM cavity parameters from ZM sounding of 11 fast ZM cases. The parameters are date and time, traces observed, altitude in km, L-shell, duct half-width (in L-shell) in the equatorial plane, duct depletion level, ZM cavity bandwidth, and ZM cavity length.

Date Time	Traces	Alt(km)	L-shell	Half-width ΔL(Equator)	Depletion ΔN/N	ZM Cavity BW (kHz)	ZM Cavity Length (km)
10 Jul 2001 08:10 UT	CD Duc fZM	4138	2.6770	160-510 km	1% - 4%	39 kHz	8670 km
26 Jul 2001 08:23 UT	AB Duc fZM	3834	3.2070	160510 km	2% - 5%	50 kHz	11,400 km
19 Jun 2004 10:22 UT	CD Nduc fZM	5340	3.8080	NA	NA	29 kHz	15200 km
03 Aug 2005 19:14 UT	AB NDuc fZM + SR-WM	2354	2.5850	NA	NA	53 kHz	8500 km
27 Jun 2005 10:36 UT	A NDuc fZM + SR-WM	1936	10.4627	NA	NA	NA	NA
27 Jun 2005 10:39 UT	A NDuc fZM + SR-WM	2278	5.1897	NA	NA	NA	NA
27 Jun 2005 10:42 UT	A NDuc fZM + SR-WM	2729	3.4139	NA	NA	NA	NA
27 Jun 2005 10:45 UT	CD Duc fZM	3299	2.6297	160-380 km	1.5% - 4%	50 kHz	8600 km
27 Jun 2005 10:48 UT	CD Duc fZM	3936	2.2733	160-380 km	3% - 6%	35 kHz	6550 km
27 Jun 2005 10:51 UT	D Duc + Direct fZM	4598	2.1160	250 km	2%	24 kHz	4520 km
27 Jun 2005 10:54 UT	D Duc + Direct fZM	5288	2.0589	250 km	2%	12 kHz	3770 km

Table 6.2 Summary of the comparison of measured N_e from ZM sounding and in-situ and empirical density models for 11 fast ZM cases. The parameters are date and time, percent difference of N_e measured from Ionosonde, CHAMP satellite (∼350 km), DMSP f-13 satellite (∼850 km), RPI active experiment(f_{pe} resonance) at the satellite, RPI passive experiment near the equator, IRI-2012 model, Ozhogin 2012, Carpenter and Anderson 1992, and Gallagher 2000 empirical models.

Date Time	INSD	CHAMP (350km)	DMSP (850km)	RPI (Plg,Sat)	RPI (DS,Equ)	IRI2012 (F2)	Oz2012 (2000km)	Oz2012 (Sat)	Oz2012 (Equ)	CA1992 (Equ)	G2000 (Equ)
10 Jul 2001 08:10 UT	-	-	∼20%	-	∼18%-22%	-	∼10%	∼11%	∼51%	-	∼45%
26 Jul 2001 08:23 UT	-	-	∼12%	-	∼37%-41%	-	∼31%	∼38%	∼5%	-	∼34%
19 Jun 2004 10:22 UT	-	-	∼35%	∼10%	∼54%-57%	-	∼36%	∼54%	∼27%	-	∼44%
03 Aug 2005 19:14 UT	∼65%	∼4%	∼33%	-	-	∼46%	57%	∼58%	∼15%	∼10%	∼28%
27 Jun 2005 10:36 UT	-	∼25%	∼15%	∼1%	-	∼22%	-	-	-	-	-
27 Jun 2005 10:39 UT	-	∼48%	∼48%	∼19%	-	∼47%	-	-	-	-	-
27 Jun 2005 10:42 UT	-	∼58%	∼29%	∼19%	-	∼35%	∼67%	98%	∼78%	∼38%	∼85%
27 Jun 2005 10:45 UT	-	-	∼23%	∼4%	13%-17%	-	∼101%	107%	∼73%	∼51%	∼81%
27 Jun 2005 10:48 UT	-	-	∼32%	∼3%	8%-12%	-	∼114%	106%	∼83%	∼49%	∼109%
27 Jun 2005 10:51 UT	-	-	-	∼1%	-	-	∼58%	99%	∼83%	∼43%	∼117%
27 Jun 2005 10:54 UT	-	-	-	∼1%	-	-	∼32%	94%	∼85%	∼44%	∼121%

References

Angerami, J. J., and J. O. Thomas, Studies of planetary atmospheres 1. The distribution of electrons and ions in the Earth's exosphere, J. Geophys. Res., 69(21), 1964.

Angerami, J.J., Whistler duct deduced from VLF observations made with the Ogo 3 satellite near the magnetic equator, J. Geophys. Res, 75(31), 6115, 1970.

Banks, P. M., and T. E. Holzer, High-latitude plasma transport: The polar wind, J. Geophys. Res., 74(26), 6317-6332, 1969.

Barbosa, D. D., W. S. Kurth, S. L. Moses, and F. L. Scarf, Z mode radiation in Jupiter's Magnetosphere: The source of Jovian Continuum Radiation, J. Geophys. Res., 95(A6), 8187-8196, 1990.

Barker, F.S., D.R. Barraclough, V.P. Golovkov, P.J. Hood, F.J. Lowes, W. Mundt, N.W. Peddie, G.Z. Qi, S.P. Srivastava, R. Whitworth, D.E. Winch, T. Yukutake, and D.P. Zidarov, International Geomagnetic Reference Field Revision 1985, EOS, Trans. Am. Geophys. Union 67, 523-524, 1986.

Bauer, S. J., and R. G. Stone, Satellite observations of radio noise in the magnetosphere, Nature, 218, 1145-1147, 1968.

Beghin, C., J. L. Rauch, and J. M. Bosqued, Electrostatic plasma waves and HF auroral hiss generated at low altitude, J. Geophys. Res., 94, 1145-1147, 1989.

Bell, T. F., U. S. Inan, N. Haque, and J. S. Pickett, Source regions of banded chorus, Geophys. Res. Lett., 36(11), 2009.

Benson, R.F. ,and W. Calvert, ISIS-1 observations at the source of auroral kilometric radiation, Geophys. Res. Lett., 6, 479-482, 1979.

Benson, R. F., Remote detection of the maximum altitude of equatorial ionospheric plasma bubbles, Symposium on the Effect of the Ionosphere on Radiowave Systems, Washington, DC, April 14-16, 1981, Preprints., 1982.

Benson, R. F., Field-aligned electron density irregularities near 500 km: Equator to polar cap topside sounder observations, Radio Science, 20(3), 477-485, 1985.

Benson, R. F., Elusive upper hybrid waves in the auroral topside Ionosphere, Geophysical Monograph, Auroral Plasma Dynamics, 80, 267-274, 1993.

Benson, R.F., Evidence for the stimulation of field-aligned electron density irregularities on a short time scale by ionospaheric topside sounders, J. Atmos. Solar Terres. Phys., 59(18), 2281-2293, 1997.

Benson, R.F., V.A. Osherovich, J. Fainberg, and B.W. Reinisch, Classification of IMAGE/RPI-stimulated plasma resonances for the accurate determination of magnetospheric electron density and magnetic field values, J. Geophys. Res., 108(A5), 2003.

Benson, R.F., P.A. Webb, J.L. Green, L. Garcia, and B.W. Reinisch, Magnetospheric electron densities inferred from upper-hybrid band emissions, Geophys. Res. Lett., 31(20), L20803, 2004.

Benson, R.F., P.A. Webb, J.L. Green, D.L. Carpenter, V.S. Sonwalkar, H.G. James, and B.W. reinisch, Active wave experiments in space plasmas: The Z mode, Lect. Notes Phys., 687, 3-35, 2006.

Benson, R.F., Four Decades of Space-Borne Radio Sounding, Rad. Sci. Bull., 333, 24, 2010.

Budden, K. G., The Propagation of Radio Waves: The thoery of radio waves of low power in the Ionosphere and Magnetosphere, 669 pp., Cambridge University Press, New York, 1985.

Burch, J. L., IMAGE mission overview, Space Sci. Rev., 91, 1-14, 2000.

Burgess, W. C., and U. S. Inan, The Role of ducted Whistlers in the precipitation loss and equilibrium flux of radiation belt electrons, J. Geophys. Res., 98(A9), 15643-15665, 1993.

Burtis, W. J., Users' guide to the Stanford VLF ray tracing program, Radioscience Laboratory, Stanford University, Stanford, California, 1974.

Cairns, I. H., and J. D. Menietti, Radiation near $2f_p$ and intensified emissions near f_p in the dayside and nightside auroral region and polar cap, J. Geophys. Res., 102(A3), 4787, 1997.

Cairns, I. H., Measurement of the plasma density using the intensification of Z mode waves at the electron plasma frequency, Physical Review Letters, 82(3), 1999.

Calvert, W., and G. B. Goe, Plasma resonances in the upper ionosphere, J. Geophys. Res., 68(22), 6113-6120, 1963.

Calvert, W., and C. W. Schmid, Spread-F observations by the Alouette topside sounder satellite, J. Geophys. Res., 69(9), 1839-1852, 1964.

Calvert,W., Oblique Z-mode echoes in the topside ionosphere, J. Geophys. Res., 71(23), 5579-5583, 1966.

Calvert, W., and T. E. VanZandt, Fixed-frequency observations of plasma resonances in the topside ionosphere, J. Geophys. Res., 71(7), 1799-1813, 1966.

Calvert, W., The detectability of ducted echoes in the Magnetosphere, J. Geophys. Res., 86(A3), 1609-1612, 1981.

Calvert, W., Ducted Auroral Kilometric Radiation, Geophys. Res. Lett., 9(1), 56-59, 1982.

Calvert, W., and K. Hashimoto, The Magnetoionic modes and propagation properties of auroral radio emissions, J. Geophys. Res., 95(A4), 3943-3957, 1990.

Calvert,W., Wave ducting in different wave modes, J. Geophys. Res., 100(A9), 17491-17497, 1995.

Carpenter, D. L., Whistler evidence of a 'Knee' in the magnetospheric ionization density profile, J. Geophys. Res., 68(6), 1675-1682, 1963.

Carpenter, D. L., R. R. Anderson, T. F. Bell, and T. R. Miller, A comparison of equatorial electron densities measured by Whistlers and by a satellite radio technique, Geophys. Res. Lett., 8(10), 1107-1110, 1981.

Carpenter, D. L., and D. M. Sulic, Ducted Whistler Propagation Outside the Plasmapause, J. Geophys. Res., 93(A9), 9731-9742, 1988.

Carpenter, D. L., and H. R. Anderson, An ISEE/Whistler model of equatorial electron density in the Magnetosphere, J. Geophys. Res., 97(A2), 1097-1108, 1992.

Carpenter, D. L., B. L. Giles, C. R. Chappell, P. M. E. Decreau, R. R. Anderson, A. M. Persoon, A. J. Smith, Y. Corcuff, and P. Canu, Plasmasphere dynamics in the duskwide bulge region: A new look at an old topic, J. Geophys. Res., 98(A11), 19243-19271, 1993.

Carpenter, D.L., M.A. Spasojevic, T.F. Bell, U.S. Inan, B.W. Reinisch, I.A. Galkin, R.F. Benson, J.L. Green, S.F. Fung, and S.A. Boardsen, Small-scale field-aligned plasmaspheric density structures inferred from the Radio Plasma Imager on IMAGE, J. Geophys. Res., 107(A9), 1258, 2002.

Carpenter,D.L., T.F. Bell, U.S. Inan, R.F. Benson, V.S. Sonwalkar, B.W. Reinisch, and D.L. Gallagher, Z-mode sounding within propagation "cavities" and other inner magnetospheric regions by the RPI instrument on the IMAGE satellite, J. Geophys. Res., 108(A12), 1421, 2003.

Chapman,S.,and J. Bartels, Geomagnetism, Oxford Univ. Press, London, 1940.

Chapman, S., and V.C.A. Ferraro, A new theory of magnetic storms, Terr. Magn. Atmosph. Elec., 36, 171-186, 1931.

Clilverd, M. A., C. J. Rodger, R. Gamble, N. P. Meredith, M. Parrot, J.-J. Berthelier, and N. R. Thomson, Ground-based transmitter signals observed from space: Ducted or non-ducted?, J. Geophys. Res., 113, A04211, 2008.

Cohen, R., and K.L. Bowles, On the nature of equatorial spread F, J. Geophys. Res., 66, 1081-1106, 1961.

Colin, L., and K. L. Chan, Model studies of the Kinked Z trace in topside ionograms, Proceedings of The IEEE, 57(6), 1143-1147, 1969.

Colpitts, C. A., J. LaBelle, C. A. Kletzing, and P. H. Yoon, Further sounding rocket observations of structured Whistler mode auroral emissions, J. Geophys. Res., 115(A10), 2010.

Darrouzet, F., Dcrau, P. M. E., De Keyser, J., Masson, A. Gallagher, D. L., Santolik, O., Sandel, B. R., Trotignon, J. G., Rauch, J. L., Le Guirriec, E. Canu, P., Sedgemore, F.,

Andr, M., Lemaire, J. F., Density structures inside the plasmasphere: Cluster observations, Ann. Geophys., 22(7), 2577-2585, 2004.

Darrouzet, F., D.L. Gallagher, N. Andre, D.C. Carpenter, I. Dansouras, P.M.E. Decreau,J.De Keyser, R.E. Denton, J.C. Foster, J. Goldstein, M.B. Moldwin, B.W. Reinisch, B.R. Sandel, and J. Tu, Plasmaspheric density structures and dynamics: Properties observed by the CLUSTER and IMAGE missions, Space Sci. Rev., 145, 55-106, 2009.

Denton, R. E., J. Goldstein, and J. D. Menietti, Field line dependence of magnetospheric electron density, Geophys. Res. Lett., 29(24), 2002.

Denton, R. E., J. D. Menietti, J. Goldstein, S. L. Young, and R. R. Anderson, Electron density in the magnetosphere, J. Geophys. Res., 109, A09215, 2004.

Denton, R.E., K. Takahashi, I.A. Galkin, P.A.Nsumei, X. Huang, B.W. Reinisch, R.R. Anderson, M.K. Sleeper, and W.J. Hughes, Distribution of density along magnetospheric field lines, J. Geophys. Res., 111, A04213, 2006.

Denton, R. E., Y. Wang, P. A. Webb, P. M. Tengdin, J. Goldstein, J. A. Redfern, and B. W. Reinisch, Magnetospheric electron density long-term ($>$ 1 day) refilling rates inferred from passive radio emissions measured by IMAGE RPI during geomagnetically quiet times, J. Geophys. Res., 117, A03221, 2012.

De Soria-Santacruz, M., M. Spasojevic, and L. Chen, EMIC waves growth and guiding in the presence of cold plasma density irregularities, Geophys. Res. Lett., 40(10), 1940-1944, 2013.

Dougherty, J. P., and J. J. Monaghan, Theory of resonances observed in ionograms taken by sounders above the ionosphere, Proceedings of the Royal Society of London Series A, Mathematical and Physical Sciences, 289(1417), 214-234, 1966.

Dyson, P. L., Direct Measurements of the Size and Amplitude of Irregularities in the Topside Ionosphere, J. Geophys. Res., 74(26), 6291-6303, 1969.

Dyson, P. L., and R. F. Benson, Topside sounder observations of equatorial bubbles, Geophys. Res. Lett., 5(9), 1978.

Eckersley, T. L., Discussion of the ionosphere, Proc. Roy. Soc., A141, 708-715, 1933.

Eckersley, T. L., Coupling of the ordinary and extraordinary rays in the ionosphere, Proc. Phys. Soc., 63, 49-58, 1950.

Edgar, B. C., The structure of the magnetosphere as deduced from magnetospherically reflected whistlers, Ph.D. Thesis, Stanford University, Stanford, California, 1972.

Ellis, G. R., The Z propagation hole in the ionosphere, Journal of Atmospheric and Terrestrial Physics, 8, 43-54, 1956.

Farrell, W. M., Are Neptune's highly dispersed Whistlers really Z-mode radiation?, Geophys. Res. Lett., 23(5), 587-590, 1996.

Franklin, C.A. and M.A. Maclean, The design of swept-frequency topside sounders, Proc. IEEE, 57, 897-929, 1969.

Fung, S. F., R. F. Benson, D. L. Carpenter, B. W. Reinisch, and D. L. Gallagher, Investigations of irregularities in remote plasma regions by radio sounding: Applications of the radio plasma imager on IMAGE, Space Science Reviews, 91, 391-419, 2000.

Fung, S.F., R.F. Benson, D.L. Carpenter, J.L. Green, V. Jayanti, I.A. Galkin, and B.W. Reinisch, Guided echoes in the magnetosphere: Observations by the Radio Plasma Imager on IMAGE, Geophys. Res. Lett., 30(11), 1589, 2003.

Fung, S.F., and J.L. Green, Modeling of field-aligned guided echoes in the plasmasphere, J. Geophys. Res., 110, A01210, 2005.

Galkin, I., G. Khmyrov, A. Kozlov, B. Reinisch, X. Huang, and G. Sales, New tools for analysis of space-borne sounding data, paper presented at Proc. 2001 USNC/URSI Nat. Radio Sci. Meeting, Boston, MA, 2001.

Galkin, I. A., A pre-attentive vision model for automated data exploration applied to space plasma remote sensing data, PhD Dissertation, University of Massachusetts Lowell, 2004.

Gallagher, D. L., P. D. Craven, and R. H. Comfort, An Empirical model of the Earth's Plasmasphere, Adv. Space Res., 8(8), 15-24, 1988.

Gallagher, D. L., P. D. Craven, and R. H. Comfort, A simple model of magnetospheric trough total density, J. Geophys. Res., 103(A5), 9293-9297, 1998.

Gallagher, D. L., P. D. Craven, and R. H. Comfort, Global Core Plasma Model, J. Geophys. Res., 105(A8), 18819-18833, 2000.

Gerzen, T., J. Feltens, N. Jakowski, I. Galkin, R. Denton, B. Reinisch, and R. Zandbergen, Validation of plasmasphere electron density reconstructions derived from data on board CHAMP by IMAGE/RPI data, Adv. Space Res., 55(1), 170-183, 2015.

Glauert, S. A., and R. B. Horne, Calculation of pitch angle and energy diffusion coefficients with the PADIE code, J. Geophys. Res., 110(A4), 2005.

Goertz, C. K., and R. J. Strangeway, Plasma Waves, in Introduction to Space Physics, edited by M. G. Kivelson and C. T. Russell, pp. 356-399, Cambridge University Press, New York, 1995.

Goldstein, J., R. E. Denton, M. K. Hudson, E. G. Miftakhova, S. L. Young, J. D. Menietti, and D. L. Gallagher, Latitudinal density dependence of magnetic field lines inferred from Polar plasma wave data, J. Geophys. Res., 106(A4), 6195-6201, 2001.

Goldstein, J., Plasmasphere response: Tutorial and review of recent imaging results, Space Science Reviews, 124(1-4), 203-216, 2006.

Gross, S. H., and D. B. Muldrew, Uniformly spaced field-aligned ionization ducts, J. Geophys. Res., 89(A10), 8986-8996, 1984.

Gu, X., R. M. Thorne, B. Ni, and S.-Y. Ye, Resonant diffusion of energetic electrons by narrowband Z mode waves in Saturn's inner magnetosphere, Geophys. Res. Lett., 40(2), 255-261, 2013.

Gulyaeva, T. L., and D. L. Gallagher, Comparison of two IRI electron-density plasmasphere extensions with GPS-TEC observations, Adv. Space Res., 39(5), 744-749, 2007.

Gurnett, D. A., The Earth as a radio source: Terrestrial Kilometric Radiation, J. Geophys. Res., 79(28), 4227-4238, 1974.

Gurnett,D.A., S.D. Shawhan, and R.R. Shaw, Auroral Hiss, Z mode radiation, and auroral kilometric radiation in the polar magnetosphere: DE 1 Observations, J. Geophys. Res., 88(A1), 329-340, 1983.

Gurnett, D. A., and U. S. Inan, Plasma wave observations with the Dynamics Explorer 1 spacecraft, Reviews of Geophysics, 26(2), 285-316, 1988.

Hagg, E. L., E. J. Hewens, and G. L. Nelms, The Interpretation of topside sounder ionograms, Proceedings of The IEEE, 57(6), 949-960, 1969.

Haque, N., U. S. Inan, T. F. Bell, J. S. Pickett, J. G. Trotignon, and G. Facsk, Cluster observations of Whistler mode ducts and banded chorus, Geophys. Res. Lett., 38(18), 2011.

Haselgrove, J., Ray theory and a new method for ray tracing, in Physics of the Ionosphere, pp. 355-364, Physical Society, London, UK, 1955.

Hashimoto, K., and W. Calvert, Observation of the Z Mode 'With DE 1 and its analysis by three-dimensional ray tracing, J. Geophys. Res., 95(A4), 3933-3942, 1990.

Hashimoto, K., J. L. Green, R. R. Anderson, and H. Matsumoto, Review of kilometric continuum, Lect. Notes Phys., 687, 37-54, 2006.

Helliwell, R.A., Whistlers and related ionospheric phenomena, Stanford University Press, Stanford, California, 1965.

Herman, J. R., Spread F and ionospheric F region irregularities, Reviews of Geophysics, 4(2), 255-299, 1966.

Herring, R. N., Tracing of Z-mode rays in the magnetosphere, Journal of Atmospheric and Terrestrial Physics, 42, 885-897, 1980.

Herzberg, L. and G. L. Nelms, Ionospheric conditions following the proton flare of 7 July 1966 as deduced from the topside sounding, Ann. IQSY, 3, 426, 1968.

Hice, J. D., and B. Frank, Occurrence patterns of topside spread F on Alouette ionograms, J. Geophys. Res., 71(15), 3653-3664, 1966.

Horita, R. E., and H. G. James, Enhanced Z-mode radiation from a dipole, Adv. Space Res., 29(9), 1375-1378, 2002.

Horita, R. E., and H. G. James, Two-point studies of fast Z-mode waves with dipoles in the ionosphere, Radio Science, 39, RS4001, 2004.

Horne, R. B., Propagation to the ground at high latitudes of auroral radio noise below the electron gyrofrequency, J. Geophys. Res., 100(A8), 14637-14645, 1995.

Horne, R. B., and R. M. Thorne, Potential waves for relativistic electron scattering and stochastic acceleration during magnetic storms, Geophys. Res. Lett., 25(15), 1998.

Horne, R. B., The contribution of wave particle interactions to electron loss and acceleration in the Earths radiation belts during geomagnetic storms, in The review of radio science, edited by W. R. Stone, pp. 801-828, IEEE Press, Piscataway, 2002.

Horwitz, J. L., R. H. Comfort, and C. R. Chappell, A statistical characterization of plasmasphere density structure and boundary locations, J. Geophys. Res., 95(A6), 7937-7947, 1990.

Huang,X., B.W. Reinisch, P. Song, J.L. Green, and D.L. Gallagher, Developing an empirical density model of the plasmasphere using IMAGE/RPI observations, Adv. Space Res., 33, 829-832, 2004.

Huba, J. D., and G. Joyce, Equatorial spread F modeling: Multiple bifurcated structures, secondary instabilities, large density bite-outs, and supersonic flows, Geophys. Res. Lett., 34(7), 2007.

Huba, J. D., G. Joyce, and J. Krall, Three-dimensional equatorial spread F modeling, Geophys. Res. Lett., 35(10), 2008.

Hundhausen, A. J., The solar wind, in Introduction to Space Physics, edited by M. G. Kivelson and C. T. Russell, pp. 91-128, Cambridge University Press, New York, 1995.

Inan, U. S., and T. F. Bell, The plasmapause as a VLF wave guide, J. Geophys. Res., 82(19), 28192827, 1977.

Jackson , J.E., The reduction of topside ionograms to electron-density profiles, Proc. IEEE, 57, 960-976, 1969.

Jackson, J.E., E. R. Schmerling and J.H. Whitteker, Mini-review on topside sounding, IEEE Trans. Antennas Propagat. AP-28, 284-288, 1980.

James, H. G., Wave propagation experiments at medium frequencies between two ionospheric satellite, 1, General results, Radio Sci., 13(3), 531-542, 1978.

James, H. G., Wave propagation experiments at medium frequencies between two ionospheric satellites 3. Z mode pulses, J. Geophys. Res., 84(A2), 499-506, 1979.

James, H. G., Guided Z mode propagation observed in the OEDIPUS A tethered rocket experiment, J. Geophys. Res., 96(A10), 17865-17878, 1991.

James, H. G., Ionospheric duct parameters from a dual-payload radio-frequency sounder, J. Geophys. Res., 105(A9), 20909-20918, 2000.

James, H. G., Characteristics of field-aligned density depletion irregularities in the auroral ionosphere that duct Z- and X-mode waves, J. Geophys. Res., 111, A09315, 2006.

Jones, D., Mode-coupling of Z mode waves as a source of terrestrial kilometric and jovian decametric radiations, Astron. Astrophys., 55, 245-252, 1977.

Kimura,I., effects on ions on Whistler-mode ray tracing, Radio Sci., 1(3), 269, 1966.

Kivelson, M. G., and C. T. Russell, Introduction to Space Physics, Cambridge Universiry Press, New York, 1995.

Knecht, R. W., T. E. VanZandt, and S. Russell, First pulsed radio soundings of the topside of the ionosphere, J. Geophys. Res., 66(9), 3078-3081, 1961.

Koons, H. C., Observations of Large-Amplitude, Whistler mode wave ducts in the outer plasmasphere, J. Geophys. Res., 94(A11), 15393-15397, 1989.

Kozyra, J. U., V. K. Jordanova, R. B. Horne, R. M. Thorne, Modeling of the contribution of electromagnetic ion cyclotron (EMIC) waves to stormtime ring current erosion, in Magnetic Storms, edited by B. T. Tsurutami, W. D. Gonzalez, Y. Kamide, and J. K. Arballo, pp. 187-202, American Geophysical Union, Washington D.C., 1997.

Krauss-Varban, D., Beam instability of the Z mode in the solar wind, J. Geophys. Res., 94(A4), 3527-3534, 1989.

Kurth, W. S., D. A. Gurnett, J. D. Menietti, R. L. Mutel, M. G. Kivelson, and E. al., A close encounter with a Saturn kilometric radiation Source region, in Planetary Radio Emissions VII, edited by H. O. Rucker, W. Kurth, P. Louran and G. Fischer, pp. 75-85, Austrian Acad. of Sci. Press, Vienna, Graz, Austria, 2011.

Labelle, J.W., and R.A. Treumann, Auroral radio emissions, Space Sci. Rev., 101, 295, 2002.

Larsen, B. A., D. M. Klumpar, and C. Gurgiolo, Correlation between plasmapause position and solar wind parameters, J. Atmos. Solar Terr. Phys., 69(3), 334-340, 2007.

LeDocq, M. J., D. A. Gurnett, and R. R. Anderson, Electron number density fluctuations near the plasmapause observed by the CRESS spacecraft, J. Geophys. Res., 99(A12), 23661-23671, 1994.

Lemaire, J. F., Plasma distribution models in a rotating magnetic dipole and refilling of plasmaspheric flux tubes, Phys. Fluids B, Plasma Phys., 1, 1519, 1989.

Lemaire, J. F., and K. I. Gringauz, The Earth's plasmasphere, Cambridge University Press, Cambridge, 1998.

Lockwood, G.E.K., A ray-tracing investigation of ionospheric Z-mode propagation, Can. J. Phys., 40, 1840, 1962.

Lockwood, G.E.K., and L.E. Petrie, Low latitude field aligned ionization observed by the Alouette topside sounder, Planetary Space Sci., 11, 327, 1963.

Loftus, B.T., T.E. VanZandt, and W. Calvert, Observations of conjugate ducting by fixed-frequency topside sounder satellite, Ann. Geophys., 22, 530, 1966.

Masson, A., O. Santolik, D.L. Carpenter, F. Darrouzet, P.M.E. Decreau, F. E. Mazouz, J.L. Green, S. Grimald, M.B. Moldwin, F. Nemec, and V.S. Sonwalkar, Advances in plasmaspheric wave research with CLUSTER and IMAGE observations, Space Sci. Rev., 145, 137-191, 2009.

Mayank, K.,and V.S. Sonwalkar, Observations of ducted and nonducted fast Z mode echoes from IMAGE: Measurement of Z mode duct parameters, American Geophysical Union, Fall Meeting 2011, SM13D-2118, 5-9 December, San Francisco, California, USA, 2011.

Mayank, K.,and V.S. Sonwalkar, Measurement of field aligned electron density distribution, ducts, and Z-mode cavities from the ducted and nonducted fast Z-mode echoes observed on IMAGE, American Geophysical Union, Fall Meeting 2012, SM41A-2194, 3-7 December, San Francisco, California, USA, 2012.

McIlwain, C. E., Coordinates for mapping the distribution of magnetically trapped particles, J. Geophys. Res., 66(11), 3681-3691, 1961.

Menietti, J. D., and C. S. Lin, Ray tracing of Z Mode emissions from source regions in the high-altitude auroral zone, Geophys. Res. Lett., 12(6), 385-388, 1985.

Menietti, J. D., and C. S. Lin, Ray tracing survey of Z Mode emissions from source regions in the high-altitude auroral zone, J. Geophys. Res., 91(A12), 13559-13568, 1986.

Menietti, J. D., and P. H. Yoon, Plasma waves and fine structure emission bands within a plasmapause density cavity source region, Geophys. Res. Lett., 33(15), L15101, 2006.

Moldwin, M. B., M. F. Thomsen, S. J. Bame, and M. David, The fine-scale structure of the outer plasmasphere, J. Geophys. Res., 100(A5), 8021-8029, 1995.

Moullard, O., A. Masson, H. Laasko, M. Parrot, P. Decreau, O. Santolik, and M. Andre, Density modulated Whistler mode emissions observed near the plasmapause, Geophys. Res. Lett., 29(20), 2002.

Muldrew, D.B., Radio propagation along magnetic field-aligned sheets of ionization observed by Alouette topside sounder, J. Geophys. Res., 68, p5355, 1963.

Muldrew, D.B., Medium frequency conjugate echoes observed on topside-sounder data, Can. J. Phys., 45, 3935, 1967.

Muldrew,D.B., Nonvertical propagation and delayed-echo generation observed by the topside sounders, Proceeding of the IEEE, 57(6), 1097, 1969.

Muldrew, D. B., Preliminary results of ISIS 1 concerning electron-density variations, ionospheric resonances and cerenkov radiation, Space research 10th: proceedings of open meetings of working groups, 10, 786-794, 1970.

Muldrew, D. B., Electron resonances observed with topside sounders, Radio Sci., 7(8, 9), 779-789, 1972.

Muldrew, D. B., Characteristics of ionospheric bubbles determined from aspect sensitive scatter spread F observed with Alouette 1, J. Geophys. Res., 85(A5), 2115-2123, 1980a.

Muldrew, D. B., The formation of ducts and spread F and the initiation of bubbles by field-aligned currents, J. Geophys. Res., 85(A2), 613-625, 1980b.

Nagai, T., J. H. W. Jr., J. L. Green, C. R. Chappell, R. C. Olsen, and R. H. Comfort, First measurements of supersonic polar wind in the polar magnetosphere, Geophys. Res. Lett., 11(7), 669-672, 1984.

Nelms, G. L., R. E. Barrington, J. S. Belrose, T. R. Hartz, I. B. McDiarmid, and L. H. Brace, The Alouette 2 satellite, Can. J. Phys., 44, 1966.

Neugebauer, M., and C. W. Snyder, Mariner 2 observations of the solar wind, 1: Average properties, J. Geophys. Res., 71(19), 4469-4484, 1966.

Nishimura, Y., T. Ono, T. O. Iizima, A. Shinbori, A. Kumamoto, and H. Oya, Statistical studies of fast and slow Z-mode plasma waves in and beyond the equatorial plasmasphere based on long-term Akebono observations Earth Planets Space, 58, 343-346, 2006.

Nishimura, Y., T. Ono, M. Iizima, A. Shinbori, and A. Kumamoto, Generation mechanism of Z-mode waves in the equatorial plasmasphere, Earth Planets Space, 59, 1027-1034, 2007.

Ozhogin, P., J. Tu, P. Song, and B. W. Reinisch, Field-aligned distribution of the plasmaspheric electron density: An empirical model derived from the IMAGE RPI measurements, J. Geophys. Res., 117, A06225, 2012.

Persoon, A.M. , D.A. Gurnett, W.K. Peterson, J.H. Waite Jr. , J.L. Burch, and J.L Green, Electron density depletions in the nightside auroral zone, J. Geophys. Res., 93(A3), 1871-1895, 1988.

Petrie, L.E., Topside spread echoes, Can. J. Phys., 41, 194, 1963.

Platt, I.G., and P.L. Dyson, MF and HF propagation characteristics of ionospheric ducts, J. Atmos. Terr. Phys., 51, pp 759-774, 1989.

Poeverlein, H., Strahlwege von radiowellen in der Ionosphare, Z. Angew. Phys., 1, 1949.

Ratcliffe, J. A., The magneto-ionic theory and its application to the ionosphere, Cambridge University Press, New York, 1959.

Reinisch, B. W., D. M. Haines, K. Bibl, G. Cheney, I. A. Galkin, X. Huang, and E. al., The Radio Plasma Imager investigation on the IMAGE spacecraft, Space Science Reviews, 91, 319-359, 2000.

Reinisch, B.W., X. Huang, P. Song, G.S. Sales, S.F. Fung, J.L. Green, D.L. Gallagher, and V.M. Vasyliunas, Plasma density distribution along the magnetospheric field: RPI observations from IMAGE, Geophys. Res. Lett., 28, 4521-4524, 2001.

Reinisch, B.W., X. Huang, P. Song, J.L. Green, S.F. Fung, V.M. Vasyliunas, D.L. Gallagher, and B.R. Sandel, Plasmaspheric mass loss and refilling as a result of a magnetic storm, J. Geophys. Res., 109, A01202, 2004.

Reinisch, B.W., P. Nsumei, X. Huang, and D.K. Bilitza, Modeling the F2 topside and plasmasphere for IRI using IMAGE/RPI and ISIS data, Adv. Space Res., 39(5), 731-738, 2007.

Reinisch, B. W., M. B. Moldwin, R. E. Denton, D. L. Gallagher, H. Matsui, V. Pierrard, and J. Tu, Augmented empirical models of plasmaspheric density and electric field using IMAGE and CLUSTER data, Space Science Reviews, 145(1-2), 231-261, 2009.

Rodger, C. J., B. R. Carson, S. A. Cummer, R. J. Gamble, M. A. Clilverd, J. C. Green, J.-A. Sauvaud, M. Parrot, and J.-J. Berthelier, Contrasting the efficiency of radiation belt losses caused by ducted and nonducted Whistler-mode waves from ground-based transmitters, J. Geophys. Res., 115, A12208, 2010.

Santolik, O., F. Lefeuvre, M. Parrot, and J. L. Rauch, Propagation of Z-mode and Whistler-mode emissions observed by Interball 2 in the nightside auroral region J. Geophys. Res., 106(A10), 21137-21146, 2001.

Scarf, F. L., and C. R. Chappell, An association of magnetospheric Whistler dispersion characteristics with changes in local plasma density, J. Geophys. Res., 78(10), 1597-1602, 1973.

Sheeley, B. W., M. B. Moldwin, H. K. Rassoul, and R. R. Anderson, An empirical plasmasphere and trough density model: CRRES observations, J. Geophys. Res., 106(A11), 25631-25641, 2001.

Siscoe, G., D. Baker, R. Weigel, J. Hughes, and H. Spence, Roles of empirical modeling within CISM, Journal of Atmospheric and Solar-Terrestrial Physics, 66(15-16), 1481-1489, 2004.

Smith, R.L., Propagation characteristics of Whistlers trapped in field-aligned columns of enhanced ionization, J. Geophys. Res., 66, 3699-3707, 1961.

Smith, R. L., and J. J. Angerami, Magnetospheric properties deduced from OGO 1 observations of ducted and nonducted Whistlers, J. Geophys. Res., 73(1), 1-20, 1968.

Smith, Z. B., and D. L. Gallagher, IMAGE RPI reawakens plasmaspheric refilling research, AIP Conf. Proc., 974, 118-124, 2008.

Sonwalkar, V. S., Magnetospheric LF-, VLF-, and ELF-Waves, Handbook of Atmospheric Electrodynamics; Ed. Hans Volland, 2, 408-462, 1995.

Sonwalkar, V. S., X. Chen, J. Harikumar, D. L. Carpenter, and T. F. Bell, Whistler-mode wave-injection experiments in the plasmapshere with a radio sounder, Journal of Atmospheric and Solar-Terrestrial Physics, 63, 1199-1216, 2001.

Sonwalkar,V.S., D.L. Carpenter, T.F. Bell, M Spasojevic, U.S. Inan, J. Li, X. Chen, A Venkatasubramanian, J. Harikumar, R.F. Benson, W.W.L. Taylor, and B.W. Reinisch, Diagnostics of magnetospheric electron density and irregularities at $<$ 5000 km using Whistler and Z mode echoes from radio sounding on the IMAGE satellite, J. Geophys. Res., 109, A11212, 2004.

Sonwalkar, V.S., The influence of plasma density irregularities on Whistler-Mode wave propagation, Lect. Notes Phys., 687, 141-191, 2006.

Sonwalkar, V. S., D. L. Carpenter, A. Reddy, R. Proddaturi, S. Hazra, K. Mayank, and B. W. Reinisch, Magnetospherically reflected, specularly reflected, and backscattered Whistler mode radio-sounder echoes observed on the IMAGE satellite: 1. Observations and interpretation, J. Geophys. Res., 116, A11210, 2011a.

Sonwalkar, V. S., A. Reddy, and D. L. Carpenter, Magnetospherically reflected, specularly reflected, and backscattered Whistler mode radio-sounder echoes observed on the IMAGE satellite: 2. Sounding of electron density, ion effective mass (m_{eff}), ion composition (H^+,He^+,O^+), and density irregularities along the geomagnetic field line, J. Geophys. Res., 116, A11211, 2011b.

Stix, T. H., The theory of plasma waves, McGraw-Hill, New York, 1962.

Strangeways, H. J., and M. J. Rycroft, Trapping of Whistler-waves through the side of ducts, J. Atmos. Terr. Phys, 42, 983-994, 1980.

Summers, D., R. M. Thorne, and F. Xiao, Gyroresonant acceleration of electrons in the magnetosphere by superluminous electromagnetic waves, J. Geophys. Res., 106(A6), 10853-10868, 2001.

Tsyganenko, N. A., and D. P. Stern, Modeling the global magnetic field and the large-scale Birkeland current system, J. Geophys. Res., 101(A12), 27187-27198, 1996.

Tu, J., P. Song, B. W. Reinisch, X. Huang, J. L. Green, H. U. Frey, and P. H. Reiff, Electron density images of the middle- and high-latitude magnetosphere in response to the solar wind, Journal of Geophysical Research, 110, A12210, 2005.

Tu, J., P. Song, B. W. Reinisch, J. L. Green, and X. Huang, Empirical specification of field-aligned plasma density profiles for plasmasphere refilling, J. Geophys. Res., 111, A06216, 2006.

Van Allen, J., and L. A. Frank, Radiation around the Earth to a radial distance of 107,400 km, Nature, 183, 430-434, 1959.

Walker, R. J., and C. T. Russell, Solar-Wind interactions with magnetized planets, in Introduction to Space Physics, edited by M. G. Kivelson and C. T. Russell, pp. 164-182, Cambridge University Press, New York, 1995.

Xiao, F., S. Zhang, Z. Su, Z. He, and L. Tang, Rapid acceleration of radiation belt energetic electrons by Z-mode waves, Geophys. Res. Lett., 39(3), 2012.

Ye, S.-Y., J. D. Menietti, G. Fischer, Z. Wang, B. Cecconi, D. A. Gurnett, and W. S. Kurth, Z mode waves as the source of Saturn narrowband radio emissions, J. Geophys. Res., 115, A08228, 2010.

Yearby, K. H., M. A. Balikhin, Y. V. Khotyaintsev, S. N. Walker, V. V. Krasnoselskikh, H. S. C. K. Alleyne, and O. Agapitov, Ducted propagation of chorus waves: Cluster observations, Ann. Geophys., 29(9), 1629-1634, 2011.

Appendix A Summary of Ray Tracing Analysis

Summary of ray tracing analysis of the ducted and nonducted Z mode echoes case studies

Table A.1 Wavelength of fast ZM waves at different frequencies for 10 July 2001.

Frequency (kHz)	refractive index $\mu(\theta = 0°)$	wavelength $\lambda(km, \theta = 0°)$	refractive index $\mu(\theta = 90°)$	wavelength $\lambda(km, \theta = 90°)$
380	0.082	9.65	0.116	6.82
390	0.215	3.58	0.305	2.52
400	0.289	2.6	0.411	1.82
410	0.344	2.13	0.492	1.49

Table A.2 Comparison of duct half-width (ΔL) with wavelength (λ) for 10 July 2001.

Half-width ΔL	Half-width ΔL (km, @ sat)	nλ (380 kHz)	nλ (410 kHz)
0.01	21.1km	2.2λ– 3.1λ	9.9λ– 14.2λ
0.02	42.1km	4.4λ– 6.2λ	19.8λ 14.2λ
0.025	52.6 km	5.5λ– 7.7λ	24.7λ 35.3λ
0.03	63.2 km	6.5λ– 9.3λ	29.7λ 42.4λ
0.04	84.2 km	8.7λ– 12.3λ	39.5λ 56.5λ
0.05	105.3 km	10.9λ– 15.4λ	49.4λ 70.7λ
0.1	210.5 km	21.8λ– 30.9λ	98.8λ 70.7λ

Table A.3: 10 July 2001: Table of ray parameters of nonducted C trace echo injected at initial wave normal angles of 54°, 59.507°, and 65°. The parameters listed in the table are altitude in km, geomagnetic latitude, L-shell, wave normal angle, ray angle, refractive index at wave normal angle, refractive index in parallel direction, refractive index in transverse direction, electron plasma frequency, electron cyclotron frequency, Z mode cutoff frequency, group time delay, group velocity, and critical altitude label

Alt (km)	λ_m(°)	L	θ	θ_{ray}	μ	μ(0°)	μ(90°)	f_{pe}	f_{ce}	f_z	t_g (s)	V_g (km/s)	
4138	-38.243	2.6743	**54.0**	34.3	0.283	0.230	0.326	506.7	299.9	378.4	0.0000	7.31×10^4	R_{sat}
3268	-38.531	2.4725	43.7	384.9	0.305	0.264	0.373	533.9	390.1	373.4	0.0104	9.23×10^4	$Rf_{z,min}$
2429	-39.505	2.3203	19.4	9.9	0.073	0.071	0.100	595.7	518.5	390.4	0.0216	2.33×10^4	Before Ref
2413	-39.555	2.3193	-0.2	-0.1	0.042	0.042	0.059	597.7	521.7	391.3	0.0224	9.65×10^3	Ref, $\theta \sim 0°$
2406	-39.617	2.3218	-90.5	-91.1	0.038	0.027	0.038	598.5	523.2	391.6	0.0236	1.49×10^4	Ref,$\theta \sim 90°$
2422	-39.661	2.3290	-118.8	-137.7	0.086	0.068	0.096	596.5	520.6	390.5	0.0248	2.70×10^4	After Ref
3303	-39.659	2.5620	-128.6	-148.1	0.334	0.275	0.389	532.4	391.0	371.7	0.0366	9.17×10^4	$Rf_{z,min}$
4138	-40.029	2.8134	-120.8	-139.8	0.316	0.248	0.352	506.7	306.3	376.2	0.0465	7.55×10^4	R_{sat}
4138	-38.243	2.6743	**59.507**	40.5	0.293	0.230	0.326	506.7	299.9	378.4	0.0000	7.04×10^4	R_{sat}
3302	-38.066	2.4495	49.8	30.3	0.311	0.259	0.367	532.4	383.9	374.0	0.0105	8.75×10^4	$Rf_{z,min}$
2458	-38.5	2.2627	43.9	25.7	0.076	0.066	0.093	592.3	507.4	390.6	0.0223	1.27×10^4	Before Ref
2436	-38.516	2.2582	97.2	104.1	0.000	0.000	0.000	594.8	511.2	391.8	0.0240	2.73	Ref

Continued on next page

Table A.3 continued from previous page

Alt (km)	λ_m(°)	L	θ	θ_{ray}	μ	μ(0°)	μ(90°)	f_{pe}	f_{ce}	f_z	t_g (s)	V_g (km/s)	
2459	-38.499	2.2630	-136.1	-154.4	0.078	0.068	0.096	592.1	507.1	390.5	0.0258	2.92×10^4	After Ref
3307	-38.064	2.4507	-130.1	-149.6	0.311	0.259	0.367	532.2	383.2	374.0	0.0376	8.74×10^4	$Rf_{z,min}$
4138	-38.243	2.6743	-120.5	-139.5	0.293	0.230	0.326	506.7	299.9	378.4	0.0480	7.03×10^4	R_{sat}
4253	-38.344	2.7110	-118.7	-137.3	0.287	0.223	0.316	504.1	290.7	379.3	0.0497	6.70×10^4	$R > Rsat$
4138	-38.243	2.6743	**65.0**	47.5	0.302	0.230	0.326	506.7	299.9	378.4	0.0000	6.76×10^4	R_{sat}
3352	-37.58	2.4302	55.9	36.6	0.317	0.254	0.360	530.3	375.7	374.8	0.0105	8.24×10^4	$Rf_{z,min}$
2481	-37.383	2.2006	75.7	63.0	0.052	0.038	0.053	589.6	496.8	391.4	0.0241	9.41×10^3	Before Ref
2478	-37.365	2.1988	90.4	90.8	0.037	0.026	0.037	590.0	497.3	391.6	0.0246	8.51×10^3	Ref,$\theta \sim$90°
2483	-37.305	2.1966	-179.4	-179.7	0.036	0.036	0.051	589.4	496.0	391.4	0.0258	2.08×10^4	Ref, $\theta \sim 0°$
2501	-37.251	2.1979	-155.9	-167.5	0.069	0.066	0.093	587.4	492.7	390.6	0.0268	2.95×10^4	After Ref
3306	-36.437	2.3469	-131.5	-150.9	0.287	0.241	0.341	532.1	375.5	376.5	0.0387	8.23×10^4	$Rf_{z,min}$
4138	-36.461	2.5502	-119.4	-138.3	0.268	0.210	0.297	506.6	293.3	380.7	0.0500	6.39×10^4	R_{sat}

Table A.4: 10 July 2001: Table of ray parameters of nonducted D1 trace echo injected at initial wave normal angles of 168°, 173.583°, and 178°. The parameters listed are same as in table A.3

Alt (km)	$\lambda_m(°)$	L	θ	θ_{ray}	μ	$\mu(0°)$	$\mu(90°)$	f_{pe}	f_{ce}	f_z	t_g (s)	V_g (km/s)	
4138	-38.24	2.6743	**168.0**	174.4	0.232	0.230	0.326	506.7	299.9	378.4	0.0000	8.59×10^4	R_{sat}
4500	-36.72	2.6555	170.1	175.3	0.185	0.184	0.261	499.1	266.1	383.5	0.0060	6.78×10^4	
5111	-34.02	2.6233	152.7	165.6	0.039	0.037	0.052	488.6	218.4	391.5	0.0263	7.07×10^3	Before Ref
5127	-33.85	2.6169	88.4	86.8	0.018	0.013	0.018	488.4	217.1	391.8	0.0314	7.27×10^3	Ref
5091	-33.88	2.6105	28.7	15.3	0.040	0.037	0.053	488.9	219.2	391.5	0.0363	1.51×10^4	After Ref
4495	-35.72	2.5877	3.7	1.8	0.172	0.171	0.243	499.3	263.6	384.6	0.0548	6.38×10^4	
4139	-36.98	2.5852	-0.3	-0.1	0.216	0.216	0.307	506.8	295.8	380.0	0.0607	8.15×10^4	$\sim Rsat$
3953	-37.67	2.5863	-2.4	-1.1	0.236	0.236	0.334	511.3	314.6	377.6	0.0633	8.94×10^4	$R < Rsat$
4138	-38.24	2.6743	**173.583**	177.0	0.230	0.230	0.326	506.7	299.9	378.4	0.0000	8.64×10^4	R_{sat}
4497	-36.88	2.6662	176.5	178.3	0.186	0.186	0.264	499.1	266.8	383.3	0.0057	6.90×10^4	
5184	-34.37	2.6625	-179.1	-179.5	0.027	0.027	0.037	487.6	215.3	391.7	0.0276	4.84×10^3	Before Ref
5199	-34.32	2.6626	179.6	180.0	0.000	0.000	0.000	487.3	214.3	391.8	0.0314	1.66×10	Ref
5164	-34.44	2.6625	0.8	0.4	0.040	0.040	0.057	487.8	216.6	391.4	0.0372	1.66×10^4	After Ref
4496	-36.88	2.6662	-3.5	-1.7	0.186	0.186	0.264	499.1	266.9	383.2	0.0572	6.95×10^4	

Continued on next page

Table A.4 continued from previous page

Alt (km)	$\lambda_m(^\circ)$	L	θ	θ_{ray}	μ	$\mu(0^\circ)$	$\mu(90^\circ)$	f_{pe}	f_{ce}	f_z	t_g (s)	V_g (km/s)	
4138	-38.24	2.674	-6.416	-2.969	0.23	0.230	0.326	506.68	299.9	378.4	0.0628	8.65×10^4	$\sim Rsat$
4043	-38.61	2.6774	-7.3	-3.4	0.241	0.240	0.340	508.9	309.6	377.2	0.0641	9.06×10^4	$R < Rsat$
4138	-38.24	2.6743	**178.0**	179.1	0.230	0.230	0.326	506.7	299.9	378.4	0.0000	8.65×10^4	R_{sat}
4500	-36.98	2.6739	-178.5	-179.3	0.186	0.186	0.264	499.0	266.5	383.2	0.0055	6.94×10^4	
5212	-34.75	2.6933	-158.0	-168.6	0.040	0.039	0.055	487.1	214.7	391.5	0.0260	7.16×10^3	Before Ref
5250	-34.71	2.6991	-87.4	-84.8	0.014	0.010	0.014	486.6	212.5	391.8	0.0315	7.27×10^3	Ref
5229	-34.86	2.7045	-20.7	-10.7	0.039	0.038	0.054	486.9	214.1	391.5	0.0368	1.56×10^4	After Ref
4504	-37.81	2.7347	-8.6	-4.1	0.198	0.197	0.279	499.0	269.3	382.2	0.0587	7.32×10^4	
4136	-39.27	2.7521	-10.9	-5.0	0.243	0.240	0.342	506.7	303.8	377.1	0.0643	9.03×10^4	$\sim Rsat$

Table A.5: 10 July 2001: Table of ray parameters of nonducted D2 trace echo injected at an initial wave normal angle of 107.576°. The parameters listed in the table are altitude in km, geomagnetic latitude, L-shell, wave normal angle, ray angle, refractive index at wave normal angle, refractive index in parallel direction, refractive index in transverse direction, electron plasma frequency, electron cyclotron frequency, Z mode cutoff frequency, group time delay, group velocity, and critical altitude label

Alt (km)	λ_m(°)	L	θ	θ_{ray}	μ	μ(0°)	μ(90°)	f_{pe}	f_{ce}	f_z	t_g (s)	V_g (km/s)	
4138	-38.2	2.6743	**107.576**	121.4	0.313	0.230	0.326	506.7	299.9	378.4	0.0000	6.42×10^4	R_{sat}
4100	-36.1	2.5161	102.8	113.7	0.289	0.208	0.295	507.6	295.4	380.9	0.0066	5.68×10^4	
3904	-33.2	2.3039	92.8	95.4	0.259	0.183	0.260	512.5	301.7	383.3	0.0173	4.88×10^4	$\theta > 90°$
3098	-29.9	1.9791	71.7	56.8	0.168	0.124	0.176	542.0	369.6	387.8	0.0397	3.72×10^4	
2891	-29.6	1.9245	68.3	51.5	0.062	0.047	0.066	554.1	393.5	391.2	0.0474	7.48×10^3	Before Ref
2865	-29.6	1.9181	-9.3	-4.7	0.000	0.000	0.000	555.8	396.7	391.8	0.0509	2.39	Ref
2893	-29.6	1.9249	-111.7	-128.4	0.064	0.048	0.068	554.0	393.3	391.2	0.0545	1.70×10^4	After Ref
3101	-29.9	1.9799	-108.2	-123.1	0.169	0.125	0.176	541.8	369.3	387.8	0.0623	3.76×10^4	
3901	-33.2	2.3017	-87.4	-84.9	0.259	0.183	0.259	512.5	301.9	383.4	0.0845	4.88×10^4	$\theta < 90°$
4100	-36.1	2.5168	-77.2	-66.3	0.289	0.208	0.295	507.6	295.5	380.9	0.0953	5.69×10^4	
4138	-38.2	2.6743	-72.4	-58.6	0.313	0.230	0.326	506.7	299.9	378.4	0.1019	6.44×10^4	$\sim Rsat$
4137	-39	2.7286	-71.2	-56.8	0.322	0.237	0.337	506.7	302.6	377.5	0.1039	6.69×10^4	$R < Rsat$

Table A.6: 10 July 2001: Table of ray parameters of nonducted D3 trace echo injected at an initial wave normal angle of 121.086°. The parameters listed in the table are altitude in km, geomagnetic latitude, L-shell, wave normal angle, ray angle, refractive index at wave normal angle, refractive index in parallel direction, refractive index in transverse direction, electron plasma frequency, electron cyclotron frequency, Z mode cutoff frequency, group time delay, group velocity, and critical altitude label

Alt (km)	λ_m(°)	L	θ	θ_{ray}	μ	μ(0°)	μ(90°)	f_{pe}	f_{ce}	f_z	t_g (s)	V_g (km/s)	
4138	-38.243	2.6743	**121.086**	140.2	0.292	0.230	0.326	506.7	299.9	378.4	0.0000	7.06×10^4	R_{sat}
4270	-35.074	2.4938	113.9	131.2	0.240	0.182	0.258	503.7	278.0	383.6	0.0097	5.33×10^4	
4265	-33.286	2.3892	105.3	118.2	0.214	0.156	0.221	503.9	272.3	385.8	0.0167	4.32×10^4	
4127	-31.504	2.2669	90.1	90.2	0.195	0.138	0.195	506.9	276.8	387.1	0.0259	3.64×10^4	$\theta = 90°$
3899	-30.565	2.1744	75.8	63.9	0.192	0.140	0.198	512.7	292.5	386.9	0.0336	3.91×10^4	
3412	-30.168	2.0546	56.3	397.1	0.187	0.150	0.213	528.2	336.8	386.0	0.0449	4.93×10^4	
2830	-31.152	1.9719	9.7	4.9	0.085	0.084	0.119	558.3	409.4	389.9	0.0580	3.33×10^4	Near Ref Pt
2810	-31.246	1.9715	0.2	0.1	0.077	0.077	0.109	559.7	412.6	390.2	0.0588	3.08×10^4	Near Ref Pt,θ ~0°
2766	-31.565	1.9757	-43.5	-25.3	0.071	0.062	0.087	562.9	420.1	390.8	0.0613	2.27×10^4	Near Ref Pt
2784	-32.168	2.0055	-90.3	-90.0	0.139	0.098	0.139	561.5	420.9	389.2	0.0659	2.80×10^4	Near Ref Pt,θ ~90°
2889	-32.706	2.0528	-100.2	-109.4	0.205	0.147	0.208	554.2	409.6	386.1	0.0697	4.29×10^4	Near Ref Pt
3450	-34.621	2.2764	-101.8	-111.8	0.305	0.219	0.311	526.6	351.7	379.3	0.0814	6.15×10^4	
4138	-38.2433	2.6754	-90.8	-91.7	0.326	0.230	0.326	506.6	299.8	378.4	0.0969	6.04×10^4	~Rsat

Table A.7 10 July 2001: Group velocity V_g, in km/s, for Z mode waves at various initial wave normal angles and at various frequencies for plasma condition at the satellite, f_{pe} = 506.7 kHz, f_{ce} = 300.7 kHz, and at the equator, f_{pe} = 441.8 kHz, f_{ce} = 47.9 kHz.

Satellite: f_{pe}=506.7 kHz, f_{ce}=300.7 kHz							
f / θ(°)	∼ 0°	10°	30°	45°	60°	75°	∼ 90°
378.2 ($f_{z,sat}$)	2.29×10^3	779	754	714	655	587	554
392	8.79×10^4	8.74×10^4	8.37×10^4	7.82×10^4	7.10×10^4	6.42×10^4	6.13×10^4
410	1.27×10^5	1.26×10^5	1.18×10^5	1.08×10^5	9.65×10^4	8.85×10^4	8.58×10^4
420	1.42×10^5	1.40×10^5	1.29×10^5	1.16×10^5	1.03×10^5	9.59×10^4	9.37×10^4
432	1.57×10^5	1.54×10^5	1.37×10^5	1.20×10^5	1.07×10^5	1.01×10^5	9.97×10^4
440	1.65×10^5	1.61×10^5	1.39×10^5	1.20×10^5	1.07×10^5	1.03×10^5	1.02×10^5
480	1.94×10^5	1.69×10^5	9.61×10^4	8.30×10^4	8.73×10^4	9.34×10^4	9.59×10^4
507 ($f_{pe,sat}$)	2.91×10^3	3.18×10^3	2.43×10^4	4.49×10^4	6.27×10^4	7.96×10^4	7.81×10^4

Equator: f_{pe}=441.8 kHz, f_{ce}=47.9 kHz							
f / θ(°)	∼ 0°	10°	30°	45°	60°	75°	∼ 90°
418.5 ($f_{z,sat}$)	3.11×10^3	671	649	615	564	506	477
420	2.59×10^4	2.58×10^4	2.48×10^4	2.32×10^4	2.10×10^4	1.87×10^4	1.76×10^4
426	5.75×10^4	5.68×10^4	5.11×10^4	4.43×10^4	3.72×10^4	3.23×10^4	3.06×10^4
432	7.61×10^4	7.30×10^4	5.43×10^4	4.01×10^4	3.13×10^4	2.73×10^4	2.62×10^4
436	8.60×10^4	7.54×10^4	3.90×10^4	2.53×10^4	1.98×10^4	1.80×10^4	1.76×10^4
441.8 ($f_{pe,sat}$)	3.41×10^3	1.35×10^2	8.94×10^2	1.77×10^3	2.64×10^3	3.27×10^3	3.50×10^3

Table A.8: 10 July 2001: Table of ray parameters of ducted C trace echo injected at an initial wave normal angle of −32.077°. The parameters listed in the table are altitude in km, geomagnetic latitude, L-shell, wave normal angle, ray angle, refractive index at wave normal angle, refractive index in parallel direction, refractive index in transverse direction, electron plasma frequency, electron cyclotron frequency, Z mode cutoff frequency, group time delay, group velocity, and critical altitude label

Alt (km)	λ_m(°)	L	θ(°)	θ_{ray}(°)	μ	μ(0°)	μ(90°)	f_{pe}	f_{ce}	f_z	t_g (s)	V_g (km/s)	
4138	-38.243	2.6743	**-32.077**	-16.51	0.249	0.230	0.326	506.7	299.9	378.4	0.0000	8.20×10^4	R1, R_{sat}
4021	-38.946	2.6969	-27.80	-13.88	0.254	0.239	0.339	510.2	312.7	377.2	0.0021	8.69×10^4	
3714	-40.297	2.7214	0.07	0.03	0.253	0.253	0.359	520.7	347.6	375.1	0.0063	9.75×10^4	R2, θ ∼0°
3488	-40.934	2.7115	16.89	7.92	0.280	0.274	0.387	527.1	374.8	372.0	0.0088	1.04×10^5	
3166	-41.576	2.6750	25.20	12.29	0.306	0.291	0.411	538.6	417.1	369.0	0.0120	1.10×10^5	R3, $Rf_{z,min}$
2780	-42.499	2.6424	0.17	0.08	0.260	0.260	0.366	563.4	477.0	373.3	0.0158	1.04×10^5	R4, θ ∼0°
2541	-43.667	2.6734	-36.44	-19.88	0.250	0.226	0.319	583.1	523.0	377.6	0.0189	8.69×10^4	R5
2379	-45.134	2.7598	-63.92	-45.65	0.077	0.059	0.084	610.0	561.3	390.8	0.0238	1.44×10^4	Before Ref
2379	-45.218	2.7679	-92.28	-94.54	0.052	0.036	0.052	610.8	561.8	391.4	0.0246	1.47×10^4	R6, Ref
2397	-45.241	2.7759	-148.12	-162.75	0.062	0.058	0.081	609.1	558.4	390.9	0.0259	2.74×10^4	After Ref
2538	-44.866	2.7837	179.86	180.09	0.163	0.163	0.230	592.6	529.2	384.4	0.0292	6.76×10^4	θ ∼0°
3246	-41.425	2.6850	141.62	159.32	0.326	0.290	0.410	534.9	405.7	369.2	0.0390	1.04×10^5	$Rf_{z,min}$
3654	-39.175	2.6185	179.93	179.75	0.238	0.238	0.337	523.3	348.9	377.1	0.0447	9.16×10^4	θ ∼0°

Continued on next page

Table A.8 continued from previous page

Alt (km)	$\lambda_m(°)$	L	$\theta(°)$	$\theta_{ray}(°)$	μ	$\mu(0°)$	$\mu(90°)$	f_{pe}	f_{ce}	f_z	t_g (s)	V_g (km/s)	
4139	-38.244	2.6747	-137.73	-156.37	0.263	0.229	0.326	506.5	299.5	378.5	0.0508	7.82×10^4	R_{sat}

Table A.9: 10 July 2001: Table of ray parameters of ducted D trace echo injected at an initial wave normal angle of 138.544°. The parameters listed in the table are same as given in table A.8

Alt (km)	λ_m(°)	L	θ(°)	θ_{ray}(°)	μ	μ(0°)	μ(90°)	f_{pe}	f_{ce}	f_z	t_g (s)	V_g (km/s)	
4138	-38.243	2.6743	**138.544**	156.97	0.262	0.230	0.326	506.7	299.9	378.4	0.0000	7.86×10^4	R1, R_{sat}
4255	-37.361	2.6403	145.94	162.00	0.216	0.198	0.280	505.6	287.1	382.0	0.0027	6.99×10^4	R2
4420	-36.519	2.6226	-179.97	-179.99	0.152	0.152	0.216	503.8	271.4	386.1	0.0063	5.68×10^4	R3, θ ~0°
4611	-36.122	2.6421	-134.89	-153.70	0.172	0.148	0.210	498.3	256.2	386.4	0.0103	4.96×10^4	R4
4751	-36.109	2.6747	-122.01	-141.42	0.189	0.150	0.213	494.5	246.6	386.3	0.0131	4.61×10^4	R5, Center of duct
4840	-36.148	2.6990	-122.05	-141.45	0.160	0.128	0.181	493.8	240.9	387.8	0.0152	3.92×10^4	
4972	-36.071	2.7252	-179.51	-179.76	0.051	0.051	0.071	493.9	232.4	391.2	0.0199	1.84×10^4	R6, θ ~0°
4982	-35.624	2.6972	96.25	102.24	0.139	0.099	0.140	491.4	230.5	389.5	0.0249	2.62×10^4	
4954	-35.371	2.6737	90.53	91.04	0.158	0.112	0.158	491.1	231.5	388.8	0.0269	2.88×10^4	Before Ref
4951	-35.345	2.6711	90.00	90.00	0.158	0.112	0.158	491.2	231.6	388.8	0.0272	2.87×10^4	R7, Ref
4947	-35.318	2.6685	89.46	88.94	0.157	0.111	0.157	491.2	231.8	388.8	0.0274	2.85×10^4	After Ref
4831	-35.036	2.6229	-1.92	-0.96	0.050	0.050	0.070	496.2	238.2	391.2	0.0341	1.99×10^4	θ ~0°
4745	-36.132	2.6749	-58.67	-39.35	0.191	0.151	0.215	494.6	247.1	386.2	0.0412	4.65×10^4	Center of duct
4559	-37.542	2.7290	-0.96	-0.46	0.148	0.148	0.210	501.5	264.4	386.4	0.0479	5.53×10^4	θ ~0°
4140	-38.241	2.6746	39.95	381.94	0.260	0.230	0.327	506.7	300.1	378.4	0.0545	7.93×10^4	R_{sat}

Table A.10: 10 July 2001: Ray parameters along the ray path for ducted C trace echo for 420 kHz injected at initial wave normal angles −1.481° and 13.610°. The parameters listed in the table are altitude in km, geomagnetic latitude, L-shell, wave normal angle, ray angle, refractive index at wave normal angle, electron plasma frequency, electron cyclotron frequency, Z mode cutoff frequency, group time delay, group velocity, and critical altitude label

Alt (km)	λ_m(°)	L	θ(°)	θ_{ray}(°)	μ	f_{pe}	f_z	f_{ce}	t_g (s)	V_g (km/s)	
4151	-38.100	2.6672	**-1.481**	-0.50	0.386	506.4	378.8	298.3	0.0000	1.41×10^5	R_{sat}
3153	-41.848	2.6943	-8.57	-3.20	0.419	539.8	369.2	420.0	0.0080	1.56×10^5	$Rf_{z,min}$
2485	-44.262	2.7104	0.01	0.00	0.359	591.2	381.0	536.4	0.0130	1.42×10^5	$\theta \sim 0°$
2001	-45.701	2.6942	-2.04	-0.08	0.000	668.5	419.8	644.5	0.0191	7.33	before Ref
2001	-45.701	2.6942	-104.36	-117.12	0.000	668.5	419.8	644.5	0.0191	1.62	Ref
2001	-45.701	2.6942	-93.81	-97.59	0.000	668.5	419.8	644.5	0.0191	1.86×10^4	After Ref
2486	-44.260	2.7104	179.99	180.00	0.360	591.1	381.0	536.2	0.0252	1.43×10^5	$\theta \sim 0°$
3154	-41.846	2.6942	171.43	176.80	0.419	539.8	369.2	419.9	0.0302	1.56×10^5	$Rf_{z,min}$
4152	-38.098	2.6672	178.53	179.51	0.386	506.4	378.8	298.2	0.0382	1.41×10^5	R_{sat}
4151	-38.100	2.6672	**13.61**	4.795	0.39	506.4	378.8	298.3	0.0000	1.38×10^5	R_{sat}
3577	-39.887	2.6523	0.09	0.031	0.41	522.8	372.8	360.4	0.0045	1.51×10^5	$\theta \sim 0°$
3052	-41.907	2.6705	-15.17	-5.951	0.42	544.4	369.1	434.0	0.0086	1.55×10^5	$Rf_{z,min}$

Continued on next page

Table A.10 continued from previous page

Alt (km)	$\lambda_m(^\circ)$	L	$\theta(^\circ)$	$\theta_{ray}(^\circ)$	μ	f_{pe}	f_z	f_{ce}	t_g (s)	V_g (km/s)	
2068	-46.200	2.7651	-15.75	-7.996	0.08	662.5	417.9	632.5	0.0184	1.74×10^4	before Ref
2054	-46.278	2.7685	-92.29	-94.577	0.02	665.8	419.8	636.1	0.0194	1.78×10^4	Ref
2072	-46.248	2.7713	-169.06	-174.503	0.08	662.3	417.8	631.9	0.0205	3.91×10^4	After Ref
2495	-44.951	2.7788	179.99	179.997	0.34	597.5	386.1	538.4	0.0254	1.34×10^5	$\theta \sim 0^\circ$
3252	-42.286	2.7599	168.62	175.541	0.40	541.7	374.4	409.2	0.0314	1.48×10^5	$Rf_{z,min}$
4151	-38.052	2.6637	153.28	169.242	0.41	506.5	378.9	298.1	0.0398	1.30×10^5	R_{sat}

Table A.11: 10 July 2001: Ray parameters along the ray path for ducted D trace echo for 420 kHz injected at initial wave normal angles 136.395°, 152.584° and 175.364°. The parameters listed in the table are altitude in km, geomagnetic latitude, L-shell, wave normal angle, ray angle, refractive index at wave normal angle, electron plasma frequency, electron cyclotron frequency, Z mode cutoff frequency, group time delay, group velocity, and critical altitude label

Alt (km)	λ_m(°)	L	θ(°)	θ_{ray}(°)	μ	f_{pe}	f_z	f_{ce}	t_g (s)	V_g (km/s)	
4151	-38.100	2.6672	**136.395**	157.13	0.46	506.4	378.8	298.3	0.0000	1.16×10^5	R_{sat}
5049	-33.292	2.5656	-179.974	-179.99	0.28	497.7	399.7	220.0	0.0117	9.92×10^4	$\theta \sim 0°$
6223	-30.711	2.6744	-126.933	-148.26	0.34	474.3	401.5	158.7	0.0273	7.23×10^4	Center of the duct
8182	-20.606	2.6075	90.464	90.92	0.12	461.0	418.1	90.2	0.1509	1.89×10^4	Before Ref
8173	-20.577	2.6047	90.055	90.11	0.11	461.4	418.4	90.4	0.1516	1.77×10^4	Ref
8167	-20.561	2.6032	89.781	89.56	0.11	461.6	418.5	90.4	0.1520	1.56×10^4	After Ref
6964	-27.798	2.6750	-60.231	-40.26	0.31	466.7	406.8	128.8	0.2516	5.81×10^4	Center of the duct
6039	-33.635	2.8103	-0.036	-0.02	0.23	485.4	406.9	172.1	0.2778	7.92×10^4	$\theta \sim 0°$
4155	-38.094	2.6676	39.869	379.62	0.45	506.4	378.8	298.3	0.2989	1.20×10^5	R_{sat}
4151	-38.100	2.6672	**152.584**	168.88	0.416	506.4	378.8	298.3	0.0000	1.30×10^5	R_{sat}
4796	-35.234	2.6274	179.92	179.97	0.335	496.4	390.3	241.0	0.0067	1.20×10^5	$\theta \sim 0°$
5633	-32.917	2.6739	-149.00	-166.72	0.334	481.3	396.2	188.3	0.0156	9.68×10^4	Center of the duct

Continued on next page

Table A.11 continued from previous page

Alt (km)	λ_m(°)	L	θ(°)	θ_{ray}(°)	μ	f_{pe}	f_z	f_{ce}	t_g (s)	V_g (km/s)	
10401	-3.710	2.6439	90.54	91.08	0.038	444.3	419.7	50.6	0.4774	3.91×10^3	Before Ref
10390	-3.704	2.6420	89.99	89.97	0.012	444.5	419.9	50.7	0.4804	9.28×10^2	Ref
10388	-3.704	2.6418	-12.78	-6.47	0.000	444.5	419.9	50.8	0.4818	5.08×10^3	After Ref
5552	-33.220	2.6743	30.72	13.10	0.338	482.4	395.4	193.1	0.9469	9.87×10^4	Center of the duct
4705	-35.560	2.6272	-0.11	-0.04	0.340	498.0	389.2	248.0	0.9557	1.22×10^5	θ ~0°
4151	-37.952	2.6562	-25.12	-9.95	0.408	506.8	379.3	297.8	0.9613	1.31×10^5	R_{sat}
4151	-38.100	2.6672	**175.364**	178.434	0.39	506.4	378.8	298.3	0.0000	1.40×10^5	R_{sat}
4427	-37.107	2.6651	-179.93	-179.975	0.37	500.6	382.5	272.7	0.0024	1.34×10^5	θ ~0°
5044	-35.057	2.6740	-171.37	-177.007	0.34	489.7	389.8	225.2	0.0082	1.19×10^5	Center of the duct
10671	0.198	2.6752	152.83	166.268	0.08	441.9	418.6	48.0	0.2865	2.35×10^4	Center of the duct; equator
5136	34.729	2.6742	-169.39	-176.272	0.34	488.2	390.9	218.9	0.5604	1.17×10^5	Center of the duct
4083	38.780	2.7003	179.99	179.997	0.39	508.9	378.2	306.6	0.5706	1.42×10^5	θ ~0°
2049	45.958	2.7348	-134.37	-152.948	0.11	662.7	417.3	635.2	0.5879	2.16×10^4	Before Ref
2041	46.089	2.7452	-89.49	-88.984	0.06	665.7	419.3	637.8	0.5889	2.03×10^4	Ref
2061	46.108	2.7536	-30.44	-16.329	0.09	662.6	417.7	633.4	0.5898	4.10×10^4	After Ref
4467	36.532	2.6348	-0.03	-0.010	0.36	501.7	385.3	267.9	0.6121	1.29×10^5	θ ~0°
5295	34.159	2.6745	-26.14	-10.487	0.35	485.9	392.7	208.6	0.6202	1.06×10^5	Center of the duct

Continued on next page

Table A.11 continued from previous page

Alt (km)	$\lambda_m(^\circ)$	L	$\theta(^\circ)$	$\theta_{ray}(^\circ)$	μ	f_{pe}	f_z	f_{ce}	t_g (s)	V_g (km/s)	
10667	0.180	2.6746	-72.35	-57.436	0.11	441.9	418.6	48.0	1.0190	1.79×10^4	Center of the duct; equator
6000	-31.550	2.6741	-28.68	-12.110	0.31	476.8	399.6	169.2	1.4211	9.10×10^4	Center of the duct
5211	-35.240	2.7255	0.11	0.038	0.32	490.2	394.0	216.0	1.4322	1.12×10^5	$\theta \sim 0^\circ$
4153	-38.097	2.6673	23.19	8.930	0.41	506.4	378.8	298.2	1.4420	1.33×10^5	R_{sat}

Table A.12: 10 July 2001: Ray parameters along the ray path for ducted C trace echo for 432 kHz injected at initial wave normal angles 6.415° and −19.926°. The parameters listed in the table are altitude in km, geomagnetic latitude, L-shell, wave normal angle, ray angle, refractive index at wave normal angle, electron plasma frequency, electron cyclotron frequency, Z mode cutoff frequency, group time delay, group velocity, and critical altitude label

Alt (km)	λ_m(°)	L	θ(°)	θ_{ray}(°)	μ	f_{pe}	f_z	f_{ce}	t_g (s)	V_g (km/s)	
4156	-38.047	2.6646	**6.415**	1.65	0.433	506.4	379.0	297.7	0.0000	1.54×10^5	R_{sat}
3773	-39.330	2.6613	-0.02	-0.01	0.445	516.3	374.3	337.8	0.0028	1.62×10^5	θ ∼0°
3137	-41.665	2.6743	-11.34	-3.73	0.463	540.0	369.0	421.3	0.0074	1.68×10^5	Center of the duct
3095	-41.831	2.6763	-11.91	-3.98	0.463	542.1	368.9	427.8	0.0077	1.68×10^5	$Rf_{z,min}$
1979	-46.403	2.7563	-13.00	-6.54	0.104	681.2	428.6	654.3	0.0174	2.21×10^4	Before Ref
1959	-46.506	2.7601	-92.35	-94.69	0.017	686.5	431.8	659.7	0.0185	2.14×10^4	Ref
1981	-46.461	2.7628	-172.17	-176.09	0.098	681.5	428.9	654.2	0.0196	4.71×10^4	After Ref
2228	-45.694	2.7665	179.99	180.00	0.310	633.0	402.0	594.8	0.0227	1.26×10^5	θ ∼0°
3330	-41.661	2.7283	163.40	174.32	0.460	534.9	372.2	396.6	0.0309	1.61×10^5	$Rf_{z,min}$
4155	-38.047	2.6642	160.52	174.18	0.450	506.4	379.0	297.8	0.0377	1.47×10^5	R_{sat}
4156	-38.047	2.6646	**-19.926**	-5.998	0.45	506.4	379.0	297.7	0.0000	1.46×10^5	R_{sat}
3334	-41.661	2.7294	-16.62	-5.691	0.46	534.9	372.3	396.1	0.0068	1.60×10^5	$Rf_{z,min}$

Continued on next page

Table A.12 continued from previous page

Alt (km)	$\lambda_m(^\circ)$	L	$\theta(^\circ)$	$\theta_{ray}(^\circ)$	μ	f_{pe}	f_z	f_{ce}	t_g (s)	V_g (km/s)	
2127	-46.048	2.7690	0.01	0.007	0.26	651.2	411.6	618.5	0.0161	1.05×10^5	max excursion, $\theta \sim 0^\circ$
1982	-46.515	2.7685	0.94	0.465	0.09	682.0	429.2	654.4	0.0182	1.97×10^4	Before Ref
1963	-46.573	2.7684	90.07	90.145	0.00	686.4	431.8	659.1	0.0192	1.07×10^2	Ref
1963	-46.573	2.7684	94.21	90.145	0.00	686.4	431.8	659.1	0.0192	4.20×10^2	After Ref
2130	-46.036	2.7690	179.97	179.984	0.26	650.5	411.3	617.7	0.0224	1.07×10^5	max excursion, $\theta \sim 0^\circ$
3332	-41.666	2.7293	163.30	174.306	0.46	534.8	372.3	395.9	0.0316	1.60×10^5	$Rf_{z,min}$
4154	-38.053	2.6645	160.20	174.031	0.45	506.4	379.0	297.5	0.0384	1.46×10^5	R_{sat}

Table A.13: 10 July 2001: Ray parameters along the ray path for ducted D trace echo for 432 kHz injected at initial wave normal angles 155.695° and −168.421°. The parameters listed in the table are altitude in km, geomagnetic latitude, L-shell, wave normal angle, ray angle, refractive index at wave normal angle, electron plasma frequency, electron cyclotron frequency, Z mode cutoff frequency, group time delay, group velocity, and critical altitude label

Alt (km)	λ_m(°)	L	θ(°)	θ_{ray}(°)	μ	f_{pe}	f_z	f_{ce}	t_g (s)	V_g (km/s)	
4156	-38.047	2.6646	**155.695**	172.07	0.460	506.4	379.0	297.7	0.0000	1.42×10^5	R_{sat}
4920	-34.900	2.6349	179.89	179.97	0.388	493.6	390.9	232.2	0.0069	1.36×10^5	$\theta \sim 0°$
6013	-31.506	2.6744	-151.91	-171.20	0.385	476.6	399.7	168.6	0.0177	1.06×10^5	Center of the duct
10861	-0.019	2.7050	166.15	179.73	0.234	442.6	420.0	46.4	0.1552	6.71×10^4	Equator
3112	42.786	2.7636	178.99	179.65	0.437	548.8	374.4	429.9	0.3246	1.64×10^5	$Rf_{z,min}$
1922	45.616	2.6605	-179.15	-179.58	0.034	687.1	431.5	662.6	0.3346	7.93×10^3	Bef Ref
1920	45.631	2.6613	-88.97	-87.94	0.030	687.5	431.7	663.2	0.3350	2.44×10^4	Ref
1943	45.657	2.6713	-47.04	-28.22	0.135	681.4	427.7	657.8	0.3359	5.02×10^4	After Ref
3096	43.021	2.7802	-3.60	-1.28	0.433	550.7	375.4	432.6	0.3452	1.63×10^5	$Rf_{z,min}$
10877	-0.005	2.7075	-27.03	-3.55	0.250	442.8	420.2	46.3	0.5224	5.74×10^4	Equator
6063	-31.314	2.6742	31.27	10.54	0.391	476.1	400.2	166.2	0.6629	1.02×10^5	Center of the duct
4955	-34.657	2.6277	0.13	0.03	0.383	493.7	392.2	229.4	0.6741	1.35×10^5	$\theta \sim 0°$
4155	-38.059	2.6650	-27.54	-9.59	0.468	506.4	378.9	297.9	0.6815	1.39×10^5	R_{sat}

Continued on next page

Table A.13 continued from previous page

Alt (km)	λ_m(°)	L	θ(°)	θ_{ray}(°)	μ	f_{pe}	f_z	f_{ce}	t_g (s)	V_g (km/s)	
4156	-38.047	2.6646	**-168.421**	-176.90	0.438	506.4	379.0	297.7	0.0000	1.52×10^5	R_{sat}
5832	-32.706	2.7054	-179.98	-179.99	0.355	480.1	398.9	179.0	0.0147	1.22×10^5	$\theta \sim 0°$
7288	-26.435	2.6740	164.30	176.48	0.315	463.8	408.7	117.7	0.0337	9.71×10^4	Center of the duct
10803	-0.015	2.6960	163.56	180.26	0.244	442.1	419.3	46.9	0.1411	6.66×10^4	Equator
5106	34.459	2.6500	179.92	179.98	0.385	489.5	391.7	219.9	0.2849	1.35×10^5	$\theta \sim 0°$
4248	37.860	2.6741	-160.97	-174.44	0.446	504.2	379.9	289.4	0.2926	1.45×10^5	Center of the duct
3206	42.132	2.7334	-171.65	-177.23	0.449	541.0	372.1	414.4	0.3009	1.65×10^5	$Rf_{z,min}$
1925	45.773	2.6765	150.32	164.13	0.074	685.9	430.3	662.9	0.3114	1.44×10^4	Bef Ref
1915	45.784	2.6745	-164.77	-177.88	0.000	688.3	431.8	665.3	0.3121	1.62×10	Ref
1915	45.784	2.6745	-85.11	-80.29	0.000	688.3	431.8	665.3	0.3121	2.16×10^4	After Ref
3207	42.130	2.7334	8.37	2.78	0.449	540.9	372.1	414.3	0.3232	1.65×10^5	$Rf_{z,min}$
10803	-0.020	2.6960	-16.41	0.27	0.244	442.1	419.3	46.9	0.4831	6.68×10^4	Equator
7290	-26.425	2.6740	-15.74	-3.53	0.315	463.8	408.7	117.7	0.5904	9.71×10^4	Center of the duct
5841	-32.674	2.7054	-0.06	-0.03	0.355	480.0	398.9	178.7	0.6093	1.22×10^5	$\theta \sim 0°$
4154	-38.053	2.6644	11.54	3.09	0.438	506.4	378.9	297.9	0.6242	1.52×10^5	R_{sat}

Table A.14: 10 July 2001: Table of ray parameters of ducted C trace echo injected at an initial wave normal angle of 8.069° in a duct of half width 0.06 L and depletion 4%. The parameters listed in the table are altitude in km, geomagnetic latitude, L-shell, wave normal angle, ray angle, refractive index at wave normal angle, refractive index in parallel direction, refractive index in transverse direction, electron plasma frequency, electron cyclotron frequency, Z mode cutoff frequency, group time delay, and critical altitude label

Alt (km)	$\lambda_m(°)$	L	$\theta(°)$	$\theta_{ray}(°)$	μ	$\mu(0°)$	$\mu(90°)$	f_{pe}	f_{ce}	f_z	t_g (s)	V_g (km/s)	
4188	-37.7	2.6479	**8.069**	-24.98	0.618	0.589	0.946	506.5	293.8	380.5	0.0000	1.19×10^5	R_{sat}
4146	-38.05	2.6623	6.89	-22.42	0.613	0.592	0.947	506.7	298.6	378.9	0.0006	1.35×10^5	θ,θ_{ray} are decr.
4038	-38.79	2.6893	5.98	-15.97	0.607	0.594	0.937	509.4	310.7	377.2	0.0018	1.62×10^5	min θ
3912	-39.5	2.7106	6.56	-12.02	0.606	0.594	0.921	514.0	324.9	376.6	0.0028	1.74×10^5	θ is incr.; θ_{ray} is decr.
3630	-40.85	2.7437	9.42	-7.90	0.607	0.591	0.889	525.7	358.7	376.1	0.0049	1.79×10^5	
3121	-42.89	2.7753	13.45	-2.40	0.607	0.587	0.848	549.3	429.1	375.1	0.0083	1.87×10^5	$Rf_{z,min}$
2904	-43.63	2.7790	14.54	-0.32	0.602	0.581	0.830	562.2	463.7	376.2	0.0096	1.90×10^5	$\theta_{ray} \sim°$
1923	-46.18	2.7154	26.25	12.04	0.447	0.421	0.588	689.5	666.2	432.6	0.0154	1.57×10^5	
1622	-46.56	2.6535	27.16	14.32	0.109	0.103	0.145	782.1	747.2	493.1	0.0181	2.87×10^4	Before Ref
1610	-46.58	2.6518	-1.13	-0.56	0.035	0.035	0.050	786.9	750.7	496.4	0.0186	1.52×10^4	Ref, $\theta = 0°$
1609	-46.59	2.6524	-90.13	-90.25	0.029	0.021	0.029	787.3	751.2	496.7	0.0188	2.17×10^4	Ref, $\theta_{ray} = 90°$
1621	-46.61	2.6581	-130.99	-150.08	0.123	0.104	0.147	782.2	748.0	493.0	0.0194	4.49×10^4	After Ref
1915	-46.36	2.7312	-153.04	-167.39	0.440	0.413	0.576	693.1	668.8	435.2	0.0222	1.54×10^5	

Continued on next page

Table A.14 continued from previous page

Alt (km)	$\lambda_m(°)$	L	$\theta(°)$	$\theta_{ray}(°)$	μ	$\mu(0°)$	$\mu(90°)$	f_{pe}	f_{ce}	f_z	t_g (s)	V_g (km/s)	
2954	-43.75	2.8053	-162.02	-179.84	0.612	0.581	0.831	560.3	456.7	376.7	0.0283	1.81×10^5	θ_{ray} ~90°
3249	-42.75	2.8003	-162.42	177.08	0.622	0.586	0.853	544.5	411.5	376.3	0.0303	1.70×10^5	$Rf_{z,min}$
3662	-41.08	2.7715	-164.49	171.16	0.626	0.586	0.882	527.2	356.1	378.4	0.0334	1.53×10^5	
4188	-37.71	2.6482	-168.59	151.47	0.645	0.589	0.946	506.5	293.8	380.5	0.0397	8.98×10^4	R_{sat}

Table A.15 10 July 2001: Duct half-width in kilometers at various altitudes for ducts centered at L=2.674.

dL (half-width)	half-width @1000 km	half-width at satellite (4138 km)	half-width at Equator (10,664 km)
0.025	28 km	53 km	159 km
0.04	44 km	84 km	255 km
0.05	55 km	105 km	319 km
0.06	66 km	126 km	382 km
0.08	88 km	168 km	510 km
0.1	110 km	211 km	637 km
0.2	220 km	421 km	1274 km
0.4	440 km	842 km	2548 km
0.5	552 km	1053km	3185 km
0.6	662 km	1263 km	3822 km

Table A.16 10 July 2001: Table of variation of upper cutoff frequency of C trace with ΔL and $\Delta N/N$.

ΔL-$\Delta N/N$		-0.50%	-1%	-2%	-3%	-4%	-5%	-6%	-8%	-10%
0.025	1st Upper	No echo	406	440	450	458	525	528	528	496
	2nd lower	No echo	No echo	490	472	472	No gap	No gap	No gap	No gap
	2nd Upper	No echo	No echo	518	521	523	No gap	No gap	No gap	No gap
0.04	1st Upper	No echo	384	424	442	452	525	527	515	514
	2nd lower	No echo	No echo	491	494	468	No gap	No gap	No gap	No gap
	2nd Upper	No echo	No echo	516	521	523	No gap	No gap	No gap	No gap
0.06	1st Upper	No echo	No echo	398	422	438	448	493	520	518
	2nd lower	No echo	No echo	495	494	497	497	498	No gap	No gap
	2nd Upper	No echo	No echo	507	518	522	522	521	No gap	No gap
0.08	1st Upper	No echo	No echo	386	402	420	436	444	470	519
	2nd lower	No echo	No echo	498	494	496	498	500	501	No gap
	2nd Upper	No echo	No echo	505	511	518	520	520	517	No gap
0.1	1st Upper	No echo	No echo	No echo	392	406	420	432	450	464
	2nd lower	No echo	No echo	No echo	495	495	496	499	503	502
	2nd Upper	No echo	No echo	No echo	508	513	517	519	519	520

Table A.17 26 July 2001: Lower and upper cutoff frequency of ducted traces.

Trace	Lower	Upper
A	195.3 kHz	244.8 kHz
B	194.4 kHz	225.0 kHz
A+B	194.4 kHz	222.3 kHz
2A+B	194.4 kHz	223.2 kHz
A+2B	194.4 kHz	216.0 kHz
2A+2B	194.4 kHz	210.6 kHz
3A+2B	194.4 kHz	208.8 kHz
2A+3B	194.4 kHz	199.8 kHz

Table A.18 26 July 2001: Minimum and Maximum time delays and time delay spread of ducted traces for 208.8 kHz.

Trace	Minimum Tg (ms)	Maximum Tg (ms)	ΔTg (ms)
A	14.4	17.3	3.1
B	62.4	68.8	6.4
A+B	78.4	84.8	6.4
2A+B	97.8	103.9	6.1
A+2B	145.9	152.1	6.2
2A+2B	158.8	164.3	5.5
3A+2B	174.5	177.8	3.3
2A+3B	No Echo	No Echo	

Table A.19 26 July 2001: Duct half-width in kilometers at various altitudes for ducts centered at L = 3.19.

ΔL (half-width)	half-width @1000 km	half-width at satellite (3834 km)	half-width at Equator (13,950 km)
0.025	20	36	159
0.04	33	57	255
0.05	41	72	319
0.06	49	86	382
0.08	65	115	510
0.1	82	144	637
0.2	163	287	1274
0.4	326	574	2548
0.5	408	718	3185
0.6	489	861	3822